Ultrafast Photoluminescence and Photoconductivity Dynamics of Semiconductors

by

Mary Alvean Balmadres Narreto

A thesis submitted in partial fulfillment of the requirements for the degree of

Doctor of Philosophy

Department of Physics

University of Alberta

Abstract

In this thesis, the ultrafast photoluminescence and photoconductivity dynamics of different types of semiconductors are investigated. Using time-resolved photoluminescence and time-resolved terahertz spectroscopy techniques, the origin of the light emission and the nature of carrier transport are examined in detail. Nonlinear carrier transport is also explored using intense terahertz pulses with high peak electric fields.

We used time-resolved photoluminescence spectroscopy to study the fluorescence and phosphorescence dynamics of bismole molecular compounds. The nature of the fluorescence and phosphorescence are related to the 'heavy element effect' of bismuth. In some bismole compounds, the participation of the bismuth atom fascilitates efficient singlet to triplet intersystem crossing that led to phosphorescence. The study is conducted at various temperatures, which provides information on the relaxation processes arising from the excited singlet and triplet states.

Time-resolved photoluminescence spectroscopy is also employed in investigating the photoluminescence of two-dimensional functionalized silicon nanosheets for the first time. The emission is observed to be originating from the as-synthesized hydrogenated silicon nanosheets and thus, despite the functionalizations, all nanosheets displayed similar photoluminescence spectra. The broad photoluminescence spectra exhibit long exponential tails, which show the amorphous character of the silicon nanosheets. These observations are complimented by the photoluminescence decay dynamics that follow an inverse power law, indicating that the carrier transport is governed by a diffusion-limited bimolecular recombination, commonly associated with disordered semiconductors.

We applied time-resolved terahertz spectroscopy to probe the photoconductivity dynamics in macroporous germanium films (or referred as 'germanium films with inverse opal structures'). The disordered nature is evident in the picosecond scale transient photoconductivity and the frequency-dependent photoconductivity that follows the Drude-Smith model of carrier localization. Interestingly, the germanium inverse opals have shown to have high mobility, which makes them exceptional

as wet-chemical processed films for photovoltaic and battery applications. For comparison to an ordered semiconductor, the photoconductivity dynamics of a bulk germanium crystal is also examined and, in this case, different scattering mechanisms are responsible in the changes of its mobility.

The photoluminescence spectra of bulk germanium crystal is also investigated. Germanium is particularly interesting because both emission from its direct and indirect band gaps are observed. The interplay of the direct and indirect photoluminescence is explored at high excitation densities and at high electric field. Under intense THz electric field pulses, the quenching and enhancement of the photoluminescence intensity are interpreted to be a result of THz-induced heating and THz-induced intervalley scattering, respectively. Examining the underlying mechanisms on the ability of intense THz pulses to modulate the photoluminescence in the ultrafast time scale provides additional knowledge to the exciting research on the nonlinear effects of high THz electric fields.

These new findings provide essential information in understanding carrier transport and recombination dynamics from bulk semiconductors to novel nanomaterials.

Preface

This doctoral dissertation is a result of my own original work, at the Ultrafast Nanotools Lab under the direct supervision of Prof. Frank A. Hegmann, except for some of the conducted research which forms part of both local and international collaborations.

Chapter 6 is the result of a collaboration work with the Department of Chemistry at the University of Alberta (UofA) led by Prof. E. Rivard. The outcome of the research has been published as "S. M. Parke, M. A. B. Narreto, E. Hupf, R. McDonald, M. J. Ferguson, F. A. Hegmann, E. Rivard. Understanding the Origin of Phosphorescence in Bismoles: A Synthetic and Computational Study. Inorg. Chem. 2018, 57 (13), 7536-7549 (Journal Cover)." S. M. Parke synthesized the bismoles and performed the absorption measurements of the samples in solution, E. Hupf performed the TD-DFT calculations, while R. McDonald and M. J. Ferguson assisted them. I was responsible for the experimental work and analysis of the absorbance of the bismoles in solid form, time-resolved photoluminescence measurements, and part of the composition of the manuscript, in which Chapter 6 is based.

Chapter 7 is the result of collaborative work with Prof. P. Lugli in the Institute of Nanoelectronics at the Technical University of Munich (TUM), Prof. B. Rieger in the Macromolecular Chemistry - Catalysis Research Center (TUM), Prof. J. Veinot and Prof. V. K. Michaelis in the Department of Chemistry (UofA), and the Department of Physics (UofA) with Prof. F. A. Hegmann as the lead collaborator. A. Lyuleeva (TUM) and T. Helbich (TUM) synthesized the silicon nanosheets. A. Lyuleeva characterized the absorbance and assisted with some of the experimental work during her research exchange visit in UofA. M. Ha performed the NMR measurements. M. J. Kloberg provided the TEM images and Raman spectrum. I was responsible for the time-integrated and time-resolved photoluminescence measurements, analysis of the data, interpretation of the results, and composition of the manuscript. The manuscript, entitled "Photoluminescence Dynamics of Functionalized Two-Dimensional Silicon Nanosheets" will be submitted for a peer-review in which A. Lyuleeva and I are the lead authors (equal authorship) and Prof. F. A. Hegmann is the supervisory author.

The photoluminescence spectroscopy setup (in Section 5.1 of Chapter 5) employed in Chapters 6 and 7 was developed by L. V. Titova. G. de los Reyes performed some of the characterization and calibration of the spectrometer. I modified the setup for low temperature measurements of the time-integrated and time-resolved photoluminescence.

Chapter 9 is a collaboration between the Inorganic Chemistry with Focus on Novel Materials -

Catalysis Research Center (TUM) under Prof. T. F. Fässler and the Department of Physics (UofA), with Prof. F. A. Hegmann as the lead collaborator. M. A. Giebel synthesized the germanium films and performed the Raman spectroscopy. N. Amer assisted with some of the experimental work. I was responsible for the data acquisition and analysis, and interpretation of the results. The manuscript on this work will be submitted for a peer review, with a proposed title "High carrier mobility in photoexcited wet-chemical synthesized Ge films", in which I am the lead author and Prof. F. A. Hegmann is the supervisory author.

Lastly, some of the results presented in Chapters 8 and 10 will be submitted together as one publication. I designed and constructed the experimental setup (Section 5.4) with assistance from C. Huang of the Department of Engineering (UofA) and D. N. Purschke of the Department of Physics (UofA). I conducted the experiments, analyzed and interpreted the data.

I have also presented some of the contents of this dissertation in conferences and symposia listed in Appendix G. The names of the collaborators and contributors are included in the author lists.

For figures, data, and information in this dissertation that I did not acquire, perform, or process, corresponding footnotes are included and other sources have been identified as such.

Acknowledgments

First and foremost, my sincere appreciation to Prof. Frank A. Hegmann, who placed his confidence that I may one day earn my doctoral degree. Thank you for the trust and for sharing your precious time and resources. It is such an honor to be mentored by you in many aspects of my life.

This thesis wouldn't be possible without the Hegmann team. Thanks to Dr. Glenda de los Reyes, Dr. Naaman Amer, David Purschke, Charles Jensen, Chenxi Huang, Dr. Yang Luo, Dr. Vedran Jelic, Cameron Hough, Alex Marin, and Peter Nguyen. I've learned a lot from you. Thanks for the friendship in and outside the lab. I would also like to acknowledge Beipei Shi, Greg Popowich, James Chaulk, and Kailey Robertson for their technical and administrative support.

I would like to thank the Alberta-Technical University of Munich School of Functional and Hybrid Materials (ATUMS) for the opportunity of international and local collaborations, and professional development. It was a pleasure to have interactions with Sarah Parke, Dr. Alina Lyuleeva, Dr. Tobias Helbich, Michael Giebel, Dr. Mori Javadi, Marc Kloberg, Michelle Ha, Josef Mock, Hannah Schamoni, Prof. Vladimir Michaelis, Prof. John Veinot, Prof. Eric Rivard, Prof. Thomas Fässler, Prof. Markus Becherer, Prof. Anna Cattani-Scholz, Prof. Martin Stutzmann, Dr. Sergey Vagin, Justin Pritchard, Ms. Leah Veinot, and the rest of the ATUMS members.

Thank you for the financial support; Doctoral Recruitment Scholarship, Queen Elizabeth II Scholarship, and J Gordin Kaplan Award from the Department of Physics and Faculty of Graduate Studies and Research, ATUMS, GSA Travel Award from the Graduate Student Association, Alberta Innovates Technology Futures Scholarship from the provincial government, and the teaching and research asssitantships from the Department of Physics. In addition, my studies wouldn't go smoothly without the advice of my supervisory committee; Prof. Al Meldrum, Prof. Lindsay LeBlanc, Prof. John Beamish, and the support of the Department executives and staff; Prof. Mauricio Sacchi, Prof. Frank Marsiglio, Prof. Richard Marchand, and Sarah MacKinnon.

Apart from my lab work, I've also enjoyed teaching where I've I worked with Dr. Isaac-Yakoub Isaac, Wladek Rudzinski, Taylor Rogers, and Lorne Roth. In addition, I'd like to mention the executives of the Optical Society of America - Student Chapter and my previous colleagues; Dr. Jaechun Jeon and Dr. Serhat Alagoz, for being part of my university life.

Last but not the least, words are not enough to thank the love of my family. Thank you Mama, Papa, Dr. Ann, Dr. Al, and Angeo. To Dr. Jose Barroso, my life coach and confidante, thank you for your priceless support.

Table of Contents

List of Tables

List of Figures

List of Abbreviations

1D	one-dimensional
2D	two-dimensional
AC	Alternating current
AFM	Atomic Force Microscopy
APD	Avalanche photodetector/photodiode
Bi	Bismuth
BBO	Barium borate
$C_{12}H_{25}$	Dodecene
CCD	Charge-coupled device
CVD	Chemical vapor deposition
DC	Direct current
DS	Drude-Smith
e-h	electron-hole
EO	Electro-optic
F	Fluence
FTIR	Fourier transform infrared
GaAs	Gallium Arsenide
GaP	Gallium Phosphide
Ge	Germanium
Ge-INOP	Ge films with inverse opal structures
HOMO	Highest occupied molecular orbital
InAs	Indium Arsenide
InGaAs	Indium Gallium Arsenide
INOP	Inverse opal
ISC	Intersystem crossing
$LiNbO_3$	Lithium Niobate
LUMO	Lowest unoccupied molecular orbital
OLED	Organic light emitting diode
OR	Optical Rectification
PAA	Polyacrylic
PC	Photoconductivity
PDS	Photothermal Deflection Spectroscopy
PL	Photoluminescence
PS	Polystyrene
QW	Quantum well
QY	Quantum yield
SEM	Scanning electron microscopy
Si	Silicon
SiNSs	Silicon nanosheets
SPAD	Single photon avalanche photodiode
TADF	thermally activated delayed fluorescence
TCSPC	Time-correlated single photon counting

TD-DFT	Time-dependent density functional theory
THz	Terahertz
TIPL	Time-integrated photoluminescence
TRPL	Time-resolved photoluminescence
TRTS	Time-resolved Terahertz Spectroscopy
UV	Ultraviolet
ZnTe	Zinc Telluride

Commonly used symbols:

ΔPL	differential change in the integrated PL
$\Delta PL/PL$	fractional change in the integrated PL
$-\Delta T$	differential negative THz transmission
$\lvert -\Delta T/T_0 \rvert$	absolute relative change in the negative THz transmission
Δt	optical pump - THz probe time delay
λ_{ex}	excitation wavelength
λ_{em}	emission wavelength
λ_p	peak wavelength
E_{ex}	excitation energy
E_{em}	emission energy
E_p	peak energy
E_g	band gap
E_{THz}	THz electric field
E_U	Urbach energy
c	localization parameter [-1,0] (TRTS), inverse power law exponent [0,2] (TRPL)
$g(E)$	density of states
$h\nu$	energy
k_BT	thermal energy
μ	mobility
n	carrier density or carrier concentration
η_R	luminescence efficiency or symbol for quantum yield
$\sigma(t)$	transient photoconductivity (in the time domain)
$\tilde{\sigma}(\omega)$	complex conductivity
σ_{dc}	dc conductivity
τ	lifetime, scattering time

CHAPTER 1

Overview

Investigations of the carrier dynamics of photoexcited semiconductors has been an integral practice in understanding the physics of materials. With the advent of femtosecond pulsed lasers [1, 2] and more sensitive detectors [3] comes the opportunity to observe ultrafast transient response of semiconductors [4, 5, 6]. Ultimately, ultrafast phenomena in semiconductors [7], such as carrier scattering, relaxation, and recombination, can be studied with spectroscopic techniques that leverage time resolutions shorter than the timescale of these events. Especially in cases where the carrier motion is spatially limited by the structure of the material, such as when the average electron displacement approaches the sample's dimensions [8], measurements over ultrafast time scales can be of much more importance.

In this work, the photoluminescence (PL) and photoconductivity (PC) dynamics of different types of semiconductors are investigated using various spectroscopic tools. PL spectroscopy is employed to examine light emission from the visible to near-infrared (NIR) region (400 nm to 2800 nm). In addition, we employ time-resolved photoluminescence spectroscopy (TRPL) [3, 9] for investigating PL dynamics that has a time resolution of 30 ps. In order to access the PC dynamics, we employ time-resolved terahertz spectroscopy (TRTS) [4, 8, 10], which uses an optical pump - terahertz (THz) probe technique, for elucidating the temporal evolution of the charge carrier dynamics on sub-picosecond scales. The femtosecond scattering time of the carriers can also be extracted from the TRTS measurements [11, 12]. Therefore, immediately after the photoexcitation of carriers from their ground states, such ultrafast measurements can reveal the dynamics right from the onset of the carrier motion until carriers decay through time.

The generation of low-energy THz pulses (with a bandwidth of 0.1 - 2.5 THz) provides a means

to perfom linear THz spectroscopy (*i.e.* TRTS) in a non-contact and non-destructive fashion. Furthermore, with the recent development of powerful near-infrared laser sources, generation of THz pulses with strong electric fields (ranging from tens to hundreds of kV/cm) has been made possible in the past decade [13, 14], paving the way for conducting ultrafast nonlinear THz spectroscopy [15, 16, 17]. By combining this intense THz generation technique with other spectroscopic tools, the nonlinear effects of high THz electric field pulses in semiconductors [18, 19] are also explored in this work. The associated wavelengths (as well their corresponding photon energies and frequencies) in the selected region of the electromagnetic spectrum and the relevant timescales in this work are summarized in Figure 1.1.

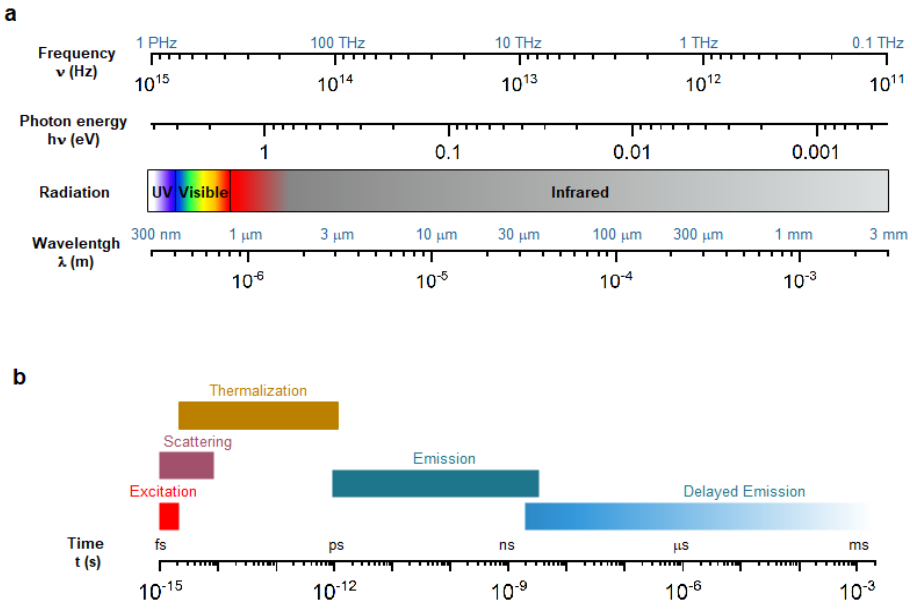

Figure 1.1: ***a)*** *Selected region in the electromagnetic spectrum, which displays the associated frequencies, photon energies, radiation and wavelengths in this work.* ***b)*** *Relevant temporal scales in the investigation of ultrafast processes in this work. Carrier transport from the sub-picosecond scale to the carrier recombination in microsecond scale are studied with various ultrafast spectroscopy techniques.*

Thus, by employing the abovementioned experimental techniques, this thesis attempts to answer fundamental questions in the study of light-matter interaction: What is the origin of the light emission? How do the structure and morphology of a material affect the carrier transport and

recombination? How are these (carrier transport and light emission) affected under strong electric fields? Lastly, would these findings be relevant in new applications, especially in the case of novel nanomaterials? In addressing these questions, the thesis is outlined as follows: Chapters 2 to 4 are dedicated for the relevant background information to support the choice of experimental methods in Chapter 5 and the analysis of the experimental results in Chapters 6 to 10.

In Chapter 2, an overview of the mechanism of photoluminescence is presented. The process of photoluminescence mainly involves the absorption of light, immediately followed by a rapid carrier relaxation, and finally the emission of light. Different recombination processes and recombination rates are discussed and how the band structure contributes to the shape of the emission spectra. As an example, the expected PL spectra of a direct and indirect gap semiconductor is presented. In addition, the mechanism of fluorescence and phosphorescence emissions from a molecular structure is also briefly introduced.

The transport of free and localized carriers is discussed in Chapter 3. Here, we look at established conductivity models in photoexcited semiconductors, namely, the Drude model of free carriers and the Drude-Smith model of carrier localization. The behaviour of the conductivity (as well as the mobility) at various temperatures is also presented. In crystalline semiconductors, the mobility is largely influenced by scattering. While in disordered semiconductors, the mobility is significantly reduced due to short-range transport. Moreover, the behaviour of carrier transport may vary depending on the mechanism of dispersive transport, such as multiple trapping or tunneling.

Topics related to THz pulse spectroscopy are presented in Chapter 4. These include generation of THz pulses by means of optical rectification and the use of tilted pulse front technique for generating THz pulses with high electric fields. The chapter also presents how low-energy THz pulses are used to perform TRTS, whereas intense THz electric field pulses are ultilized in the investigations of nonlinear effects in semiconductors.

Techniques for PL and THz spectroscopy are presented in Chapter 5. The chapter includes PL spectroscopy in the visible and NIR region, TRPL using the time-correlated single photon counting technique, TRTS for measurements of PC in the time and frequency domains, as well as the setup for the modulation of PL *via* intense THz electric field pulses.

In Chapter 6, we investigate the nature of the dual light emission in a series of bismuth-based

molecular compounds (bismoles). The fluorescence and phosphoresence are examined in detail and the experimental observations are complimented by a computational study of their molecular structures.

The PL dynamics of functionalized two-dimensional silicon nanosheets are discussed in Chapter 7. Here, we examine the origin of the light emission and how different functionalizations affect the recombination dynamics. This chapter also provides information on the PL of a disordered semiconductor.

While Chapters 6 and 7 present the PL spectra of novel semiconductors in the visible region, Chapter 8 shows the NIR spectra of undoped and doped bulk germanium (Ge) crystals. The results validate the expected emission spectra from a direct and an indirect band gap semiconductor. The interplay between the direct and indirect PL is also explored at high excitation carrier densities. Moreover, the second part of Chapter 8 examines the carrier transport in undoped Ge at picosecond timescales. By employing TRTS, the transient PC is measured at various excitation fluences and temperatures, and the effect of scattering is examined.

In Chapter 9, contrary to the transport of free carriers in bulk Ge crystals, here we investigate the transport of localized carriers in disordered Ge drop-casted films from a wet-chemical synthesis. We compare the PC dynamics in an unstructured Ge film to its inverse opal counterparts.

Finally in Chapter 10, we combine THz pulses with transient PL measurements in undoped bulk Ge. By varying the photoexcitation fluence and temperature, the interplay of the direct and indirect PL is again explored, this time, under strong THz electric fields. Possible mechanisms for the nonlinear effects of intense THz electric fields on the modulation of the PL are discussed.

The conclusions and future directions of this collective work are presented in Chapter 11.

CHAPTER 2

Photoluminescence in Semiconductors

2.1 Introduction

Photoluminescence (PL) can be simply defined as a spontaneous emission of light after an optical excitation. The process generally first involves photoexcitation of carriers (electrons e) to the excited states by absorption of light energy, leaving unoccupied states, (holes h), at the ground state. Immediately following the excitation, the electrons and holes relax non-radiatively (usually to the lowest possible electronic states by distributing energy among various relaxation channels or by phonon emission) before recombining in the ground state. The recombination involves competition of non-radiative and radiative processes. Finally, the e-h recombination yields to an emission of a photon that has an energy usually lower than the excitation energy. Thus, a PL would typically have three general processes; photoexcitation, relaxation (in the vibrational states), and recombination. Figure 2.1 illustrates the mechanism.

By applying the conservation of energy, the sum of the carrier's initial energy at the ground state E_i and the excitation energy E_{ex} should equate to the final energy of the carrier E_f at the final excited state,

$$E_f = E_i + E_{ex}. \tag{2.1}$$

Thus, the photoluminescence process is generally made possible if the photon energy of the excitation light is greater than or equal to the emission of light, $E_{ex} \geq E_{em}$ (resonance absorption and emission). In a situation where the absorbed photon energy is less than the emitted light, the material may have undergone nonlinear process (nonresonant absorption) such as multiphoton absorption [20, 21].

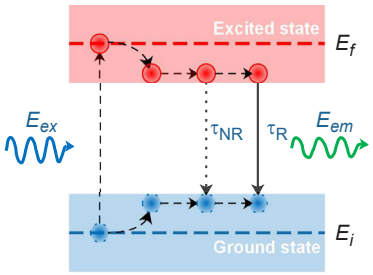

Figure 2.1: Schematic of photoluminescence processes. An electron (red circle) is excited at higher energy states, leaving a hole (blue circle) at the ground state. The carriers rapidly relax to the lowest electronic excited state before the e-h recombination that results to luminescence. The luminescence involves competition of the non-radiative (NR) and radiative processes (R) with their associated lifetimes τ.

As depicted in Figure 2.1, the photoluminescence dynamics in a material is governed by a competition of both non-radiative (NR) and radiative (R) recombinations, where the recombination rates are given as $\frac{1}{\tau_{NR}}$ and $\frac{1}{\tau_R}$, respectively. Thus, the total probability of the transition per unit time is given as

$$\frac{1}{\tau} = \frac{1}{\tau_R} + \frac{1}{\tau_{NR}}. \tag{2.2}$$

The luminescent efficiency η_R, is then determined by the rate of radiative recombination as a fraction of the total recombination rate [22], expressed as

$$\eta_R = \frac{\tau}{\tau_R} = \frac{1}{(1 + \frac{\tau_R}{\tau_{NR}})}, \tag{2.3}$$

where $\eta_R \leq 1$. Therefore, a maximum photoluminescence can be obtained when $\tau_R \ll \tau_{NR}$, indicating that the photoexcited *e-h* pair is more probable to recombine by an emission of photon, than undergo non-radiative recombination. There are a number of possible non-radiative recombination processes. The most common ones are excitation energy being transferred into lattice vibration (phonons), and recombination via impurities and lattice defects [23, 24]. An overview of the recombination processes will be discussed in the next section.

Note that the quantities τ and η_R can be experimentally measured. Hence, one can estimate the radiative lifetime τ_R. In most cases, the η_R is referred as 'quantum yield' (QY) [23, 25], whereby for $\eta_R = 1$, QY = 100%.

The PL process is a non-contact method because it only requires a direct photoexcitation of light (as compared to electroluminescence which needs bias electric fields through contacts [26, 27]). Additionally, with the use of spectroscopic tools employing sensitive detectors for spatially resolving PL spectra and ultrafast measurements for temporally resolving PL decay lifetimes, PL spectroscopy has become a powerful tool in investigating semiconductors. It can deduce the carrier dynamics, transport mechanisms, recombination processes, and band structures [23, 28, 29]. It can also provide information on the materials' optical properties, purity and disorder, as well as their practicality as a light absorber or emitter for scientific and technological applications. Long before the emergence of quantum theory, the investigation of PL mechanisms has already been an active pursuit among scientists in understanding the physics and chemistry of materials [30].

2.2 Photoluminescence decay kinetics

The intensity of the PL decay through time is governed by different carrier recombination dynamics. Here, the kinetics of the carrier population involving the electron concentration n and hole concentration p during the time of recombination can be generally described by the rate equation of the temporal and spatial evolution of the photogenerated carriers [25, 31, 32, 33],

$$\frac{dn}{dt} = D\frac{d^2n}{dx^2} - An - Bn^2 - Cn^3 + G(x,t), \tag{2.4}$$

where D is the diffusion coefficient. A, B, and C represent the coefficients for monomolecular, bimolecular, and Auger recombination rates, respectively. G is the carrier generation rate. The first term in Equation 2.4 accounts for the one-dimensional diffusion from the surface ($x = 0$) to the bulk of the sample (at a spatial dimension x) [31, 32, 34, 35]. Using the Einstein relation, the diffusion coefficient is given as $D = \frac{\mu k_B T}{e}$, where μ is the mobility, k_B is the Boltzmann's constant, T is the temperature, and e is the elementary charge [34]. The second term represents the monomolecular recombination (one-body process, *i.e.* n or p) with a cofficient that gives a constant carrier lifetime $A = 1/\tau$ [23, 28, 31]. The third term is the bimolecular or band-to-band radiative recombination (two-body processes, *i.e.* np) while the fourth term is referred as Auger recombination (three-body process, *i.e.* n^2p or p^2n) [32, 36], which is non-radiative. Lastly, $G(x,t)$ is the rate of optical carrier

generation (*i.e.* by means of laser excitation) [31, 32], expressed as

$$G(x,t) = \delta(t)e^{-\alpha x}, \tag{2.5}$$

which decreases exponentially from the surface of the sample according to the absorption coefficient α, at a specific optical (or laser) wavelength, and $\delta(t)$ is the photon flux temporal profile [34].

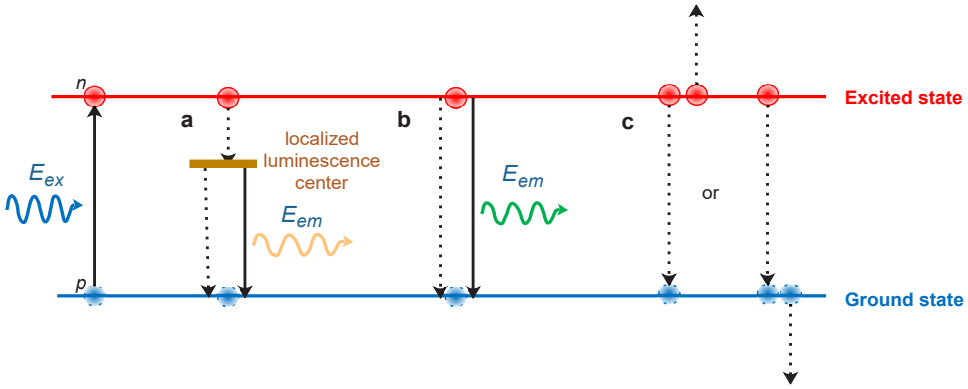

Figure 2.2: Generalized schematic diagram of the three recombination processes, namely, ***a)*** *molecular,* ***b)*** *bimolecular, and* ***c)*** *Auger after the optical excitation. The solid and dashed downward arrows represent the radiative and non-radiative recombinations, respectively.*

For a simple case, the one-dimensional diffusion can be neglected in the assumption that the carrier distribution throughout the sample is treated uniformly [31, 33]. The recombination processes are then illustrated in Figure 2.2. Here, the intensity of the PL decay is calculated from the time integral of the recombination rate, $I(t) \propto \frac{dn(t)}{dt}$, when the optical excitation is turned off ($G(x,t) = 0$).

2.2.1 Monomolecular recombination

The 'one body' process in monomolecular recomobination may constitute an electron or hole, a minority carrier (*e.g.* at low excitation levels or at doped semiconductors) [32], or an exciton that is composed of an already bound *e*-*h* pair [25]. In this recombination process, a localized luminescence center is involved [23]. These centres are usually due to defects and impurities, *e.g.* grain boundaries,

vacancies, dislocations, donors, and acceptors [22, 23, 37]. As exemplified in Figure 2.2a, the photoexcited carrier is captured to one of this intermediate energy-level luminescence center [37] before returning to the ground state. The PL decay rate can be directly solved from the time integral of the second term of Equation 2.4, where

$$I(t) = I(0)e^{-\frac{t}{\tau}}. \tag{2.6}$$

Thus, in most cases where localized radiative centers are involved in the recombination process, the PL decay follows an exponential rate. When two kinds of luminescence centres are involved, then the rate can be described by a bi-exponential decay

$$I(t) = I_1(0)e^{-\frac{t}{\tau_1}} + I_2(0)e^{-\frac{t}{\tau_2}}, \tag{2.7}$$

where τ_1 and τ_2 denote two recombination lifetimes. In addition, there are some actual measurements of PL decay that do not behave exactly exponential but instead follows a stretched exponential decay in the phenomenological form of

$$I(t) = I(0)e^{-\left(\frac{t}{\tau}\right)^{\beta}}, \tag{2.8}$$

where β is called the dispersion factor that ranges at $0 < \beta < 1$ [38]. This PL decay is often observed in disordered systems with broad distribution of lifetimes [39].

In some semiconductors, especially those that are low-dimensional, the recombination processes arising from the surface states (monomolecular) and $e - h$ recombination in the bulk (bimolecular) often compete, which results to variation in the effective recombination rate unless the latter process becomes more dominant [40]. For example, a combination of both monomolecular and bimolecular recombination processes has been observed in luminescence of GaAs quantum wells (QWs) [41]. In this report, the monomolecular case has a coefficient A represented by two competing processes: excitonic radiative and nonradiative recombination due to defects in the barriers or through interface states.

2.2.2 Bimolecular recombination

If the recombination is dominated by a bimolecular process, where electrons and holes recombine directly (as shown in Figure 2.2b), then the PL intensity is proportional to the product $np = n^2$. Therefore, the decay process when the excitation is turned off can be described as

$$\frac{dn(t)}{dt} = -Bn^2, \tag{2.9}$$

which is the third term in Equation 2.4. The parameter B is the bimolecular coefficient, given as $B = B_R + B_{NR}$, which is the sum of the radiative and nonradiative components, respectively. Equation 2.9 leads to

$$n(t) = \frac{n(0)}{(Bn(0)t + 1)}, \tag{2.10}$$

with $n(0)$ as the initial carrier concentration at $t = 0$. The PL intensity, derived as the first order derivative of $n(t)$ [23], is therefore

$$I(t) = \frac{B_R n^2(0)}{(Bn(0)t + 1)^2} = \frac{I(0)}{(Bn(0)t + 1)^2}. \tag{2.11}$$

For longer times, such that $Bn(0)t \gg 1$, then $I(t) \approx I(0)t^{-2}$. Hence, Equation 2.11 illustrates that for a bimolecular recombination, the PL intensity follows an inverse power law decay.

2.2.3 Auger recombination

Lastly, the fourth component in Equation 2.4 represents an Auger recombination, which is a non-radiative process [24], whereby the optical excitation of the material does not result in an emission of light, unlike the monomolecular and bimolecular processes. Because the emission follows $\frac{dn}{dt} = -Cn^3$, Auger recombination is therefore a nonlinear, three-body process. Here, instead of a recombination of an e-h pair, the photoexcited carrier (either e or h) gives off its energy to a third carrier that is promoted to a higher energy level, as illustrated in Figure 2.2c [36]. Such mechanism occurs at high carrier density (usually $\gg 10^{18}$ cm^{-3}), due to high laser excitation fluences. The lifetime, which is

expected to be very fast, can be solved from the fourth component of Equation 2.4 as

$$\tau = \frac{1}{Cn^2} \tag{2.12}$$

As an example, at extremely high excitation energies ($\sim 10^{19}$ cm^{-3}), a competition between Auger process and bimolecular recombination has been observed in the recombination kinetics of GaAs [42]. The Auger decay curve is observed at the initial decay (< 120 ps) before the bimolecular recombination dominates.

2.3 Photoluminescence of Semiconducting Materials

2.3.1 Interband photoluminescence in solid semiconductors

As mentioned earlier in Section 2.1, PL can be essentially described by three processes; (1) absorption, (2) relaxation and finally, the (3) emission of light. This is depicted in Figure 2.3 for the interband transitions in a semiconducting solid. The onset of absorption occurs when the excitation energy E_{ex} is greater than the band gap E_g between the valence and the conduction bands, $E_{ex} > E_g$, which can also be expressed as $h\nu > E_g$, where h is the Planck constant and ν is the frequency of light. Immediately after the photoexcitation, the carriers undergo a rapid relaxation process, typically in the femtosecond to few picosecond scale [5], by giving off phonons as they quickly settle in the conduction band minima (E_c) and valence band maxima (E_v). At this moment, the e-h pair created between these bands recombines radiatively while releasing a photon energy that is close to the band gap energy.

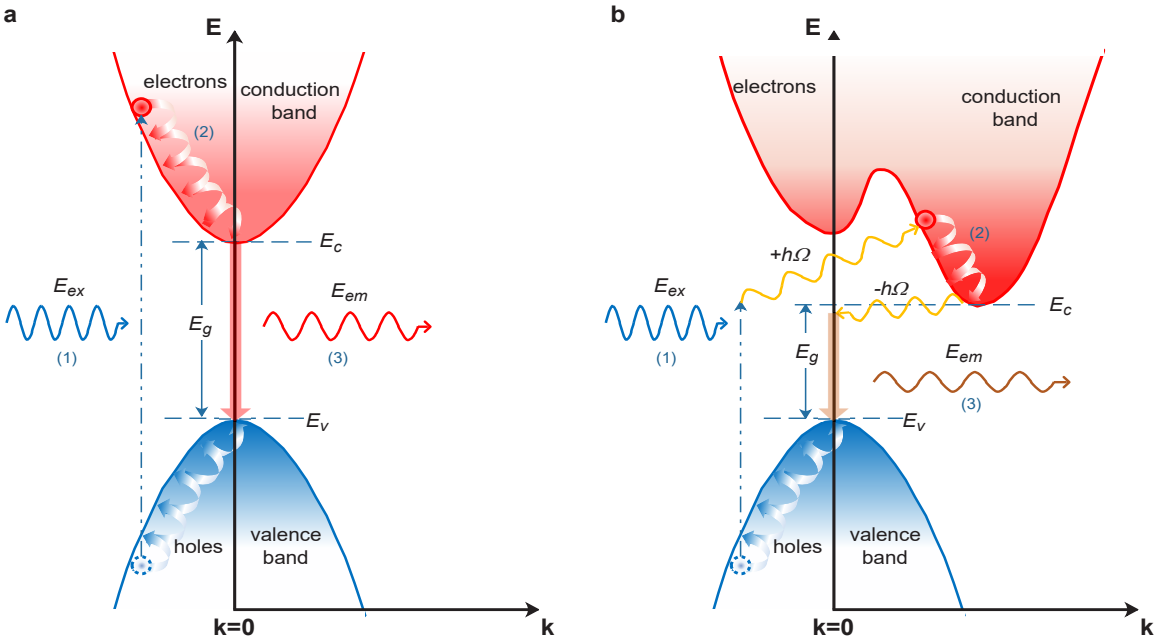

*Figure 2.3: A schematic showing a **a)** direct and **b)** indirect $E-k$ band diagrams of a solid semiconductor with the processes involved in the interband and intraband transitions; 1) absorption, 2) relaxation, and 3) recombination.*

The following sections describe the spontaneous emission from a direct and indirect gap semiconductor. Unlike the radiative transition rates discussed in the recombination statistics in Sections 2.2, here, a semi-classical approach is presented [23, 28, 43].

2.3.1.1 Direct transition

Firstly, the rate of the absorption and spontaneous emission of light is largely determined by transition probabilities. The rate of transitions from the initial to final states is described by the Fermi's golden rule,

$$W_{i\to f} = \frac{2\pi}{\hbar}|M_{if}|^2 g(E), \tag{2.13}$$

which is determined by the quantum-mechanical probability of matrix element M_{if} and the joint density of states $g(E)$ [28], with $\hbar = h/(2\pi)$ as the reduced Planck constant. The matrix element represent the electric-dipole moment in the transition, where the Dirac notation is $M_{if} = \langle f|H'|i\rangle$. H' is the perturbation as a result of the interaction of the material with the light wave (electric field).

Thus, the PL intensity of the spontaneous emission from a direct transition I_{sp-dir} is proportional to the transition rate in Equation 2.13 given as

$$I_{sp-dir} \propto |M_{if}|^2 f(E) g(E), \tag{2.14}$$

where $f(E)$ is included as the probability of occupancy in states, based on the Fermi-Dirac distribution [23].

In an atom or a molecule, the energy states are discrete and thus $g(E)$ is simply the photon density of states in free space. However, for a solid, the initial and final energy states are broadened into continuous bands. In the simplest form, the valence and conduction bands are parabolic in shape due to the energy distribution in the k-space near E_v and E_c (Figure 2.3). In this case, $g(E)$ is described as the number of final states per unit volume that fall within the energy range $E = E_g + \frac{\hbar^2 k^2}{2m_r}$, where m_r is the reduced mass of the electron and hole given as $m_r = \left(\frac{1}{m_e} + \frac{1}{m_h}\right)^{-1}$ [28]. The wavenumber k is expressed as $k = \frac{2\pi}{\lambda}$, where λ is the wavelength of light. Thus, for $h\nu > E_g$, the joint density of electron and hole states gives a numeric value which is calculated as

$$g(E) = \frac{(2m_r)^{3/2}}{\pi\hbar^2}(h\nu - E_g)^{\frac{1}{2}}. \tag{2.15}$$

In order for the e-h recombination to occur, the conduction band states should be occupied while the valence band is empty. Thus, the probability of occupancy is $f(E) = f(E_f)\,[1 - f(E_i)]$ and the e-h recombination gives a photon with energy $h\nu = E_f - E_i$. Here, $f(E_{i,f})$ is the Fermi-Dirac distribution, given as $f(E_{i,f}) = \left[exp\left[\frac{E_{i,f} - E_{Fv,c}}{k_B T}\right] + 1\right]^{-1}$, where $E_{Fv,c}$ is the quasi-Fermi energy level. In the classical limit, such that $(E_i - E_{Fv}) \gg k_B T$ and $(E_f - E_{Fc}) \gg k_B T$, the Fermi-Dirac distribution reduces to a Boltzmann distribution expressed as $f(E_f) \approx exp\left(\frac{E_{Fc} - E_f}{k_B T}\right)$ and $1 - f(E_i) \approx exp\left(\frac{E_i - E_{Fv}}{k_B T}\right)$, respectively [28]. Hence, the probability of occupancy leads to

$$f(E) = f(E_f)[1 - f(E_i)] \approx exp\left(\frac{E_{Fc} - E_{Fv} - E_g}{k_B T}\right) exp\left(-\frac{h\nu - E_g}{k_B T}\right) \tag{2.16}$$

In an equilibrium case (*i.e.* intrinsic semiconductor) at very low temperature, such that $k_B T \ll E_g/2$, $E_{Fv,c}$ stays in the middle of the band gap, whereby $E_{Fv} = E_{Fc}$ [23]. In a non-equilibrium case, the

quasi-Fermi levels E_{Fc} and E_{Fv} determines the population of electrons separately in the conduction and valence bands, respectively, and can be altered at higher doping or at higher injection of carriers by means of photoexcitation, and in this case $E_{Fv} \neq E_{Fc}$.

Then finally, by substituting $f(E)$ and $g(E)$ to Equation 2.14, it is shown that the intensity of the PL from a direct interband transition follows the function

$$I_{sp-dir} \approx D\left(h\nu - E_g\right)^{1/2} exp\left[-\frac{h\nu - E_g}{k_B T}\right], \tag{2.17}$$

where $D = \frac{(2m_r)^{3/2}}{\pi\hbar^2} exp\left(\frac{E_{Fc}-E_{Fv}-E_g}{k_B T}\right)$. By plotting the PL spectral line shape of a direct gap crystalline semiconductor, the full width - half max (FWHM) is estimated as $\sim 1.8 k_B T$, as shown in Figure 2.4.

2.3.1.2 Indirect transition

The band structure for an indirect gap semiconductor is schematically illustrated in Figure 2.3b. In indirect transitions, the absorption and emission is mediated by phonons $\hbar\Omega$ (vibrational energy in the lattice) in order to conserve momentum, whereby $\hbar k_f - \hbar k_i = \hbar k \pm \hbar\Omega$.

Starting with Equation 2.14 and considering the energies at different k-space, the intensity of the spontaneous PL in an indirect transition I_{sp-ind} can be mathematically described by the integration over all pairs of energy states in the conduction and valence bands [23],

$$I_{sp-ind} \approx |M|^2 \int_0^{h\nu+\hbar\Omega-E_g} g_c(E_e) f_c(E_e) g_v(E_h) f_v(E_h)\, dE_e, \tag{2.18}$$

where E_e and E_h are the electron and hole energies with respect to the conduction band and valence band minima, E_c and E_v, respectively (or $E_e = E_f - E_c$ and $E_h = E_v - E_i$). The upper limit of the integral includes all contributions to the flux of emitted photons. With the phonon contribution, the total energy in the transition is $h\nu = E_e + E_g + E_h - \hbar\Omega$. By referring to the solution to Equation 2.15, the density of states $g_c(E_e)g_v(E_h)$ in the conduction and valence bands, in this case, would also have the form

$$g_c(E_e)g_v(E_h) \approx (E_e)^{\frac{1}{2}}(E_h)^{\frac{1}{2}} \approx (E_e)^{\frac{1}{2}}(h\nu + \hbar\Omega - E_g - E_e)^{\frac{1}{2}}. \tag{2.19}$$

In the same manner with Section 2.3.1.1, the expression for the probability of occupancy $f(E)$ in the classical limit follows the Boltzmann approximation, where $f_{c,v} \propto exp\left(-\frac{E_{e,h}}{k_B T}\right)$[28]. This leads to

$$f_c(E_e) f_v(E_h) \approx exp\left[-\frac{h\nu - (E_g - \hbar\Omega)}{k_B T}\right]. \tag{2.20}$$

Hence, Equation 2.18 can be readily expressed as

$$I_{sp-ind} \approx exp\left[-\frac{h\nu - (E_g - \hbar\Omega)}{k_B T}\right] \int_0^{h\nu+\hbar\Omega-E_g} (E_e)^{\frac{1}{2}} (h\nu + \hbar\Omega - E_g - E_e)^{\frac{1}{2}}\, dE_e. \tag{2.21}$$

Using the definite integral solution $\int_0^a x^{\frac{1}{2}}(a-x)^{\frac{1}{2}} dx \approx a^2$ [23], we eventually arrive to the expression for the PL intensity from an indirect gap semiconductor,

$$I_{sp-ind} \approx [h\nu - (E_g - \hbar\Omega)]^2\, exp\left[\frac{-(h\nu - (E_g - \hbar\Omega))}{k_B T}\right]. \tag{2.22}$$

By looking at the spontaneous PL intensity lineshapes of Equations 2.17 and 2.22, it shows that the intensity of the PL is proportional to $(h\nu - E_g)^{\frac{1}{2}}$ for a direct gap semiconductor and $(h\nu - E_g \pm \hbar\Omega)^2$ for an indirect gap semiconductor. Figure 2.4 illustrates the expected PL spectra for both transitions at room temperature (T = 295 K).

The fact that these interband transitions should satisfy both conservation of energy and momentum, the PL in direct transition is more probable compared to that of the indirect because there is no need for the participation of phonons in the absorption and emission processes. The recombination rate happens in a faster scale in a direct gap semiconductor, typically in the nanosecond scale, as compared to an indirect transition, which is in the microsecond scale [44].

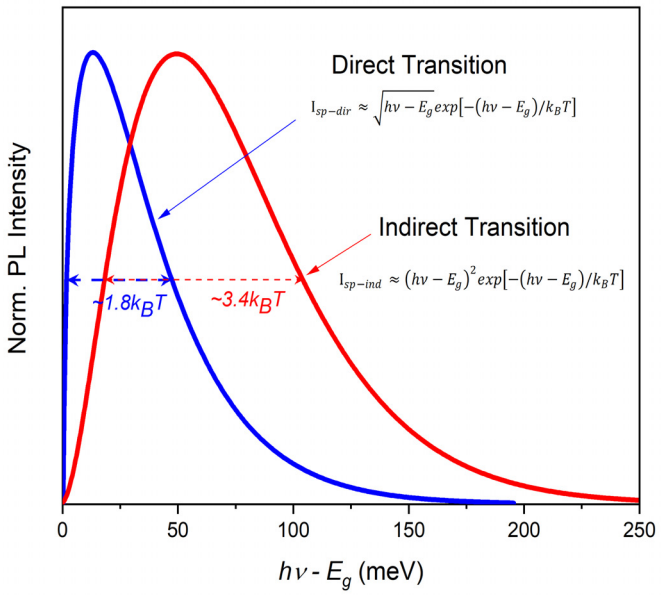

Figure 2.4: PL spectral line shapes of a direct and an indirect gap semiconductor, where the FWHM of each spectrum are indicated. For the indirect gap semiconductor, the $\hbar\Omega$ is considered negligible in the above energy plot. The normalized PL intensities are plotted using $T = 295$ K.

2.3.2 Disordered semiconductors

In disordered systems such as amorphous semiconductors, the bond lengths and bond angles vary, which destroy the long-range ordering of the lattice [45]. Thus, a distribution of shallow localized states would be expected, which influences the behaviour of free electrons in the energy bands [46, 47]. The Mott-Davis model [48] describes this distribution as a tail of localized states extending at the band edge. This band tail was first experimentally observed by Urbach (1953) in the absorption spectrum of semiconductors [49] and was later described by Tauc [50] as the exponential part of the absorption edge, $\alpha \approx exp[h\nu/E_U]$, where E_U is the characteristic energy (Urbach energy) of the band tail (Urbach tail) [26, 51, 52, 53, 54, 55]. Additionally, doping in amorphous semiconductor results in donor and acceptor energy levels that are broadened and become part of this exponential band tail [23]. Thus, for an amorphous semiconductor, the band diagram would look differently from that of a crystalline semiconductor, as depicted in Figure 2.5.

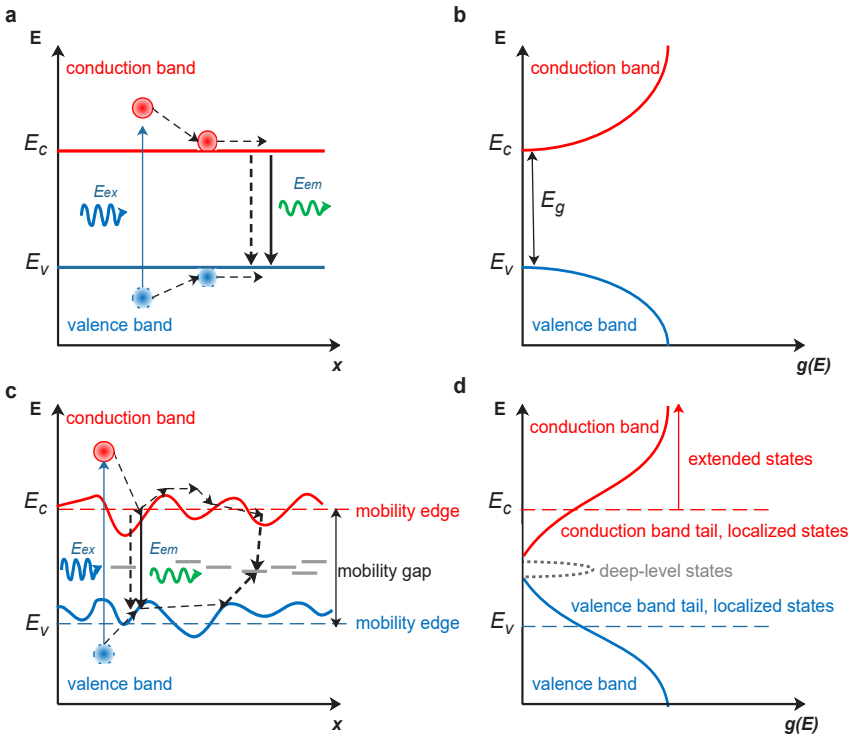

Figure 2.5: Schematic depicting the band diagrams of ***a-b)*** *pristine (free of defects) and* ***c-d)*** *disordered semiconductors.* ***a)*** *The photoexcited electrons and holes rapidly relax or thermalize non-radiatively above the band edges and freely move until they undergo radiative (solid arrows) or non-radiative (dashed arrows) bimolecular recombination.* ***b)*** *The density of states $g(E)$ in the conduction and valence bands follows a parabolic shape.* ***c)*** *After photoexcitation, the electrons and holes undergo rapid thermalization (or relaxation) in the localized states before recombining (which can be described as bimolecular tail-to-tail recombination [45]). Because of the presence of deep-level states, non-radiative trap-assisted recombination in the middle of the band gap may also occur. Alternatively, before the recombination processes, the electrons may undergo multiple trapping or tunneling between the localized states.* ***d)*** *The fluctuations in the energy landscape near the mobility edge (adapted from the 'Alpine' model [47]) still results to a fairly defined conduction and valence bands but with exponential band tails below the mobility edges due to the density of localized states. Electrons are free to move in the extended states above the conduction band mobility edge whereas, they undergo trapping or tunneling in the band tail states. Additionally, the density of deep-level states results in an 'impurity band' in the middle of the mobility gap [48].*

Moreover, breakage or discontinuity in a material may produce unpassivated dangling bonds and vacancies, which act as effective carrier traps. In addition to impurities, these defect concentrations would yield to a density of deep-level states existing in the middle of the band gap [47, 56]. Thus, the gap between the bands are no longer forbidden and there exists a non-vanishing density

of states in the Fermi level that is 'pin' as midgap states [48, 57].

The density of states $g(E)$ above the mobility edges of the conduction and valence bands has a parabolic shape, similar to crystalline semiconductors (Equation 2.15). Below the mobility edge, $g(E)$ scales down exponentially (Figure 2.5d), given as

$$g_l(E) = g_0 \, exp\left(\frac{-E}{E_0}\right), \tag{2.23}$$

where $g_l(E)$ represents the density of the localized states in the conduction and valence bands that starts with an initial density of states g_0 [23]. The energy E used here refers to the energy states below the mobility edge. E_0 is the width of the exponential band tails, which can be directly measured as the Urbach tail slope parameter from an absorption spectrum [58, 59] or PL spectrum [60].

2.3.2.1 Temperature dependence of the photoluminescence intensity

Thermal quenching of the PL has been observed as a common feature in disordered semiconductors [23, 61, 62]. Furthermore, the temperature dependence of the PL intensity $I(T)$ seems to follow an exponential behaviour,

$$\frac{I_0}{I(T)} - 1 = exp\left(\frac{T}{T_0}\right), \tag{2.24}$$

where I_0 and T_0 are both constant values. A collection of experimental observations [61, 62] shows that by properly selecting the value of I_0, Equation 2.24 holds true for all the temperature range of measurements, and that the value of T_0 can be extracted from the slope of the log plots. The characteristic temperature T_0 is related to the width of the band tails.

Here, a model is proposed to satisfy Equation 2.24 [23, 61, 62, 63]. Thermal quenching of the PL can be interpreted according to the models of geminate recombination at low temperature [64], which could be applied in amorphous semiconductors [63]. After photoexcitation and thermalization, the separated *e-h* pair remains bound by their mutual Coulumb interaction (like a geminate pair). At low temperatures, there is a higher probability for the *e-h* pair to recombine radiatively as the electron diffuse to deeper localized states. At high temperatures, the electron can escape from the hole by being thermally activated to higher states in the band tails or above the mobility edge (as

depicted in Figure 2.5c). Thus, the thermal excitation yields to a lower probability of radiative recombination. To distinguish between these two competing mechanisms (whether electrons would escape or not) in the band tails, a temperature dependent binding energy is defined, $E_D(T)$, such that

$$\frac{1}{\tau_R} = \nu_0 \, exp\left(\frac{-E_D}{k_B T}\right), \tag{2.25}$$

where the prefactor ν_0 is the phonon frequency [65]. The above expression entails that $E_D(T)$ is a demarcation energy whereby electrons with this energy have the same probability of non-radiative (escape to the mobility edge) and radiative recombination, and that they are thermalized and have a Boltzmann distribution [23, 61, 66]. The quantum yield (Equation 2.3) is therefore temperature dependent and the rate-limiting process depends on the escape of the electron. It is assumed that the thermal excitation of electron always results to non-radiative recombination, even though this is not an actual non-radiative process [61]. Moreover, for the sake of simplicity, this model neglects the temperature independent non-radiative recombination in the deep-level states [23]. With these assumptions, the temperature dependent quantum yield can be simply solved as

$$\eta_R(T) = \frac{\frac{1}{\tau_R}}{\frac{1}{\tau_R} + \frac{1}{\tau_{NR}}} = \frac{\int_{E_D(T)}^{\infty} g_l(E)dE}{\int_0^{\infty} g_l(E)dE} = exp\left(\frac{-E_D(T)}{E_0}\right). \tag{2.26}$$

Finally, this model acquires an expression of $\eta_R(T)$ that has the same form with the experimentally observed temperature-dependent PL intensity in Equation 2.24. If the quantum yield solely determines the thermal quenching, then $I_0/I(T) - 1 \cong 1/\eta_R(T)$, assuming that $\eta_R(T) \ll 1$. Then both expressions (Equations 2.24 and 2.26) can be combined whereby

$$ln\left(\frac{I_0}{I(T)} - 1\right) = \frac{T}{T_0} = \frac{E_D(T)}{E_0}. \tag{2.27}$$

Therefore, the characteristic temperature T_0 can be related to the band tail widths E_0. Similar to Equation 2.25, this relation can be obtained as

$$E_0 = k_B T_0 ln(\nu_0 \tau_r). \tag{2.28}$$

This also means that the parameter T_0 is very sensitive to the degree of disorder in semiconductors [23].

2.3.2.2 Diffusion-limited bimolecular recombination

Amorphous semiconductors that follow a temperature dependent PL intensity described above (Equation 2.24) would often have PL decays that follow a power law, characteristic of bimolecular recombination. Therefore, such PL decays with bimolecular kinetics can be described using the model presented earlier based on the concept of geminate pair recombination [61, 64, 67].

At earlier times, the PL decays can be well fitted with an empirical power law equation [68, 69, 251, 252],

$$I(t) = \frac{I(0)}{(Bn(0)t+1)^{1+\alpha}}, \tag{2.29}$$

which has the same form in Equation 2.11 but with an exponent of $-(1+\alpha)$ instead of -2. At longer times, such that $Bn(0)t \gg 1$, the PL decay follows

$$I(t) \approx t^{-(1+\alpha)}, \tag{2.30}$$

which has been a general feature of radiative e-h recombination in the band tail states of amorphous semiconductors [61, 72, 73, 74] and polaron recombination in the band tail states of organic semiconductors [75]. It has been observed that α do not reach unity, where $0 < \alpha < 1$. Hence, Equations 2.29 and 2.30 are termed as 'diffusion-limited bimolecular recombination' [68, 75], which refers to a bimolecular recombination resulting from the diffusion of carriers that is limited by the trapping in the band tail states.

The inverse power tail feature was first observed in the transient photocurrent of amorphous semiconductors using time-of-flight (TOF) measurements [76, 77]. It was pointed out that the power law decay of the photocurrent is a result of the distribution of carrier hopping times in an exponential density of traps [66]. The model applied here is the same with the temperature dependence of the PL intensity described in Section 2.3.2.1. Using Equation 2.23 as the density of these trap states and Equation 2.25 as the thermal release time, the distribution of the hopping times would yield to a power law expressed as

$$\psi(t) = \frac{T}{T_0}\nu_0(\nu_0 t)^{-(1+T/T_0)} \sim t^{-(1+T/T_0)} \tag{2.31}$$

for $t > \nu_0^{-1}$ and $0 < T/T_0 < 1$ [66, 67]. Such concept has been the basis of many studies in

explaining the power law dependence of the PL decays in amorphous semiconductors [61]. However, the relation of the exponents in Equations 2.30 and 2.31 is not well established [67]. Some studies [67, 73, 74, 78] have attempted to relate the value of exponent α in Equation 2.30 to different mechanisms of dispersive diffusion of photoexcited carriers in the localized states.

2.3.3 Molecular materials

In comparison with the PL of solids discussed in Section 2.3.1, the concept does not quite differ when it comes to molecular materials such as organic and inorganic compounds. Generally, molecules are composed of elements covalently bonded with groups of atoms. An example is a conjugated system composed of carbon chain of alternating single and double bonds [28], which allows special stability and electron delocalization. Specifically, π-conjugation (*e.g.* electrons in the p orbital of carbon are shared by other atoms) is preferable for producing delocalized electrons. Figure 2.6 shows a generalized schematic diagram for a typical π-conjugated system. The energy difference between the highest occupied molecular orbital (HOMO) and the lowest unoccupied molecular orbital (LUMO) constitutes the energy gap (HOMO-LUMO gap), the E_g counterpart in molecule. The HOMO corresponds to the π-type orbital and the LUMO corresponds to an empty π^*-type orbital, as shown in the unexcited state in Figure 2.6. HOMO and LUMO are the frontier orbitals which establish the way the molecule interacts with other species. The closeness of the orbitals of the different molecules induce the splitting of the HOMO and LUMO energy levels, resulting in vibrational sublevels [79].

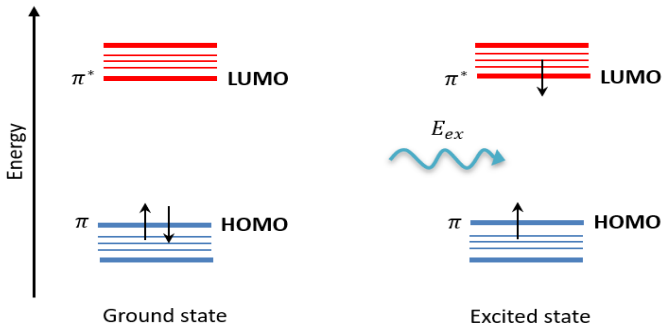

Figure 2.6: Schematic diagram depicting the HOMO-LUMO gap in π-conjugated molecule.

Each occupied orbital in the molecule will contain paired electrons with anti-parallel spins in accordance with the Pauli exclusion principle. In the excitation process, an unpaired electron can be excited to the LUMO level, leaving the other unpaired electron in the HOMO level (as shown in the excited state in Figure 2.6). Then, in the similar manner with PL processes, the photoexcited electron undergoes non-radiative vibrational relaxation before it decays to the ground state accompanied by an emission of light.

In any given electronic state, the spin multiplicity can be either a singlet (electrons having opposite spin orientation (paired)) or triplet (electrons with the same spin orientation (unpaired)) [80]. The selection rules dictate that the spin multiplicity should be maintained during the excitation process, thus the initial transition happens between singlet states, as illustrated in the Jablonski diagram in Figure 2.7. If the excitation energy is much higher than the onset of absorption, the electron can be excited to a higher vibrational level or a higher singlet state (*e.g.* S_0 to S_2). Then, the excited electron undergoes relaxation non-radiatively (*e.g.* from S_2 to S_1) by means of 'internal conversion' of *like* spin multiplicity, which occurs typically in picosecond scale [80]. Finally, the recombination process (*e.g.* from S_1 to S_0) results to an emission of photon energy that is less than the absorbed photoexcitation energy. The difference between the absorption and emission spectra is referred to as 'Stokes shift'. In some cases, the electronic levels can be perceived as the multiple peaks occuring in the absorption and emission spectral profiles.

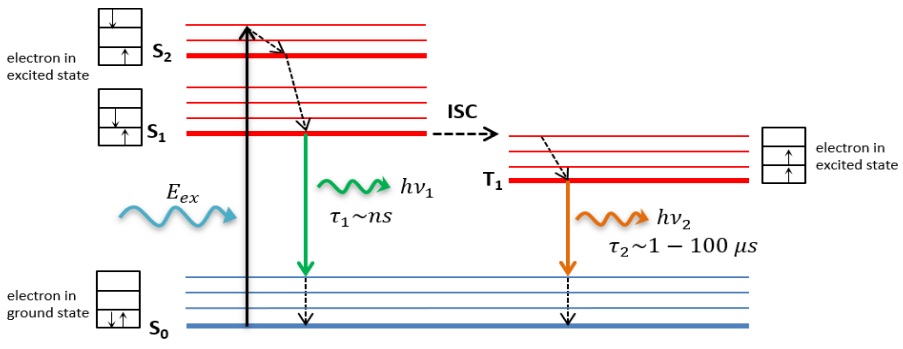

Figure 2.7: Jablonski diagram describing a general mechanism in molecular materials where emission of light happens in both singlet to singlet ($h\nu_1$) and singlet to triplet states ($h\nu_2$).

In addition, in some molecular materials, a small probability of emission from the triplet state can also occur by means of intersystem crossing (ISC), as shown in Figure 2.7 [28, 30, 80]. In the ISC process, the electrons undergo a spin-coupling exchange due to the *different* spin multipicity. Thus at this point, the spins in triplet and singlet ground state are parallel, making the de-excitation process highly improbable due to the 'forbidden' nature of the transition. If the recombination from the triplet to singlet states (*e.g.* T_1 to S_0) is to occur, the process will take longer because the electron has to undergo a spin-flip before it returns to the ground state.

Therefore, the PL in such materials can be classified into two forms; fluorescence, which is a short-lived emission of typically nanosecond scale that occurs from the singlet-singlet transition, and the phosphorescence, which is a long-lived emission that can last from microsecond to second timescales occurring from the triplet-singlet transition [28]. In most cases, the triplet state is of lower energy compared to the singlet state, which results to phosphorescent light that has a longer wavelength as compared to the fluorescence.

CHAPTER 3

Photoconductivity in Semiconductors

3.1 Introduction

Photoconductivity (PC) describes how a material becomes electrically conductive upon the absorption of light. With the photogeneration of free carriers (as depicted in Figure 3.1), the semiconductor becomes more conductive, which can be influenced by factors such as electric field, carrier density, and mobility. Investigating the PC could provide significant information on different carrier transport mechanisms and can offer insights on the structure and electronic properties of the semiconductor [57]. In describing the PC in different semiconductors, fundamental terms such as mobility, carrier lifetimes, and drift velocity are commonly used. Additionally, understanding the mechanism of the PC dynamics may require the use of appropriate models. In this Chapter, it is hoped that these concepts can be explained briefly, in line with the analysis of experimental results in the latter part of this thesis.

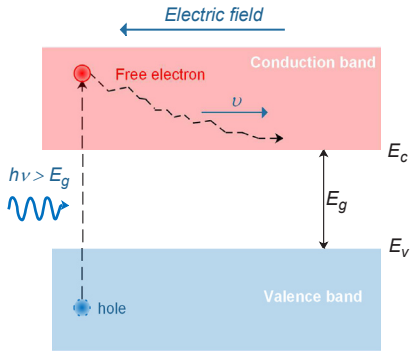

Figure 3.1: Schematic of the photoconductivity in semiconductors. The excitation of light that has an energy greater than the band gap generates a free electron in the conduction band. The photoexcited electron moves freely in the conduction band with a mean drift velocity v in the opposite direction of the applied electric field.

3.2 Transient photoconductivity

Measurement of the time dependent PC is a powerful technique for studying the mechanism of charge transport in photoexcited semiconductors. In a standard transient PC measurement, the free carriers are excited into the transport band at $t = 0$ by a short pulse of light, as illustrated in Figure 3.1. The photogenerated free carriers are then moved along by the electric field until their eventual disappearance through recombination [81]. Hence, the magnitude of the photoconductivity is governed by the photogeneration of free carriers (which depends on the excitation energy and fluence), the transport of these free carriers under the influence of the electric field (which can be limited by scattering events), and the recombination of the photoexcited electrons and holes [57]. Therefore, the transient PC is proportional to the decay of the photogenerated carriers, $\sigma(t) \propto n(t)$. Since transient PC measurements can be accessed using ultrafast techniques, different carrier transport mechanisms can be explained from picoseconds to longer times, and a wealth of information on the properties of the material can be obtained.

3.2.1 Monomolecular and bimolecular processes

As discussed in Section 2.2.1, a monomolecular process involves an excess charge carrier. The population of the carriers $n(t)$ decays in an exponential manner given by

$$n(t) = n(0)e^{-\frac{t}{\tau}}, \tag{3.1}$$

where $n(0)$ can be described as the number of free carriers excited at $t = 0$ using an ultrashort pulse of light, and τ is the average mean lifetime of the carriers [23]. The monomolecular process mostly competes with the bimolecular processes in bulk semiconductors and thus, in most cases the single exponential decay is only observable in the earliest timescale. A single exponential behavior has been observed in the picosecond scale transient PC of organic semiconductors [82, 83, 84], which has been attributed to carrier trapping at grain boundaries and deep-level traps at the interfaces between crystallites.

For the bimolecular process, presented in Section 2.2.2, the carrier density decays in the following form,

$$n(t) = \frac{n(0)}{(Bn(0)t + 1)}, \tag{3.2}$$

where B is the bimolecular coefficient. Equation 3.2 also entails that at higher excitation densities $n(0)$, the PC should decay faster. However, at longer times such that $Bn(0)t \gg 1$, the carrier density would have the time dependence of

$$n(t) \sim t^{-1}, \tag{3.3}$$

and the decay becomes independent of $n(0)$. The t^{-1} dynamics has been experimentally shown in transient PC of highly ordered conjugated polymers [6, 85].

3.2.2 Dispersive photoconductivity in disordered semiconductors

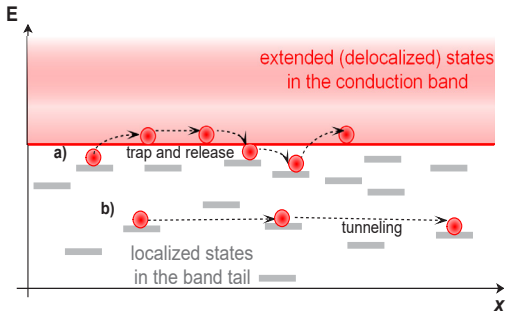

Figure 3.2: Illustration of the two carrier hopping mechanisms: ***a)*** *multiple trapping and release, and* ***b)*** *tunneling.*

The carrier transport in disordered semiconductors is determined by the carrier hopping in the band tails (refer to Section 2.3.2.2 and Figure 2.5). Figure 3.2 illustrates the carrier hopping either by multiple trapping and release or tunneling. Scher and Montroll (1975) were among the first to desribe such carrier transport in the the transient PC of disordered systems [76]. Due to the dispersion in the separation distance between the nearest-neighbor localized sites available for the hopping of carriers, the distribution of these hopping times would have a long tail, following the form,

$$\psi(t) \sim t^{-(1+\alpha)}, \quad 0 < \alpha < 1. \tag{3.4}$$

Thus, the 'transit-time' dispersion in amorphous solids does not follow the bimolecular process of t^{-1} dependence. Instead, α is included in the power law exponent indicating large hopping-time dispersion. The theory is also based on the concept of charge carriers undergoing a random walk along the preferred direction by the applied electric field. The addition of the dispersion factor α implies that as time becomes longer, the succession of carrier hopping from one site to another becomes increasingly longer. The carrier tranport can be pictured as a Gaussian 'carrier packet' that suffers a wider statisical dispersion at longer times due to the variation of hopping distances [77]. At $t > 0$, the mean position of the carrier packet increases with time, but with a decreasing rate. In other words, shallower states release trapped carriers sooner, then retrapping of these carriers will lead to increased occupation of the deeper states, which results in a reduction of the photocurrent

[57].

The inverse power law behaviour was first observed in photocurrent decay dynamics of amorphous chalcogenide (As_2Se_3) [53] and hydrogenated amorphous Si (a:Si-H) [86] using time-of-flight (TOF) measurements. It was observed that the initial current decay is slower and then undergoes a transition to a faster inverse power law decay. When a reasonable fraction of carriers (10%) reach the electrode, the current begins to decrease at a faster rate due to carrier loss [76, 87]. The measured current decay has a crossover point at the transit time t_r such that

$$I(t) = \begin{cases} \sim t^{-(1-\alpha)}, & t < t_r \\ \sim t^{-(1+\alpha)}, & t > t_r. \end{cases} \tag{3.5}$$

The approximation of t_r was found out to be related to the thickness of the sample d and applied electric field E, which remarkably provides the value of the drift mobility in dispersive transport, defined as $\mu_d = d/(t_r E)$ [77, 88].

Subsequent studies performed by Tiedje *et al.* [66, 89] proposed that the dispersion parameter α reveals information on the degree of the disorder in the amorphous semiconductor. The value of α changes at low temperatures, where

$$\alpha = \frac{T}{T_0}. \tag{3.6}$$

The characteristic temperature T_0 is related to the width of the exponential band tail of localized states (expressed in Equation 2.28) but the temperature-dependence (Equation 3.6) only applies in the context of thermally-activated multiple trapping mechanism (as discussed in Section 2.3.2.1). At low temperatures, carriers tend to condense deeper into the traps which follows an exponential distribtution (exponentail tail states) [90]. At high temperatures, electrons with sufficient thermal energy can undergo multiple trapping and release between localized tails and above the conduction band mobility edge. However, more elaborate investigations could not confirm the temperature dependence of the power law exponent in Equation 3.6 [91, 92]. Also, for a transport mechanism of hopping by tunneling, Equation 3.6 no longer applies. In this case, the photoexcited electrons either tunnel to neighboring localized sites with the same energies [93]. Thus, temperature may not play a role in the hopping by tunneling mechanism unless thermally assisted [75].

3.3 Drude model of free carriers

In this section, the dc and ac photoconductivity in semiconductors is described in accordance with the Drude model. This model is essential in investigating the THz photoconductivity of semiconductors, presented in Chapters 8 and 9.

In the 19th century, Paul Drude proposed a model of thermal and electrical conductivity, where he treated metals as a classical gas of electrons executing a diffusive motion [94]. The assumption in this model is that scattering only occurs between electrons and ions, impurities, lattice vibration, etc. and not between them (electron-electron interaction is neglected). In the absence of an electric field, the electrons in a solid move in all possible directions with an average thermal velocity $\upsilon_{th} = \sqrt{3k_BT/m}$ and a mean free path of $l = \upsilon_{th}\tau$, where τ is the average time between scattering events [57, 95]. The random motion results in the individual velocities of the electrons cancelling with each other, leaving a zero net drift velocity υ. With an applied electric field E, the electrons acquire a mean υ (that is opposite in the direction of E (Figure 3.1)). The electron motion can be described with the velocity distribution due to the electrostatic force and friction force, given by

$$m\frac{d\upsilon}{dt} = -m\frac{\upsilon}{\tau} - eE. \tag{3.7}$$

3.3.1 DC photoconductivity

For a steady-state case (dc electric field), $\frac{d\upsilon}{dt} = 0$. Thus, from Equation 3.7, the electrons eventually reach a maximum drift velocity

$$\upsilon = \frac{e\tau}{m}E. \tag{3.8}$$

The above expresssion introduces an important parameter in DC transport, which is the carrier mobility μ, defined as

$$\mu = \frac{e\tau}{m} = \frac{\upsilon_d}{E}, \tag{3.9}$$

describing how quickly an electron moves through the material with an applied electric field.

For a carrier concentration n, the drift velocity gives rise to a current density J given by $J = ne\upsilon$. Using Ohm's law, where $J = \sigma E$, we can now express the dc conductivity σ using

Equations 3.8 and 3.9 as

$$\sigma_{dc} = \frac{J}{E} = \frac{ne^2\tau}{m} = ne\mu = \omega_p^2\epsilon_0\tau, \tag{3.10}$$

which shows that the conductivity of the material is highly dependent on the carrier concentration. Knowing σ_{dc} would also allow us to extract an important parameter in materials, which is the plasma frequency given by

$$\omega_p^2 = \frac{ne^2}{\epsilon_0 m}, \tag{3.11}$$

where ϵ_0 is the permittivity in free space.

3.3.2 AC photoconductivity

With an applied ac electric field of frequency ω, the corresponding conductivity of a material will also be frequency-dependent. Using a Fourier transform property $\frac{d^n[f(t)]}{dt^n} \longrightarrow (i\omega)^n F(\omega)$ to Equation 3.7, the frequency dependent free electron Drude model takes the form,

$$-im\omega v(\omega) = eE(\omega) - m\frac{v(\omega)}{\tau}. \tag{3.12}$$

We again solve for the conductivity from the Ohm's law, $\sigma(\omega) = J(\omega)/E(\omega) = nev(\omega)/E(\omega)$, where $v(\omega)$ can be obtained from Equation 3.12. The solution brings us to the expression of a complex ac conductivity

$$\tilde{\sigma}(\omega) = \frac{ne^2\tau}{m(1 - i\omega\tau)}. \tag{3.13}$$

By incorporating σ_{dc} from Equation 3.10, we can re-write the above expression as

$$\tilde{\sigma}(\omega) = \frac{\sigma_{dc}}{1 - i\omega\tau} = \sigma_1(\omega) + i\sigma_2(\omega), \tag{3.14}$$

where the real and imaginary parts of the complex ac conductivity can be expressed as

$$\sigma_1(\omega) = \sigma_{dc}\frac{1}{1 + (\omega\tau)^2} \tag{3.15}$$

$$\sigma_2(\omega) = \sigma_{dc}\frac{\omega\tau}{1 + (\omega\tau)^2}, \tag{3.16}$$

and these parts would yield $\sigma_2(\omega)/\sigma_1(\omega) = \omega\tau$.

For well-known bulk semiconductors, typical scattering times range from 200 - 400 fs, as presented in Table 3.1. Taking a value of $\tau = 200$ fs, would produce an ac conductivity plot displayed in Figure 8.6. Notice that the frequency at which the real and imaginary parts of $\tilde{\sigma}(\omega)$ intersect at $f_c = 1/(2\pi\tau)$, which is equivalent to 0.8 THz. This "crossover" frequency [10], where $\sigma_1(\omega) = \sigma_2(\omega)$, happens to be in the THz frequency. This illustration implies that a spectroscopic technique utilizing a THz probe with a bandwidth of 0.1 to 3 THz would be ideal for measuring the complex conductivities of typical bulk semiconductors.

Table 3.1: Electron mobilities of well-known semiconductors at T = 300 K [96].

Semiconductor	**Mobility** μ_e (cm^2/V·s)	**Effective mass*** $m_{e,\sigma}/m_0$	**Scattering time**** τ (fs)
Germanium	≤ 3900	0.12	≤ 266
Silicon	≤ 2000	0.26	≤ 296
Gallium Arsenide	≤ 9200	0.067	≤ 351

*effective mass for conductivity calculations, **calculated using Equation 3.9

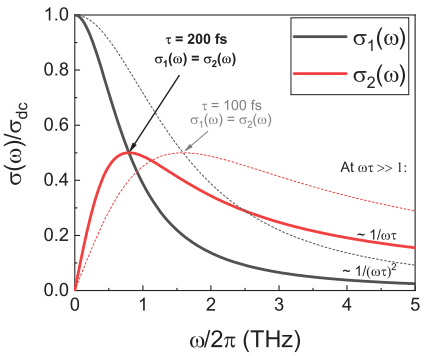

Figure 3.3: Plot of the ac complex conductivity at THz frequencies following the Drude model. The solid and dashed lines are plots for $\tau = 200$ fs and $\tau = 100$ fs, respectively.

3.4 Drude-Smith model of carrier localization

In many experimental cases, a departure from the Drude model for free carriers has been observed. The ac complex photoconductivity response of these cases show distinct behaviour; 1) a suppressed $\sigma_1(\omega)$ and negative $\sigma_2(\omega)$ at lower frequencies, and 2) the oscillator strength is shifted to higher frequencies. To account for these effects, Smith developed a modification of the Drude model, which goes beyond the relaxation time approximation [97, 98]. In Drude photoconductivity, as presented in Section 3.3.2, scattering of the carriers results in a velocity (or momentum) that is completely randomized. In the Drude-Smith model, which was derived using an impulse response approach and Poisson statistics, memory effects in the scattering of carriers are incorporated [97, 98]. This means that a fraction of the electron's original velocity is retained after the first and subsequent collisions. Simply put, a memory of the velocity prior to scattering influences its velocity after the scattering. The Drude-Smith model is expressed as

$$\tilde{\sigma}(\omega) = \frac{\sigma_{dc}}{1 - i\omega\tau}\left[1 + \sum_n \frac{c_n}{(1 - i\omega\tau)^n}\right], \tag{3.17}$$

where the last term in square brackets is a correction term to the Drude formula shown in Equation 3.14. The coefficient c_n represents the 'persistence of velocity' at the nth collision, and the value ranges from 0 to -1. For a single scattering event, the above equation is reduced to

$$\tilde{\sigma}(\omega) = \frac{\sigma_{dc}}{1 - i\omega\tau}\left[1 + \frac{c}{1 - i\omega\tau}\right], \tag{3.18}$$

which can be separated into the real and imaginary parts,

$$\sigma_1(\omega) = \frac{\sigma_{dc}}{[1 + (\omega\tau)^2]^2}[1 + (\omega\tau)^2 + c(1 - (\omega\tau)^2)] \tag{3.19}$$

$$\sigma_2(\omega) = \frac{\sigma_{dc}\omega\tau}{[1 + (\omega\tau)^2]^2}[1 + (\omega\tau)^2 + 2c]. \tag{3.20}$$

The scattering rate in the context of Drude-Smith model of carrier backscattering would have the form

$$\frac{1}{\tau_{DS}} = \frac{1}{\tau}(1 + c), \tag{3.21}$$

and thus the macroscopic mobility is reduced to

$$\mu_m = \frac{e\tau_{DS}}{m}. \tag{3.22}$$

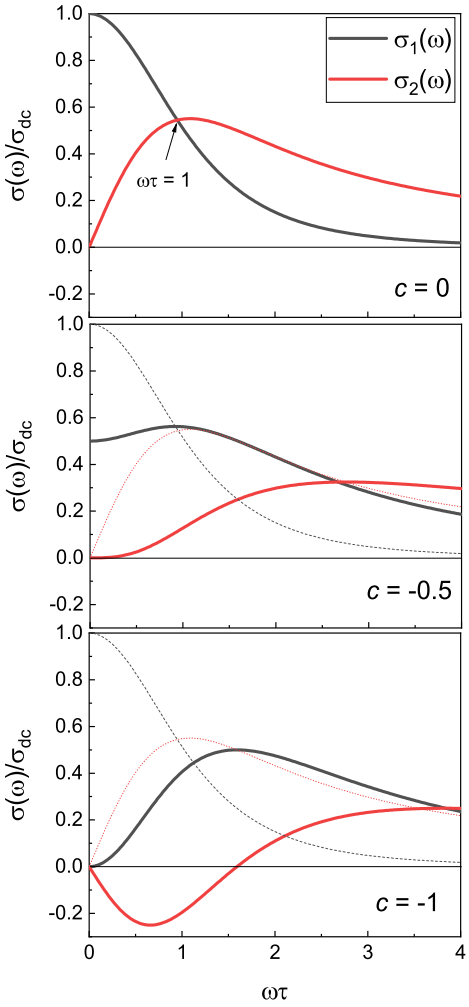

Figure 3.4: Illustration of the Drude-Smith complex conductivity with the changes in the c parameter. Dashed and dotted lines are guides to the eye for the Drude response with $c = 0$, respectively.

The value for c describes the degree of carrier localization. For $c = 0$, the Drude-Smith conductivity (Equation 3.18) is recovered to the Drude formula (Equation 3.14), which is characterized

by an elastic collision of carriers with isotropic scattering [99]. For negative values of c, the carriers undergo backscattering due to carrier localization effects in the material. For full localization or 100% probability of carrier backscattering, where $c = -1$, the complex conductivity results in a $\sigma_1(\omega)$ that is completely suppressed, such that it reaches a value of $\sigma_1(0) = 0$, becoming an insulator for DC fields. Also, $\sigma_2(\omega)$ would have the most negative value. This behaviour is shown in Figure 3.4.

The crude approximation made in Equation 3.18, with the assumption that carrier backscattering happens at single sattering event, has drawn a few criticisms. Thus, other models have also been applied, such as effective medium theories (EMT), Maxwell-Garnett, and Bruggeman EMT, which take into consideration local fields around nanostructures, nanostructure shape, and filling fraction [100]. However, these models require multiple fit parameters in contrast to the simplicity of the Drude-Smith model that already describes the overall conductivity of the entire system without considering other contributions. Nevertheless, the Drude-Smith model, in its phenomenological form, has been fairly accurate in describing carrier dynamics in materials which exhibit carrier confinement or disordered systems, where the confining structure is comparable to the carrier mean free path [11]. Firstly, Smith was able to fit the Drude-Smith model to the conductivity of liguid metals, such as Hg and Te, and quasicrystals which are on the borderline of nonconducting behaviour [97]. Subsequently, the model has been extensively applied in other kinds of structurally confined photoexcited semiconductors. Some of these examples are: nanocrystalline Si (carrier localization within grains and immobile at SiO_2 insulating barriers) [101, 102], polycrystalline silicon thin films (in addition to structural confinement, higher carrier density also impedes conduction at the surface of the films) [103], metal-insulation transition in vanadium dioxide (VO_2) (carrier confinement within the nanograins during the formation and decay of metallic state) [104, 105], indium tin oxide nanowire networks (morphological changes affecting the conductivity), organic semiconductors [10] and conjugated polymers such as polymer-fullerene films (charge carriers are partially localized while some undergo complete localization or charge neutral state (exciton)) [106], and two-dimensional nanomaterials such as graphene nanoribbons (GNRs) and carbon nanotubes (CNTs) (carrier backscattering along the long axis of GNRs and CNTs) [107].

In general, the Drude-Smith model has been successful in describing carrier localization in the mesoscopic scale. Besides the coefficient c, another important parameter that can be extracted

using the Equation 3.18 is the scattering time, which could be very short at only few femtoseconds. This corresponds to a carrier mean free path on the order of intermolecular distance and thus results to significantly lower values of mobilities [4]. With this in mind, the Drude-Smith model is also considered as one of the conductivity models of 'weak localization' in disordered systems that lack long-range carrier transport.

3.5 Temperature dependent mobility and photoconductivity

Charge transport in photoexcited semiconductors may vary depending on the band structure, the degree of crystallinity, and the purity of the material. Investigating the conductivity and mobility under different conditions, such as temperature, may provide these information.

3.5.1 Bulk crytalline semiconductors

The mobility in crystalline semiconductors can be influenced by a variety of scattering mechanisms. For instance, in different temperature regimes, different scattering events can occur; 1) scattering due to lattice vibrations (deformation potential), and 2) scattering due to ionized impurities. The average scattering time τ in these scattering mechanisms can be estimated, assuming a Maxwell-Boltzmann distribution and a parabolic band [57], which yields a dependence of the mobilities as a function of temperature,

$$\mu_L \propto \frac{4e}{m\sqrt{9\pi k_B}} T^{-\frac{3}{2}}, \tag{3.23}$$

$$\mu_I \propto \frac{8e k_B^{-\frac{3}{2}} n_I}{m\sqrt{\pi}} T^{+\frac{3}{2}}, \tag{3.24}$$

where μ_L and μ_I are the mobilities influenced by lattice and impurity scattering, respectively, and n_I is the concentration of ionized impurities. The two scattering mechanisms dominate within certain temperature regimes. As temperature is lowered, the suppression of lattice vibrations cause the mobility to increase (with $T^{-\frac{3}{2}}$ dependence). But at a certain point, the mobility starts to decrease due to ionized impurity scattering (with $T^{+\frac{3}{2}}$ dependence). As the charged carriers (*e.g.* electrons) lose thermal velocity, they can no longer escape from interacting with ionized impurities. Thus, at short distances, the local Coloumb field, created between the impurity ion and the charged

carrier within the vicinity, causes the mobility to decrease [108]. This typically occurs at very low temperature, when the thermal energy k_bT becomes much less than the ionization binding energies. Thus, the behaviour of an experimentally measured mobility (or conductivity) at extremely low temperatures may act as a tool for determining the purity of the material. An illustration of the temperature dependent mobility is shown in Figure 3.5.

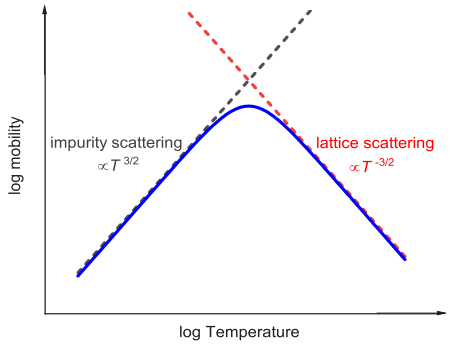

Figure 3.5: Schematic of expected mobility as a function of temperature (blue solid line) for bulk crystalline semiconductors, with the lattice (red dashed line) and impurity (black dashed line) scattering contributions.

For example, in Ge, the dominant scattering transitions at T $\sim$ 100 K from μ_I to μ_L. Note that this temperature dependence may only hold for nonpolar crystals such as Ge and Si. In polar semiconductors like GaAs, besides deformation potential, polar optical scattering may also dominate at higher temperatures [54].

Impurities can be deliberately introduced by doping a semiconductor. In practice, for covalent semiconductors (*e.g.* Si, Ge), the decreasing mobility behaviour is only observed at higher concentration of dopants ($n_D + n_A > 10^{15}$) cm^{-3} where n_D and n_A are the densities of donors and acceptors, respectively) [54, 109, 110]. However, a deviation from the $T^{3/2}$ dependence can be observed due to the degree of compensation determined by n, n_D, and n_A, which weights in the total ion concentration n_I [111].

3.5.2 Disordered semiconductors

In disordered semiconductors, the conductivity (and mobility) is determnined by the trapping of carriers in the localized tail states that extend below the mobility edge, as discussed in Section 3.2.2. The carrier transport becomes dispersive resulting in a significantly reduced mobility, *e.g.* amorphous Si (a-Si) has $\sim$1 cm^2/V·s [112]. The mechanism of the dispersive transport in these disordered systems that are governed by localized states has been explained by various models [113].

3.5.2.1 DC photoconductivity

At elevated temperatures, the thermally-activated band conduction is given by

$$\sigma = \sigma_0 \, exp\left(-\frac{E_a}{k_B T}\right), \tag{3.25}$$

where σ_0 is a constant and E_a is the activation energy that can be extracted from the slope of a $ln(\sigma)$ *vs.* $1/T$ plot. At very low temperature, different hopping mechanisms between the localized states may dominate [113]. One of the commonly known models is the variable-range-hopping (VRH) model by the Nobel laureate Sir Nevill Mott, which explains the temperature dependent carrier diffusion in the localized states in the middle of the mobility gap [114] (refer to the band structure in Figure 2.5). In the VRH model, carriers hop between the occupied and unoccupied states above and below the Fermi level, respectively, and the carrier hopping distance may vary. For a three-dimensional system, as in bulk semiconductors, the Mott's law of conductivity obeys

$$\sigma_{VRH} = \sigma_0 \, exp\left[-\left(\frac{T_0}{T}\right)^{1/4}\right]. \tag{3.26}$$

The characteristic temperature T_0 pertains to the degree of disorder in the material, defined as

$$T_0 = \frac{18.1\alpha^3}{k_B N(E_F)}, \tag{3.27}$$

where $N(E_F)$ is the density of states at the Fermi level E_F, and α is the localization length of the localized states. Conductivities that follow Mott's law have been experimentally observed in many disordered semiconductors, with first reports in a-Si and a-Ge [86].

3.5.2.2 AC photoconductivity

The Drude-Smith model, discussed in Section 3.4, is an effective model in describing carrier localization not only in low-dimensional materials, but also in disordered semiconductors. In contrast to this Drude-like response, some of the frequency-dependent photoconductivities of disordered semiconductors behave differently at various temperatures, which are found to exhibit a power law dependence,

$$\sigma(\omega) \propto \omega^s, \tag{3.28}$$

where $s \leq 1$ is a temperature dependent parameter [53]. However, the $s(T)$ dependence may vary in different types of materials [115]. Equation 3.28 is sometimes referred as the 'Jonscher power law' [115], and is explained theoretically within Mott's variable range hopping model of localized carriers [116]. The power law dependence arises from a high frequency dielectric loss when an ac field is applied against the natural frequency of the carrier hopping between two centres [115, 117, 118]. The value of s represents the average hopping events, ranging between 1.0 (single hop) and 0.5 (multiple hops). Such frequency dependence was demonstrated in the ac conductivity of a-Ge [117], nanostructures, and various disordered materials at MHz, GHz and THz ranges [116, 119, 120].

CHAPTER 4

Terahertz Pulses for Linear and Nonlinear Transport in Semiconductors

4.1 Introduction

The frequency of light in the terahertz region (1 THz = 10^{12} Hz) lies between the microwave and infrared range in the electromagnetic spectrum (Figure 1.1). The photon energy of 1 THz is only 4.1 meV, way below the room temperature thermal energy of 25 meV. In the study of light-matter interaction, spectroscopists may also find the far-infrared THz frequency of great importance. Reviews of THz science and technology are well presented in Refs. [121, 122, 123, 124, 125], which include THz applications in imaging, remote sensing, radio astronomy, planetary and space science, etc. In addition, due to the non-ionizing effect of THz waves, THz sources are being used in biological exposures [126] to study the interaction of THz radiation and biological systems [127], as well as inspection of art and artifacts [128]. The emission or detection of light in the THz frequency is also utilized in imaging science with microscale to atomic scale resolution. Recent advances in this field use THz pulses coupled to the tip of an atomic force microscopy (AFM) [129, 130] or a scanning tunneling microscopy (STM) [131], providing both spatial and temporal images of photoexcited semiconductors using pump-probe techniques.

In the investigation of condensed matter, the frequency range of 0.1 to 30 THz corresponds to low-energy excitations in electronic materials, internal transition energies of excitons in semiconductors, density oscillations of carrier plasmas, superconducting energy gaps, spin waves, vibrational modes, and rotational transitions in molecules [19, 132, 133]. Therefore, THz spectroscopy has been

an efficient tool in exploring some of these carrier dynamics. THz pulses with low electric fields can be used in linear spectroscopy such as time-resolved THz spectroscopy (TRTS) for bulk semiconductors and nanomaterials [4, 8, 134]. While intense THz pulses with peak electric fields that exceed hundreds of kV/cm have paved the way for investigating nonlinear light-matter interactions at very low photon energies [17, 18, 135].

4.2 Table-top generation of Terahertz electric field pulses

With the advent of intense femtosecond pulsed laser sources, table-top generation of freely propagating THz pulses has been made possible in the past decades [125, 136]. With this development comes an opportunity to perform both linear and nonlinear spectroscopy in a non-contact manner. Various experimental approaches can be considered in generating THz pulses. These include the use of relativistic laser-plasma, air-plasma, photoconductive antennae (PCA), excitation of semiconductor surfaces, and optical rectification (OR) methods [124, 132, 137, 140]. Among these methods, the OR method is commonly used due to its simple experimental configuration and high stability [137].

4.2.1 Optical Rectification

As a strong oscillating electric field (optical excitation beam) interacts with a non-centrosymmetric crystal (nonlinear medium), generation of a dc electric field (THz electric field) can be induced (hence, the OR term). A simple illustration of the OR process is shown in Figure 4.1. For a non-centrosymmetric crystal, the second-order optical susceptibility $\chi^{(2)}$ is non-zero [141], and thus a second-order macroscopic polarization $\vec{P}^{(2)}(t)$ can be induced by a strong optical excitation beam. The THz generation in the OR method is a result of a quasi-DC polarization arising from this second-order nonlinear process [137].

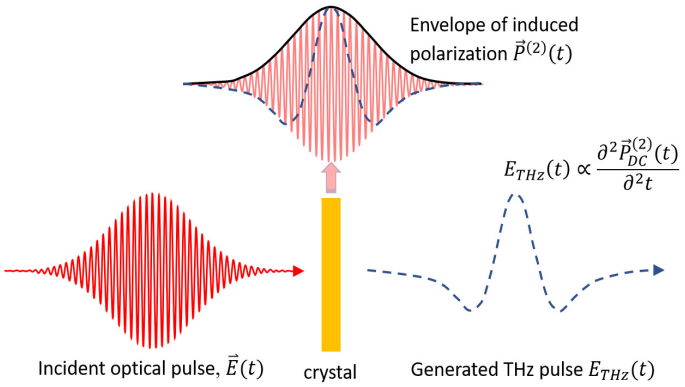

Figure 4.1: An illustration of the optical rectification process for the generation of a THz pulse using a non-centrosymmetric crystal, adapted from Ref [143].

The electric polarization is expressed as $\vec{P}(t) = \varepsilon_0 \chi \vec{E}(t)$, where ε_0 is the permittivity of free space [133]. Thus, the time-varying second-order polarization $\vec{P}^{(2)}(t)$ can be derived from a power series expansion of the the electric field $\vec{E}(t) = Ee^{-i\omega t} + c.c$, which results in

$$\vec{P}^{(2)}(t) = 2\varepsilon_0 \chi^{(2)} EE^* + (\varepsilon_0 \chi^{(2)} E^2 e^{-i2\omega t} + c.c). \tag{4.1}$$

The first term in the above expression of $\vec{P}^{(2)}(t)$ is the dc component, which is responsible in the THz generation resulting from the rectification of the incident optical electric field pulse (OR method). The latter term pertains to second harmonic generation, at 2ω, of the optical pulse frequency.

Hence, it can be deduced that the generation of THz using the OR process results from a transient current element, $\vec{J}(t) = \frac{\partial \vec{P}}{\partial t}$ [11]. This leads us to the expression of the generated THz electromagnetic wave from the wave equation (derived from Maxwell's equations), while only taking into account the time-varying second-order polarization $P^{(2)}(t)$ as the source term [142],

$$\bigtriangledown^2 \vec{E} - \epsilon\mu \frac{\partial^2 \vec{E}}{\partial t^2} = \mu \left(\frac{\partial^2 \vec{P}_{dc}^{(2)}(t)}{\partial t^2} \right), \tag{4.2}$$

where ϵ and μ denote the the electric permittivity and the magnetic permeability, respectively. The term $\partial^2 \vec{P}_{dc}^{(2)}(t)/\partial^2 t$ in the above expression (Equation 4.2) shows that the generation of the electromagnetic radiation arises from the acceleration of charges in a nonlinear optical medium.

Therefore, we arrive at the $E_{THz}(t)$ that is expressed as the second derivative of the dc polarization of $\vec{P}^{(2)}(t)$,

$$E_{THz}(t) \propto \frac{\partial^2 \vec{P}^{(2)}_{dc}(t)}{\partial^2 t}. \tag{4.3}$$

As illustrated in Figure 4.1, the nonlinear polarization $P^{(2)}(t)$ is the envelope of the femtosecond optical pulse, and the shape of the generated THz electric field pulse *via* the OR method, $E_{THz}(t)$, is the second derivative of this corresponding envelope based on Equation 4.3.

Table 4.1: Properties of ZnTe and $LiNbO_3$.*

Crystal	Structure/ space group	Electro-optic coefficient (pm/V)	Index of refraction at 800 nm	THz index of refraction, n_{THz}	THz absorption coefficient (cm^{-1})
ZnTe	Zincblende / $F\overline{4}3m$	$r_{41} = 4.0$	$n_{vis} = 2.85$ $n^g_{vis} = 3.24$	~3.17	1.3
$LiNbO_3$	Trigonal / R3c	$r_{33} = 30.9$	$n_{vis} = 2.18$ $n^g_{vis} = 2.35$	~4.98	16

*Data taken from Ref. [133, 137, 138, 139, 142]. ZnTe is used in the THz source generation in the TRTS setup (Section 4.3) and electro-optic detection of THz pulses (Section 4.2.3), while $LiNbO_3$ is used for the intense THz source generation (Sections 4.2.2 and 5.4).

Among non-centrosymmetric crystals (such as GaSe, CdTe, GaAs, $LiTaO_3$, and $LiNbO_3$), ZnTe is one of the most commonly used THz emitter because the values of its optical and THz indices of refraction (n_{vis} and n_{THz}, respectively) are of close proximity, as presented in Table 4.1 [137]. Within a non-dispersive linear medium, where both optical and THz refractive indices are the same, the propagating optical pulse and the emitted THz radiation will travel at the same speed. Such conditions allow the amplitude of THz radiation to increase linearly with distance because both optical and THz pulse are in phase (phase-matching) [143]. However, there is still a small difference in the refractive indices of ZnTe, where $n_{THz} - n_{vis} = 0.32$ and $n_{THz} - n^g_{vis} = 0.07$, resulting in imperfect phase-matching. For $n_{THz} > n_{vis}$, the optical pulse leads the generated THz pulse after

a walk-off length of

$$l_w = \frac{c\tau_p}{n_{THz} - n_{vis}}, \tag{4.4}$$

where c is the speed of light and τ_p is the duration of the femtosecond laser pulse [132, 143]. Thus, for efficient THz generation, the non-centrosymmetric crystal should have a long l_w and must be thinner than the l_w. For a very thin ZnTe crystal (< 10 μm) and for an 800 nm optical pulse with a width of ∼100 fs (typical pulse width from a Ti:sapphire amplifier laser system), ideally, a bandwidth of 10 THz can be expected using the OR method. However, the imperfect phase-matching at higher THz frequencies in addition to the onset of the optical phonon absorption at $\sim$ 3.5 THz (whereby the transverse-optical (TO) phonon resonance in ZnTe is at 5.3 THz) [132, 144] limit the spectral bandwith of the THz generation down to $\sim$ 3 THz only.

4.2.2 Intense Terahertz generation

Intense THz radiation can also be generated *via* the OR method using a powerful optical pump and a good selection of a non-centrosymmetric crystal. Although ZnTe is widely used, it is less ideal in the generation of high THz electric fields compared to the use of $LiNbO_3$ [17, 145]. ZnTe has a lower band gap of 2.6 eV, which may experience two-photon absorption from a commonly used intense optical pump of 1.55 eV (800 nm). Whereas, with a band gap of 3.7 eV, $LiNbO_3$ provides a higher threshold to multiphoton absorption at powerful laser excitation at 800 nm. In addition, the electro-optic tensor, $r_{33} = 30$ pm/V (Table 4.1), which is an order of magnitude higher than that of ZnTe, makes $LiNbO_3$ ideal in achieving higher THz electric fields. However, the large phase-mismatch in $LiNbO_3$ between optical pump excitation at 800 nm and THz frequencies, where $n_{vis} \sim 2$ and $n_{THz} \sim 5$, respectively, prohibits optimum THz generation in a collinear geometry. To satisfy the phase-matching condition, a 'tilted pulse front technique' can be employed [14, 17, 19, 145].

4.2.2.1 Tilted pulse front technique

In order to have efficient generation of THz waves *via* the OR method, the velocity phase-matching condition of the frequencies involved should be satisfied [14, 145]. Here, the group velocity of the pump pulse at 800 nm illuminating the $LiNbO_3$ and the phase velocity of the generated THz pulse

propagating within the crystal should be equivalent,

$$\upsilon^{g}_{vis} = \upsilon^{ph}_{THz}. \tag{4.5}$$

However, as presented in Table 4.1, $LiNbO_3$ crystal is highly dispersive, having a large difference in the optical (800 nm) and THz refractive indices. As the femtosecond optical pump pulse propagates inside the $LiNbO_3$ medium, it travels faster than the phase velocity of the generated THz pulse ($\upsilon \propto 1/n$). The velocity mismatch causes the emission of the THz electromagnetic wavefronts to be spatially extended and propagate along a Cherenkov cone [146, 147]. Here, the THz Cherenkov wave fronts depart at an angle determined by

$$\theta_c = cos^{-1}\left(\frac{\upsilon^{ph}_{THz}}{\upsilon^{g}_{vis}}\right) = cos^{-1}\left(\frac{n^{g}_{vis}}{n_{THz}}\right) \simeq 60°. \tag{4.6}$$

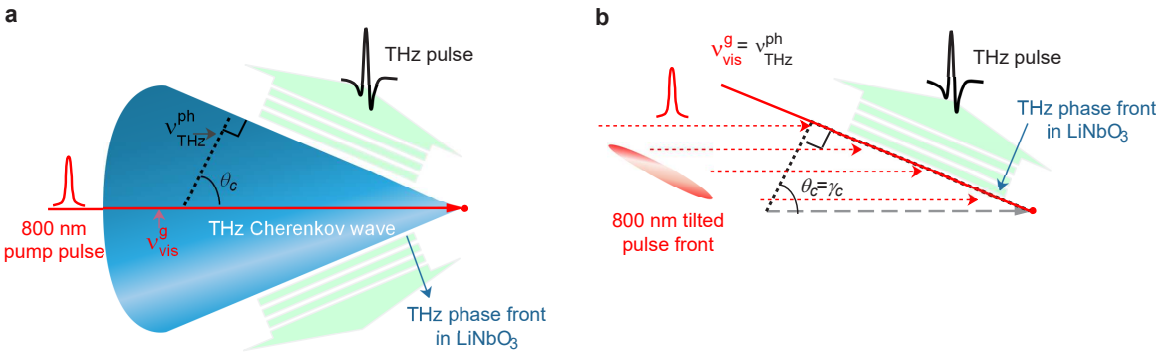

*Figure 4.2: A schematic illustrating THz generation using $LiNbO_3$ with a **a)** mismatched group velocity of the NIR pump pulse, υ^{g}_{vis}, and phase velocity of the generated THz, υ^{ph}_{THz}, resulting in a Cheronkov radiation, and **b)** phase-matched υ^{g}_{vis} and υ^{ph}_{THz} using a tilted pulse front technique, resulting in an efficient generation of a collimated THz beam.*

Figure 4.2a illustrates the optical pump pulse arriving perpendicularly on the $LiNbO_3$ crystal resulting in THz radiation generated bidirectionally along the Cheronkov cone [147]. Such configuration restricts efficient THz generation and makes it difficult to direct or collect the THz radiation propagating along the Cherenkov phase fronts. Ideally, the THz radiation should propagate as a plane wave. An approach to rectify the geometry and maximize the collection of THz is to tilt the

optical pump pulse front, as demonstrated in Figure 4.2b. Such excitation geometry generates a collimated THz beam with a phase velocity that matches the group velocity of the optical pump pulse, according to Huygen's principle. This is the concept behind the 'velocity matching' applied in the novel 'tilted pulse front technique' [14, 19, 145]. Here, the tilt angle γ_c between the 800 nm pump pulse and the THz propagation directions should be adjusted as large as $\theta_c \sim 60°$, thus the relation of the velocities is given as

$$\upsilon^{g}_{vis} \cdot cos\gamma_c = \upsilon^{ph}_{THz}. \tag{4.7}$$

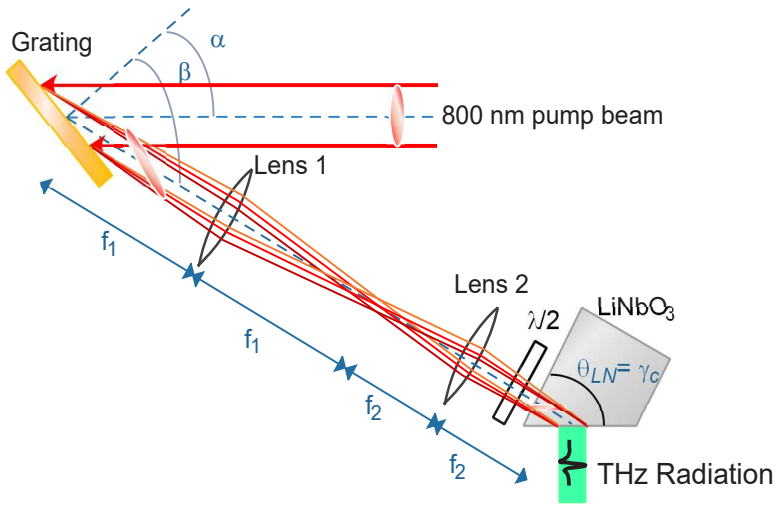

Figure 4.3: Intense THz generation from a $LiNbO_3$ crystal via the OR method utilizing a tilted pulse front technique. The grating tilts the incident NIR pump intensity front at an angle γ_c and a 4f lens configuration is employed to collimate and demagnify the pump beam onto the $LiNbO_3$ crystal. A half-wave plate, $\lambda/2$, is placed before the crystal to correct the polarization direction. The figure is adapted from Ref. [19].

In the tilted pulse front technique, the large tilt angle γ_c can be achieved by a set of diffraction grating and two cylindrical lenses, as illustrated in Figure 4.3. The 800 nm pump pulse front is incident on the grating tilted at an angle α, which creates a tilted pump pulse front diffracted at an angle β. These angles correspond to the grating equation,

$$sin\alpha + sin\beta = mp\lambda_0, \tag{4.8}$$

where m is the order of diffraction, p is the groove density of the grating, and λ_0 is the central wavelength of the pump pulse. The grating equation shown above is related to the tilt angle γ_c for $LiNbO_3$,

$$tan\gamma_c = \frac{mp\lambda_0}{n^g_{vis}M_1 cos\beta}, \tag{4.9}$$

where $M_1 = f_2/f_1$ is the magnification of the *4f* lens configuration, and f_1 and f_2 are the focal lengths of the two cylindrical lenses. In order to obtain optimal THz generation, the tilt angle of the grating image inside the $LiNbO_3$, θ_{LN}, should also coincide with the angle of the tilted pulse front γ_c. In this case, we apply the Scheimpflug principle [19] to correct the orientation of the pulse front, where the supposed tilt angle in the $LiNbO_3$ can be calculated as

$$tan\theta_{LN} = n^g_{vis}M_2 tan\beta, \tag{4.10}$$

where M_2 is the magnification of the pump beam image from the grating to the image plane tilt inside the $LiNbO_3$. Ideally, using a *4f* lens configuration, $M_1 = M_2$. Hence, for the design of the setup based on Figure 4.3, the magnification $M_{1,2}$ can be determined as a function of diffraction angle β using Equations 4.9 and 4.10 with a specfic value of γ_c. This technique is applied in Section 5.4 of the experimental method.

A recent report shows that intense THz generation from a $LiNbO_3$ crystal, employing the tilted pulse front technique described above, can reach an electric field of up to 1 MV/cm using a 4 mJ optical pump and a small THz beam spot size of ~ 300 μm [13]. The THz electric field waveform is measured by employing a free-space electro-optic (EO) detection technique.

4.2.3 Electro-optic sampling of Terahertz pulses

Detection of the THz electric field pulses in the time domain can be performed by means of an electro-optic (EO) sampling technique. The EO setup is presented in Figure 4.4 [148].

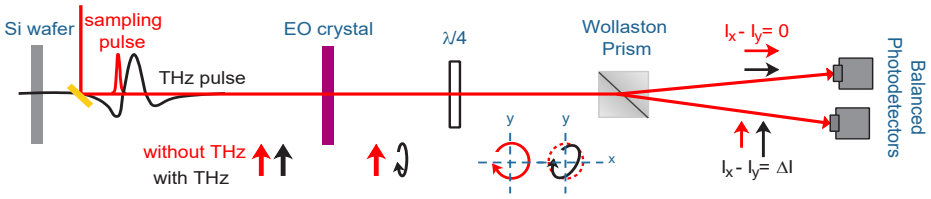

Figure 4.4: Detection scheme of the free-space THz pulse using the electro-optic sampling technique. The silicon wafer is included to attenuate the THz electric field amplitude for manageable EO signals from the balanced photodetectors.

In this setup, a femtosecond optical pulse (sampling beam) probes the THz waveform that is freely copropagating through the EO crystal. With the presence of a THz electric field, a birefringence is induced in the EO crystal, termed as the Pockel's effect [149]. The sampling beam is refracted in two ways due to the changes of the refractive indices in the anisotropic crystal. Thus, the THz electric field causes a phase modulation $\Delta\phi$ in the sampling beam and the induced phase shift is proportional to THz electric field E_{THz} by

$$\Delta\phi = \frac{2\pi n_0^3 r_{ij} L}{\lambda_0} E_{THz}, \tag{4.11}$$

where n_0 is the refractive index of the EO crystal at the center wavelength λ_0 of the optical sampling beam, r_{ij} is the EO coefficient (represented by the ij notation for the electro-optic tensor), and L is the thickness of the active layer of the EO crystal [132]. The phase modulation expressed in Equation 4.11 can be experimentally detected as an intensity modulation using a combination of a quarter-wave plate ($\lambda/4$), a Wollaston prism, and balanced photodetectors. A quarter-wave plate converts a linearly polarized sampling beam into a circularly polarized light (without an electric field). With the Pockel's effect of the THz electric field, an elliptically polarized light is produced instead. The THz-induced elliptically polarized sampling beam is then split into two orthogonal linearly polarized light using a Wollaston prism. Lastly, the intensities of the horizontal and vertical components of the polarized light are measured by the balanced photodetectors, which output their corresponding transient currents,

$$I_x = \frac{I_0}{2}(1 - sin\Delta\phi) \approx \frac{I_0}{2}(1 - \Delta\phi), \tag{4.12}$$

$$I_y = \frac{I_0}{2}(1 + sin\Delta\phi) \approx \frac{I_0}{2}(1 + \Delta\phi), \tag{4.13}$$

where I_0 is the intensity of the sampling beam incident on the EO cyrstal [132]. Based on Equation 4.11, the THz-induced photomodulation, $\frac{I_x - I_y}{I_x + I_y} = \frac{\Delta I}{I}$, is proportional to the amplitude and direction of the E_{THz} [13, 148], such that

$$E_{THz} = \frac{sin^{-1}(\frac{\Delta I}{I})\lambda_0}{2\pi n_0^3 r_{ij} T_{EOC} T_{Si} L}, \tag{4.14}$$

where T_{EOC} and T_{Si} are the Fresnel transmission coefficients of the EO crystal and Si wafer, respectively. To remain in the linear response of the EO detection (linear regime in the sunusoidal function curve of $\Delta I/I$), Si wafers can be placed before the EO sampling to attenuate the THz electric field (Figure 4.4), thus the THz transmission in Si, $T_{Si} = 0.7$, is added to Equation 4.14. The commonly used EO crystals are ZnTe and GaP. For the detection of high THz electric fields ($>$ 10 kV/cm), GaP is preferred due to smaller r_{ij} component, which allows manageable EO signals from the photodiodes. GaP has $r_{41} = 0.88$ pm/V, $n_0 = 3.2$ at $\lambda_0 = 800$ nm, and $T_{GaP} = 0.46$. In addition, the phonon absorption of relatively thin GaP [150] is at higher THz frequencies compared to that of ZnTe [144], thus providing a wider bandwidth for THz detection.

4.3 Probing linear transport by means of Time-resolved Terahertz Spectroscopy (TRTS)

We now turn our attention to using THz pulses in THz spectroscopy. At low THz electric fields ($\ll$ 10 kV/cm), linear spectroscopy such as TRTS can be carried out where THz pulses are used to probe carrier dynamics within a photoexcited material. Since the THz photon energy is much less than the electronic state transitions in most semiconductors (with band gaps on the order of eV) and since typical phonon energies are above 5 THz [10], low frequency THz pulses are then ideal for probing free carrier absorption, relaxation dynamics, and transient photoconductivity. In TRTS, the changes in both amplitude and phase of the THz pulse propagating through the sample provide essential information on the scattering and decay of the photoexcited carriers.

TRTS is an all optical technique (non-contact). Therefore, there are numerous advantages

offered by TRTS compared to conventional (contact) methods for exploring optoelectronic properties of materials [4, 8, 134]. Within the THz bandwidth, the complex conductivity of the sample can be deduced without Kramers-Kronig transformation. Secondly, the transient photoconductivity of a sample can be resolved with sub-picosecond time resolution, thereby providing information on the material's response on ultrafast time scales. Hence, using appropriate conductivity models, both dc and ac conductivity can be measured in a non-contact fashion, which is especially ideal for nanostructured materials and thin films.

4.3.1 TRTS for photoconductivity measurements

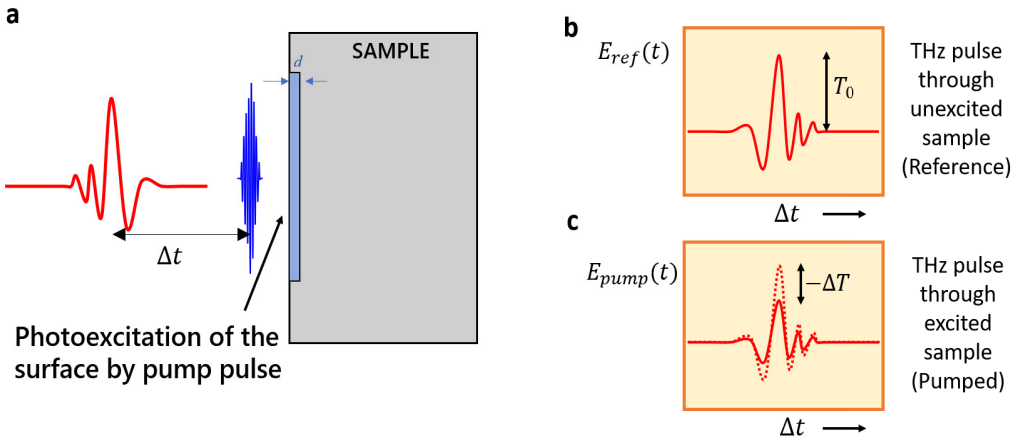

Figure 4.5: ***a)*** *Schematic diagram of a typical TRTS measurement, which illustrates the optical pump - THz probe technique. The THz pulse (red) arrives at the sample after a delay time Δt with respect to the optical pump pulse (blue).* ***b-c)*** *The transmitted THz pulses, $E_{ref}(t)$ and $E_{pump}(t)$, are measured for the unexcited ($\Delta t \ll 0$) and photoexcited ($\Delta t > 0$) sample surface, respectively. Figure adapted from Ref. [10].*

Figure 4.5a illustrates the basic TRTS method where an optical pump pulse photoexcites a sample within the optical penetration depth, d, of the surface and a THz probe propagates through the sample at a time delay Δt relative to the peak of the pump pulse. The changes in the amplitude and phase of the transmitted THz electric field waveforms are measured at varying Δt. Firstly, at negative optical pump-THz probe delay time ($\Delta t \ll 0$), a transmitted THz pulse through an

unexcited (reference) sample is measured, $E_{ref}(t)$ (Figure 4.5b). Second, a transmitted THz waveform is measured when the sample is photoexcited, $E_{pump}(t)$, which happens at positive delay times ($\Delta t > 0$) (Figure 4.5c). The measured $E_{ref}(t)$ and $E_{pump}(t)$, as well as the modulation of the THz electric field, $\Delta E = E_{ref}(t) - E_{pump}(t)$, provide the information needed for extracting the complex photoconductivity of the sample. An example of measured E_{ref}, E_{pump}, and ΔE in both time and frequency domains is shown in Figure 4.6, as taken from a transmission through an undoped 0.5 mm thick Ge wafer. Details of the TRTS experimental method are presented in Section 5.3.

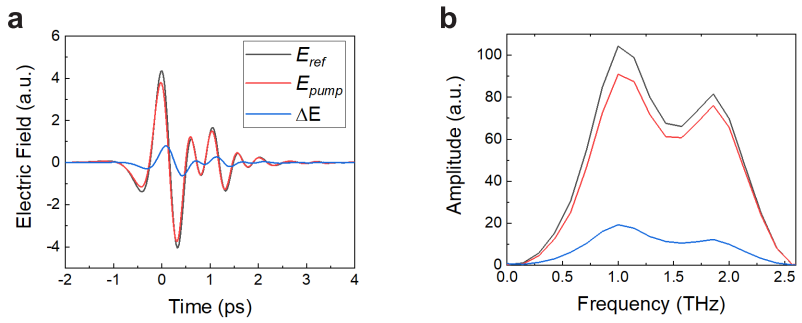

Figure 4.6: ***a)*** *THz electric field waveforms in the time domain, $E_{ref}(t)$, $E_{pump}(t)$, and $\Delta E = E_{ref}(t) - E_{pump}(t)$, measured from the transmission through an undoped Ge sample (at F = 7.67 $\mu J/cm^2$, E_{ex} = 1.55 eV, T = 300 K), and* ***b)*** *their corresponding Fourier transforms, which shows a THz bandwidth of 0.2 - 2.5 THz. The THz electric field pulses were generated and detected using ZnTe crystals via the optical rectification method (Section 4.2.1) and EO sampling technique (Section 4.2.3), respectively. The amplitude and phase differences of $E_{ref}(t)$ and $E_{pump}(t)$ is related to the complex transient photoconductivity of the sample.*

4.3.1.1 Complex conductivity

We begin by obtaining the transmitted electric field spectrum $T(\omega)$ from the Fourier-transform of the experimentally measured time domain electric fields,

$$T(\omega) = \frac{E_{pump}(\omega)}{E_{ref}(\omega)}. \tag{4.15}$$

If the response of the material results in a phase shift, where $\phi = \phi_{pump} - \phi_{ref}$, then the transmitted electric field becomes a complex function expressed as

$$T(\omega)e^{i\phi(\omega)} = \frac{E_{pump}(\omega)}{E_{ref}(\omega)}. \tag{4.16}$$

To relate the complex conductivity $\tilde{\sigma}(\omega)$ from the experimentally measured $T(\omega)$, we consider the dielectric response of the material. By incorporating the Fresnel transmission and reflection coefficients in the propagation of the incident THz electric field in a thin film medium with thickness d, the complex conductivity $\tilde{\sigma}(\omega)$ can be extracted from the well-known Tinkham equation for optically thin films [151],

$$\tilde{T}(\omega) = \frac{1+N}{1+N+Z_0 d\tilde{\sigma}(\omega)}, \tag{4.17}$$

where N is the refractive index of the sample substrate at THz frequencies and $Z_0 = 1/\epsilon_0 c = 377\ \Omega$ is the impedance of free space. From Equations 4.16 and 4.17 [11], the real and imaginary parts of $\tilde{\sigma}(\omega)$ can therefore be solved as

$$\sigma_1(\omega) = \frac{N+1}{Z_0 d}\left[\frac{1}{|T(\omega)|}cos(\phi) - 1\right], \tag{4.18}$$

$$\sigma_2(\omega) = -\frac{N+1}{Z_0 d}\left[\frac{1}{|T(\omega)|}sin(\phi)\right]. \tag{4.19}$$

4.3.1.2 Transient photoconductivity

The transient photoconductivity (in the time domain) is related to the changes in the peak magnitude T_0 of the THz waveform as a function of Δt. The mechanism is illustrated in Figure 4.7a. A reduced THz transmission (ΔT) is observed immediately at the arrival of the optical pump pulse at $\Delta t = 0$ [10, 11, 12]. The decrease of the transmitted THz radiation is due to the free carrier absorption, which makes the surface of the sample more conductive. Eventually, the photoexcited carriers will decay through time, thus, by continually measuring the pump-induced change in the THz magnitude against Δt, the THz magnitude will recover in the long run. Hence, the method utilizes the peak THz magnitude as a probe to monitor the rise and decay of the photoexcited carriers.

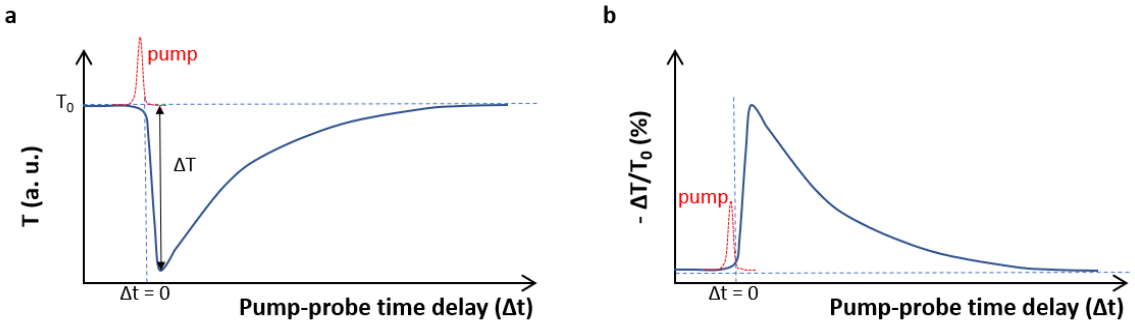

Figure 4.7: Illustration of ***a)*** *normal transmission mode and* ***b)*** *differential transmission mode for the measurement of the transient photoconductivity.*

In analogy to the carrier decay, the relative change in the THz magnitude $-\Delta T/T_0$ can be plotted instead, as illustrated in Figure 4.7b. By referring back to Equation 4.17 for the derived expression of $T(\omega)$ (Tinkham equation), the measured $-\Delta T/T_0$ can now be related to the transient photoconductivity, given as,

$$\frac{-\Delta T(t)}{T_0} = \frac{\Delta E(t)}{E_{ref}} = 1 - \frac{N+1}{N+1+Z_0\Delta\sigma(t)}. \tag{4.20}$$

We now resolve for time domain conductivity $\Delta\sigma(t)$ expressed as

$$\Delta\sigma(t) = \frac{N+1}{Z_0 d}\left[\frac{-\Delta T((t))}{T_0}\right]\left[\frac{1}{1+\frac{\Delta T((t))}{T_0}}\right]. \tag{4.21}$$

From the above equation, we can infer that $\sigma(t)$ is proportional to the experimentally acquired $\left[\frac{-\Delta T(\omega)}{T_0}\right]$, with the conditions that 1) the relative change in the THz magnitude should be less than 20% (otherwise the proportionality will not be linear), 2) the conductivity is almost purely real, that is $\tilde{\sigma}(\omega) = \sigma(t)$ in the $\omega\tau \ll 1$ regime, and 3) there is no significant phase shift between $E_{ref}(\omega)$ and $E_{pump}(\omega)$ [11]. Details of experimental method in measuring $-\Delta T/T_0$ can be found in Section 5.3.1.

4.4 Nonlinear transport at intense Terahertz electric field pulses

Going beyond the use of low-field THz pulses in linear spectroscopy, we then discuss the high-field case by which intense THz electric fields may cause nonlinear interactions with matter. These possibilities opened up a new category of exciting research areas in the investigation of nonlinear transport in materials and non-resonant control over matter [18] - that is, the ability of intense THz pulses to accelerate electrons to high energies beyond the THz photon energy of 4.1 meV. Thus, in such investigations, the importance of generating high THz electric field pulses comes into play.

For the past couple of decades, there has been quite a number of reports on intense THz field-induced nonlinear transport. A summary of the experiments, nonlinear mechanisms, and recent developments can be found in these review papers [17, 18, 19, 135, 152, 153]. As this thesis is not solely focused on this field, we shall briefly enumerate some of these processes [20, 154, 155] in the following sections.

4.4.1 Tunneling ionization of impurities

Shallow and deep localized states in semiconductors can be due to dopants and deep impurities, respectively, as presented in Section 2.3.2. A shallow center and a deep center have a bound state, which phenomenologically may be attributed to a potential well [154]. With the application of an intense electric field, the potential well can be distorted which allows the electron to escape either by phonon-assisted tunneling [156] or direct tunneling [157]. The tunneling ionization of shallow and deep impurities can also occur with intense radiation that has a photon energy much less than the ionization binding energy of the impurities (*i.e.* far-infrared radiation such as THz pulses) [158, 159]. For example, a direct tunneling ionization of the shallow acceptors in Ga-doped Ge was observed through a nonlinear transmission of intense THz pulses [160]. In another report of doped p-type Ge and doped AlGaAs, as the THz electric field is increased up to 60 kV/cm, the ionization of charge carriers in deep impurities transitioned from phonon-assisted tunneling to direct tunneling [161].

Such nonlinear phenomena was first described by Keldysh [162]. He pioneered a nonperturba-

tive theory explaining that intense electromagnetic fields with a lower frequency than the ionization potential of an atom can induce electron tunneling. By doing so, he introduced a critical parameter, commonly known as Keldysh parameter γ, to account for the two strong field processes: multiphoton ionization ($\gamma > 1$) and tunneling ionization ($\gamma < 1$). The Keldysh parameter is given as

$$\gamma = \frac{\omega}{\omega_t}, \quad \text{where} \qquad \omega_t = \frac{eE}{\sqrt{2m_e I_p}} \tag{4.22}$$

is the tunneling frequency, E is the electric field amplitude, and I_p is the ionization potential [163, 164, 165]. For the case of intense THz electric fields, then $E = E_{THz}$ and $\omega = \omega_{THz}$ so that Equation 4.22 becomes

$$\gamma = \sqrt{\frac{I_p}{2U_p}}, \quad \text{where} \qquad U_p = \frac{e^2 E_{THz}^2}{4m_e \omega_{THz}^2} \tag{4.23}$$

is the ponderomotive energy, which is defined as the sub-cycle averaged kinetic energy of an electron in an oscillating electric field (*i.e.* the quiver energy of an electron under a monochromatic laser source). U_p becomes an important parameter when the interaction between light and matter changes from the low-field perturbative regime to high-field tunnel ionization regime at increasing laser field strength [166]. Equation 4.23 shows that U_p increases quadratically with the inverse square of the frequency. Thus, a longer wavelength light source, such as in the THz frequency range, U_p could be $\sim 10^4$ larger than a visible light source. For instance, for an E_{THz} of 300 kV/cm at $\omega_{THz}/2\pi = 1$ THz, the U_p value can reach up to 1 eV, comparable to most band gap energies of semiconductors and hence, high enough to induce nonlinear charge transport [19]. As an example, with a low effective mass ($\sim 0.1 m_e$) in single-walled carbon nanotubes (SWNTs), an interaction with a 0.7 MV/cm THz electric field contributed to a high U_p that even exceeded the band gap of the SWNTs itself, resulting in generation of excitons [166].

THz electric fields with high U_p has been a key concept in explaining THz nonlinear tranport phenemena, not only in terms of tunnel ionization of impurity states, but also in Zenner tunneling, impact ionization, and intervalley scattering [19].

4.4.2 Ballistic transport

The value of U_p also becomes valuable when we consider ballistic acceleration of electrons in the conduction band [17], and this becomes more pronounced if other scattering events (*e.g.* carrier-carrier interaction, electron-phonon, ionized impurity) become less dominant (Equation 3.7) [167]. For example, it has been reported in n-type GaAs that intraband tunneling, which even covered a major part of Brillouin zone, can be driven by E_{THz} = 300 kV/cm at room temperature [168]. At lower temperature, the authors reported generation of additional e-h pairs by means of tunneling of electrons from valence to conduction band. Another report shows that U_p on the order of keV and with a Keldysh parameter of only $\gamma \approx 2\times10^{-2}$, a carrier population on the order of 10^{19} cm^{-3} can be injected in an undoped bulk GaAs with a gold metamaterial array by means of interband tunneling and impact ionization, thereby resulting in THz-induced electroluminescence [169]. These reports are quite extraordinary, demonstrating extreme nonlinear effects of intense THz electric fields with additional photogeneration of free carriers in semiconductors.

4.4.3 Impact Ionization

Impact ionization is a non-equilibrium generation process by which an energetic charge carrier loses its kinetic energy to an electron in the valence band that is excited to the conduction band (or creation of another hole in the valence band), thereby creating other free carriers: $e \rightarrow 2e + h$ or $h \rightarrow 2h + e$. In some way, this is the reverse of an Auger process because an e-h pair can be generated through impact collision [170]. The process can occur with an external electric field that allows an electron to have a threshold kinetic energy E_{th} that is higher than the band gap E_g, given as $E_{th} = E_g \times (2m_e + m_{hh})/(m_e + m_{hh})$, where m_{hh} is the effective mass of the heavy hole [169, 171]. This mechanism was explained to be responsible for the increased absorption coefficient in the small band gap InSb (E_g=0.17 eV) [172, 173] and increased conductivity in n-doped InSb and p-doped InAs (E_g=0.35 eV) [180] by means of THz pump - THz probe measurements. The enhanced absorption (or conductivity) after THz excitation strongly indicates generation of new carriers *via* impact ionization.

4.4.4 THz-induced intervalley scattering or Absorption bleaching

In contrast with the impact ionization, THz-induced intervalley scattering results in absorption bleaching. Here, the amplitude of the transmitted THz pulse through the semiconductor becomes enhanced at higher field strengths, indicating a decrease in the absorption due to reduced conductivity. This was demonstrated in highly n-doped InGaAs on InP [174, 175], silicon-based metamaterials [176], and photoexcited GaAs [177, 178]. Absorption bleaching was also observed in the reduced conductivity of n-doped GaAs and n-doped InAs (at $\Delta t < 1$ ps) in a reflection geometry [179]. These reports explain that the reduced conductivity is due to intervalley scattering from the Γ valley to the nearest satellite valley (*i.e.* L valley), which has a lower mobility (for an example of band structure, refer to Figure 8.1 for Ge). THz-induced intervalley scattering can occur as long as the electrons acquire enough kinetic energy at high THz electric fields to overcome the nearest intervalley energy separation.

A dynamic Drude-based model, which incorporates the Γ - L intervalley scattering and the nonparabolicity of the bands was used to explain the mechanism of the absorption bleaching in these reports [175, 177, 178]. Based on the model, it was shown that, at low THz electric field regimes, there is no enhancement in transmission of the THz electric field through the samples, which implies that intervalley scattering does not take place. At high THz electric fields, the minimum threshold energy for intervalley scattering to occur was overcome [177]. However, it has been observed that at higher carrier densities, the effect of the THz-induced intervalley scattering is reduced. This was attributed to a reduction in the THz pulse transmission in a more conductive sample [15], in addition to enhanced e-h scattering that limits the maximum kinetic energy for the carriers [178].

CHAPTER 5

Experimental Methods

The following sections describe the methods employed for the experimental results presented in the next chapters. In Chapters 6 and 7, the visible photoluminescence (PL) spectra and the PL decays of bismoles and functionalized silicon nanosheets (SiNSs) were obtained using the time-integrated photoluminescence spectroscopy (TIPL) and time-resolved photoluminescence spectroscopy (TRPL) presented in Sections 5.1.1 and 5.1.2, respectively. For the PL of Ge in Chapter 8, the method for the photoluminescence spectroscopy in the NIR region is presented in Section 5.2. The transient and complex photoconductivity (PC) of bulk Ge in the second part of Chapter 8 as well as the Ge thin films in Chapter 9 were measured using time-resolved terahertz spectroscopy (TRTS) presented in Section 5.3. Lastly, the setup for intense THz generation and detection, and for measurements of the modulation of the PL of Ge, the results of which are presented in Chapter 10, is shown in Section 5.4.

5.1 Photoluminescence Spectroscopy: Visible to NIR region (400-1000 nm)

5.1.1 Time-integrated photoluminescence (TIPL)

Figure 5.1 shows the experimental setup for TIPL and TRPL spectroscopy. Samples in UV-fused cuvettes can be positioned on an optical stage while solid samples can be placed on the copper finger of the optical microscopy cryostat (Cryo Industries). A low temperature compatible Apeizon grease is used to adhere the edges of the solid samples or the UV-fused quartz glass substrate onto the

copper sample holder. The optical cryostat is evacuated by a turbo pump station (Varian Vacuum Technologies TPS-compact) down to a pressure of $\sim 2.2 \times 10^{-7}$ mbar. For the photoexcitation of the samples, a 400 nm laser pulse is used from a frequency-doubled 800 nm Ti:Sapphire ultrafast laser (Coherent RegA 900) *via* second harmonic signal generation from a barium borate (BBO) crystal. The laser pulse train has a 65 fs pulse width and 250 kHz repetition rate. The optical excitation and the PL collection is configured in a basic confocal setup. An objective (20x Mitutoyo M Plan Apo) is used to focus the laser beam onto the sample while simultaneously collecting the PL, which is filtered by a 435 nm long pass filter (Edmund Optics) in order to block scattered 400 nm light. The collected PL is focused by a lens onto a multimode optical fiber with a core size of 550 μm optimized for a wavelength range from 400 to 2200 nm (Thorlabs M37L). The other end of the optical fiber is coupled to the entrance slit of the spectrometer (Princeton Instruments Acton SP2500 Spectrometer) using an SMA coupler which directs the PL to a 1200 g/mm grating (3rd grating in the turret) blazed at 750 nm. The dispersed PL from the grating is re-focused by a concave mirror to the CCD camera (Acton Pixis 400B CCD). The CCD array has a size of 26.8 mm $\times$ 8 mm with 1340 $\times$ 400 pixels. At an entrance slit of 20 $\times$ 20 μm, the PL spectrum has a center wavelength with a bandwidth of $\pm$ 86.05 nm. This provides a CCD resolution of 6.42 nm/mm. Thus, for a 200 μm entrance slit, used during the measurements, the resolution is 1.28 nm, which agrees to the expected resolution based from a calibration of the spectrometer using a 546.5 nm mercury line [9]. An entrance slit wider than 200 μm can significantly compromise the spectral resolution. To acquire a desirable intensity of the TIPL, the user can set the exposure time of the CCD *via* a Labview program.

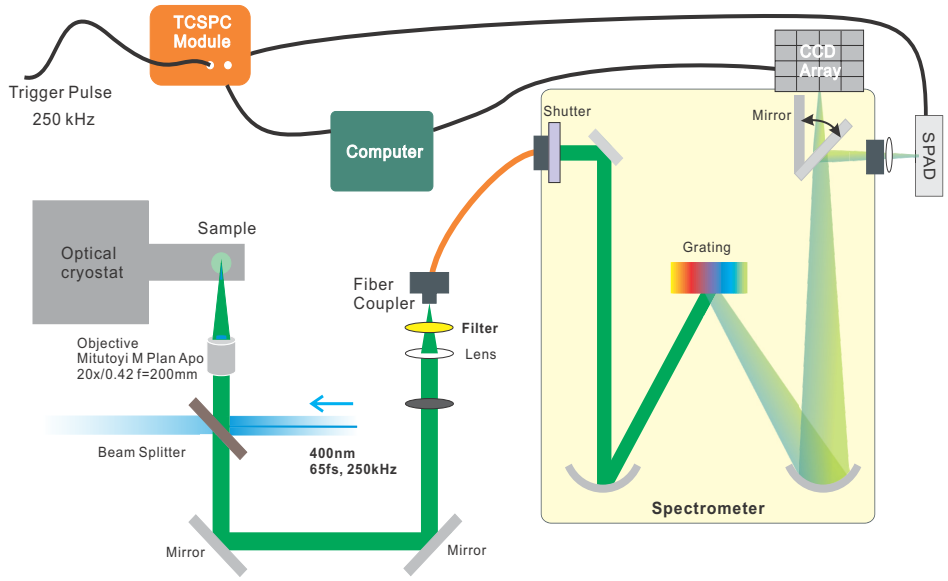

Figure 5.1: Experimental setup for TIPL and TRPL spectroscopy.[1]

5.1.2 Time-resolved photoluminescence (TRPL)

5.1.2.1 Nanosecond scale TRPL

For the measurements of nanosecond scale TRPL, a time-correlated single photon counting (TCSPC) technique was employed. TCSPC is useful for low-level, high-repetition rate signals [181]. In the setup shown in Figure 5.1, a mirror inside the Princeton Instruments spectrometer redirects the PL from the CCD array onto the single-photon avalanche photodiode (SPAD, PDM Series, 50CT, PicoQuant Systems) *via* the single channel exit slit. The SPAD is connected to a TCSPC module (PicoHarp 300, Picoquant Systems) that is triggered by the laser pulse at 250 kHz repetition rate. Every arrival of a single photon pulse detected by the SPAD is referenced to the trigger pulse. This allows the TCSPC module to discriminate the incoming single photon pulses from the laser pulse train. The time delays between the single photon pulses and the trigger are binned to create a histogram that represents the time-resolved PL decay. It is therefore imperative that the TCSPC

[1]The TRPL and TIPL experimental setup were developed by L. V. Titova. G. de los Reyes contributed in the characterization of the setups [9]. M. A. B. Narreto modified the setup with the cryostat.

technique can detect no more than a single photon per excitation pulse. Two or more photon pulses detected by the SPAD at a single excitation event can distort the binning of the photon counts. Based on Poisson statistics, to maintain a low probability of registering more than one photon per cycle, a rule of thumb is to acquire a number of counts that is less than 10 % of the laser repetition rate. This results to a relative statistical error in the time histogram of less than $\sigma = 10$ % [3]. In the experiments, the counts per bin were maintained at less than 10,000 at low excitation power.

Compared to analog recording techniques, TCSPC delivers a higher time resolution (or rise time of the PL decay). The bandwidth is only limited by the transit time spread of the pulses in the SPAD [181], which is also wavelength-dependent. In order to distinguish the fast instrument response from the actual PL decay, the response function can be extracted from their convolution

$$M(t) = (f * g)(t) = \int_{-\infty}^{\infty} f(t-\tau)g(\tau)d\tau, \tag{5.1}$$

where $M(t)$ is the measured overall PL decay, $f(t)$ is the PL decay function and $g(t)$ is the impulse response. The convolution formula implies that the $M(t)$ is shifted by the contribution of the impulse response by $g(-\tau)$ at a given time t. Because the impulse response is expected to be extremely fast, which is in the picosecond scale as compared to typically nanosecond scale PL decay, this response can be represented by a Gaussian function,

$$g\,(t) = G \times exp\left(-\frac{4ln\,(2)\cdot(t-t_0)^2}{w^2}\right). \tag{5.2}$$

The coefficient G is an arbitrary amplitude and t_0 is the time at the peak of the Gaussian pulse. The $FWHM$, w, is related to the width of the Gaussian pulse, c, by $FWHM = 2\sqrt{2ln2}c$. Solving for the value of c gives the time resolution of the impulse response of the instrument. Examples of the TRPL of GaAs with the convolution fits to Equation 5.1 are shown in Figures A.1 and A.2 in Appendix A. The instrument response determined from the fits is in the order of 30 ± 5 ps. Similar time resolution was obtained from the TRPL of silicon nanosheets in Figure C.1 in Appendix C.

5.1.2.2 Microsecond scale TRPL

When measuring microsecond scale TRPL, a simple setup can be employed using a fast photodector that has a time resolution in the sub-microsecond range (or bandwidth in the MHz range). For example, a Si avalanche photodetector (Thorlabs APD130A, 50 MHz, 20 ns time resolution) coupled to a fast oscilloscope (Tektronix DPO 2024B, 200MHz) can be used instead. Excitation with the 250 kHz Ti:Sapphire ultrafast laser (Coherent RegA 900) allows PL decay up to 4 μs to be measured. Longer PL decays will require laser pulses with lower repetition rate. In this case, an 800 nm, 1 kHz repetition rate, Ti:Sapphire ultrafast laser (Legend Coherent) with 50 fs pulse width is used. The setup for such configuration is shown in Figure 5.2.

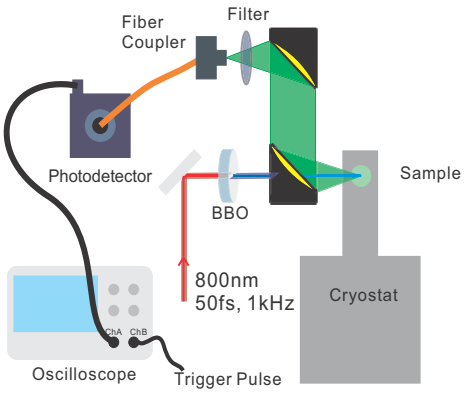

Figure 5.2: Experimental setup for the microsecond scale TRPL measurements.

5.1.2.3 Low temperature measurements

For low temperature measurements, the samples were cooled in a continuous flow optical cryostat with liquid nitrogen (LN2 from a dewar *via* a transfer line). A temperature controller (Lakeshore 335) , set the sample temperature for at least 20 minutes before taking any PL measurements using appropriate PID values for the temperature sensor and heater feedback loop.

5.2 Photoluminescence Spectroscopy: NIR region (900 - 3000 nm)

5.2.1 Integrated PL spectra

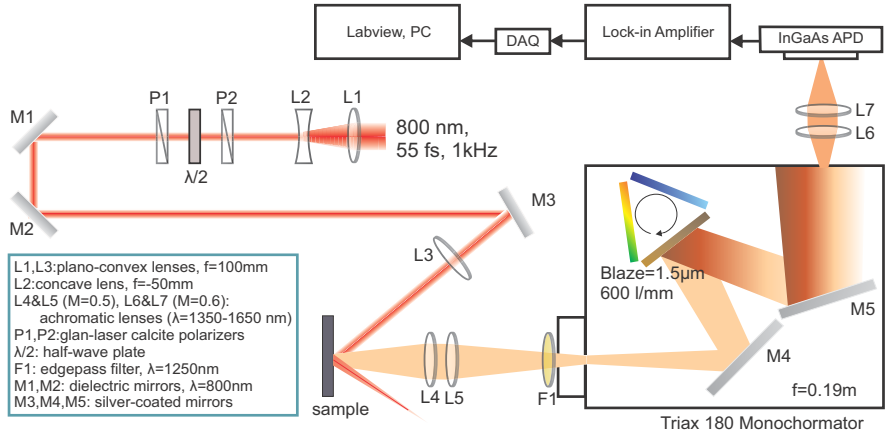

Figure 5.3: Experimental setup for the measurement of NIR PL spectra. A photo of the setup can be found in Figure A.3.

Since the spectrometer in Figure 5.1 does not include a grating in the NIR region, a separate setup is employed in the NIR PL measurement. For the PL measurements of crystalline bulk Ge wafers (MTI Corp.), presented in Chapter 8, an excitation source of 800 nm with 55 fs pulse width and 1 kHz repetition rate (Coherent Legend-Elite) was used as shown in Figure 5.3, where the laser source is attenuated by a set of two polarizers separated by a half-wave plate before being focused by a lens. The tight focus is located after the sample, so that the size of the beam spot on the sample can be fairly large (2 mm) to avoid damaging the surface at higher excitation fluences. The PL is then collected in a noncollinear manner using a two lens configuration (Thorlabs, achromatic doublets optimized from 1.0 to 1.7 μm) with a demagnification of 2 to 1 mm beam spot onto the entrance slit of the monochromator. The monochromator (Triax 180, Horiba) has a grating in the NIR blazed at 1500 nm with 600 lines/mm, which is controlled by a turret and a sliding motor.

The dispersed light from the grating is reflected by a silver mirror and directed to the exit slit. Another set of two achromatic lenses (with a demagnification of 1:0.67) is used to refocus the PL to an InGaAs avalanche photodetector (APD130C, Thorlabs) with a wavelength range of 900 - 1700 nm or a thermoelectronically-cooled InGaAs amplified photodetector (PDA10DT, Thorlabs), which has a broader responsivity in the wavelength range of 900 - 2700 nm and a maximum of 1MHz bandwidth at 70 dB gain. At the zeroth order of the grating, the PL of the Ge sample obtained by the photodetector is at maximum intensity, which can be easily observed using an oscilloscope (TDS3032B, Tektronix). This aids the user to set the boxcar integrator (Standford Research Systems) by 'gating' or selecting the time window in the PL decay. Hence, the dc output of the boxcar integrator, triggered at the frequency of excitation pulses, provides the time-integrated PL intensity. If the grating is not in zeroth order, the PL intensity at each selected wavelength becomes significantly small. In this case, the dc output from the boxcar integrator is further extracted using a DSP lock-in amplifier (SR830, Standford Research) referenced at the frequency of the excitation pulse. Using a Labview program that controls the monochromator and acquires the signal from the lock-in amplifier, a spectral measurement of the PL is obtained.

In order to determine the resolution of the monochromator, a white light from a tungsten filament source (Ocean Optics) was placed before the entrance slit. The output light at the exit slit was focused onto an optical fiber (M29L, 600 μm core size, 0.39 NA, Thorlabs) coupled to a NIR spectrometer (Ocean Optics). At 2 mm entrance and exit slits (the maximum slit allowed in the monochromator) and at each wavelength, the measured FWHM of the emission spectra was found to be within the range of 4 to 7 nm from 1000 to 1600 nm (Figure A.4). Thus, the maximum spectral resolution does not exceed $\pm$5 nm.

5.2.2 Spectral correction

The responsivity of the setup may not be the same over all wavelengths. The use of NIR achromatic lenses only allows maximum transmission over a certain wavelength range, the grating inside the monochromator is blazed, and the responsivity of the InGaAs detector is certainly not flat. All of these contribute to the measured PL spectra and therefore need to be corrected.

The experimentally measured PL intensity at each wavelength $I_{exp}(\lambda)$ is a combination of the

spectral response of the whole setup, $Q(\lambda)$, and the actual PL intensity, $I(\lambda)$, of the sample [23], where

$$I_{exp}(\lambda) = Q(\lambda)I(\lambda). \tag{5.3}$$

Thus, the acquired spectrum can be corrected by dividing it with the correction function $Q(\lambda)$. A common method of taking $Q(\lambda)$ is by extracting the blackbody response from a calibrated light source. The correction function $Q(\lambda)$ can be calculated using the equation

$$Q(\lambda) = \frac{w(\lambda)}{S(\lambda, T)}, \tag{5.4}$$

where $\omega(\lambda)$ is the experimentally acquired spectrum from a blackbody radiation source and $S(\lambda, T)$ is the blackbody curve. Here, we use a tungsten filament lamp (Ocean Optics) with a temperature of $T = 3100$ K as the blackbody source. The spectral energy density as a function of wavelength can be determined from the Planck's law calculated as

$$S(\lambda, T) = \frac{8\pi hc}{\lambda^5} \frac{2}{e^{(hc/\lambda k_B T)} - 1}. \tag{5.5}$$

Plotting Equation 5.5 shows a spectral peak at $\lambda_{peak} = 934$ nm in Figure 5.4a, having a $\lambda_{peak} \cdot T = 2.9 \times 10^{-3}$ m$\cdot$ K. Notice that the blackbody curve does not show similarity with the actual emission intensity curve $w(\lambda)$, shown in Figures 5.4b and 5.4c, due to the overall responsivity of the experimental setup.

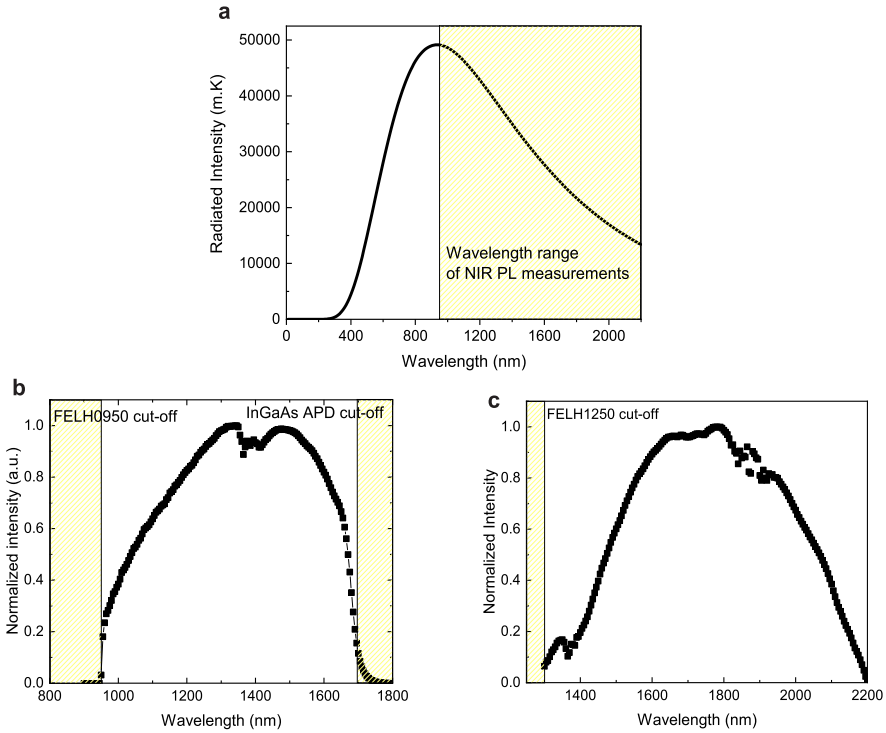

Figure 5.4: ***a)*** *The blackbody curve of a tungsten filament light source at T = 3100 K. Actual emission intensity measured by the whole experimental setup* ***b)*** *with a long pass filter at 950 nm (FELH950nm, Thorlabs) in the monochromator input and an InGaAs Avalanche Photodetector (APD130C, Thorlabs) at the output, and* ***c)*** *with a long pass filter at 1250 nm (FELH1250nm, Thorlabs) in the monochromator input and InGaAs amplified photodetector (PDA10DT, Thorlabs) at the output.*

For the actual measurement of PL, as an example, we take the PL direct transition from an undoped Ge (Ge-undoped), antimony doped Ge (Ge-Sb doped), and gallium doped Ge (Ge-Ga doped). Figure 5.5a shows the *uncorrected* PL spectra of the samples using an InGaAs avalanche photodiode (900 - 1700 nm). Using Equation 5.4, where we include the correction function $Q(\lambda)$, we extract the *corrected* PL spectra shown in Figure 5.5b. Clearly, the differences are evident. First, the PL intensity at $\lambda = 1700$ nm is not diminished and may continually increase at higher wavelengths, which is an onset of the indirect PL. Secondly, the PL peak has red-shifted by $\sim$10 nm. For the whole spectral range of the PL of the Ge, we replace the exit slit channel with an InGaAs amplified photodetector which has a responsivity up to 2800 nm. The normalized *uncorrected* and *corrected* PL spectra obtained for the Ge samples are shown in Figure 5.6. A noticeable red-shift in

the indirect PL peak can be observed and a narrowing of the indirect PL bandwidth. With these considerations, spectral corrections have been appropriately applied to the experimental results of the NIR PL spectra.

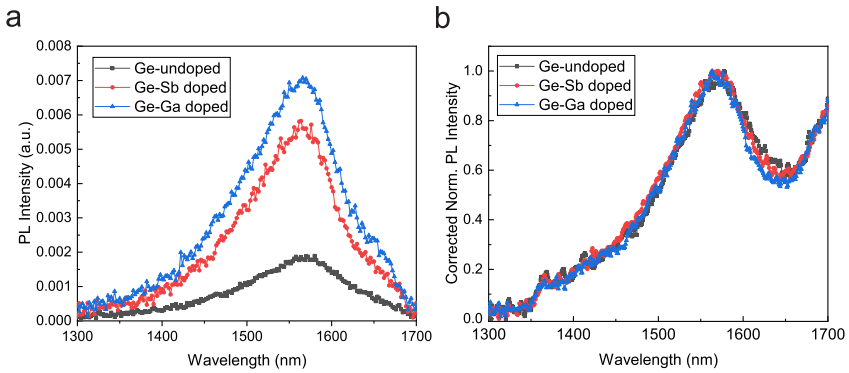

Figure 5.5: ***a)*** *Uncorrected PL spectra and* ***b)*** *Corrected normalized PL spectra of the Ge samples using an InGaAs Avalanche Photodetector (APD130C, Thorlabs).*

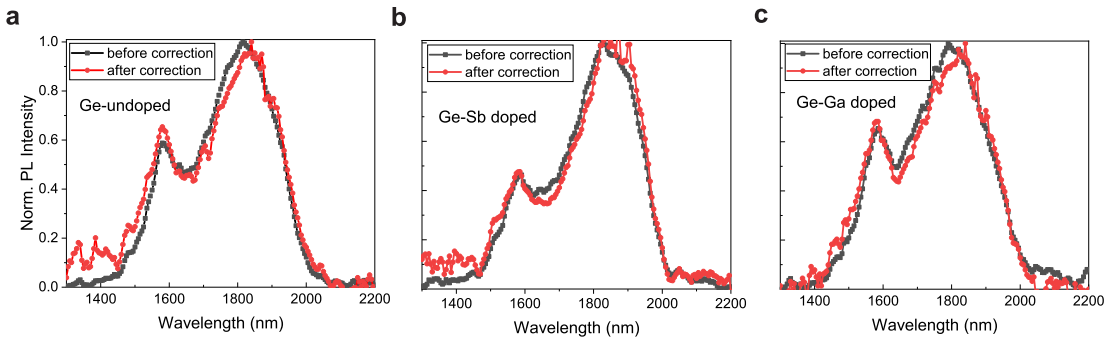

Figure 5.6: Normalized uncorrected (grey) and corrected PL spectra (red) of ***a)*** *Ge-undoped,* ***b)*** *Ge-Sb doped, and* ***c)*** *Ge-Ga doped samples using an InGaAs Amplified Photodetector (PDA10DT, Thorlabs).*

5.3 Time-resolved terahertz spectroscopy (TRTS)

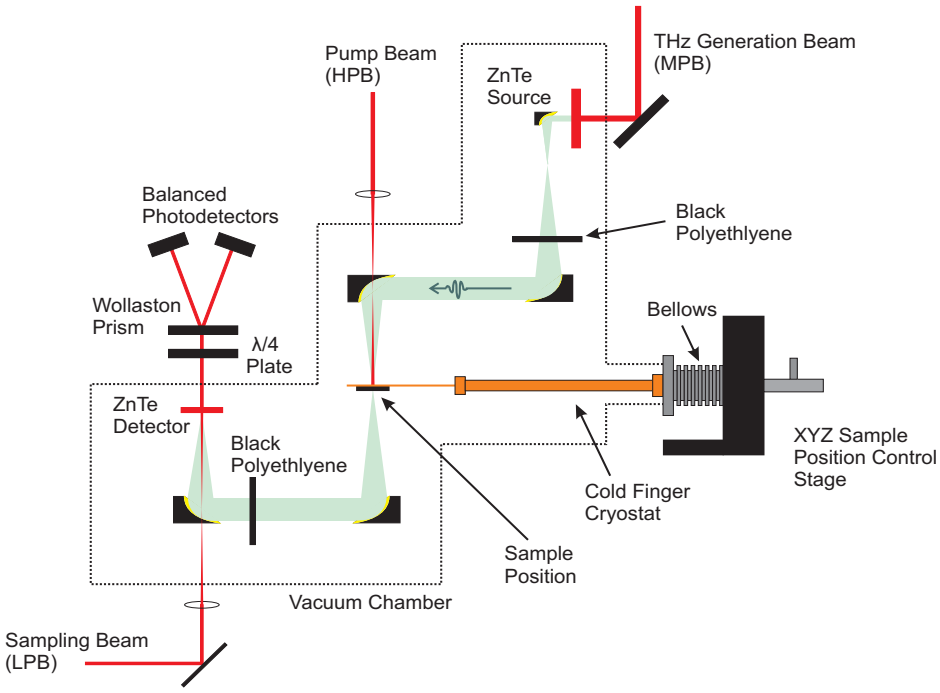

Figure 5.7: Schematic diagram of the time-resolved terahertz spectroscopy experimental setup.[2]

The TRTS setup employs an optical pump - THz probe technique that is driven by an amplified Ti:Sapphire laser source at 810 nm (1.53 eV) with 1.04 kHz repetition rate and 100 fs pulse width. The 650 mW average output of the laser was divided into three beam lines: high (80%), medium (16%) and low power (4%) beams (LPB, MPB and HPB, respectively). The HPB is used for the optical excitation of the sample, the MPB is for generating THz pulses from a ⟨110⟩ ZnTe crystal *via* the OR method, and the LPB acts as a sampling beam for the EO detection. Details of the OR

[2]Figure adapted from Ref. [12]. Experimental setup was designed and developed by F. A. Hegmann and recently re-aligned by N. Amer.

method and EO detection have been discussed in Sections 4.2.1 and 4.2.3.

The THz beam is collected by a set of off-axis parabolic mirrors and then focused onto the sample. A hole at the center of the parabolic mirror before the sample allows the HPB to go through and spatially overlap with the focused THz beam. The sample is photoexcited with a spot size of 4 mm, which is much larger than the THz beam spot of 0.8 mm so one can assume a uniform distribution of pump beam across the focused THz beam.

The TRTS measurements are carried out in a transmission mode. As the THz pulses propagates through the sample, another set of off-axis parabolic mirrors is used to collect the transmitted THz beam and focus it onto a second $\langle 110 \rangle$ ZnTe crystal for the EO detection. Here, the sampling beam (LPB) is spatially overlapped with the focused THz beam onto the ZnTe detection crystal.

The samples are placed on a copper sample holder with 1.5 mm apertures. The sample holder is then connected to the cold finger of the cryostat, the position of which can be adjusted by a 3D translation stage. The THz setup, comprised of the $\langle 110 \rangle$ ZnTe crystals (acting as emitter and gate), parabolic mirrors, and the sample holder, are all enclosed in a chamber that can be evacuated to 5×10^{-6} Torr. Evacuating the chamber allows low temperature measurements and detection of the THz pulses without the contribution of water vapour absorption. Fused silica windows are used for optical access to the chamber. To cool the samples, the cold finger is attached to a transfer line that allows LN2 to flow through. Finally, Labview was integrated with the setup for data acquisition and analysis.

5.3.1 TRTS scan methods

TRTS was initially discussed in Section 4.3. TRTS can provide the transient photoconductivity of a dielectric sample in the time domain, $\sigma(t)$, and in the frequency domain, $\tilde{\sigma}(\omega)$, which can be measured by employing either 1-chop or 2-chop scan methods, respectively [11, 12, 182]. The configuration of the measurements is shown below and the scan methods are described in the following sections.

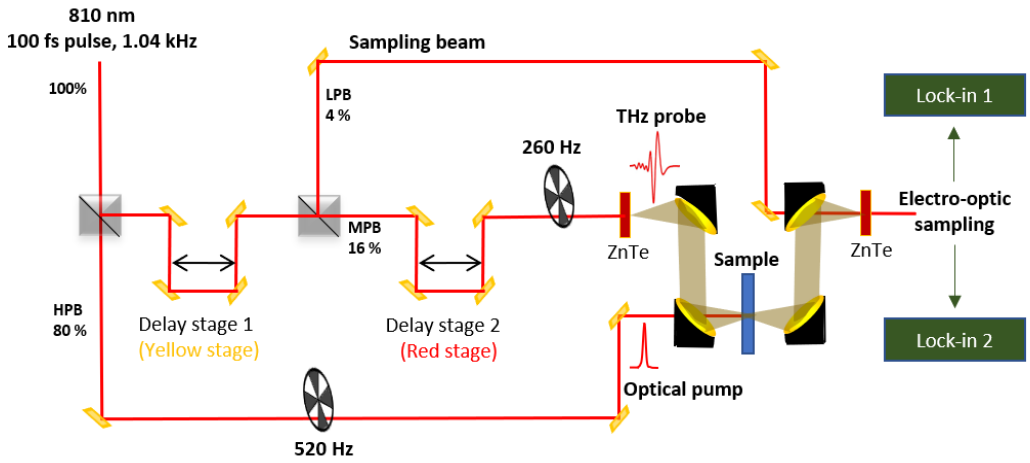

Figure 5.8: Configuration for the scanning methods. For the 1-chop method, only one of the choppers is used at a time. The 520 Hz chopper is turned ON when measuring $-\Delta T$ while the 260 Hz chopper is OFF. Conversely, the 260 Hz chopper is turned ON for the T_0 measurement with the 520 Hz chopper OFF. In both cases, only one lock-in is used, which is referenced to the chopper frequency. For the 2-chop method, both 520 Hz and 260 Hz choppers are turned on and the two lock-in amplifiers are referenced to either one of these frequencies.

5.3.2 Time-dependent photoconductivity

The time domain transient photoconductivity $\sigma(t)$ is related to the measurement of $|-\Delta T/T_0|$, where $-\Delta T$ is the change in the transmission of the peak THz amplitude (T_0) in a photoexcited sample as a function of the optical pump - THz probe delay time (Δt), as discussed in Section 4.3.1.2. In measuring $|-\Delta T/T_0|$, we employ a 1-chop scan method, whereby $-\Delta T$ and T_0 is measured separately and only one chopper is used at a time. The time domain measurements are acquired by varying the Δt using delay stages. The chopping configuration is shown in Figure 5.8 and the timing of the pulses based on the chopping frequency is depicted in Figure 5.9. The following paragraphs describe the details of the 1-chop scan method.

First, the peak THz amplitude, T_0, should be measured. This can be obtained by acquiring a waveform of the THz probe pulse that is transmitted through an *unexcited* sample (E_{ref}). In this case, the optical pump should be at a negative delay ($\Delta t \ll 0$), which can be set by fixing the 'yellow' stage. The E_{ref} waveform is then acquired from the lock-in by varying the delay stage of

the THz probe (red stage). While doing so, the 260 Hz chopper (THz probe chopper) is used and the lock-in is referenced to this frequency. When the THz waveform has been obtained, the peak amplitude of the wave (T_0) can now be selected by fixing the red stage. As illustrated in Figure 5.9c, only two THz probe pulses are being detected by the lock-in within ∼4 ms interval. Thus, the lock-in output corresponds to $2E_{ref}$. Because two pulses are measured in half of a sinusoidal wave reference of the lock-in (with each pulse at $\pi/4$ below the peak), a factor of $1/\sqrt{2}$ should be multiplied to each of the E_{ref} peak magnitude. Hence, the T_0 value is given as

$$T_0 = \frac{2E_{ref}}{\sqrt{2}}. \tag{5.6}$$

Secondly, we move on to measuring $-\Delta T$, which is the changes in the T_0 in a *photoexcited* sample. Here, the optical pump beam is chopped at 520 Hz and the lock-in is referenced to this frequency. This allows the lock-in to distinguish the pumped pulses (at 520 Hz) from the THz probe pulses repetition rate of 1040 Hz. A schematic diagram of the timing of the optical pump and THz probe is depicted in Figures 5.9a and 5.9b. To obtain the time domain $-\Delta T$, the yellow stage is varied at $\Delta t \geq 0$. As the time-delayed optical pump propagates through the sample, the value of $-\Delta T$ can be calculated from the lock-in output, which is related to the E_{ref} and E_{pump},

$$-\Delta T(t) = 2\left(E_{ref}(t) - E_{pump}(t)\right). \tag{5.7}$$

A factor of 2 is included because only half of the total THz probe magnitude is being detected by the lock-in within ∼4 ms interval using a 520 Hz chopper.

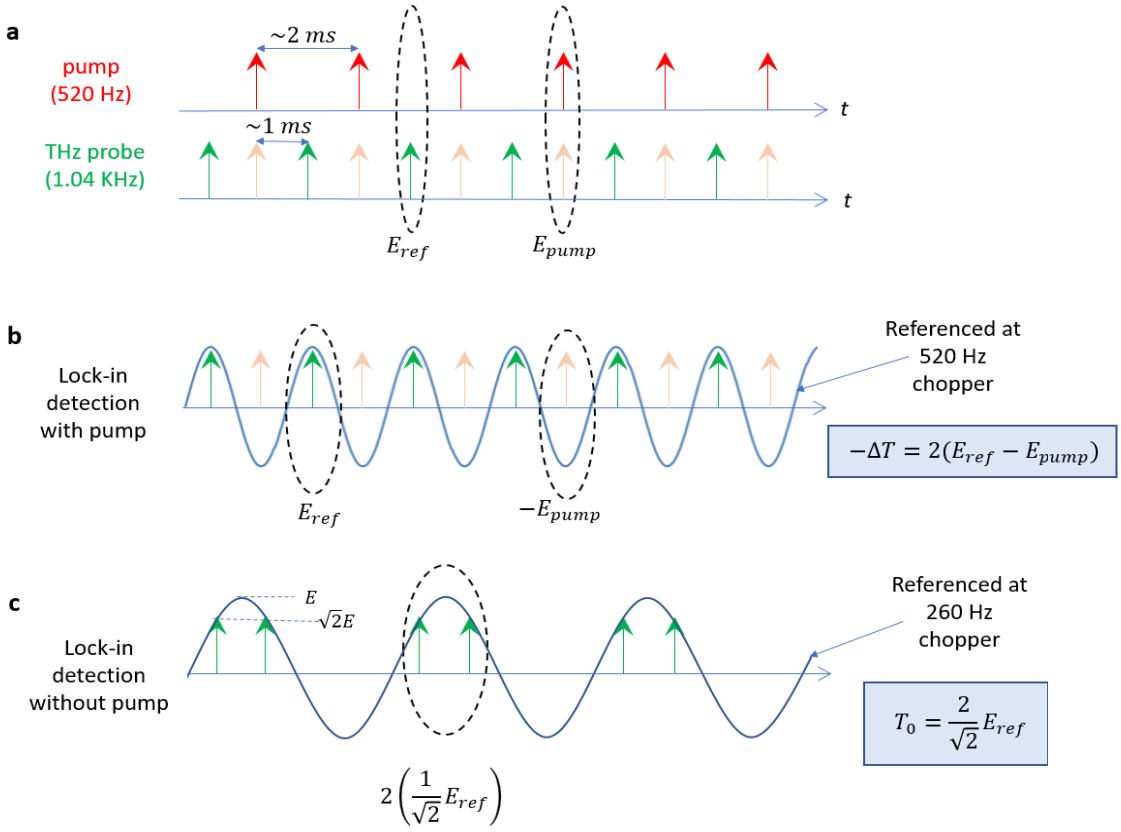

Figure 5.9: An illustration of the timing of the optical pump and THz probe pulses. ***a - b)*** *For the measurement of $-\Delta T$, a 520 Hz chopper is used for the optical beam, thus the sample is only photoexcited at every ~ 2 ms. No chopper is used for the THz pulses, therefore the THz pulse arrives every ~ 1 ms. In this configuration, the lock-in, referenced at the optical beam chopper of 520 Hz, is able to measure half of the total E_{ref} and $-E_{pump}$ voltage.* ***c)*** *For the measurement of T_0, the THz probe 260 Hz chopper is used and there is no optical excitation of the sample. The lock-in is referenced to the THz probe frequency and therefore only detects two consecutive THz pulses in half of the sinusoidal wave. In this case, a factor of $1/\sqrt{2}$ of the $2E_{ref}$ magnitude is measured.*

In order to determine the $\Delta t = 0$ ps in the time domain plot of the $|-\Delta T/T_0|$, the impulse response of the setup should be obtained. Here, we consider the impulse response to be limited by the width of the optical pump pulse. We assume a Gaussian pulse that follows the function, $f(t) = exp(-\frac{t^2}{2c^2})$, thus the width c is calculated as $c = 42.55$ fs based on the 100 fs FWHM of the pump pulse. At 1% or $f(t) = e^{-4.6}$, which is at the arrival of the optical pulse, the time is calculated as $t = 260$ fs. Hence, $\Delta t = 0$ ps can be located 260 fs immediately after the onset of the rise of the $|-\Delta T/T_0|$.

5.3.3 Frequency-dependent photoconductivity

For the frequency domain complex conductivity, we employed the 2-chop scan method [11, 12, 182], where both the transmitted THz pulse through the optically excited and unexcited sample are measured simultaneously. The ac complex conductivity can be extracted from the Fourier transform of the THz waveforms measured at a specific time delay after the photoexcitation of the sample.

Unlike the 1-chop method where the optical pump - THz probe delay (Δt) is varied, in the 2-chop method, Δt is fixed. First, the conductivity measurement of interest at specific pump-probe delay time is set by fixing the yellow stage. This is normally done at sometime after $\Delta t = 0$ when the time domain $|-\Delta T/T_0|$ has been obtained. Then, at specific Δt, the relative change in the entire THz waveform should be obtained. Therefore, the THz probe red stage should be varied within the time window of the THz pulse. In addition, two choppers are used during the measurements. The EO voltage output is both measured by two lock-in amplifiers whereby Lock-in 1 is referenced to the optical beam frequency of 520 Hz and Lock-in 2 operates at the THz probe chopping rate of 260 Hz.

The 2-chop configuration allows alternating optical pulses to photoexcite the sample (at every $\sim$ 2 ms) and alternating two consecutive THz pulses (at every $\sim$ 4 ms) to transmit through the sample, as depicted in Figure 5.10a. This implies that only one of the THz probe pulse can be temporally overlapped with the pump pulse on the sample, allowing us to simultaneously measure E_{ref} and E_{pump} in both lock-ins (illustrated in Figures 5.10b and 5.10c, respectively). Lock-in 1 and Lock-in 2 provide both the time domain values of E_1 and E_2, respectively, given as

$$E_1(t) = -E_{ref}(t) + E_{pump}(t), \tag{5.8}$$

$$E_2(t) = \frac{E_{ref}(t) + E_{pump}(t)}{\sqrt{2}}. \tag{5.9}$$

By auto-phasing (phase shift is zero) the two lock-in amplifiers, the values of E_{ref} and E_{pump} in the time domain should be the same from the above $E_1(t)$ and $E_2(t)$ equations, respectively. Again, a factor of $1/\sqrt{2}$ is included in Equation 5.9 because the probe pulses are measured at $\pi/4$ below the sinusoidal peak. From Equations 5.8 and 5.9, the values of $E_{ref}(t)$ and $E_{pump}(t)$ can be easily extracted. Obtaining the Fourier transformed $E_{ref}(\omega)$ and $E_{pump}(\omega)$ from the 2-chop method finally allows us to determine the real and imaginary parts of the complex conductivity $\tilde{\sigma}(\omega)$, as presented

in Equations 4.18 and 4.19, of the photoexcited sample.

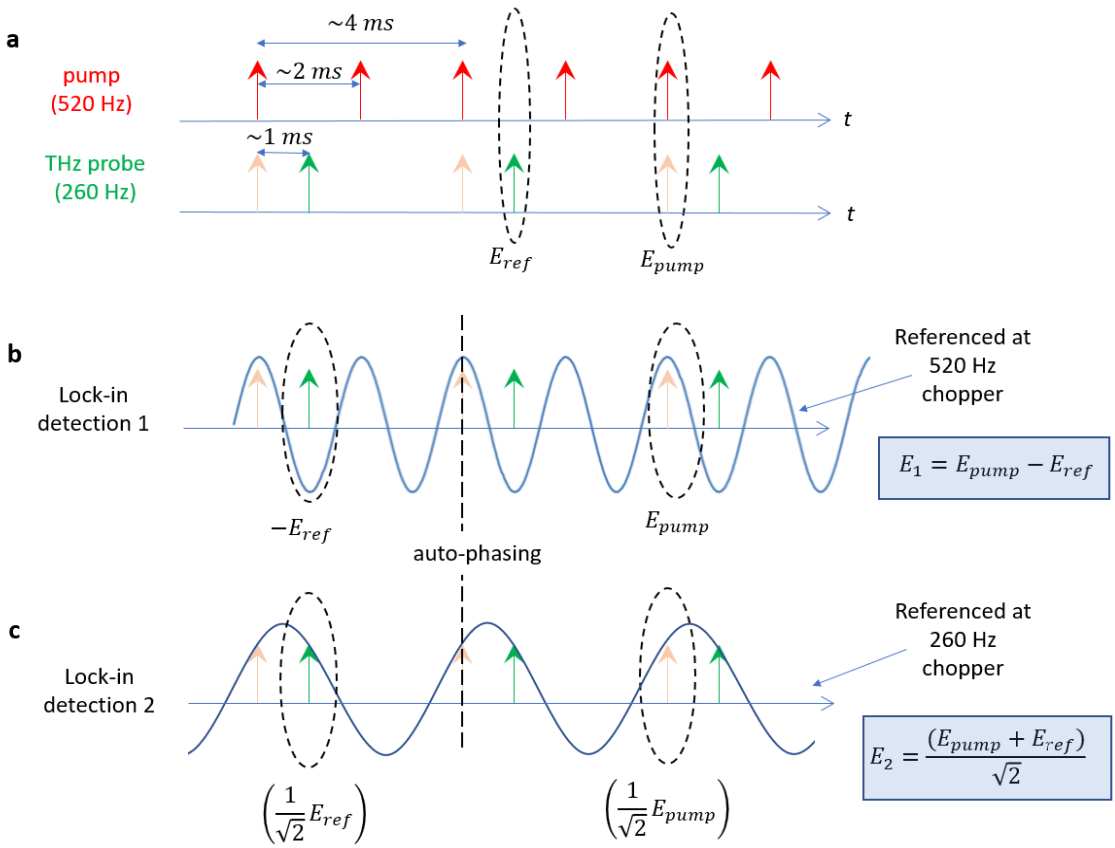

*Figure 5.10: An illustration of the timing of optical pump and THz probe pulses with the lock-in measurements of E_{ref} and E_{pump}. **a)** Both 520 Hz and 260 Hz choppers are used for the pump and THz pulses, respectively. Thus, the pump photoexcites the sample at every ~ 2 ms but the EO detection only measures the reduced THz amplitude (E_{pump}) at every ~ 4 ms. The THz amplitude of the unexcited sample, E_{ref}, is also obtained ~ 1 ms immediately after the E_{pump}. In order for the two lock-ins to obtain exact values of both E_{ref} and E_{pump}, Lock-in 1 and Lock-in 2 should be auto-phased. **b)** In this way, Lock-in 1, referenced at the pump beam chopper of 520 Hz, is able to measure E_{pump} - E_{ref}. **c)** Lock-in 2 is referenced to the 260 Hz chopper, which therefore measures the sum of the E_{ref} and E_{pump}. A factor of $1/\sqrt{2}$ is again included because the pulses are phased at $\pi/4$ below the peak of the sinusoidal wave reference of the lock-in.*

5.4 Photoluminescence modulation by intense THz pulses

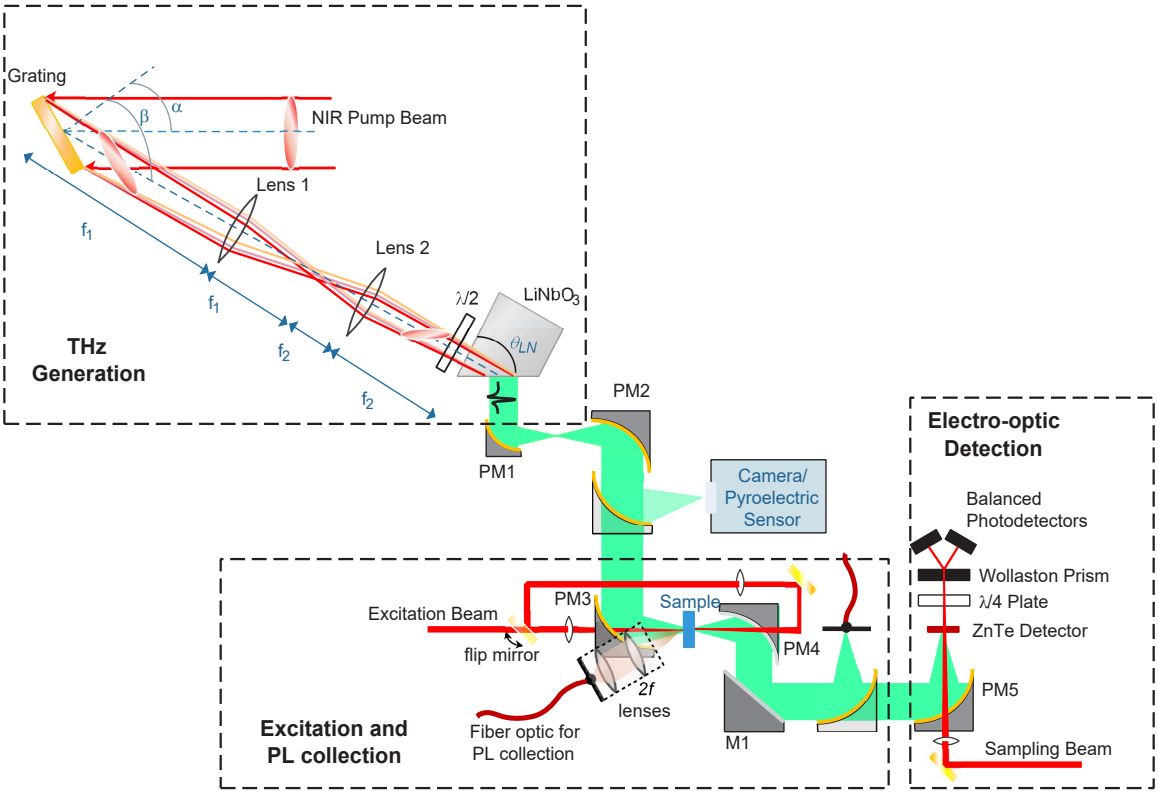

Figure 5.11: Experimental setup for the THz-modulation of PL which comprises three main sections: THz pulse generation, PL measurement, and the electro-optic detection.

Figure 5.11 is a schematic diagram of the experimental setup for the modulation of PL *via* intense THz electric fields. The setup is composed of three main components: (1) intense THz pulse generation, (2) PL measurement, and (3) the EO detection.

The laser system for the setup is composed of an oscillator-amplifier system. The Ti:Sapphire laser (Coherent Legend-Elite) amplifies a low-energy 800 nm seed pulse from a mode-locked laser oscillator (Coherent Micra). Using a beam splitter, 80% of the laser output (pump beam) is allocated for the generation of intense THz pulses while the 20% is for the photoexcitation of the sample (excitation beam) and EO detection (sampling beam). The 20% beam goes through an internal compressor in the Ti:Sapphire laser system while the high energy pump (80%) of ∼3.5 mJ goes

through an external home-made compressor which outputs a down-chirped pulse with 300 - 400 fs width. The down-chirping and pulse duration of the pump pulse significantly contributes to the magnitude and bandwidth of the generated THz electric field from a $LiNbO_3$ crytal [15].

After down-chirping, the pump beam is reshaped by a telescope with a set of cylindrical lenses (Figure A.5). This allows the pump beam to be demagnified into a cylindrical horizontal beam. It is found that a demagnification of ∼0.7 in the vertical dimension of the pump beam results to a maximum THz energy from the $LiNbO_3$ crytal (Figure A.6). Thus, the distances between the cylindrical lenses in the telescope was fixed to provide 0.7 demagnification throughout the experiments. Right after the telescope, a 500 Hz chopper was placed (Figure A.7) to block half of the total pump pulses, which is at 1 kHz repetition rate. This allows THz pulses to be generated at 500 Hz rate, so it can be easily distinguished from the 1 kHz excitation beam (for the PL measurement of sample) and sampling beam (for the EO detection).

To optimize the THz generation efficiency, a tilted pulse front technique was employed (see Section 4.2.2). The pump pulse front is tilted by a grating with a groove density of $p = 1800$ cm^{-1}. Afterwards, the pump beam is demagnified by a set of two cylindrical lenses. The first cylindrical lens mounted after the grating has a focal length of $f_1 = 250$ mm which focuses the pump beam in the horizontal dimension. The 2nd cylindrical lens, which also focuses at the horizontal dimension, has $f_2 = 150$ mm. This $4f$ lens configuration, which is a combination of four focal lengths, provides a demagnification of $M_{g1} = f_2/f_1 = 0.6$ of the pump beam image from the grating to the front of the $LiNbO_3$ crytal. By employing Equations 4.8 - 4.10 and by using the optimum $LiNbO_3$ tilt angle of $\gamma_c = 62°$, center wavelength of $\lambda = 805$ nm, and refractive index of the optical pump at the $LiNbO_3$ of n_g=2.208, the tilt angles for the grating are calculated to be $\beta = 54.4°$ and $\alpha = 39.5°$ (Figure A.7).

A demagnification of $M_{g1} = 0.6$ provided by the $4f$ lens configuration results in a pump beam spot size of about 4 to 6 mm^2, which should correspond to the size of the collimated THz beam generated by the $LiNbO_3$ crystal. The THz beam is collected by the first off-axis parabolic mirror (PM1) that has a diameter of $D = 0.5$" and an effective focal length of $f = 0.59$". The collected THz radiation is further directed by a set of off-axis parabolic mirrors. In order to preserve the f-number ($N = f/D$), the second mirror (PM2) was chosen to have $D = 2$" and $f = 4$", which outputs a

collimated THz beam. The third mirror (PM3) which has $D = 2$" and $f = 3$" is used to refocus the THz beam onto the sample location. For the EO detection, the parabolic mirrors PM4 and PM5 are chosen to have the same specifications (D and f) with PM3 to maintain similar THz beam spot size when focused onto the sample and onto the ZnTe detector in the EO setup. The addition of a flat mirror (M1) in between PM4 and PM5 allows placement of a removable parabolic mirror for measurement of the THz energy (using a pyroelectric detector, SPJ-D-8, Spectrum Detector Inc.) or THz beam image (using a thermal imager, PV320 Electrophysics). The removable parabolic mirror can also be used to focus the measured PL from the back surface of the sample to an optical fiber thus, the mirrors PM4 and M1 are silver-coated to minimize loss upon the reflection of visible light. Alignment of the parabolic mirrors were crucial for the optimum THz wave propagation, thus a strict alignment procedure was applied [183] (see details in Figure A.8).

For the photoluminescence measurement, a collinear excitation beam is directed onto the sample through a 1 mm hole at the center of PM3. This configuration allows both the focused THz beam and the excitation beam to be spatially overlapped. The photoexcited spot on the sample was maintained at < 0.8 mm, which is smaller than the THz beam spot size of 1.2 - 1.5 mm^2. Hence, only the relative changes in the PL with the incident THz electric field pulses were measured. The PL is collected by a set of two achromatic lenses (Thorlabs, achromatic doublets optimized at 1.0 to 1.7 μm) that have focal lengths of 50 mm and 30 mm, respectively, providing a demagnification of 5:3. In this manner, the lenses refocused the collected PL into a smaller spot size of $\sim$0.5 mm, just appropriate for the 550 μm core size of a coupled optical fiber (Thorlabs M37L, optimized at a wavelength range of 400 to 2200 nm). The other end of the fiber is coupled to an InGaAs detector connected to a boxcar integrator. The boxcar integrator is referenced at the repetition rate of the excitation pulses at 1 kHz, which then provides a dc output of the integrated PL. The dc output is further processed by a lock-in amplifier, which is referenced to the THz pulses repetition rate of 500 Hz. The reference frequency of the lock-in is from the reference output of the 500 Hz chopper (Thorlabs MC2000). This configuration allows the lock-in to only measure the relative change in the integrated PL due to the excitation of THz pulses.

The arrangement of the elements of the experimental setup on the optical table is illustrated in Figure A.7 and pictures of the THz source, sample position, and EO setup are shown in Figures A.9, A.10, and A.11, respectively.

CHAPTER 6

Flourescence and Phosphorescence of Bismoles[1]

6.1 Introduction

The development of novel phosphorescent material from organic compounds has gain attractions in the past years due to their potential applications in photochemistry, photobiology, and possibly as organic light emitting diodes (OLEDs) [184, 185]. Some of the applications in these fields require long-lived emission with the highest possible quantum yield. In OLEDs, stable phosphorescent emitters are highly sought due to a possible maximum device efficiency of 100% versus 25% in traditional fluorescence-based emitters [186]. Furthermore, phosphorescent compounds that can exhibit longer wavelength in red or in infrared emission are of great value for bio-imaging, as there is less interference with undesired background emission [187]. One way to achieve these characteristics is to incorporate heavier p-block elements into a luminescent π-conjugated material that can greatly enhance the possibility of phosphorescence. To facilitate this process, the excess metastable vibrational energy of the triplet state must be removed by collisions, thus a molecule with sufficiently dense phase is preferable [188]. The method affords the probability of accessing the triplet state by increasing the rate of the intersystem crossing (ISC) from the singlet state in order to facilitate the process of phosphorescence. Such mechanism is referred as the 'heavy element effect' and has been

[1]Contents of this chapter is published at "Parke, S. M.; Narreto, M. A. B.; Hupf, E.; Mcdonald, R.; Ferguson, M. J.; Hegmann, F. A.; Rivard, E. Understanding the Origin of Phosphorescence in Bismoles: A Synthetic and Computational Study. Inorg. Chem. 2018, 57 (13), 7536-7549." (featured as a journal cover)

practiced in synthetic methods of π-conjugated materials containing inorganic Group 13-16 main group elements [189].

Bismuth (Bi), as a heavy metal, can be a better alternative to rare-noble-metal or rare-earth-metal centers that were normally used in efficient phosphorescent materials [185]. Bi has low toxicity and is more abundant than rare-earth elements. Synthesis of the first photoluminescent conjugated polymer with Bi was only reported recently (2006) [190] which may have a fluorescence nature of emission (λ_{ex}=310 nm, λ_{em}=440 nm) due to the short Stokes shift. Another conjugation to Bi, dithienylbismoles, showed broad PL at 600 - 640 nm which was attributed to weak phosphorescence with a concurrent fluorescence at 400 nm [185]. However, among these few studies, time-resolved PL measurements were not presented and the effect of the heavy element Bi on the PL dynamics of these π-conjugated materials was not discussed.

6.2 Bismoles

Here, we present three bismuth-containing five-membered heterocycles, or so-called 'bismoles'. The schematic diagrams of their distinct molecular structures are presented in Figure 6.1. For the Bismole 1, a mesitylene represented by the aryl ring, and a thiophene, which is a heterocyclic compound represented by the aromatic rings with S, are incorporated on the Bi, as shown in the general structure in Figure 6.1a. In Figure 6.1b, the aryl-substituted Bismole 2 contains proximal -CH_2NMe_2 group that could be used to modulate the PL *via* a possible hypercoordinate Bi$\cdots$$Me_2N$ interaction. In addition, the placement of pinacolboronate (BPin) groups in the periphery facilitate Suzuki-Miyaura cross-coupling [191]. Lastly, Bismole 3 is a by-product of the synthesis of Bismole 2 with a copper chloride (CuCl) adduct, as schematically shown in Figure 6.1c.

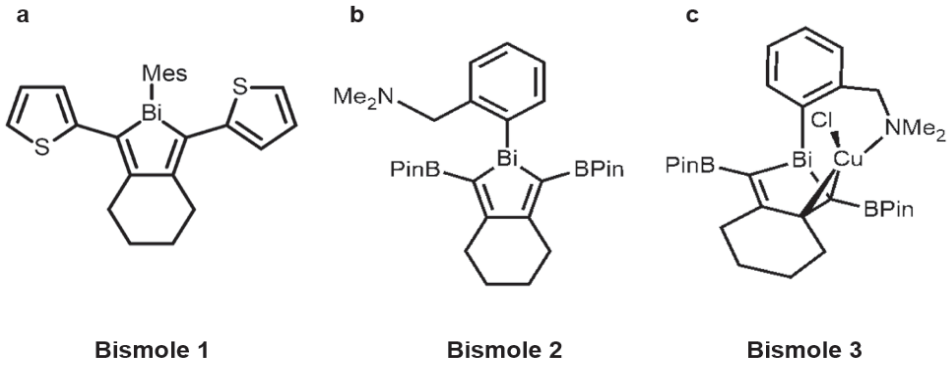

Figure 6.1: Product scopes of the synthesis of Bismoles 1, 2, and 3.[2]

6.3 Details of the experimental method

The bismole samples were dissolved in toluene or tetrahydrofuran (THF) (∼10 mg/mL) and were drop-cast onto a 1 mm thick optical grade fused quartz substrate (Starna Scientific Ltd.). These samples were then placed on the cold finger of an optical microscopy cryostat (Cryo Industries). The subsequent methods for the measurements of the time-integrated PL (TIPL) spectra and time-resolved PL (TRPL) were conducted in the same manner as described in the Experimental Method (Section 5.1) of Chapter 5. For the measurements of the nanosecond scale TRPL, a frequency-doubled 800 nm Ti:sapphire ultrafast laser (Coherent RegA 900) with 65 fs pulse width and 250 kHz repetition rate was used to optically excite the samples at $\lambda_{ex} = 400$ nm *via* the second harmonic signal generation from a BBO crystal. All measurements were carried out at an average of 2 ± 0.2 mW laser excitation power and in a span of 15 minutes, avoiding the contribution of noticeable PL degradation that occurs in $>$ 25 minutes. As for the recording of the microsecond lifetime component, a frequency-doubled 800 nm Ti:sapphire with 1 kHz repetition rate (Coherent Legend Elite) was used for the excitation instead. A set of parabolic mirrors collected the PL onto an optical fiber coupled to a Si avalanche photodetector (Thorlabs APD130A, 20 ns time resolution) with a band-pass filter of 705 ± 5 nm. The PL decay was recorded using a 200 MHz oscilloscope (Tektronix

[2]Synthesis performed and schemes provided by S. M. Parke. Details of the synthesis can be found in the publication.

DPO 2024B).

6.4 Results and Discussion

The bismoles display UV-vis absorption profiles that extend up to $\sim$ 425 nm in THF, with Bismole 1 showing the most red-shifted absorption of the compound series (Figure 6.2a). This afforded an opportunity to conduct both ultrafast TRPL and TIPL studies using a common excitation source at 400 nm. It was hoped that such ultrafast measurements would enable us to examine the emission behavior of these bismoles at various temperatures under high vacuum and to probe for possible competing emission pathways such as thermally activated delayed fluorescence (TADF) [192]. Despite being structurally distinct, all bismole samples have displayed substantial light absorption at 400 nm. To rule out possible quenching interactions by solvent and to suppress molecular rotations, the bismoles in the solution form were drop-casted as films for each PL measurement.

Upon excitation at 400 nm, Bismole 1 displayed green PL, with weak emission noted at room temperature (Figure 6.2a), and which became much more intense upon cooling to T = 77 K (refer to Figure B.1 in Appendix B). The dominant emission peak arising at $\sim$ 530 nm and the resulting small Stokes shift is in line with fluorescence. The PL spectra peak is more than $\sim$ 90 nm than the predicted absorption maximum (Figure B.5a), and decreasing at 550 - 600 nm, similar to the experimentally measured absorbance. The calculated absorption maximum corresponds to a HOMO-LUMO transition of 443 nm (Figure B.6a), which implies that the experimentally obtained PL spectra is of π-π^* character with little contribution of the Bi atom.

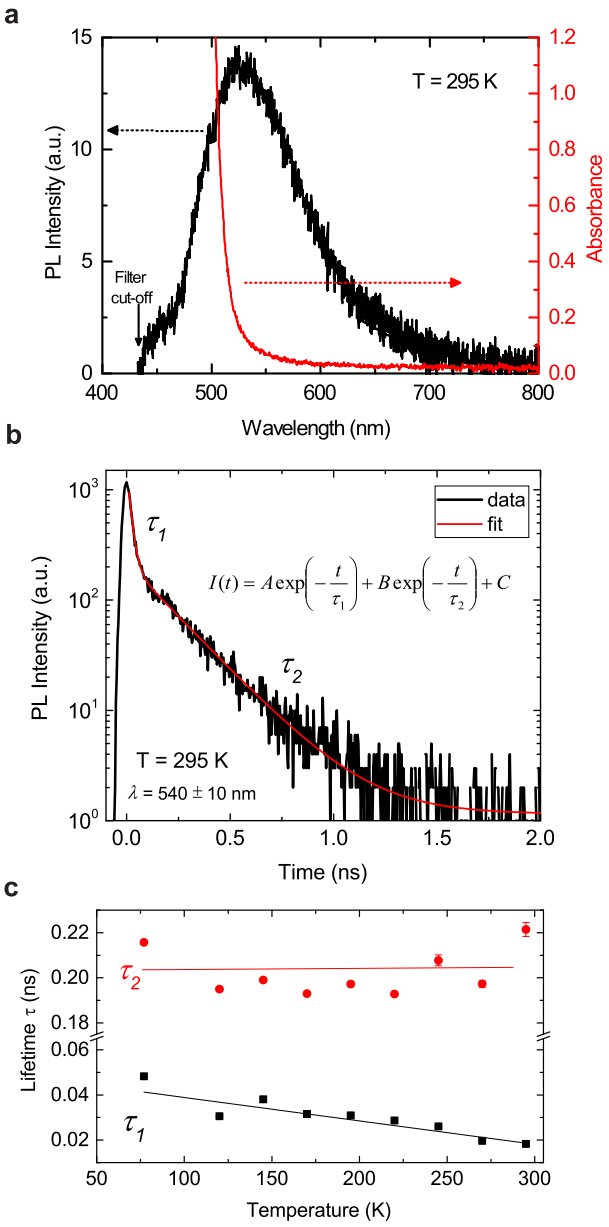

Figure 6.2: ***a)*** *TIPL spectra (left axis) and absorbance (right axis) associated with a drop-cast film of Bismole 1 at T = 295 K. A long pass filter was used to cutoff wavelengths below 435 nm.* ***b)*** *TRPL of Bismole 1 taken at T = 295 K and at a wavelength range of 540 Âś 10 nm. The TRPL follows a bi-exponential decay (red line), I(t).* ***c)*** *Lifetimes τ_1 and τ_2 extracted from the bi-exponential fits of TRPL at low temperatures.*

The fluorescence nature of the PL of Bismole 1 is further confirmed by the measured nanosecond scale TRPL. At 540 ± 10 nm, the TRPL follows a bi-exponential decay,

$$I(t) = A \cdot exp\left(-\frac{t}{\tau_1}\right) + B \cdot exp\left(-\frac{t}{\tau_2}\right) \tag{6.1}$$

where A and B are relative magnitudes of the PL intensity $I(t)$, τ_1 and τ_2 are the estimated lifetimes (see also Equation 2.7). The time offset was also considered in the fits. An example of the bi-exponential decay fit is shown in Figure 6.2b at T = 295 K with the values of the lifetimes τ_1 and τ_2 presented in Figure 6.2c. For the bi-exponential fits to the TRPL at low temperature, refer to Figure B.2 in Appendix B. The "fast" component at < 0.08 ns of the bi-exponential decay could be attributed to vibrational modes (Figure B.2a) that are suppressed at low temperature; thus, τ_1 becomes larger, as shown in Figure 6.2c, and fluorescence intensity is enhanced. The "slow" component at t > 0.1 ns was assigned as fluorescence from a low-lying singlet transition, which has a consistent lifetime τ_2 at different temperatures. In accordance to the Time-dependent density functional theory (TD-DFT) calculations[3](refer to Figure B.7a), the energy difference between the excited S1 and the T2 states is only 0.035 eV thus one might expect ISC to yield phosphorescence (after rapid internal decay from T2 to an emissive T1 state). However, the lack of phosphorescence is likely partly due to the absence of substantial orbital character at Bi in these states [193]; thus, spin-orbit coupling (which facilitates ISC) arising from the presence of the heavy element is minimized.

[3]TD-DFT calculations were performed by E. Hupf. Figures are shown in Appendix B.

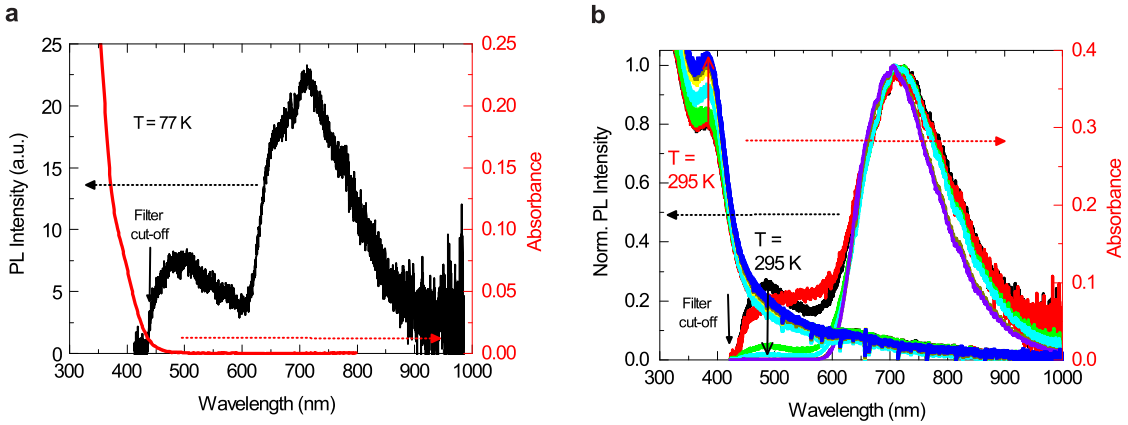

Figure 6.3: ***a)*** *TIPL intensity at T = 77 K (left axis) and absorbance (right axis) at T = 295 K for Bismole 2 (drop-cast film from THF).* ***b)*** *Normalized TIPL intensity (left axis) and absorbance (right axis) at various temperatures of the copper complex Bismole 3.*

Bismole 2 remarkably shows two broad PL peaks at 77 K, as depicted in Figure 6.3a. The first peak at $\sim$ 485 nm comprises 32% of the total integrated emission intensity compared to the second low-energy peak at $\sim$ 720 nm. The two peaks are indicative of fluorescence and phosphorescence, respectively; however, TRPL could not be measured due to the fast photodegradation of the sample in the excitation beam. Note that the weak absorption at 400 nm is responsible for the weak PL, which was only observed at 77 K, where molecular motions are inactivated and phosphorescence then becomes observable [194]. The experimentally measured absorbance corroborate the predicted UV-vis absorption *via* TD-DFT calculations (Figure B.5b and B.6b), where a considerable oscillator strength to low-lying singlet states is predicted at 348 nm for the HOMO-1 to LUMO transition, and that the absorption decreases at 400 - 450 nm. In addition, the TD-DFT calculation also show another HOMO-2 to LUMO transition at 361 nm which is due to the significant contribution of the Bi atom. These two HOMO-LUMO transitions could be attributed to the two PL peaks, but with a Stokes shift from the absorption spectrum.

The CuCl complex counterpart, Bismole 3, does not yield luminescence that is visible by eye when excited at 365 nm using a hand-held lamp; however, under the stronger laser excitation at 400 nm, clear PL is found at room temperature (Figure 6.3b). In addition, this compound

undergoes much less photodegradation compared to Bismole 2, and becomes almost negligible when it is progressively cooled to 77 K (see Figure B.3), thus enabling TRPL to be measured at various temperatures. Relative to the first peak at $\sim$ 485 nm, the second red-shifted phosphorescence peak at $\sim$ 720 nm accounts for 73% of the integrated PL intensity at room temperature. As the temperature is lowered from 200 to 77 K, the overall integrated PL intensity increases with a linear trend (Figure 6.4a), leading to an intense long wavelength (phosphorescence) emission and eventually accounting for 99.75% of the total PL at 77 K. This observation implies improved ISC efficiency and pronounced participation of the Bi atom in the excitation process. Additionally, it can be noticed in Figure 6.3b that as the intensity of the phosphorescence is enhanced, the corresponding emission maximum becomes blue-shifted by 16 nm (0.04 eV) from room temperature to 77 K with slightly narrowing bandwidth, suggestive of the suppression of low-lying vibrational levels (acting as nonradiative pathways) from the excited triplet state. Similar to Bismole 2, transitions at the HOMO-2 to LUMO and HOMO-1 to LUMO were predicted, at 361 nm and 398 nm, respectively (refer to TD-DFT calculations in Figure B.6c), which corresponds to the shifted two PL peaks.

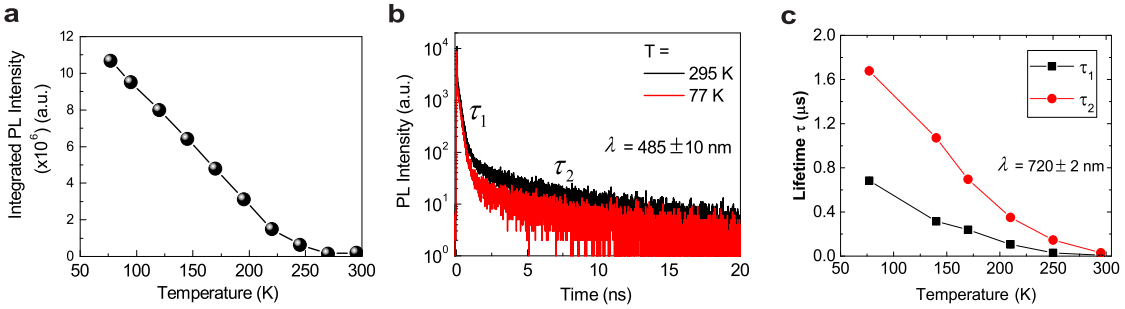

Figure 6.4: ***a)*** *Variation of the PL intensity of Bismole 3 with an increase in temperature from 77 to 300 K.* ***b)*** *TRPL in nanosecond scale (TRPL-ns) for Bismole 3 taken at 485 ± 10 nm.* ***c)*** *Lifetime in microsecond scale for Bismole 3 taken from the TRPL fits to bi-exponential decay at 705 ± 5 nm and at various temperatures.*

Analysis of the emission data by TRPL confirmed the presence of dual fluorescence and phosphorescence in Bismole 3, as evidenced by concurrent short-lived (ns time scale) and long-lived (0.1-10 μs) emission, measured at different energy states, thus ruling out TADF. For the short-lifetime emission (ns), bi-exponential curves were observed (Figure 6.4b) with $\tau_1 = 0.226 \pm 0.006$ ns and $\tau_2 = 1.1 \pm 0.3$ ns that do not significantly change at low temperature. It is also noticeable that

at t $\leq$ 0.2 ns, another fast exponential decay is observed, which may again represent vibrational relaxations being thermally quenched, enabling rapid ISC and the emergence of the phosphorescence long-lifetime emission profile. At the phosphorescence peak, the dramatic increase of intensity is accompanied by a longer TRPL event in the microsecond time scale, and the emission again follows bi-exponential decay; the lifetime values are shown in Figure 6.4c (see fits at Figure B.4). As the temperature is lowered to 77 K, enhanced phosphorescence is observed accompanied by a longer microsecond lifetime up to $\sim$2 μs. The nature of the bi-exponential decay is unclear; it could be due to mixed metastable triplet states at $\sim$ 720 nm or possibly morphological effects within the cast films.

For the three samples, the possible mechanisms of the light emission are hereby explained; phosphorescence occurs from the initial photoexcitation to an S_n state with subsequent ISC to an energetically similar T_n state, followed by relaxation to the lowest T_1 triplet state, then finally phosphorescence and relaxation to the S_0 ground state. From the TD-DFT calculations of the singlet and triplet states (Figure B.7), all bismoles show the existence of close-lying $S_{1,2,3}$ and T_n states, thus resulting in a high probability for ISC to occur. However, as mentioned earlier, Bismole 1 do not show phosphorescence due to small energy difference between the S1 and the T2 states of 0.035 eV in contrast to Bismoles 2 and 3 with about 0.2 eV, which facilitates the ISC. In addition, as Bi is an element strongly affected by relativisitic effects, enhanced spin-orbit coupling should lead to significant mixing of singlet and triplet states, thus further increasing the probability of ISC. It was determined that Bismoles 2 and 3 show a low-lying singlet state with considerable mixing of singlet and triplet character (Bismole 2: 55.8% S, 44.0% T and Bismole 3: 63.4% S, 36.0% T). In the presence of CuCl, Bismole 3 has the highest degree of mixing. This also explains the dramatic increase of PL intensity of Bismole 2 and 3 at low temperature due to suppressed metastable states. In contrast, Bismole 1 have a low degree of mixing (92% S and 8% T), which may additionally explain the absence of phosphorescence.

The phosphorescence energy can be defined as the difference in the adiabatic energy between the S_0 ground state and the T_1 triplet state or the zero-point energy corrected difference between these states (E_{0-0}). The phosphorescence energy of Bismole 2 (E_{0-0} = 1.76 eV) matches well the observed phosphorescence energy of 1.73 eV (720 nm). The predicted phosphorescence energy of Bismole 3 (E_{0-0} = 1.33 eV) is underestimated by 0.36 - 0.42 eV in comparison to the experimentally

observed 1.75 eV (709 nm). On the other hand, Bismole 1 have $E_{0-0} = 1.22$ eV which has a predicted emission in the near-infrared region (1016 nm) and are in line with the lack of experimentally observed phosphorescence. However, the lack of substantial mixing of excited singlet and triplet states in Bismole 1, because there is minimal orbital participation from Bi in the excitation processes and thus reduced spin-orbit coupling, likely hinders effective ISC to an excited triplet state. In contrast, Bismoles 2 and 3 show considerable orbital character from Bi associated with the excited states; thus, spin-orbit coupling becomes more pronounced, and phosphorescence is observed experimentally. While the enhancement of ISC *via* an external heavy element effect remains a possibility, the lack of observed phosphorescence in Bismole 1 suggest that participation of the heteroatom in the excitation process seems to be necessary for phosphorescence to occur [193].

6.5 Summary

In summary, light emission from a series of bismole compounds were successfully obtained and the luminescence properties of these three bismoles were studied in detail. Bismole 1 was found to exhibit only fluorescence at low temperatures, and this is most likely due to the lack of participation of the Bi atom in the excitation process leading to minimal singlet and triplet mixing in the lower-energy excited states. Bismoles 2 and 3 were found to exhibit both fluorescence and phosphorescence, and this can be attributed to the increased orbital participation from the Bi in the excitation processes leading to significant mixing of triplet and singlet character in the lower-energy excited states. The CuCl interaction in Bismole 3 facilitated higher probability of ISC which resulted to a more pronounced phosphorescence. The findings of this work and the successful synthesis of the fluorescent and phosphorescent bismoles may be essential in the ongoing research in phosphorescent compounds with the application of the 'heavy element effect' for potential applications in OLEDs and bioimaging.

CHAPTER 7

Photoluminescence of Two-Dimensional Functionalized Silicon Nanosheets

7.1 Introduction

Research on 2D van der Waals layered materials has exploded in the past decade as an aftermath of the discovery of graphene [195, 196]. One of which that has gained attention recently is the fabrication of freestanding chemically exfoliated 2D nanosheet [197, 198] that distinguish itself from the mechanically exfoliated graphene and chemically grown monolayers on a substrate such as silicene [199] and germanene [200]. With the considerable number of reported 2D nanosheets [197, 201, 202, 203, 204], silicon nanosheets (SiNSs) have the advantage of being compatible with the existing Si-based technology [205] and thus poise to be a promising candidate in nanodevice applications [206, 207].

Being a 2D silicon allotrope, freestanding SiNSs have a buckled honeycomb lattice, where one of the two sublattices are vertically displaced with respect to each other in contrast to the planar sp^2-hybridized graphene [205]. The nonplanar Si=Si bonds, however, are too reactive to be isolated compared to its 2D carbon counterparts such as graphene [205, 207]. Hence, a rather straightforward approach for achieving a chemically stable monolayer SiNSs is by complete hydrogenation [206, 208]. The hydrogenated SiNSs is also commonly known as silicane, which is ideally sp^3-hybridized [209]. The challenge is that hydride termination alone is prone to oxidation in ambient conditions, thus subsequent surface modifications with various functional groups could provide protection [210] and additional thermal stability [204, 211, 212]. Consequently, the sp^3-hybridization by means of

hydrogen adsorption and surface passivation introduce a finite band gap from its Dirac-like band structure [209, 211, 212, 213, 214, 215, 216], a similar case with the non-zero band gaps arising from the sp^3-hybridization of hydrogenated graphene (graphane) [217, 218] and 2D transition-metal dichalcogenides [219].

The opening of the band gap can be visualized using photoluminescence (PL) spectroscopy. For example, among freestanding functionalized 2D SiNSs, Nakano *etal*. synthesized organically modified SiNSs that showed blue emission [210, 220, 221, 222]. Meanwhile, depending on the nature of the organic molecule on the surface of the sheets, the SiNSs exhibited PL from blue to green [223]. On the other hand, we have recently reported the synthesis of hydrogenated and covalently functionalized SiNSs that consistently emit green [206, 208, 224], which is unique compared to the aforementioned studies. Thus, the ability for these freestanding SiNSs to emit light paves a way to a new class of 2D material with promising technological applications in optoelectronics [221, 225]. But besides the interest on considering SiNSs as potential candidates for practical devices, exploring the fundamental science on the photoluminescent properties of SiNSs also needs to be addressed.

Understanding where the PL of the SiNSs comes from, would not only elucidate the nature of their light emission, but also help discriminate other influences that suppress the emission of light, as well as provide a possibility to control and optimize the PL. PL spectroscopy, which is a non-contact and powerful technique for probing the optical properties, can give information about the band structures, carrier lifetime and charge transport in nanomaterials [29]. Additionally, PL measurements can reveal the structural integrity of 2D materials, whether they are pristine or disordered, or have defects and impurities [201, 226]. Although PL measurements have been carried out in freestanding 2D functionalized SiNSs [206, 208, 210, 220, 221, 222, 223, 224], so far there has been very little work done on their analysis.

Thus, in this work, we explore for the first time the PL dynamics of freestanding 2D functionalized SiNSs. In addition, low temperature PL measurements were carried out as an integral component in the examination of the mechanisms of carrier transport; a study which has not been reported in photoluminescent SiNSs. Using pulsed laser excitation, we investigate the time-integrated PL spectra and the time-resolved PL of the as-synthesized and variously functionalized SiNSs in solution and solid forms. Our findings show that the PL originates from the as-synthesized hydro-

genated SiNSs with a PL peak energy that agrees to calculated band gap energies. The broad PL spectra is attributed to the inherent structural disorder of the SiNSs which remains static at low temperature. Subsequent functionalizations did not affect the PL spectrum of the as-synthesized SiNSs however, the functional groups play a role in the PL dynamics by influencing the dispersive carrier transport.

7.2 Functionalized Silicon Nanosheets

Figure 7.1 shows the synthesis of the hydrogenated and covalently functionalized SiNSs. The hydrogenated SiNSs (SiNS-H) are synthesized *via* chemical exfoliation from $CaSi_2$. By adding the monomers dodecane ($C_{12}H_{25}$), polystyrene (PS) and polyacrylic acid (PAA), together with the radical starter azobisisobutyrolnitril (AIBN), hydrosilylation reaction can be initiated [206, 208]. Thus, the different functionalizations of the SiNSs surface were performed. Here, the samples dispersed in toluene are SiNS-H(toluene) and SiNS-$C_{12}H_{25}$(toluene) (Figures 7.1a and 7.1b, respectively). SiNS-$C_{12}H_{25}$(toluene) is additionally drop-deposited on UV-fused quartz glass for SiNS-$C_{12}H_{25}$(solid). Also, SiNSs functionalized and embedded in polymer (SiNS-polymer@polymer) have been deposited on a quartz glass *via* melting; SiNS-PS@PS and SiNS-PAA@PAA (Figure 7.1c and 7.1d, respectively). Additional information on the synthesis can be found in Appendix B and in these reports [206, 208]. The thicknesses of the modified sheets were measured to be around 2 - 6 nm depending on the functionalization and the lateral size can render from hundreds of nanometers up to several micrometers. As an example, the atomic force microscopy (AFM) image of SiNS-$C_{12}H_{25}$ is shown in Figure 7.1e. Because the lateral dimensions of the SiNSs are relatively large, there should be no considerable quantum confinement effects from the inhomogeneity of the sheet sizes.

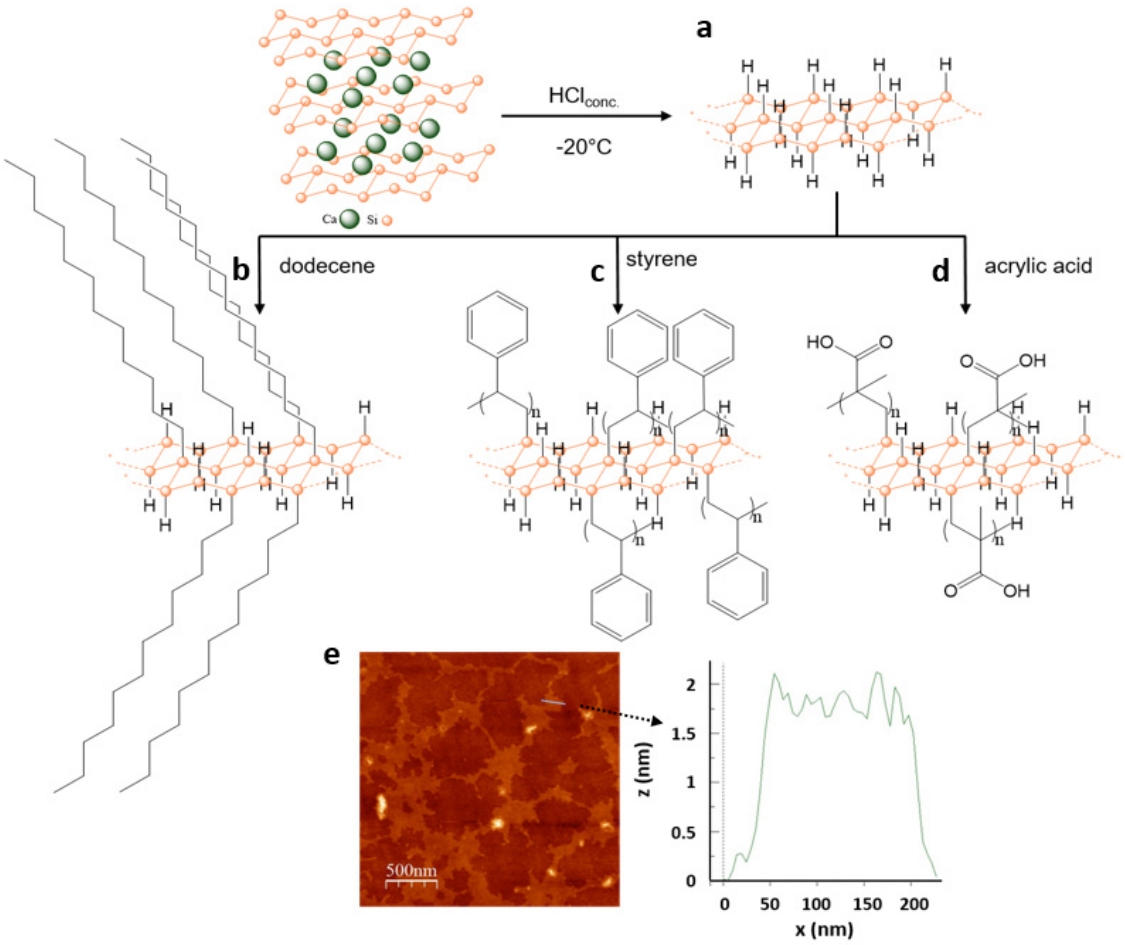

Figure 7.1: Synthesis of functionalized SiNSs starting from the chemical exfoliation of ***a)*** *SiNS-H from* $CaSi_2$*. Dodecane, polystyrene, and polyacrylic acid were chosen as substrates for the hydrosilylation reaction to form* ***b)*** *SiNS-*$C_{12}H_{25}$*,* ***c)*** *SiNS-PS@PS and* ***d)*** *SiNS-PAA@PAA, respectively.* ***e)*** *Atomic force microscope (AFM) image (non-contact tapping mode) of SiNS-*$C_{12}H_{25}$ *spin-coated on Si++/SiO2 substrate (left) and corresponding height profile along the blue line (right).*[1]

[1]Synthesis performed by A. Lyuleeva and T. Helbich. AFM conducted by A. Lyuleeva. Images provided by A. Lyuleeva.

7.3 Details of the experimental method

The nitrogen-filled cuvettes containing the SiNS substrate(toluene) were placed on an optical stage while the solid samples were placed on the copper finger of an optical microscopy cryostat (Cryo Industries). All samples were photoexcited at 400 nm from a frequency-doubled 800 nm Ti:Sapphire ultrafast laser (Coherent RegA 900) with 65 fs pulse width and 250 kHz repetition rate. All TIPL and TRPL measurements were carried out at an average of 435 $\pm$ 5 μW excitation power with a 0.50 $\pm$ 0.10 mm spot size. For the TRPL measurements, the rise time were found to be 35 $\pm$ 1 ps from the convolution fits (see example in Figure C.1). In view of this, the PL decay fits to Equation 7.2 were taken at times greater than 0.1 ns to prevent the contribution of the instrument response.

7.4 Results and Discussion

7.4.1 PL Spectra

All SiNSs exhibit green PL that peaks at a center wavelength of λ_p = 502-516 nm (E_p = 2.40-2.47 eV) regardless of surface functionalization, as shown in Figure 7.2a. Since there are no dramatic shifts overall, the consistency in the PL peaks and line shapes implies that the applied modifications on the surface do not significantly influence the PL spectrum, preserving the emission from the as-synthesized hydrogenated 2D SiNSs. Subsequent radical hydrosilylation on the surface of the sp^3-hybridized SiNSs does not cause any Si-Si bond cleavage, which would lead to the formation of a new Si backbone structure. The H-termination is simply replaced by another residue, linked with the surface *via* covalent Si-C bond (as shown in the Fourier-transform infrared spectroscopy (FTIR) in the previous report on the synthesis and characterization of the functionalized SiNSs [208]). Additionally, the radical-induced hydrosilylation reaction does not involve introduction of transition metal impurities, which could alter the PL [206]. Therefore, the slight shifts in the PL spectra of the functionalized SiNSs can be due to its surrounding environment, underlying substrates or the difference when the SiNSs are isolated in the solution form compared to when they are stacked in solid phase. These could change the dielectric function of the material or induce strain in the band structure, as was discussed in the case of MoS_2 [227]. An example is a slight red shift of the

peak energy (E_p) by 37 meV when SiNS-$C_{12}H_{25}$ is drop casted on glass compared to freestanding SiNS-$C_{12}H_{25}$ sheets dispersed in toluene.

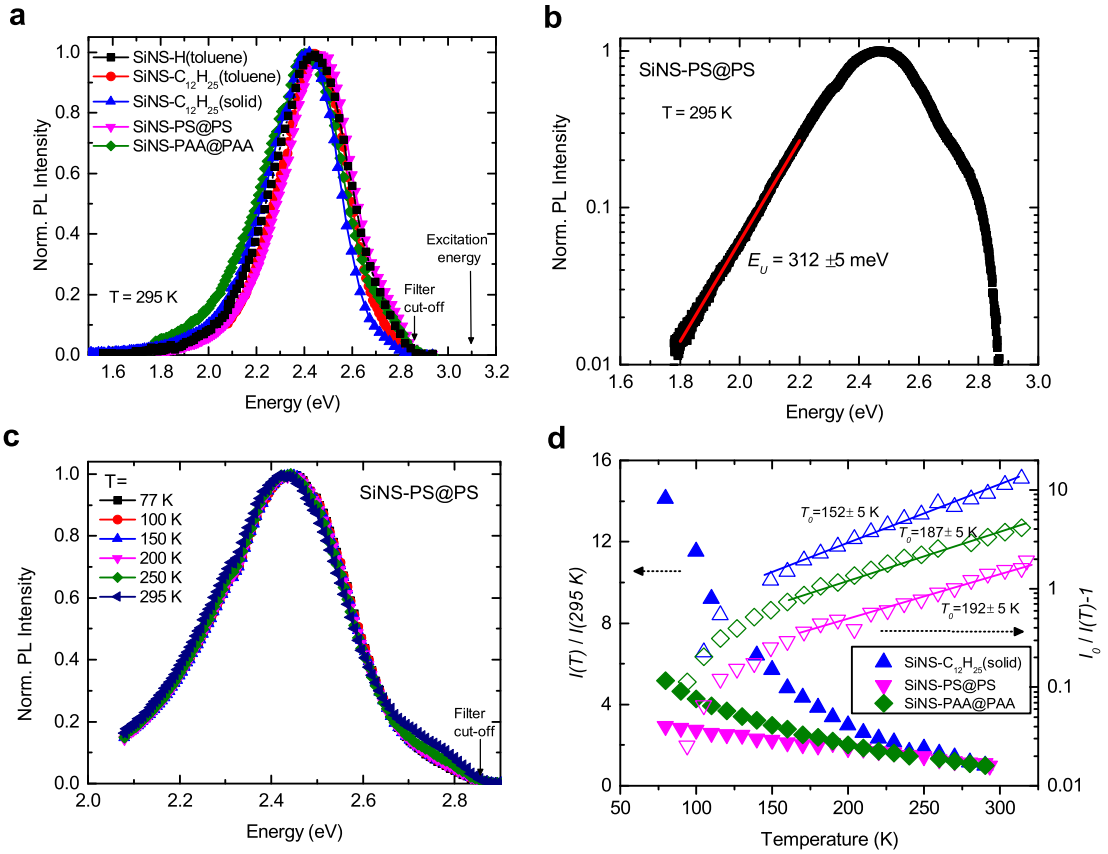

Figure 7.2: ***a)*** *Normalized PL spectra of SiNS-H(toluene), SiNS-$C_{12}H_{25}$ and SiNS polymer@polymer samples having peak energies ranging at E_p= 2.40 - 2.47 eV (λ_p = 502 - 516 nm) measured at room temperature. The excitation source is an ultrafast laser of E_{ex} = 3.1 eV (λ_{ex} = 400 nm), with an average power of 435 ± 5 μW (average fluence of 0.61 $\mu J/cm^2$), blocked by a long pass filter at 435 nm.* ***b)*** *Semi-log plot of the normalized PL spectra of SiNS-PS@PS indicating an exponential band tail at photon energies below E_p. The Urbach energy E_U is taken from the linear fit at $E < 2.2$ eV. Low temperature measurements of the PL spectra;* ***c)*** *the PL spectra of SiNS-PS@PS normalized to the E_p = 2.45 eV at 77 K, and* ***d)*** *the integrated intensity of the PL spectra, $I(T)$, at low temperature for the solid samples (SiNS-$C_{12}H_{25}$(solid), SiNS PS@PS and SiNS PAA@PAA). Left axis shows the normalized integrated PL to room temperature ($I(T)/I(295\ K)$) (filled symbols). Right axis shows $I_o/I(T) - 1$ shown in Equation 7.1 where I_0 is the integrated PL at 80 K (open symbols). T_0 is extracted from the slope of the linear fits at $T < 150$ K. Error bars are within the symbols.*

Because the light emission originates from the hydrogenation of the SiNSs, the E_p of 2.40 - 2.47 eV is close to calculated band gap energies (E_g). Using a simple quantum well model, the calculated E_g for hydride-terminated 2D Si network [228] (or so called polysilanes in earlier studies) is 2.5 eV. Whereas using density functional theory (DFT), E_g is $\sim$ 1.6 eV to 2.41 eV for a fully hydrogenated silicane [212, 214, 215, 216] whether it is a direct or indirect gap semiconductor. Experimentally, the observed green PL of the SiNSs is comparable to the measured optical band gaps of Si films/sheets grown by chemical vapor deposition (CVD) method: $\sim$2.3 eV for $\sim$3.4 nm ultrathin hydrogenated amorphous Si (a:Si-H) [229] and $\sim$2.3 eV measured from the PL of 3 - 9 nm crystalline Si with H2 passivation on the surface [230].

For many cases where the band-to-band PL is not preserved, oxygen-related passivation and defects acting as radiative centers give rise to blue emission, as was reported in other Si-based nanostructures, such as amorphous silica nanosheets [231], porous Si [232] and Si nanocrystals [233]. Thus, when the SiNSs are exposed to air, the E_p is blue-shifted and another peak arises at $\sim$ 2.78 eV (Figure C.2) , accompanied by quenching of the green PL intensity. Here, H atoms, terminating the Si dangling bonds, can be easily replaced with O or OH as confirmed by Si-OH and Si=O bonds in the FTIR spectrum, which was measured in air [208]. Thus, the green PL (measured in vacuum) cannot be attributed to oxidized surface states. This further supports that the PL originates from the band gap of hydrogenated SiNSs.

It can also be observed in Figure 7.2a that the PL spectra are considerably broad having a full width half max (ΔE_{PL}), ranging from $\sim$330 to 375 meV. Note that PL from bulk crystalline direct gap semiconductor has only a ΔE_{PL} of $\sim$47 meV at room temperature (see Figure 2.4). Broad ΔE_{PL} that goes to hundreds of meV has been commonly reported in disordered Si such as a-Si:H. [234]. Moreover, PL spectra having such a broad ΔE_{PL} oftentimes have long exponential tails at photon energies below E_p, a signature of Urbach tail [235]. The Urbach tail is known to occur in disordered materials such as ultrathin a:Si-H films [236] and organic semiconductors [237] due to shallow localized states below the mobility edge [66, 76]. The disordered structure produces local fluctuations in the bandgap, which would consequently lead to the increase of the width of the PL peak. Since the PL intensity follows $I\,(hv) \sim exp(hv/E_U)$ [60] at photon energies below E_p, the characteristic energy of the width of the Urbach tail (E_U) can be estimated from the inverse tail slope at $E < 2.2$ eV of the semi-log plot of the PL spectra of the hydrogenated and functionalized

SiNSs at room temperature as illustrated in Figure 7.2b (and Figure C.3). The E_U ranges from 272 to 387 meV, comparable to their ΔE_{PL}. Furthermore, the E_U taken from the PL is confirmed by the exponential tail in the absorption spectra (Figure C.4).

The Urbach tail can either originate from the 'static' structural disorder or 'dynamic' thermal contribution from electron-phonon interaction [238, 239]. Therefore, the behavior at various temperatures is examined in more detail. The measurements were carried out for the solid samples: SiNS-$C_{12}H_{25}$(solid) and SiNS-polymer@polymer composites (SiNS-PS@PS and SiNS-PAA@PAA). In contrast to reported a-Si:H where there is a suppressed dynamic phonon disorder, a considerable increase in the E_g as well as a reduced E_U at low temperature [238], there is no obvious thermal contribution in the PL spectra of the SiNSs, as shown in Figure 7.2c for SiNS-PS@PS (see Figure C.5 for SiNS-$C_{12}H_{25}$(solid) and SiNS PAA@PAA). Therefore, the static PL spectra that remains persistent at low temperature is a result of a locked-in structural disorder. The as-synthesized SiNS-H, even before the surface modifications, already shows an inherent structural disorder accounting for an E_U of ∼300 meV (Figure C.3a).

Although there is no change in the shape of the PL spectra at low temperature due to the locked-in structural disorder, a dramatic increase of PL efficiency is observed, as displayed in Figure 7.2d. At 80 K, the normalized integrated PL ($I(T)/I(295K)$) reaches up to 14 times the room temperature value for the SiNS-$C_{12}H_{25}$(solid), as an example. The improvement in the PL intensity can be explained satisfactorily in terms of quenched non-radiative recombination. Non-radiative recombination is mediated by deep localized states in the middle of the band gap associated with impurities and lattice defects [24] such as dangling bonds and vacancies [240]. At low temperature, the photo-excited carriers in the band tails cannot 'escape non-radiatively' due to lower thermal energy [23]. Eventually, the localized *e-h* pair 'recombine radiatively', resulting in a more efficient luminescence. The competition between the radiative and non-radiative processes yields to the expression of the characteristic temperature dependent PL intensity in disordered semiconductor [23, 61] given as

$$\frac{I_0}{I(T)} - 1 = exp\left(\frac{T}{T_0}\right). \tag{7.1}$$

$I(T)$ is the integrated PL intensity over the whole PL spectrum at temperature T and I_0 was taken at $T = 80$ K. The expression provides the characteristic temperature T_0, which is related to the

valence band tail width E_{v0}, given as $E_{v0} = k_B T_0 ln(\nu_0 \tau_r)$, where $\nu_0 \approx 10^{13}$ s^{-1} is the phonon frequency [241] and τ_r is the radiative recombination lifetime (see Section 2.3.2.1) [23]. The value of the E_{v0} is considered here because it is usually wider than the conduction band tail. Also, E_{v0} directly influences the rate of recombination. The electrons cannot radiatively recombine unless free holes have migrated through the sample and in the same manner, thermally liberated electrons from the shallow localized states cannot non-radiatively recombine unless the holes have occupied the deep-level states [23, 65]. Because the value of E_{v0} gives the width of the exponential tail states that extends below the mobility edge, then we can directly relate it to the Urbach energy, $E_{v0} \approx E_U$.

As shown in Figure 7.2d, the increase of the PL intensity at low temperature follows Equation 7.1 and values of T_0 can be extracted at $T > 150$ K. At lower temperatures, the log plot of $(I_0/I(T) - 1)$ starts to deviate from the linear dependence. Such behavior has also been reported in the temperature dependence of the PL intensity of a-Si:H alloys where Equation 7.1 is obeyed at $T > 150K$ [62, 65]. In Figure 7.2d, the value of I_0 is $I(80K)$, which is experimentally accessible. In Figure C.6, it is shown that by that by arbitrarily deciding the I_0 value, which is much larger than $I(80K)$, yields to a linear dependence over all the temperature regime and that the values of T_0 are only slightly affected. Regardless, the I_0 value is only an experimental parameter, whereas the extracted value of T_0 is a characteristic material constant [23]. Based on the extracted T_0 values and the measured E_U (Figure 7.2 and Figure C.3), the expected total lifetime τ, can be estimated given that the PL quantum yield η_R is known (Equation 2.3). Thus, for η_R of 0.01-0.02, taken at room temperature (see Table C.2), the expected τ is $\sim 10^{-4}$ to 10^{-7} s. Note that these are over-estimated values, because the straightforward approach of estimating τ relies on the assumption that carriers have equal non-radiative and radiative recombination rates which is not the case given that $\eta \ll 1$. Also, η_R increases accordingly at low temperatures. Thus, these estimated lifetimes could be slower than the measured values (which will be presented later). Nevertheless, the temperature dependence of the PL intensity further demonstrates the disordered nature of the SiNSs characterized by the Urbach tail.

7.4.2 PL Dynamics

Besides the PL spectra, the TRPL elucidates the carrier dynamics and charge transport during the recombination processes. To the best of our knowledge, among the reported 2D Si nanosheets, only Kim *et al.* have demonstrated TRPL results measured from a monolayered Si grown by CVD. They showed nanosecond lifetime from an exponential decay [242]. In our case, the TRPL of all freestanding functionalized SiNSs also show nanosecond lifetime decay rate (as presented in Figure 7.2a), however the slow power law decay that lasts up to $t \sim 90$ ns expresses a long diffusion and energy relaxation within the bands. No microsecond lifetime component was detected. We have compared the absorbance against the PL spectra in Figure C.7 to determine whether the transition could be direct or indirect. Due to the broad PL spectra and long exponential tails, unfortunately the type of transition is not easily distinguishable.

The TRPL data, measured at the PL peak wavelength of $\lambda = 510 \pm 5$ nm ($E = 2.43 \pm 0.02$ eV), all have a universal fit to an empirical inverse power law function:

$$I(t) = \frac{I(0)}{(bt+1)^c}, \tag{7.2}$$

which represents band-to-band or bimolecular recombination dynamics (see Section 2.2.2) [69]. Here, $I(0)$ is the PL intensity at time $t = 0$, b is a parameter related to the bimolecular coefficient and carrier density, and c is the power law exponent. The inverse power law shown in Equation 7.2 is fitted to all TRPL data with a y-offset to include the baseline as the average of the dark counts. To confirm the non-exponential nature of the TRPL, the data were also fitted to stretched exponential decay and bi-exponential decay shown in Equations 2.8 and 2.7 (Section 2.2.1), respectively. Both bi-exponential and stretched exponential decays have been demonstrated in other Si nanostructures.

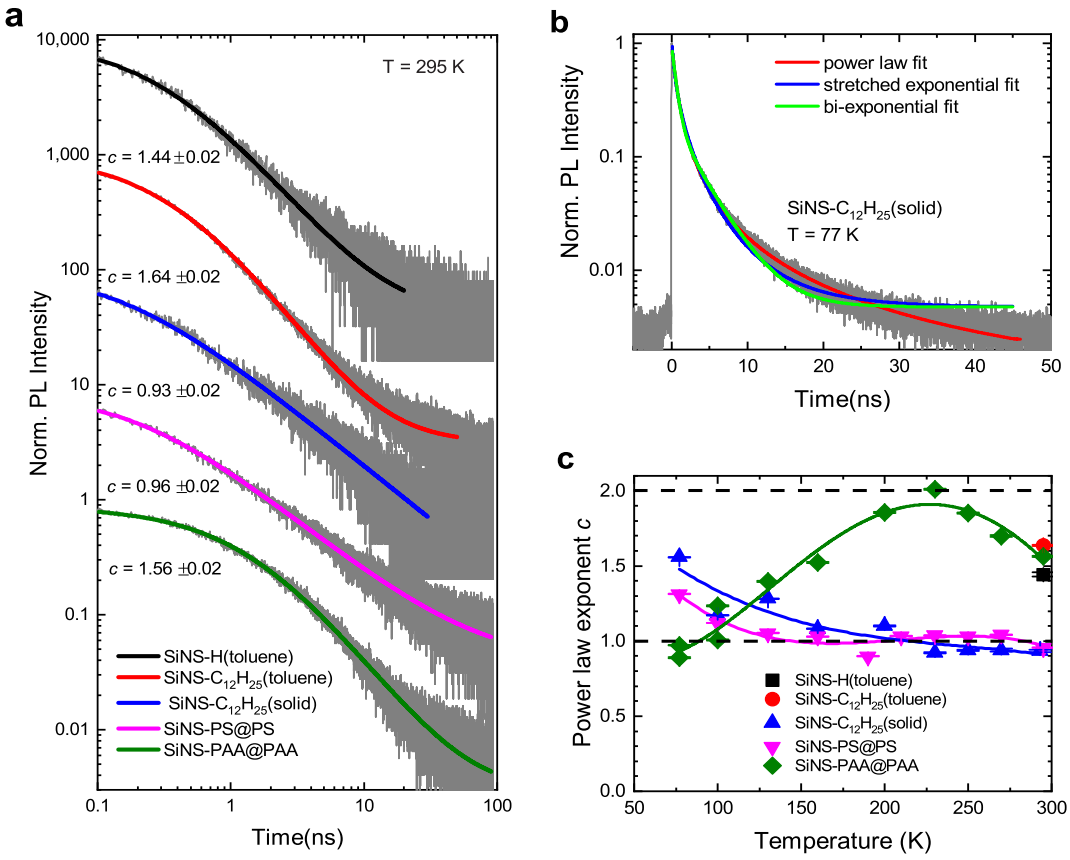

Figure 7.3: ***a)*** *Log-log plot of the TRPL of all SiNS samples measured at room temperature and at the peak of the PL spectra, $\lambda = 510 \pm 5$ nm ($E = 2.43 \pm 0.02$ eV). The intensities are offset on the order of 10. The solid lines represent the fits to Equation 7.2.* ***b)*** *Semi-log plot showing an example of three fits; power law, stretched exponential, and bi-exponential decay for the TRPL of SiNS-$C_{12}H_{25}$(solid) at $T = 77$ K.* ***c)*** *The inverse power law exponent c taken from the TRPL fits. Low temperature data were taken from the fits of the TRPL of solid samples only. The horizontal dashed line serves as guide to eye for $c = 1$. Error bars are within the data points.*

Bi-exponential PL decay was observed for surface passivated colloidal Si nanocrystals, which describes charge transfer from the Si core to the environment [243]. In thin film of Si nanocrystals, a stretched exponential PL decay has been related to distribution of lifetimes resulting from variations in nanocrystal sizes [245], disorder induced by hydrogen [244], and disorder arising from the surface states of oxidized nanocrystallites [246]. Whereas in porous Si, stretched exponential decay represents the interplay between excitonic recombination within the quantum dots and carrier

diffusion among their disordered interconnections [39]. Furthermore, in few reported semiconductors and nanomaterials, the PL decay is a combination of both exponential and power law, which requires multiple fit parameters and describes various mechanisms in the PL dynamics involving *e-h*, exciton-like and polaron-pair recombination with carrier trapping [247, 248, 249]. In the presented case of functionalized SiNSs, the TRPL clearly obeys a power law decay as demonstrated in Figure 7.3b for the TRPL of SiNS-$C_{12}H_{25}$(solid) at 77 K (refer to Figures C.8, C.9, and C.10 for more comparisons).

The value of the inverse power law exponent in Equation 7.2 plays a significant role in understanding the PL kinetics and carrier transport. The power law exponent is $c = \alpha + 1$ in which α reaches unity for a band-to-band or non-dispersive bimolecular recombination process [23]. In the case where $\alpha < 1$, such that the power law exponent becomes $1 < c < 2$, Equation 7.2 is then used to describe a diffusion-limited bimolecular recombination, which has been shown in transient absorption of polymer films [68, 250] and PL of disordered semiconductors [69, 251, 252]. At longer times ($t >> 1$), Equation 7.2 becomes a simplified inverse power law: $I(t) \propto t^{-c}$, which has a similar form in the transient photocurrent of a:Si-H and other disordered systems obtained from time-of-flight (TOF) experiments [66, 76]. Here, the inverse power law decay of the transient photocurrent is a result of the dispersive transport of carriers either by tunneling or 'trapping and release' in an exponential distribution of shallow trapping states (we have referred to this as localized states in the Urbach tail). Within the framework of the time-dependent PL, at longer times the simplified inverse power law has been observed to be a universal feature in radiative recombination of electrons and holes in the band tails states [72] and recombination dynamics involving charge release from trapping centers [74], with power law exponents ranging at $1 < c < 2$. The authors [74] mentioned some reports ascribing $c = 2$ for diffusive case, $c = 1.5$ for a combination of diffusion and tunneling, and $c = 1$ for tunneling between localized states, but a unified interpretation remains unclear. It is proposed that the power law time dependence is a result of many-body interactions between trapping levels and the c value depends on the degree of correlation between the centres (with $c = 1$ for weakly correlated centers) [74], but a specific mechanism of carrier transport was not discussed. It was then argued that PL decays that typically have $1.5 > c > 0.95$ [73] involves tunneling from electron traps to a random distribution of recombination centers, where c approaches a limit of 0.95 for the smallest number of recombination centers. On the other hand, the power law exponent of

$1.5 > c > 1$ [67, 72] is explained in the context of multiple trapping mechanism in the band tail states [66]. It is suggested that the PL power law decay should have $c = 1.5$ under normal carrier diffusion and $c = 1$ for dispersive diffusion [67, 72]. Although the physical meaning of the value of c is not yet well established and that it may vary depending on the mechanism of carrier transport, it can be summarized from these reports that PL decays with power law exponents of $c < 2$ indicates electron-hole recombination with diffusion of carriers that is limited by traps (as with the term 'diffusion-limited bimolecular recombination').

The universal fit of the TRPL to inverse power law decay re-affirms that the PL dynamics is governed by $e - h$ recombination but the power law exponents of $c < 2$ (Figure 7.3c) indicates that the PL originates from the recombination of electrons and holes from the band tail states. Thus, the PL dynamics is characterized by a diffusion-limited bimolecular recombination and reflects the disordered nature of the SiNS. The amount of this disorder can be related to the value of the power law exponent c. The suspended SiNSs in toluene, SiNS-$C_{12}H_{25}$(toluene) and SiNS-H(toluene), have power law exponents closer to 2 at room temperature with $c = 1.64$ and 1.44, respectively. Among the solid samples, SiNS-PAA@PAA has c = 1.56 at 295 K while both SiNS-$C_{12}H_{25}$(solid) and SiNS-PS@PS have the least value of power law exponent at $c \approx 1$. Based on the c values, such as in the case of SiNS-$C_{12}H_{25}$, there is less structural deformation among the SiNSs when freely dispersed in toluene than stacked on solid substrates that facilitates the interaction between the functional groups. Depending on the nature of the functional groups on the SiNSs, they can interact with each other, being adjacently located on the surface [253]. The molecules with a specific functionality could arrange and order themselves after their attachment, *e.g.* $\pi - \pi$ interactions in case of the adjacent styrene moieties, or hydrogen bond formations, which might be present between the acrylic acid groups. This could be a potential factor for additional deformation of the surface and thus lead to different angles in the buckling of the SiNSs as depicted in Figures 7.4a and 7.4b. Hence, in SiNSs being a 2D system, it is highly plausible that the locked-in structural disorder arises from the variations in the buckling. This disorder in the SiNSs is also confirmed by the solid-state nuclear magnetic resonance (NMR) spectroscopy, as shown in Figure 7.4c. The buckling-induced distortion and the NMR results will be discussed in detail later.

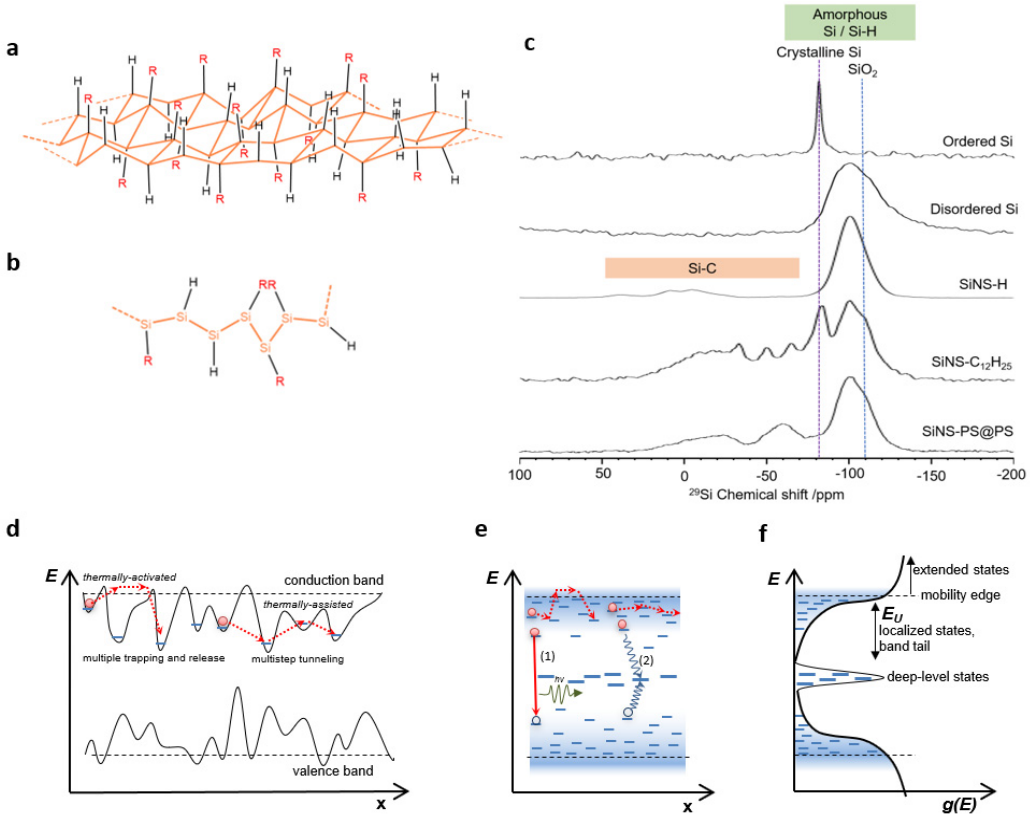

Figure 7.4: ***a)*** *Schematic diagram depicting the distorted buckling of the SiNSs functionalized with* $R = C_{12}H_{25}$*, PS, and PAA via radical induced hydrosilylation reaction, and* ***b)*** *corresponding side view.* ***c)*** *Silicon-29 NMR spectra of representative ordered silicon (measured from 44* μ*m silicon particles), disordered silicon, SiNS-H, and* $C_{12}H_{25}$ *(solid), and SiNS-PS@PS.*[2] ***d)*** *The buckling-induced distortion in the monolayer sheets creates disorder in the energy landscape, therefore the electron experiences dispersive transport either through multiple trapping and release or multistep tunneling mechanism.* ***e)*** *Similar illustration is provided along the spatial coordinate. In addition, the (1) diffusion-limited radiative bimolecular recombination is illustrated with e-h pair (red and white circles, respectively) between localized states while the (2) non-radiative recombination is mediated by deep-level states.* ***f)*** *These schematic diagrams correspond to a density of states* $g(E)$ *that has a distribution of localized band tail states spreading exponentially below the mobility edge of the conduction band (or above the valence band). The* $g(E)$ *of deep-level states is in the middle of the mobility gap.*

[2]NMR Spectroscopy performed by M. Ha.

The mechanism of diffusion-limited bimolecular recombination can be better understood when investigating the PL dynamics at various temperatures. In Figure 7.3c, the power law exponents of SiNS-PAA@PAA have shown to have a different temperature dependent behaviour compared to the SiNS-$C_{12}H_{25}$(solid) and SiNS-PS@PS. For SiNS-PAA@PAA, the power law exponent almost linearly approaches the value $c = 2$ at $T > 230$ K. At $T < 230$ K, c decreases until it reaches $c \approx 1$ at $T = 80$ K. Such behaviour resembles a temperature dependent charge transport attributed to carrier 'multiple trapping and release' [75]. In this mechanism, electrons hop between nearby localized sites acting as charge traps, gets thermally activated above the mobility edge before falling again into the distant trap [23], as illustrated in the energy landscape in Figure 7.4d and recombination dynamics in Figure 7.4e. The thermal activation allows the electrons to migrate above the mobility edge, thereby resulting in c value closer to 2. However, in this mechanism, it is assumed that the thermal excitation (which allows the electron to escape from the holes) always yields to a lower probability of radiative bimolecular recombination and hence, the thermal quenching of the PL intensity. At decreasing temperature, the electrons tend to diffuse into the deep localized sites, allowing a higher probability to recombine with the trapped holes in the valence band tail resulting in increased PL efficiency. The mechanism may differ for SiNS-$C_{12}H_{25}$(solid) and SiNS-PS@PS, where the power law exponents of $c \approx 1$ are observed to be almost constant until 150 K (Figure 7.3c). This behavior agrees to a hopping transport mechanism *via* thermally-assisted multistep tunneling [75] where the value of c is not significantly affected by temperature because tunneling occurs between neighboring sites with almost equivalent energies [254]. At much lower temperature ($T < 150$ K), the c values slightly increase from $c \approx 1$ up to $c \approx 1.5$ which could imply improvement in the bimolecular recombination. It is most probable that the tunneling to neighboring localized states are no longer thermally-assisted and thus, in this temperature regime, the efficient radiative recombination could be due to direct tunneling of electrons in the conduction band tail to the trapped hole in the valence band tail (Figure 7.4f). This results to the dramatic increase of their PL intensities at $T < 150$ K, as shown in Figure 7.2d. In line with this, SiNS-$C_{12}H_{25}$(solid) have shown to have relatively higher c and higher PL intensity compared to the SiNS-PS@PS.

We have presented a case where the buckling-induced distortion is responsible to the disorder in the 2D SiNSs. In a-Si:H, it was demonstrated that deviations in the bond angles [239] significantly affects the EU. Furthermore, the buckling-induced distortion has been observed in epitaxially grown

SiNSs [256]. In this report, the constraint imposed by the silver substrate induced a differently buckled $sp^2 - sp^3$ arrangements, which provoked an intrinsic disorder in the SiNSs. The local vertical distortions in the Si lattice were associated to the Raman-inactive vibrational mode A_{1g}. In our case, this A-mode peak also appear in the Raman spectrum of the SiNS-$C_{12}H_{25}$(solid) (Figure C.12). However, because our SiNSs are freestanding, the hydrogenation and functionalization of the Si sheets result in ideally sp^3-hybridized structure, and thus the A-mode peak in the Raman may not conclusively point to the disorder in the SiNSs. In terms of X-ray diffraction (XRD), our previous report [206] showed XRD spectra of SiNS-H and SiNS-$C_{12}H_{25}$(solid) that has relatively broad peaks, which are commonly observed in amorphous materials [257]. The XRD, however, was measured on the powdered form of the samples and thus, the broad peaks could only be due to the finite sizes and stacking of the nanosheets, and not necessarily on the amorphous character. In view of these complimentary measurements, we have decided to perform solid-state nuclear magnetic resonance (NMR) spectroscopy, which is a non-perturbing technique that provides structural information about the local atomic chemical environment over several bonds. Thus, it is a sensitive local probe of short- and medium-range order in the structure of nanomaterials. The ^{29}Si cross-polarization magic-angle spinning (CPMAS) NMR spectra of SiNS-H and SiNS-$C_{12}H_{25}$(solid) has the presence of a broad resonance ranging from -80 to -120 ppm and lacks the sharp isotropic chemical shift (δ_{iso} = -81 ppm) corresponding to crystalline (ordered) silicon (Figure 7.4c). This broadness mirrors those features seen in disordered silicon nanoparticles [258], as well as NMR studies of other metal nanoparticles ([259, 260, 261, 262, 263, 264, 265, 266, 267]. Due to the deviations in bond angles from the buckling-induced distortion in the SiNSs, a distribution of chemical shifts culminates as the broad featureless resonance. In regard to the SiNS-$C_{12}H_{25}$(solid) spectrum, features between +20 to -90 ppm associated with the functionalized surface are also present with residual SiO_2 oxidation present at -110 ppm [268, 269]. The disordered nature of the SiNSs observed via ^{29}Si NMR spectroscopy is consistent with the our observations, suggesting that the SiNSs are non-crystalline 2D sheets imposed by the the buckling-induced distortions.

7.5 Summary

In summary, we have investigated the PL of variously functionalized freestanding SiNSs at different temperatures. The SiNSs consistently emit green PL and the PL peak emission agrees to the calculated band gaps of hydrogenated 2D silicon. The origin of the PL is band-to-band recombination, however the the PL spectra are broad and exhibit long exponential tails, representing the band tail states arising from the locked-in structural disorder in the SiNSs. The effect of the disorder in the SiNSs is further demonstrated in the PL dynamics. The time-resolved PL has a universal fit to an inverse power law decay that represents a diffusion-limited bimolecular recombination. Although the subsequent functionalizations of the hydrogenated SiNSs do not change the nature of the PL, the functionalizations affects the dispersive charge transport near the mobility edge.

To the best of our knowledge, this work provides a more comprehensive picture of the PL dynamics among reported freestanding functionalized SiNSs. The information presented here is important for the optimization of the optical and transport properties of SiNSs, where less disorder is desirable. Though, the nature of the PL may be analogous to a disordered semiconductor, it paves the way for the 2D SiNSs into the established and emerging applications of amorphous Si in optoelectronics industry; such as thin film transistors, photo detectors and solar cells [225, 255]. The study may also provide essential understanding on the carrier dynamics in 2D systems.

CHAPTER 8

Photoluminescence and Photoconductivity of Bulk Germanium

8.1 Overview of the Ge band structure

Ge has an indirect band gap as shown in Figure 8.1. By taking the valence band maximum as $E = 0$, at room temperature (T = 300 K), the indirect and direct band gap energies are $E_{g-ind} = 0.664$ eV (Γ-$L_{[111]}$ minimum point of the Brilloin zone) and $E_{g-dir} = 0.805$ eV (Γ-Γ point), respectively [96, 273]. Because of the indirect gap nature of Ge, the study of carrier dynamics has not advanced at the same pace with Group III-V direct gap semiconductors such as GaAs [273]. Indirect transitions are much less probable than direct ones, as it requires a two-step process with the participation of phonons to fulfill conservation of quasi-momentum [44] (see Section 2.3.1.2).

Photoexcitation can occur from Γ to Γ valleys, as depicted in Figure 8.1b, as well as excitation from the continuum valence band to the $L_{[111]}$ valley if the excitation energies are much higher than the band gaps, $E_{ex} > 2$ eV. Thus, at high excitation levels, possible direct e-h recombination could occur, *e.g.* from Γ-Γ point, as well as indirect recombinations *via* phonon-assisted intervalley scattering (*e.g.* scattering from $L_{[111]}$ valley to Γ valley). Note that there are four similar valleys in the entire [111] direction, and thus injected electrons may also scatter from these side bands. For a nonpolar semiconductor such as Ge, electron scattering in k-space is mainly determined by the first-order optical phonon deformation scattering [43, 273, 274]. Because the first-order optical phonons are only restricted in a narrow region of the Brillouin zone, intervalley scattering from the L valley is probable but it is forbidden from the $X_{[100]}$ valleys due to symmetry restrictions [273].

This might explain as to why indirect PL has not been observed from the $X_{[100]}$ valley in Ge. The PL measurements will be presented in the next section.

Because of the degeneracy of the upper two valence bands (heavy-hole and light-hole) at elevated temperatures, recombination of electrons to hole can be considered only at the heavy-hole band [273]. Moreover, the density of states of the lowest valence band (split-off) is small compared to the upper two valence bands, and the energy is only 28 meV lower (comparable to thermal energy at room temperature), thus its contribution to the overall recombination dynamics could be negligible.

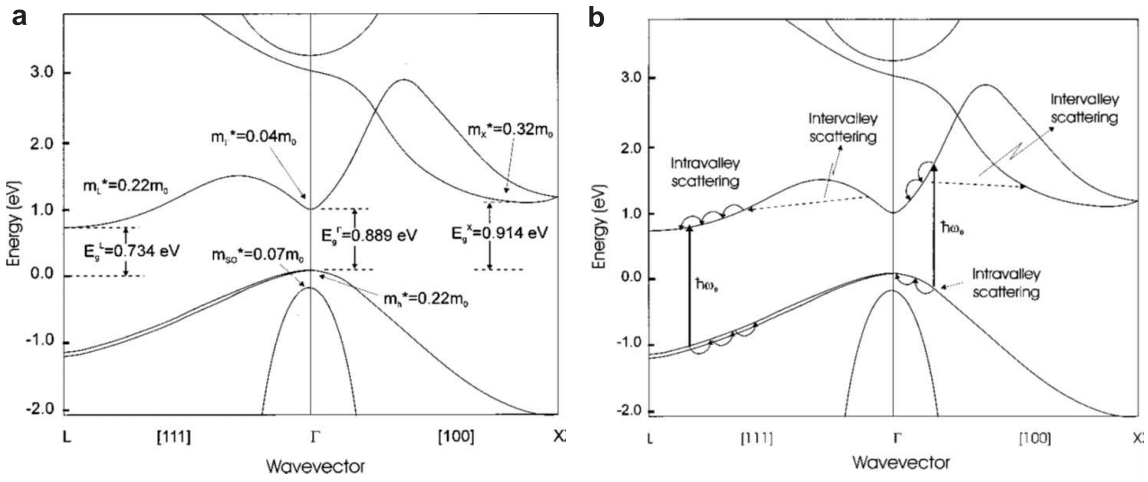

Figure 8.1: ***a)*** *Energy band diagram of Germanium at T = 77 K. E = 0 is assummed at the maximum of the heavy hole valence band. The band gap energies of the direct and nearest indirect valleys are shown, as well as the density of state masses in both conduction and valence bands.* ***b)*** *The corresponding allowed transitions (vertical solid arrows), possible intervalley scattering (dashed arrows), and intraband relaxation (curved solid arrows) are illustrated. Both figures are taken from Ref. [273].*

8.2 Photoluminescence (PL)

NIR PL spectroscopy is an effective tool to demonstrate the *e-h* recombination across the direct and indirect band gaps of Ge. Steady-state indirect PL of bulk crystalline Ge has been shown first in earlier experiments subjected to liquid Helium temperature ($T \leq 5$ K) [276, 277, 278, 279], where the PL intensity is observed to be more pronounced. With the advent of more sensitive

NIR detectors in the past decade and by using continuous wave (cw) excitation with high photon energies, the indirect PL spectrum of bulk Ge can be readily obtained at room temperature [280]. On the other hand, enhanced steady-state direct PL can be easily achieved by means of heavy doping [281], tensile strain [282, 283], and/or increased temperature [284]. At high excitation fluences, both direct and indirect steady-state PL can be observed in both bulk and nanowire Ge [285, 286]. For the past few years, more studies that involve PL of Ge have been rapidly being reported in terms of device fabrication. Through quantum confinement, different preparations such as mixing with other elements (Ge alloys), application of strain using different substrates, and nanoscale technology [287, 288, 289, 290, 291, 292, 293], radiative processes can be enhanced and/or PL spectra can be shifted from the NIR to the visible wavelengths.

In this report, we use ultrafast laser pulses for the photoexcitation of bulk Ge instead of a cw laser. At smaller laser excitation energy of 1.55 eV, both direct and indirect PL are obtained from undoped and doped bulk Ge samples at room temperature. The samples are crytalline Ge wafers oriented at the 100 direction with 0.5 mm thicknesses (MTI Corp.). The NIR PL spectroscopy was employed (see Section 5.2) to obtain the PL spectra. At different excitation fluences, an interplay between the direct and indirect PL is demonstrated. To the best of our knowledge, investigating the interplay between the direct and indirect PL in Ge at 1.55 eV pulse laser excitation has not been reported so far.

8.2.1 Results and Discussion

8.2.2 Fluence dependence of the PL of Ge

An excitation of 800 nm (1.55 eV) is expected to fill both indirect (L) and direct (Γ) valleys of the conduction band with population of electrons. In order to obtain reasonable PL spectra in the Ge samples, higher optical fluences with carrier densities of up to 400×10^{18} cm^{-3} were used. Such high laser pumping power could result in shifting the quasi-Fermi energy levels near the conduction band [37, 294] (Figure D.1).

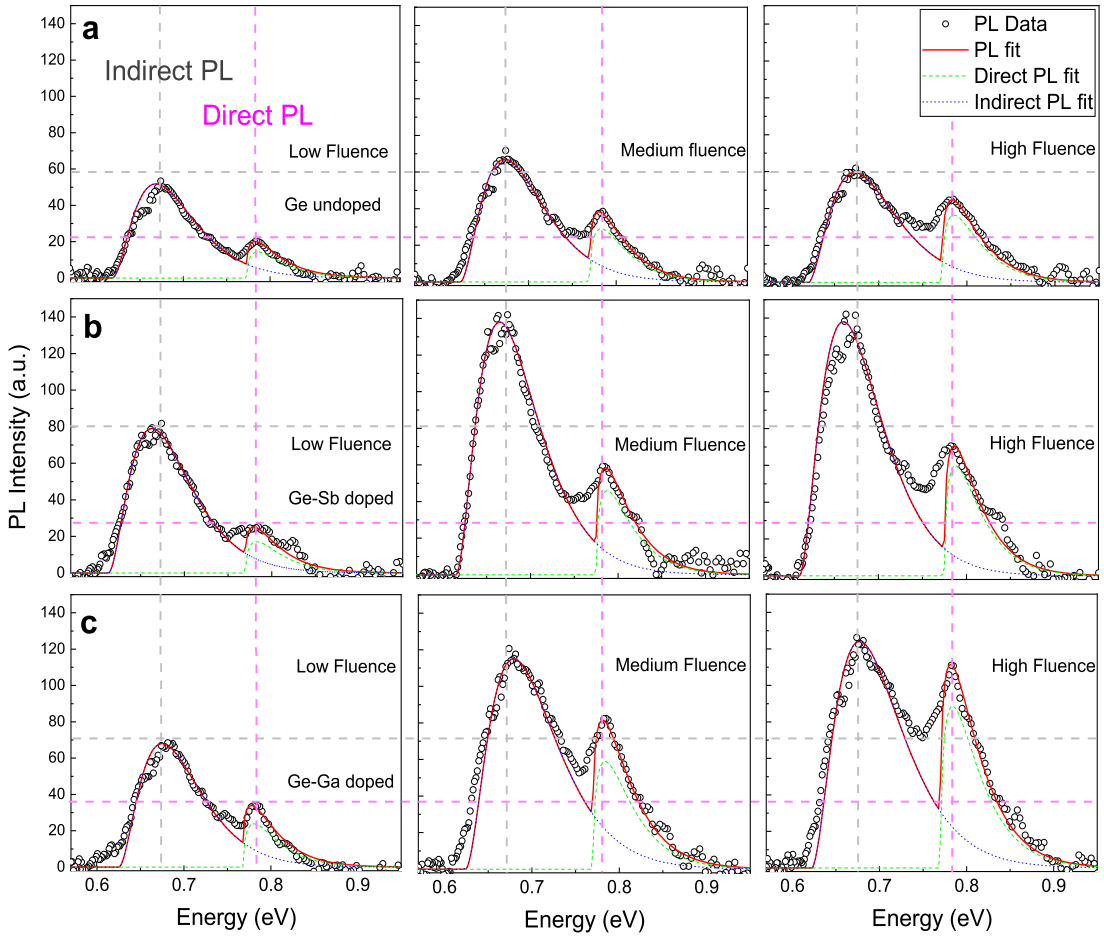

Figure 8.2: Examples of PL spectra of ***a)*** *undoped Ge,* ***b)*** *Ge-Sb doped (n-doped), and c) Ge-Ga doped (p-doped) at low (28 mW), medium (104 mW), and high (199 mW) pumping power. The green dashed and blue dotted lines represent the best fits to the Equations 2.17 and 2.22 for the direct and indirect transitions, respectively, while the red solid line is the overall PL fit. Horizontal and vertical dashed lines were included as guides to the eye for the peaks of the direct and indirect PL, respectively, relative to the low fluence PL spectra.*

The population of both bands results to a PL spectrum that has two distinct peaks at the NIR region, shown in Figures 8.2. The PL data were fitted to Equations 2.17 and 2.22 for the PL intensities from a direct and an indirect gap semiconductor. It can be observed that the direct PL, which is the most probable recombination, has less PL intensity as compared to the indirect PL. There are possible reasons to this: 1) There are more population of carriers in the L valley because

of higher density of states. The effective mass m^*_{L} is ∼5 times higher than m^*_{Γ} and considering that there are four valleys in the L region. At 1.55 eV excitation, the ratio of the density of states in the L valley to the Γ valley is estimated to be 1:0.02 [295]. 2) Moreover, higher energetically carriers can scatter from the $\mathrm{X}_{[100]}$ space of the band to the L valley. Note that the X valley is even more populated where the ratio of the density of states of X to the L valley is 2.7:1 [295] and that the mobility in the X valley is nearly five times higher than the L valley [296]. 3) The indirect recombination process could have been mediated by a faster intervalley scattering from Γ to L valley at ∼230 fs, which competes to the carrier thermalization process of $<$ 1 ps in the Γ valley [5, 297].

Contrary to the use of cw lasers, with high photon energies, practiced by most studies (514 nm [280], 515 nm [282], 532 nm [285, 286, 288, 298], and 671 nm [284]), here, a reasonable PL spectra with good S/N ratio can already be obtained using an ultrafast 800 nm excitation. With 50 fs pulses every 1 ms, the pulsed excitation might have resulted to better radiative efficiency as compared to steady-state measurements because it prevents possible build up of quasi-equilibrium distribution of trapped photogenerated carriers [57] and may allow enough time for the free carriers to go through the scattering and relaxation (femtosecond to picosecond scale) and recombination (picosecond to mirosecond scale) processes. Our observation is similar to Ref. [299] where PL spectra with both direct and indirect peaks were observed at room temperature using 200 μs laser pulses at 1.06 μm wavelength.

The doping by Sb (n-doping) and Ga (p-doping) increased the carrier concentration of undoped Ge in 4 orders of magnitude ($n_{Ge-undoped}$ = 2.33×10^{13} cm^{-3}, n_{Ge-Sb} = 1-40×10^{17} cm^{-3}, and n_{Ge-Ga} = 1.2-4×10^{17} cm^{-3} based on the manufacturer's resistivity values, MTI Corp.). The doping results to enhanced PL intensity, as exemplified in Figure 8.2b-c. The indirect PL is mostly enhanced by n-doping, which implies higher electron population filling in the L valley [282], as a result of higher density of states. In the case of p-doping, the presence of more holes in the valence band resulted to more enhancement in the direct PL intensity as compared to the indirect PL. This compliments the fact that the direct transition is faster, allowing more electrons from the direct valley to easily find holes to recombine with in the valence band. The PL spectra of both doped and undoped bulk Ge were fitted to the PL spectral shape of a direct and an indirect gap semiconductor expressed in Equations 2.17 and 2.22, respectively. The extracted best fit parameters are shown in Figure 8.3.

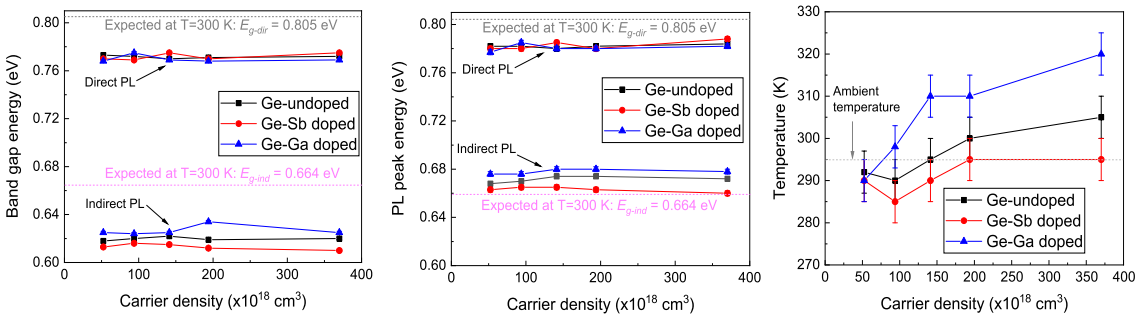

Figure 8.3: Parameter values taken from the best fits of the PL spectra of Ge samples to Equations 2.17 and 2.22 (Chapter 2): ***a)*** *Band gap energies,* ***b)*** *PL peak energies, and* ***c)*** *lattice temperature of the samples plotted against increasing carrier density. Guides to the eye are included for the expected band gap energies taken from Ref. [96].*

Based on the best fits, the undoped Ge has a direct and indirect band gap energies of E_{g-dir} ~0.77 eV and E_{g-ind} ~0.62 eV, respectively, which are 0.03 - 0.04 eV lower than the reported band gap values at room temperature [96], as displayed in Figure 8.3a-b. Because the band tails (Urbach tail) [49] at the low energy range of the direct and indirect PL spectra were not considered in the fits, the fitting is slightly red-shifted which gave lower values of E_g [35, 284, 300]. At increasing excitation density, whereby the quasi-Fermi level is increased, an expected slight Burstein-Moss shift [301] of the PL peaks to higher energy (Figure 8.3b) is observed, which is more noticeable at the indirect PL. Due to state-filling of the conduction band, the absorption edge is pushed to higher energies, resulting in shifted PL peaks. However, at $n > 150 \times 10^{18}$ cm^{-3}, the PL peak tends to shift back, which could imply narrowing of the band gap. Band gap narrowing are typically observed at very high carrier concentrations ($\sim 10^{19}$ cm^{-3}), due to interaction within the bands (arising from the anisotropy of Ge band structure) or increased carrier-impurity interaction (as seen in highly doped semiconductors) [302, 303]. Thus, in this case, there appears to be a competition of the Burstein-Moss effect and the band gap narrowing as observed in other semiconductors [304, 305].

The band gap and PL peak energies of both doped samples are slightly shifted by 3 to 14 meV relative to the undoped Ge, which is more noticeable in the indirect PL (Figure 8.3a-b). If we assume that the small energy differences of the doped Ge samples, relative to the undoped Ge, are due to the ionization binding energies of shallow acceptor and donor levels at the band edge, these

values are close to the reported ones for Ge-Sb (E_D=10.29 meV) and Ge-Ga (E_A=11.32 meV) [96]. In terms of the width of the PL spectra, the FWHM remains at $\sim 1.8k_BT$ (direct PL) and $\sim 3.4k_BT$ (indirect PL) (see Figure 2.4). At higher excitation fluences, the lattice temperature is shown to increase by 10 - 20 K (Figure 8.3c). This is not relatively significant and thus, any competition between the direct and indirect PL is not solely influenced by the elevated temperature within the crystal as exemplified in Ref. [284].

8.2.2.1 Interplay between the direct and indirect PL of Ge

We now investigate the interplay arising from the direct and indirect PL. From Figure 8.4, it is observed that the PL intensity increases with the excitation fluence. However, when comparing the direct and indirect PL peaks in general, there is more noticeable increase in the direct PL at higher fluences, while the indirect PL peaks appears to saturate. The continual enhancement in the direct PL intensity is due to the higher recombination rate across the direct gap (compared to the phonon-assisted recombination across the indirect gap) even though the population of electrons is higher in the indirect band [299]. By taking the integrated PL as a function of fluence, the relative changes between the direct and indirect PL show that there is more enhancement in the direct PL, as shown in Figure 8.4a. When the overall integrated PL (across the whole PL spectrum) is considered, the PL reaches a saturation point at much higher carrier density ($>150\times10^{18}\text{cm}^{-3}$), as shown in Figure 8.4b. Because the direct PL is continually increasing, the saturation region of the overall integrated PL means that there is a balancing effect between the direct and indirect integrated PL.

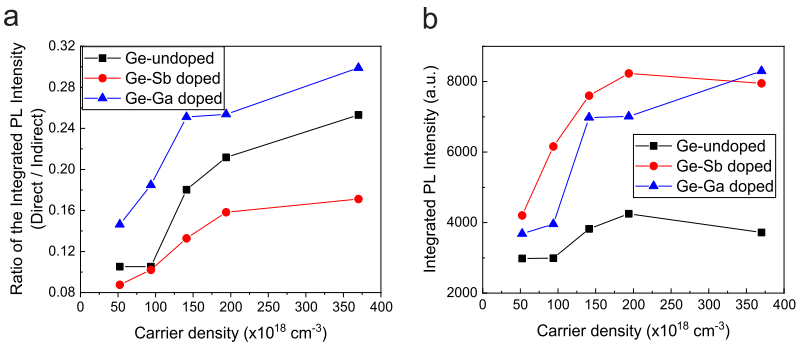

Figure 8.4: ***a)*** *The ratio between the integrated direct and indirect PL increases against the excitation fluence, however* ***b)*** *the overall integrated PL (across the whole PL spectrum) shows saturation at higher laser pumping power.*

The saturation at higher carrier densities points to a nonlinear behaviour, indicative of non-radiative processes which hamper further light emission. Instead of a two-body process, which is the *e-h* pair recombination, a three-body process (referred as Auger recombination) could be involved due to very high excitation fluence. To check the carrier concentration at the regime of Auger process, we consider the calculated bimolecular coefficient B of 2.5$\times$ 10^{-13} cm^3/s [306] and the Auger coefficient C ranging from $\sim$$10^{-31}$ cm^6/s [307] to 4$\times$ 10^{-32} cm^6/s [308]. At our excitation levels with carrier densities of 15 to 40$\times$ 10^{19} cm^{-3}, the radiative bimolecular recombination rate is calculated as Bn^2 $\sim$$10^{27}$cm^{-3}/s, which is much less than the Auger recombination rate of Cn^3 $\sim$$10^{29}$ cm^{-3}/s. This means that in order to avoid Auger processes to occur, the carrier density should be less than $\sim$4$\times$ 10^{19} cm^{-3}. Thus, our minimum excitation fluence is within the onset of having non-radiative Auger recombination.

On the other hand, the saturation of the PL intensity occuring in the indirect band, could also be related to less efficient phonon-assisted intervalley scattering to the L valley. However, addition of carriers *via* intervalley scattering to the more populated L valley is less probable due to state-filling effects. Further investigation could be made in this case, such as modeling of state-filling effects in the direct and indirect bands of Ge.

Regardless, an interplay of the direct and indirect PL has been shown by simply increasing the photoexcited carriers. The ability to modulate the PL peaks may allow us to understand the carrier

dynamics involved. Moreover, it could possibly open up potential photonic applications because the direct PL wavelength of 1550 nm is the current standard telecommunication wavelength. In addition to varying the excitation fluence, other possible means of enhancing or quenching the PL peaks could be explored. This effect is further presented in Chapter 10.

8.3 Photoconductivity (PC)

While photoluminescence measurements allow us to study a subset of transitions that are radiative, investigating the photoconductivity allows us to monitor a subset of photocarriers which have an appreciable mobility [92]. Here, we employ time-resolved THz spectroscopy (TRTS) (see Section 4.3) in acquiring the transient PC in bulk Ge. The advantage of TRTS is that we can capture the PC dynamics as early as ∼300 fs after the photoexcitation. At very early time (in the picosecond scale), the transport of the photoexcited electrons at the conduction band is dominated by thermal relaxation and scattering [310]. At latter time ($\gg$ 1 ps), the photoexcited carriers undergo recombination processes. Thus, exploring the PC dynamics in different time regimes may reveal different mechanisms that govern the carrier transport in bulk crystalline Ge.

8.3.1 Picosecond scale transient photoconductivity

As shown in Figure 8.5a, the transient photoconductivity of Ge exhibits a long decay, in line with the long-range transport in crystalline semiconductor. At higher fluence, the decay tends to be relatively faster, indicating a decreasing effective carrier lifetime. The measured $|-\Delta T/T_0|$ was attempted to be fitted in a simple inverse power law of bimolecular recombination but was unsuccessful, which means that bulk recombination is not the only main contribution in the decay. Considering that the optical penetration depth is only 220 nm at an excitation of 1.55 eV, surface recombination or possibly recombination through more defect concentration start to dominate at higher carrier density and the diffusion of carriers into the bulk becomes more ineffective [309]. The faster photoconductive decay due to surface recombination is more noticeble in the $|-\Delta T/T_0|$ using 3.10 eV pump, as seen in Figure 8.5b, whereby the penetration depth is only limited to 15 nm. To account both surface and bulk recombinations, the fitting of $|-\Delta T/T_0|$ to a combination of exponential decay (monomolec-

ular recombination) and inverse power law (bimolecular recombination) was performed but was not deemed successful. Therefore, it is recommended that the diffusion and the optical absorption of the sample should be included in the spatial and temporal evolution of the photogenerated carriers (see Equation 2.4) [11, 34] and that the fitting should be performed at much longer times. Here, the behaviour of the $|-\Delta T/T_0|$ is relatively constant at long times ($>$ 200 ps), comparable with the indirect gap Si that also has longer recombination lifetimes [311] and unlike the direct gap GaAs, which has shown to have faster $|-\Delta T/T_0|$ decay [11, 311].

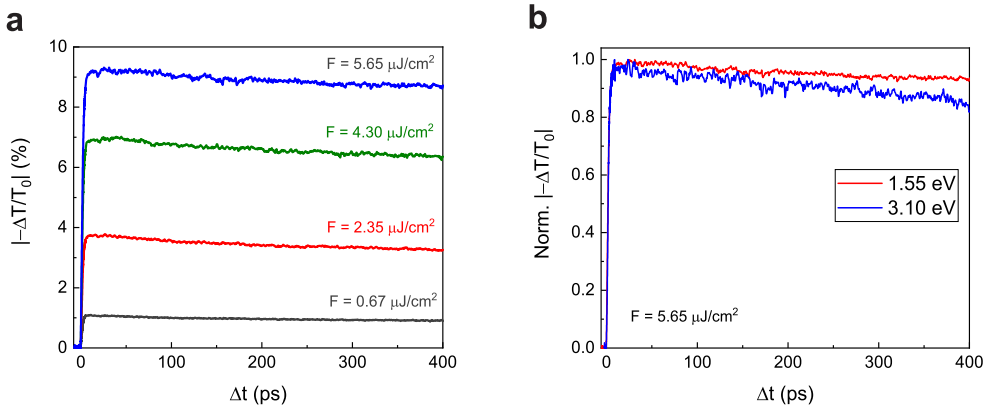

Figure 8.5: ***a)*** *Absolute differential THz transmission of photoexcited Ge at excitation energy of 1.55 eV measured at different fluences and* ***b)*** *a comparison of 1.55 eV and 3.10 eV excitation.*

8.3.2 Complex conductivity of photoexcited Ge

To better grasp the mechanisms of the carrier transport, we employ the 2-chop scan method of the TRTS (Section 5.3.3) in obtaining the conductivity in the frequency domain and in extracting relevant parameters that would describe the PC dynamics. Figure 8.6 shows the complex conductivity plots obtained from the values of E_{ref} and E_{pump}, measured at different pump fluences. The solid lines represent the fits to Equations 3.15 and 3.16 for the real and imaginary parts of the complex conductivity, respectively, according to the Drude model of free carriers. The good fits of the experimental results to the Drude model demontrates a proof-of-concept to the effectivity of TRTS in probing the complex conductivity at the THz regime of photoexcited bulk semiconductors.

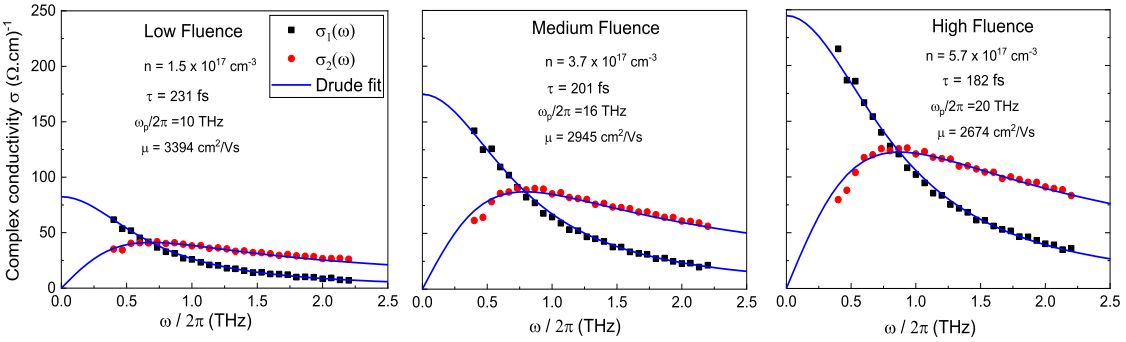

Figure 8.6: Complex conductivity (with $\sigma_1(\omega)$ and $\sigma_2(\omega)$ as the real and imaginary parts, respectively) of undoped n-type Ge acquired using 2-chop scan method of TRTS at $\Delta t = 100$ ps. The solid blue lines represent the Drude model fits. An electron effective mass of $0.12m_0$ (for conductivity measurements) and substrate refractive index of $N = 4.0$ were used in the best fits.

The extracted parameters from the fit at various pump fluences is shown in Figure 8.7a-d. The scattering time decreases at higher excitation density while the plasma frequency and dc conductivity increases, as expected (Figure 8.7a-c). Because the scattering time is within 180 to 250 fs, the crossover points, $\sigma_1(\omega) = \sigma_2(\omega)$ falls at $0.5 < \omega/2\pi < 1.0$, thus our THz bandwidth is ideal in demonstrating the Drude model of free carriers in Ge. At much lower fluence, with a carrier concentration of $0.65 \pm 0.1 \times 10^{17}\text{cm}^{-3}$, the scattering time is 248 ± 6 fs, which yields an electron mobility value of 3642 ± 88 $\text{cm}^2/\text{V}\cdot\text{s}$ (Figure 8.7d). This closely agrees with the expected μ_e of < 3900 $\text{cm}^2/\text{V}\cdot\text{s}$ at T = 300 K [96]. At higher carrier concentration, the mobility is reduced due to the increased overall scattering rate $(1/\tau)$ arising from a combination of defects, carrier-carrier scattering, phonons, and ionized impurities. Ionized impurity scattering can reduce the mobility down to 40% but it only occurs at extremely low temperature [312]. While at higher temperature, the other contributions (defects, carrier-carrier interaction, phonons) start to dominate especially at higher carrier densities, in the order of 10^{16} to 10^{17} cm^{-3}. Since our measurements lie within this range of carrier concentration, we plotted the overall scattering rate as a function of the carrier concentration as shown in Figure 8.8, to analyze the dominant scattering contribution. The behaviour agrees well to a carrier-carrier scattering contribution, which vary approximately linear to the carrier concentration, given by $\frac{1}{\tau} \sim n|ln(n)|$ [11, 312], with an offset due to phonon scattering. The offset value of $1/\tau_{ph}$ = 3.4 ± 0.2 THz is within the vicinity of expected phonon scattering rate in Ge at $T = 300$ K [313].

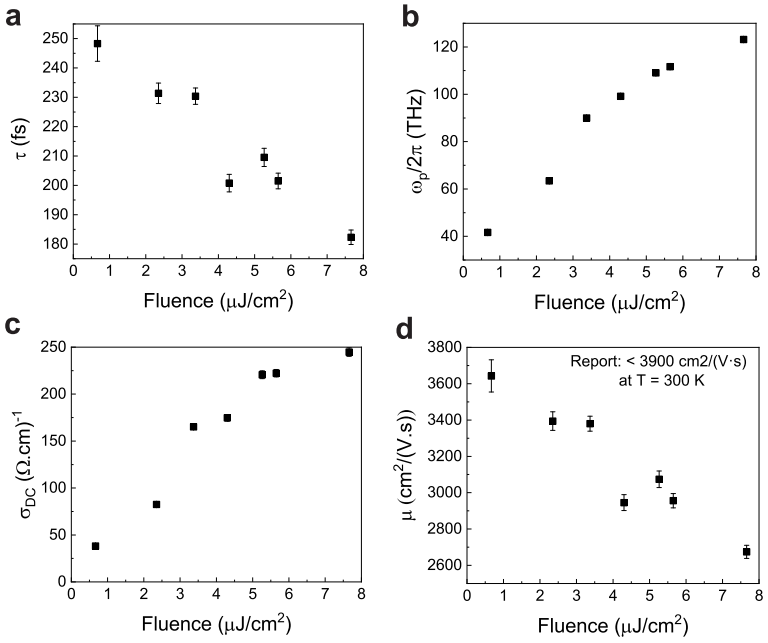

Figure 8.7: Parameters taken from the Drude model fits to the measured complex conductivity of Ge: ***a)*** *Scattering time* τ, ***b)*** *Plasma frequency* ω_p, ***c)*** *dc conductivity* σ_{dc}, *and* ***d)*** *Mobility* μ.

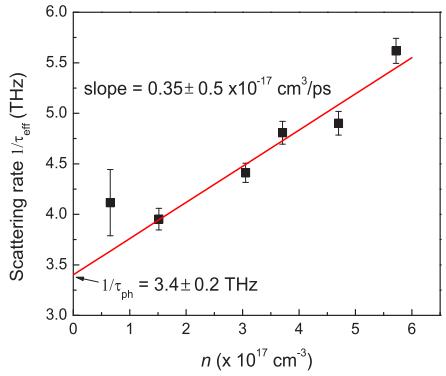

Figure 8.8: The effective scattering rate $(1/\tau_{eff})$ *increases linearly as a function of the carrier density* (n). *The y-intercept corresponds to the phonon scattering rate* $(1/\tau_{ph})$ *at* $T = 300$ *K.*

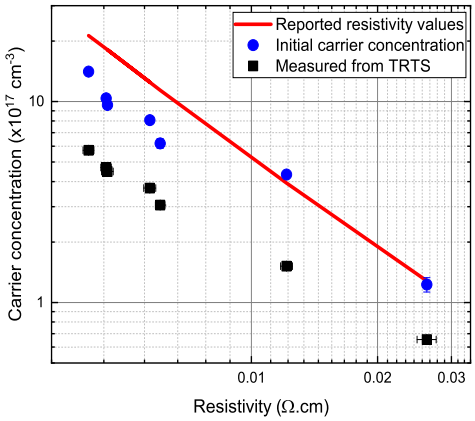

Figure 8.9: The resistivity values of Ge extracted from TRTS (black squares) compared to the reported resistivity (red line) of n-type Ge in Ref. [314]. The carrier concentration values from TRTS (black squares) were calculated using the relation, $n = \sigma_{dc}/(e\mu)$. Here, the σ_{dc} and μ values were taken from the Drude fits to the complex conductivities measured at $\Delta t = 100$ ps. For the initial carrier concentration (blue circles), the values were directly calulated from the optical excitation fluences. For the reported data (red line), the resistivity values were measured using Haynes and Shockley circuit [315] and Hall effect [314] methods at low and high ranges of carrier concentrations, respectively.

Furthermore, we plotted the the resistivity ($1/\sigma_{dc}$) as a function of carrier concentration (n) in Figure 8.9. The σ_{dc} values were extracted from the Drude fits to the complex conductivities at $\Delta t = 100$ ps. The initial carrier concentrations (blue circles), which were directly calculated from the optical fluences, corresponded to resistivity values that are closer (especially at lower n values) to the reported resistivity of an n-type Ge using contact methods (red line) [314, 315]. The measured carrier concentrations (black squares), which were derived using the relation, $n = \sigma_{dc}/(e\mu)$, are much lower. It shows here that the TRTS can provide the values of n, μ, and σ_{dc} at a specific time after the excitation of a laser pulse (Δt), which are not accessible in steady-state measurements. Thus, the TRTS is an effective tool when investigating the electrical properties based on the transient response of a photoexcited semiconductor. Also, when comparing the efficiency of non-contact TRTS measurements to contact methods, it was shown that the TRTS provided reasonable values compared to the resistivities measured using Hall Van der Pauw method due to poor electrical contacts [311].

8.3.2.1 Low temperature

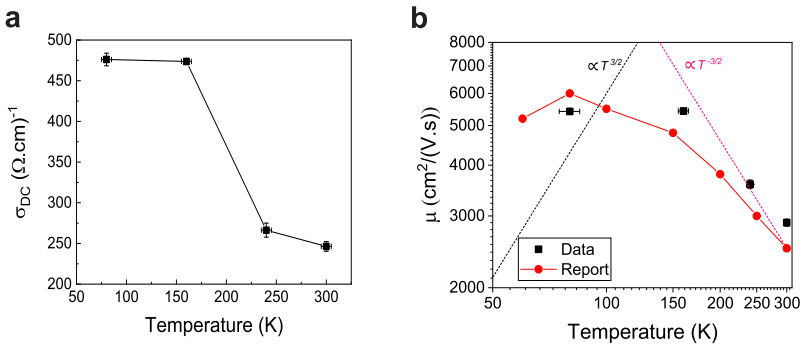

Figure 8.10: Parameters taken from the Drude model fits to the measured complex conductivity of Ge; ***a)*** *dc conductivity σ_{dc}, and* ***b)*** *mobility μ. The measurements were carried out at a fluence of $F = 5.6\ \mu J/cm^2$ ($n = 4.7 \pm 0.3 \times 10^{17}\ cm^{-3}$). The reported mobility values for carrier concentration in the order of $\sim 10^{17}\ cm^{-3}$ [109] are overlaid in* ***b)*** *plot.*

The complex conductivity of Ge was also investigated at temperatures below $T = 300$ K using an excitation fluence of F = 5.6 μJ/cm^2 ($n = 4.7 \pm 0.3 \times 10^{17}$ cm^{-3}). The extracted σ_{dc} and μ values, from the Drude model fits to the measured complex conductivities, are shown in Figures 8.10a and 8.10b, respectively (ω_p values are shown in Figure D.2). The mobility increases at low temperature, as expected due to the suppression of lattice scattering [316] (see Section 3.5.1), and reaches up to a maximum of $\sim$5500 cm^2/V·s at $T = 160$ K. With the suppression of lattice scattering, the mobility is expected to follow $T^{-1.5}$ dependence, as depicted by the magenta dashed line in Figure 8.10b. However, the mobility dependence departs from $T^{-1.5}$ due to the competition against impurity scattering, which follows a $T^{1.5}$ dependence at much lower temperature (black dashed line). The observed temperature-dependent mobility is in close agreement with the behaviour of reported Hall mobilities of Ge [109] for a carrier concentration in the order of $\sim 10^{17}$ cm^{-3}. In this report [109], the mobility increases from room temperature value to a maximum of $\sim$5000 cm^2/V·s at $T = 150$ K. For $T < 150$ K, the mobility reduced down to a minimum value of $\sim$ 4000 cm^2/V·s at $T = 10$ K. Additionally, it has been observed by other report [317] that ionized impurity scattering is not the only contributing factor to the reduced mobility. By accounting the contribution from *e-h* scattering into the expected temperature dependent mobility, in addition to the lattice and impurity

scattering, it was shown that the expected behaviour is more consistent with the experimentally measured mobilities in Ge [317].

8.4 Summary

In summary, the photoluminescence and photoconductivity of bulk Ge were investigated. The PL from both direct and indirect band gaps was measured and the interplay of the direct and indirect PL was examined at various excitation fluences. As the excitation density becomes higher, the direct PL is shown to continually increase whereas the indirect PL tends to saturate possibly due to Auger processes. This demonstration entails that the photoexcitation of carriers can modulate the direct and indirect PL.

The THz complex conductivity of photoexcited Ge was also investigated using TRTS. The measurements agree well with the Drude model for conductivity of free carriers. Particularly, the mobility values extracted from the Drude model fits were examined at various excitation densities and temperatures. The behaviour of the fluence and temperature dependent mobilities showed the effect of carrier-carrier, impurity, and lattice scattering. This demonstrates a proof-of-concept to the capability of TRTS as a non-contact tool in effectively probing conductivities as well as carrier dynamics in the ultrafast scales in semiconductors.

CHAPTER 9

Time-resolved Terahertz Spectroscopy of Photoexcited Germanium Inverse Opal Films

9.1 Introduction

Ge has higher carrier mobility [320] and longer wavelength absorption [321] compared to silicon that is commonly used in optoelectronics industry. However, due to the expensive Ge material, fabrication of cost-effective nanostructured Ge including nanowires (NWs) [322, 323, 324], nanocrystals (NCs) [325], and porous thin films [326, 327] have attracted significant interest lately. These low-dimensional materials have shown excellent properties. In particular, nanoporous Ge has been shown to exhibit tunable photoluminescence [328], serve as a potential agent of adsorption and catalysis [329], and act as a high-performance battery electrode [330, 331]. Potential applications such as hybrid solar cells and thin film anodes for lithium ion batteries [327, 332] have also been explored, however, the optoelectronic properties on the ultrafast and macroscopic scales, which are important in device fabrications, remain unknown.

Ultrafast optical spectroscopy such as time-resolved optical pump-optical probe [322, 324] and TRTS [323] have been used to investigate the properties of Ge NWs, and TRPL for Ge NCs [325]. But to the best of our knowledge, investigation of the fundamental ultrafast carrier dynamics has not been reported for porous Ge films. Among the spectroscopies used in bulk semiconductors and nanoscale materials [107, 311, 333, 334], TRTS has been an established non-destructive technique for

probing transient photoconductivity on the ultrafast scale. TRTS technique does not only provides substantial information regarding their optoelectronic properties, such as carrier mobilities, but also elucidates the transport dynamics of carriers such as those confined within limited dimensions [4, 8, 134]. Among porous materials, Lloyd-Hughes *et al.* employed TRTS in photoexcited InP consisting of 2D 50 nm pores [335]. In this chapter, we present the TRTS of a 3D macroporous Ge film, also referred as 'Ge with inverse opals' [327]. We determine fast transient photoconductivities that last < 100 ps and frequency-resolved complex conductivities that follow the Drude-Smith model of carrier localization, both suggesting short-range transport in the Ge films. However, despite the disordered nature of the films, they show significantly high carrier mobilities of ~ 190 cm^2/(V·s), which is remarkable for materials prepared from a wet-chemical synthesis. The Ge inverse opal films were also compared to the TRTS of unstructured Ge film.

9.2 Ge films from wet-chemical synthesis

In this study, we explore the electrical properties and carrier dynamics of photoexcited unstructured (continuous film) and macroporous Ge films. The fabrication of macroporous and unstructured Ge films allows the excellent optoelectronic properties of Ge to be translated into a large surface area to volume ratio. $[Ge9]^{4-}$ Zintl clusters were used as wet soluble Ge source for the bottom-up wet-chemical fabrication of the Ge nanomorphologies. For the macroporous strucure, the inverse opal (INOP) structures were introduced by using polymethylmethacrylate (PMMA) beads as template molds. These PMMA beads were removed by annealing the structure at 500 °C for only 5 minutes followed by dissolution in tetrahydrofuran (THF), resulting in a Ge film with macroporous matrix (refer to Appendix E for details of the synthesis). Because the films did not undergo additional and longer annealing processes, they are expected to be amorphous. Investigating the samples in its amorphous phase offers an opportunity to be considered in the emerging applications of amorphous materials in the microelectronics industry [255]. Maintaining high degree of crystallinity and purity has been a challenge when fabricating cost effective microscale materials [4] and thus amorphous materials, which do not need further processing, can be immediately useful. As compared to more elaborate methods such as chemical vapor deposition [336] and electrochemical etching [337], the wet chemical synthesis of the Ge inverse opal structures is rather straightforward

with an exceptional control over the shape, size, and spatial arrangement of the pores [327].

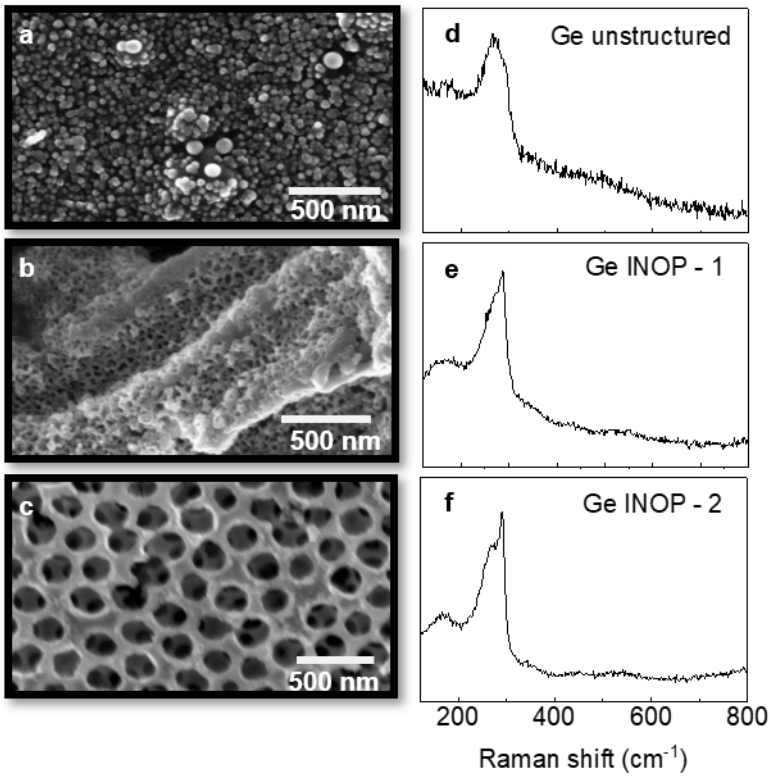

Figure 9.1: SEM images of the ***a)*** *Ge unstructured film,* ***b)*** *Ge INOP-1, and* ***c)*** *Ge INOP-2, and* ***d-f)*** *their Raman spectroscopies with broad amorphous peak at* $\sim$ *270* cm^{-1} *and slight sharp crytallinity peak at* $\sim$ *290* cm^{-1}*.*[1]

The samples investigated herein are Ge film without INOP structures (Ge unstructured) and two Ge films with INOPs (Ge INOPs). The scanning electron microscopy (SEM) images of the samples are shown in Figure 9.1a-c. Enlarged SEM images are displayed in Figures E.1 to E.3. The Ge unstructured film shows an amorphous matrix with loose granular structures while the Ge INOP films show a rather continuous Ge flat structure with INOPs. The removal of 150 nm and 340 nm PMMA beads in the Ge films resulted to the formation of INOP diameters ranging from 40 to 65 nm and 205 to 285 nm, respectively. For simplicity, we shall refer to these films as 'Ge INOP-1' and 'Ge

[1]Synthesis was performed by M. A. Giebel. Raman spectroscopy was performed by S. Geier and D. Boeh (TUM).

INOP-2'. The pore wall thicknesses range from 19 to 29 nm for the Ge INOP-1 and from 54 to 126 nm for the Ge INOP-2. As displayed in Figure 9.1b-c, the formation of distinct and uniform inverse opals was only effective at larger PMMA beads. Raman spectroscopy confirms an amorphous Ge for all the samples with a Raman peak at ~ 270 cm^{-1}, however, there appears a slight crystallinity especially on the Ge INOP counterparts at ~ 290 cm^{-1} (see Figures 9.1d-e).

9.3 Photoconductivity of Ge films probed by TRTS

We employed TRTS to investigate the ultrafast carrier dynamics and photoconductivities of these samples with different morphologies. Because the estimated optical band gap of unstructured Ge is $E_{g-ind} = 0.95$ eV, determined from the Photothermal Deflection Spectroscopy (PDS) (Appendix E.3), we used pulsed laser with an energy of 1.53 eV (and with 100 fs pulse width) to momentarily excite charge carriers within the net Ge material of the films. The measured E_{g-ind} is close to reported Tauc plots of amorphous Ge (a-Ge) with $E_{g-ind} = 0.88$ - 0.92 eV [338] and $E_{g-ind} = 0.84$ - 0.94 eV of a-Ge ultra-thin films [339]. From the measured absorption coefficient, the optical penetration depth is only ~ 450 nm from the surface of the Ge film with a thickness of 2.1 - 3.0 μm. Figure 9.2a shows an enlarged image of the Ge INOP-2 film on a quartz substrate, which was placed on a 1.5 mm aperture of the cold finger in the TRTS setup. Figure 9.2b schematically illustrates the TRTS experiment where the transmitted THz electric field without the optical pump (reference) and with the optical pump (pumped) are measured both in time and frequency domain. Here, both transient and complex conductivities were measured. For the transient photoconductivity, the THz probe is used to monitor the rise and decay of the photo-excited carriers. As the time-delayed (Δt) THz probe propagates through the sample, a reduced THz transmission ($-\Delta T$) is observed immediately after the excitation. Therefore, the time evolution of the optically-induced relative changes between the reference and pumped THz electric field amplitude peaks, $|-\Delta T/T_0|$, provides a good indication of the dynamics of the photoexcited carriers in sub-picosecond scale.

The measured transient photoconductivities of the Ge unstructured film and Ge INOPs, $|-\Delta T/T_0|$ shown in Figure 9.2c, have fast rise times of ~ 0.35 - 0.50 ps (Figure E.5). These values are comparable to the minimum response time of our THz pulse detection setup which suggest a fast photoexcitation of mobile carriers that typically occurs in less than 0.50 ps [254]. The process among

the Ge film samples mainly involves intraband relaxation of carriers [297, 323] which accounts for the fast rise time. In contrast, the rise time of bulk crystalline Ge is $\sim$ 3.5 ps (Figure E.5d), which is relatively slow due to phonon-assisted scattering to the low mobility satellite valleys [34, 296] especially at high excitation energy of $E_{ex} > E_{g-dir}$.

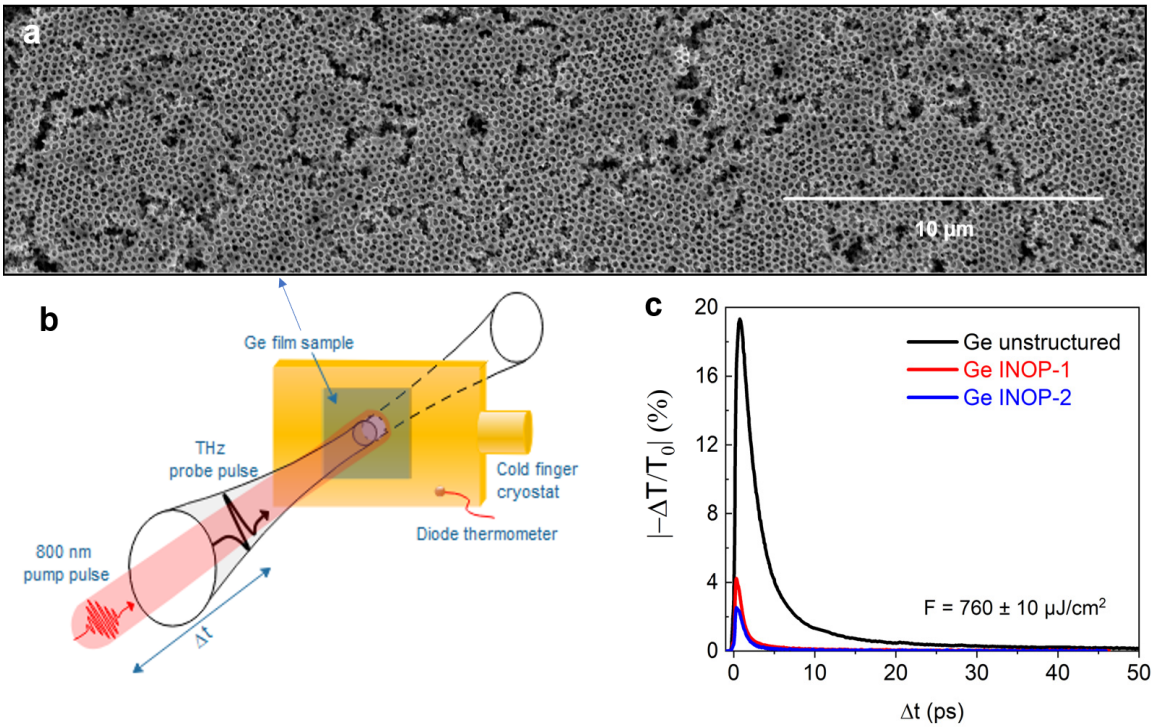

Figure 9.2: ***a)*** *SEM image of the inverse opal Ge film fabricated from a wet-chemical synthesis. The 3D inverse opals in the Ge film were formed from the removal of 340 nm PMMA beads (sample referred as 'Ge INOP-2 film').* ***b)*** *A schematic diagram illustrating the Ge film sample on a quartz substrate mounted on a cold cryostat finger. The sample is illuminated with an 805 nm optical pump and a THz electric field probe that overlap at a pump-probe delay time $\Delta t = 0$.* ***c)*** *The optically-induced relative changes in the THz electric field amplitude peaks, $|-\Delta T/T_0|$, are obtained for the Ge film without inverse opals (Ge unstructured) and the inverse opal counterparts (Ge INOP-1 and Ge INOP-2 nm films), which lasts < 50 ps.*

As the THz transmission recovers, the decay mechanism of the transient photoconductivities can be deduced. Figures 9.3a-c shows the log-log plots of the $|-\Delta T/T_0|$ of the Ge films. In Figure 9.3a, the Ge unstructured has a fast decay time of < 100 ps as opposed to a bulk crystalline Ge which typically have mobile carrier lifetimes that last up to microseconds (refer to Figure 8.5). As expected

from the nature of the amorphous or disordered material, the lack of long-range order in Ge material impedes carrier migration, resulting in localization of charge carriers and short photoconductivity. For the Ge INOP samples, the $|-\Delta T/T_0|$ peaks are further decreased which are mainly attributed to reduced photoexcited carrier density within the Ge material when INOPs were introduced (see also Figure E.6). Furthermore, the transient photoconductivities of Ge INOP-1 and Ge INOP-2 are shortened to $<$ 50 ps and $<$ 30 ps, respectively. Regardless, such decay times are still significantly longer than that of amorphous Si which was reported to last only for $\sim$ 2 ps [102].

The ultrafast carrier dynamics can be well described by the universal fit of the transient photoconductivities to three decay components, as shown in Figure 9.3a-c. Firstly, the 'fast' initial $|-\Delta T/T_0|$ follows a single exponential decay, $A \cdot exp(-\Delta t/\tau_c)$, where the pre-factor A and carrier decay time constant τ_c can be extracted. Lastly, the 'slow' tail of the $|-\Delta T/T_0|$ in the latter time can be fitted to two power law decays; $B \cdot \Delta t^{-\beta_1}$ and $C \cdot \Delta t^{-\beta_2}$ where B, and C are pre-factors, β_1 and β_2 are the power law exponents, respectively. The carrier dynamics, represented by the behavior of $|-\Delta T/T_0|$, is unchanged at higher carrier density (Figure E.7) which shows no additional nonlinear effect such as Auger recombination processes [101, 323]. Most of the carriers, accounting to 40-55% of the integrated $|-\Delta T/T_0|$ of Ge unstructured at $<$ 4 ps and Ge INOPs at $<$ 1.5 ps, undergo an exponential decay, indicative of monomolecular process [23, 84] where carriers are effectively trapped in deep localized states possibly resulting from the unsaturated surface or defects at the grain boundaries. The unstructured Ge has τ_c of $\sim$ 2.3 to 2.5 ps while the Ge INOPs have faster τ_c of $\sim$ 0.6 to 1 ps. The Ge INOP-1 have τ_c that are 10-20% faster than that of the Ge INOP-2, suggestive of higher population of surface states in smaller INOP size. At low temperature, τ_c decreases (Figure E.8) because carriers drift faster to the localized states as they lose thermal energy.

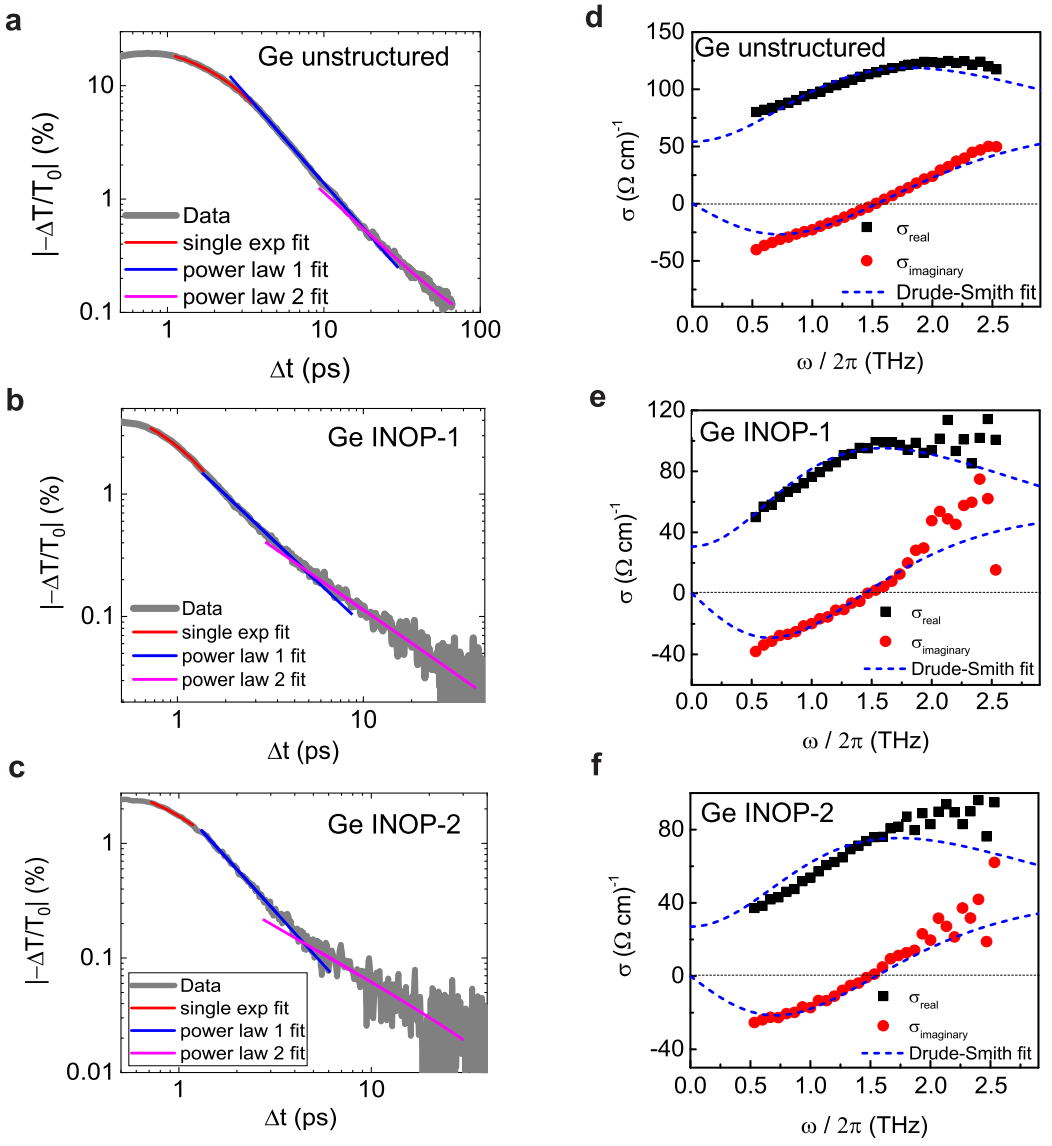

Figure 9.3: Log-log plots of $|-\Delta T/T_0|$ of ***a)*** *Ge unstructured,* ***b)*** *Ge INOP-1, and* ***c)*** *Ge INOP-2 measured at room temperature and at a fluence of $F = 760 \pm 10\ \mu J/cm^2$. Regions of the $|-\Delta T/T_0|$ were fitted to a single exponential decay (red line) and two power law decays (blue and magenta lines). As a guide to the eye, the solid lines are extended over the fitting range.* ***d-f)*** *Complex conductivity extracted from the TRTS measurements of the Ge unstructured at $-\Delta t \sim 1.25$ ps and Ge INOP samples at $-\Delta t \sim 0.85$ ps after photoexcitation, displaying both real (σ_{real}, black squares) and imaginary part ($\sigma_{imaginary}$, red circles). The blue dashed lines are the corresponding fits to the Drude-Smith model, shown in Equation 3.18 and the black dotted lines are guide to the eye at $\sigma = 0$.*

At the slower timescale, the transient photoconductivities are followed by power law decay dynamics, typically observed in amorphous or disordered semiconductors [66, 84, 88, 90, 101, 254], where long-lived carriers migrate between the localized states *via* multiple trapping. The power law time decay ($-\Delta t^{-\beta}$) relates to the carrier hopping in the trap distribution that extends below the mobility edge. This distribution corresponds to the exponential density of states [90] in the band tail which relates to the disorder of the material, referred as Urbach tail [50, 338] (see Section 3.5.2). Our PDS measurement (Figure E.4) confirms this broad exponential tail that extends at photon energies below the band gap. The mechanism of carrier multiple trapping within the bands has also been explained in earlier studies, such as in time-of-flight (TOF) transient photocurrent measurements [66, 76, 77] in disordered semiconductors.

While Figures 9.3a-c shows the time-dependent conductivity, the frequency-resolved complex conductivity spectra $\tilde{\sigma}(\omega)$ are measured within the spectral bandwidth of the THz probe. Here, both THz electric field waveforms from the unexcited (E_{ref}) and photoexcited (E_{pump}) were obtained to plot the $\tilde{\sigma}(\omega)$ for each Ge film at a fixed Δt as shown in Figures 9.3d-f. To investigate the mechanism, it is shown that the experimental $\tilde{\sigma}(\omega)$ can be approximated by a Drude-Smith model of carrier localization, presented in Equation 3.18 (refer to Figure E.10 for other fits). The Drude-Smith model has been effective in describing suppressed long-range transport in materials due to disorder [4, 101, 107], which is in agreement with our investigation in the short-lived $|-\Delta T/T_0|$.

Table 9.1: Parameters obtained from the Drude-Smith model fits (Equation 3.17) to the complex conductivities of Ge films. The $\tilde{\sigma}(\omega)$ of the Ge films were measured at a fluence of $F = 760 \pm 10\ \mu J/cm^2$ at THz probe delay of Δt = 6.75 ps for the Ge unstructured and Δt = 2.35 ps for the Ge INOP films.

Sample	τ_{DS} (fs)	c	μ_m ($cm^2/V{\cdot}s$)
Ge unstructured	61 ± 1	-0.78 ± 0.01	199 ± 6
Ge INOP - 1	47 ± 3	-0.73 ± 0.01	190 ± 13
Ge INOP - 2	48 ± 4	-0.72 ± 0.02	190 ± 11

The fit parameters extracted from the Drude-Smith model are presented in Table 9.1 where the c values were found to be -0.78 for the Ge unstructured and around -0.73 for both Ge INOP films.

Note that $c = 1$ means complete localization of carriers. Thus, the c values measured at the Δt where dispersive transport occurs are in line with the multiple trapping mechanism. Meaning, a fraction of carriers backscattered and thereby 20 - 30 % could have possibly drifted across the intergranular boundaries. Less carrier localization are observed in Ge INOPs due to relatively lower c values compared to the unstructured Ge, which may confirm the presence of more crystalline particles indicated from their Raman spectra (Figure 9.1e-f). In addition, the SEM images (Figure 9.1a-c and Figures E.1 - E.3) show that the Ge INOPs have more intergranular connections (resulting to flat structure) within the pore walls compared to that of Ge unstructured film. However, the faster scattering time τ_{DS} of $\sim$ 50 fs implies a reduced carrier mean free path as they collide against the particle boundaries [103, 340], which could be due to smaller microcrystalline grains in the Ge INOPs compared to the Ge unstructured film.

In addition, the fluence dependence of the macroscopic mobility μ_m values measured at the earlier timescale ($\Delta t \sim$ 1.25 ps and $\sim$ 0.85 ps) and at the regime where the dispersive transport occurs ($\Delta t \sim$ 2.35 ps and $\sim$ 6.75 ps) are presented in Figure 9.4. We use the effective mass of electron in Ge for conductivity measurements, given as $0.12m_0$, which provides a good estimate of the mobility in bulk Ge (refer to Figure 8.7). As the majority of the hot carriers are eventually trapped, the long-lived carriers (at $\Delta t \sim$ 2.35 ps and $\sim$ 6.75 ps) undergo multiple trapping thus, the momentum scattering time τ_{DS} (Figure E.11) becomes almost constant against carrier density, providing an efficient measure of their mobilities at $\Delta t \sim$ 6.75 ps (Ge unstructured) and at $\sim$ 2.35 ps (for Ge INOPs). Consequently, the μ_m values that are almost constant agrees with the multiple trapping transport, contrary to an electron-hole recombination process observed at latter Δt in polycrystalline silicon where the free carrier mobilities increase at higher optical fluences [103], as well as the increase of mobilities in bulk Ge (see Figure 8.7).

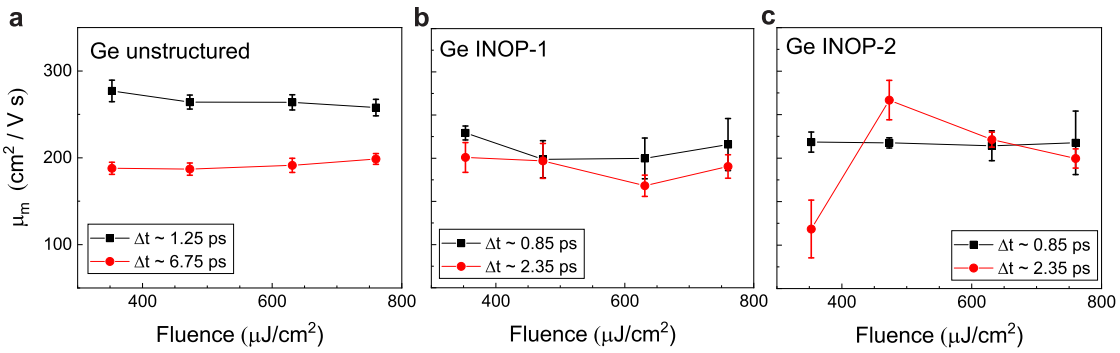

Figure 9.4: Macroscopic mobilities, μ_m, of the ***a)*** *Ge unstructured,* ***b)*** *Ge INOP-1 and* ***c)*** *Ge INOP-2 measured at the hot regime ($\Delta t \sim$ 1.25 ps, 0.85 ps) and at the regime where dispersive transport occurs ($\Delta t \sim$ 6.75 ps, 2.35 ps) against different pump fluences. All plots have the same y-axis scale with* ***a)****.*

The average macroscopic mobilities of 190 ± 13 cm^2/V·s for the Ge INOPs are comparable to that of the Ge unstructured of 199 ± 6 cm^2/V·s, thus introducing INOPs do not compromise the Ge film's electrical property. Using the Einstein relation where the diffusion coefficient can be taken as $D = \frac{\mu k_B T}{e}$ (see Equation 2.4), the characteristic length L can be approximated as $L = \sqrt{2D/f}$ at the THz frequency regime of f = 0.5 - 2.5 THz [100, 333]. Thus, by taking the μ_m value of 200 cm^2/V·s, it is estimated that the charge carriers travel a distance of 20 - 45 nm, which is within the average grain size of 64 ± 31 nm estimated from the SEM image of the Ge unstructured film. Also, the distance is less than the pore wall thickness of Ge INOP-2 (90 ± 36 nm) and comparable to the pore wall thickness of a-Ge INOP-1 (24 ± 5 nm). Moreover, note that both Ge INOPs have same values of c and τ_{DS}, which strongly indicates that they have similar particle topology. Therefore, the morphology of the Ge material in the Ge INOPs are responsible to the carrier confinement and not the INOP sizes.

Remarkably, our measured carrier mobility values are significantly high compared with typical values of reported a-Si with electron-drift-mobilitiy (using Schottky-diode circuit) of $\mu_o < 13$ cm^2/V·s [89] and μ_o = 10 - 20 cm^2/V·s [341], as well as the Hall mobility of a-Ge of $\mu_H < 3 \times 10^{-2}$ cm^2/V·s (at $n \sim 1 \times 10^{18}$ cm^{-3}) [342]. Typically, for an amorphous semiconductor with a free-electron effective mass, the electron wavelength at room temperature (or the mean free path) would be around 10^{-6} cm, which gives a highest possible mobility value in the order of 100 cm^2/V·s corresponding to

disorder scattering [47, 342]. Therefore, the high carrier mobility values of our Ge films cannot be entirely accounted from their amorphous character. The slight crystallinity of the samples, arising from the peaks of the Raman spectroscopy at ~ 290 cm^{-1} (Figure 9.1d-f), are therefore responsible to the high carrier mobility, in which the μ_m values are closer to reported polycrystalline Ge. The reported effective hole mobility of polycrystalline Ge fabricated by pulsed laser annealing is 295 cm^2/V·s [343] while the highest hole mobility value reported so far in polycrytalline Ge, which was fabricated on insulating substrates at temperatures below 900 °C from an a-Ge precursor, is 340 cm^2/V· [344]. The fact that our Ge films were synthesized in a rather simpler method of wet-chemical sysnthesis and did not go through long annealing process at very high temperatures, the carrier mobility of 190 ± 13 cm^2/V·s is exceptional. This makes the Ge INOPs as competitive candidates for macroporous materials in optoelectronics.

9.4 Summary

In summary, by means of time-resolved terahertz spectroscopy, we have investigated the ultrafast carrier dynamics of a Ge film and its INOP counterparts. From their transient photoconductivities, the underlying mechanisms are explained; in the sub-picosecond scale, the carriers undergo intraband relaxation and afterwards, most carriers are effectively trapped possibly in the surface states at the grain boundaries and the long-lived carriers experience multiple trapping in the localized states due to the nature of the disordered material. Introduction of the inverse opals in the Ge films did not affect the carrier dynamics. The THz complex conductivities, which are approximated by the Drude-Smith model of carrier localization, confirm the disorder-inhibited transport among the Ge unstructured and Ge INOP films. Despite of these, the measured mobilities of the Ge INOPs are remarkably high and are comparable to that of the Ge unstructured film at ~ 190 cm^2/V·s, which is significantly higher compared to reported amorphous Ge and is at par with polycrystalline Ge films. This excellent electrical property makes them potential candidates for optoelectronic applications in addition to the fact that the Ge INOPs were fabricated from a starightforward wet-chemical synthesis in contrast to more elaborate methods.

CHAPTER 10

Modulation of the Photoluminesce of Germanium *via* Intense Terahertz Electric Field Pulses

10.1 Introduction

With the advent of table top generation of intense THz electric fields [17, 19, 145], the investigation of nonlinear transport phenomena in semiconductors comes into a new height. The ability to nonlinearly manipulate light-matter interaction in an 'all optical' fashion delivers an opportunity to uncover exciting physics in the ultrafast time scale. The use of single or sub-cyle intense THz pulses provides a huge advantage in investigating its transient effects in picosecond scale. Moreover, although nonlinear transport at high external bias electric fields (*e.g.* Zener tunneling, impact ionization, hot electrons [26, 155]) have already been fully exploited in the perturbation of semiconductors using contact methods, this concept remain fairly new in terms of the application of strong electric fields at THz frequencies [18].

We are specially interested in the effects of intense THz electric field pulses in the interband luminescence in semiconductors. Recently, several groups have shown that intense THz pulses with field strengths greater than 200 kV/cm can either generate, enhance or quench the emission of light. Without optical excitation, PL can be generated from GaAs QWs through impact ionization at an incident THz pulse with $E_{THz} = 1.05$ MV/cm [171]. Remarkably, this means that the application of E_{THz} provided enough electron kinetic energy that exceeded the ionization threshold of > 1.52

eV. In the same manner, it was demonstrated that intense THz caused Zener tunneling prior to impact ionization, that resulted to the THz-induced luminescence in an undoped bulk GaAs with metamaterial THz resonators [169]. In photoexcited semiconductor, PL flashes that lasts > 15 ns have been observed in photoexcited undoped GaAs/AlGaAs QWs [345] by means of field ionization from the impurity states, which allowed the release of additional carriers.

In contrast to these THz-induced PL reports, quenching of the PL was observed in photoexcited GaAs and CdTe at the arrival of THz pulses, which could be due to THz-induced heating of the lattice reducing the efficiency of carrier recombination [346]. On the other hand, other possible mechanism was presented in the Monte Carlo simulation of these experimental results [347]. Generated phonons induced by intense THz pulses in intrinsic and photoexcited carriers can either drive carriers to other valleys or to non-radiative centers, both resulting in quenched PL. Recently, another study [16, 35] demonstrated that intense THz do not only quench PL in GaAs, it can also result in THz-induced PL enhancement that was observed at higher energy tail of the PL spectrum. Here, the authors provided a more comprehensive picture of the mechanism: the PL quenching (near the band edge) is due to THz-induced hot-carrier diffusion which reduced the overall radiative efficiency in the bulk of GaAs, while the PL enhancement (at higher energies of the PL spectrum) was due to recombination from hot electrons [35]. A simple model that unifies both the THz-induced PL quenching and enhancement was presented in this report [35]. By including the effects of THz heating into the hot-carrier temperature [348] in the 1D diffusion equation (see Equation 2.4) and the PL intensity (see Equation 2.17), the model fitted well with the experimentally observed quenching at the PL peak of GaAs (< 1.48 eV), the crossover point ($\sim$1.48 eV between PL quenching and enhancement), and the enhancement of the PL at the higher energy tail (> 1.48 eV). Moreover, the fractional change in the THz-induced PL quenching and enhancement is the same, which compliments the mechanism that THz heating drives electrons to higher energy states.

In addition, the authors [35] eluded to the idea that THz-induced intervalley scattering could also be a possible route whereby carriers could be driven to the satellite valleys that would result in quenched direct band gap PL and enhanced higher energetic PL due to hot carries being scattered back from the side valleys (which have higher band gaps) to the Γ valley. This is possible as along as the gained kinetic energy of the carriers from the E_{THz} is able to overcome the Γ - L separation energy. The pendoromotive energy (see Equaton 4.23) should be sufficient enough to fasciliate

such acceleration of carriers. This proposition is in line with observed enhanced THz transmission in photoexcited bulk GaAs and InAs [177, 178, 180] at higher E_{THz}. Here, the conductivity is reduced because carriers could have scattered into the L side valley that is less mobile (see discussion in Section 4.4.4). Unfortunately, the previous work [35] did not include effects of intense THz in intervalley scattering in their model. Also, because of the direct gap nature of Group III-V semiconductors mentioned above, THz-induced intervalley scattering could not be simply confirmed thru PL measurements from the side valleys. Motivated by these works, we choose to investigate the PL of Ge, whereby at higher excitation energy, both direct and indirect PL can be observed, as demonstrated in Section 8.2 in Chapter 8. It is hoped that intense THz electric field could also modulate the interplay between the direct and the indirect PL (as was discussed in Section 8.2.2).

10.2 Details of the experimental method

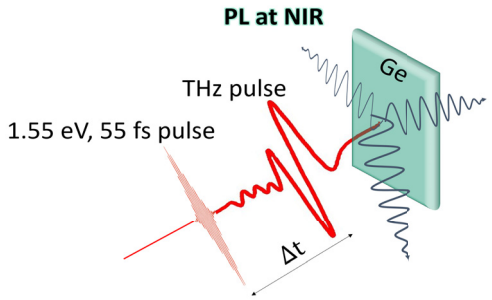

Figure 10.1: An illustration depicting the method for the THz modulation of the integrated PL of Ge. A 1.55 eV optical pulse photoexcites the surface of the Ge, which results in emission of light at the NIR wavelengths. The changes in the PL (ΔPL) are measured at different delay times (Δt) between the optical pulse and the peak of THz pulse.

The intense THz source is generated from a $LiNbO_3$ crystal by means of optical rectification method combined with tilted pump pulse front technique. Details of the experimental setup were presented in Section 5.4 in Chapter 5. The THz beam that propagates in free space are then directed by a set of parabolic mirrors and eventually focused onto the surface of the sample, which is an undoped single crystal Ge wafer with 0.5 mm thickness oriented at <100> (MTI Corp.). The sample is is photoexcited collinearly with 1.55 eV, 55 fs, 1 kHz pulses from a regenerative Ti:sapphire laser

source and spatially overlapped with the focused THz beam. The PL from the photoexcited surface of Ge is then measured at different delay times (Δt) between the peak of the THz pulse and the optical pulse, as depicted in Figure 10.1. Here, the transient PL is measured by an InGaAs avalanche photodetector (Thorlabs APD110C, 50 MHz bandwidth, 900 - 1700 nm) with a long pass filter of 950 nm and a short pass filter at 1600 nm for the direct PL, or InGaAs amplified photodetector (Thorlabs PDA10D, 15 MHz, 800 - 2600 nm) with a 1650 nm long pass filter for the indirect PL. More details on the photodetector responsivities and filter cut-off wavelength range are provided in Figure F.1. With an aid of an oscilloscope, the transient PL pulses measured by the InGaAs detector were gated using a boxcar integrator triggered at 1 kHz, which is the repetition rate of the excitation beam. The DC output from the boxcar integrator was further processed by a lock-in amplifier referenced to the THz pulses repetition rate of 500 Hz, therefore the changes in the integrated PL, ΔPL, is only due to the temporally overlapped THz and optical pulses. In this work, all measured PL are integrated. Note that this is similar with the reported spectrally integrated changes in PL referred as ΔPL_{int} in Ref. [16, 35]. For sampling the single cycle THz pulses, an electro-optic detection technique was employed using a <110> GaP crystal.

10.3 THz electric field pulses

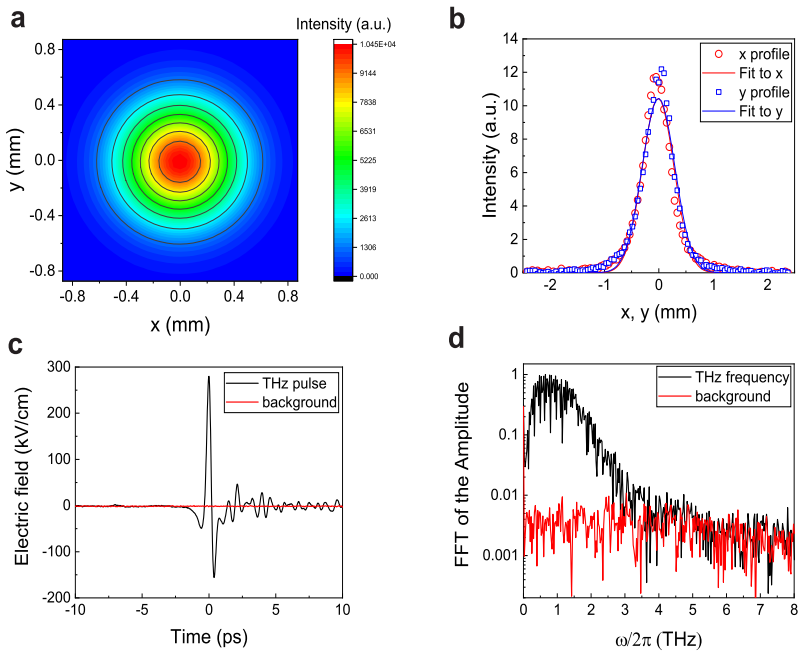

Figure 10.2: ***a)*** *The THz beam spot size measured using a pyroelectric detector which shows a circular area.* ***b)*** *The x and y line profiles from (a) are plotted with their corresponding Gaussian fits (Equation 5.2).* ***c)*** *Time-domain waveform of the THz electric field pulse which peaks at $\sim$ 290 kV/cm (black line). The background is also measured without the THz pulse (red line).* ***d)*** *Corresponding FFT of the waveforms which display a flat background and a THz electric field that peaks at $\sim$ 0.9 THz. The unsmooth curve has sharp lines due to water absorption.*

The image of the focused THz beam spot incident to the Ge surface is shown in Figure 10.2a. It has circular shape with an intensity following a Gaussian profile (Figure 10.2b). From the Gaussian fits to the x and y profiles of the focused THz beam, the dimensions ($1/e^2$ beam width) is estimated to be $x = 1.26$ mm and $y = 1.16$ mm. Thus, the excitation beam was maintained at less than $\sim$ 0.8 mm to ensure that the measured ΔPL is only due to the effect of the intense THz. At $\sim$ 2 mJ optical pump onto the $LiNbO_3$ crystal, a 1 ps single-cycle THz pulse is obtained with a maximum peak electric field of $\sim$ 290 kV/cm (Figure 10.2c). The Fourier transform of the pulse, at Figure 10.2d, shows a bandwidth of 0.1 to 3 THz with a maximum amplitude at $\sim$ 0.9 THz.

10.4 THz-modulated PL at room temperature

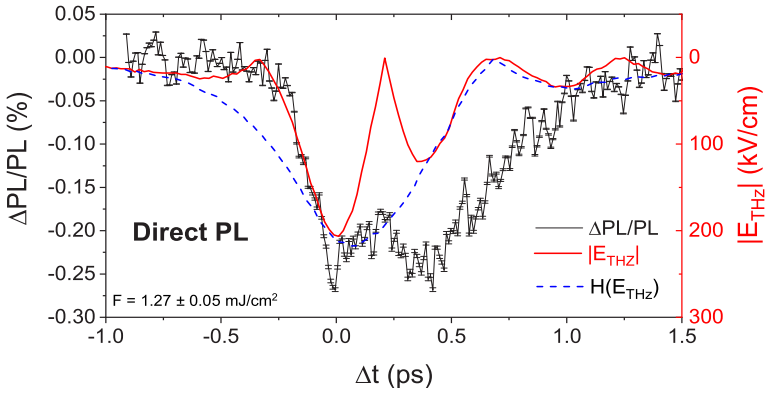

Figure 10.3: Fractional change in the integrated direct PL ($\Delta PL/PL$) plotted against the optical pump - THz pulse delay time (Δt) measured at an optical pump fluence of $F = 1.27$ mJ/cm^2 (left axis) with an applied peak THz electric field of $E_{THz} = 210 \pm 10$ kV/cm ($|E_{THz}|$ right axis). The Hilbert transform of the E_{THz}, $H(E_{THz})$ is also overlayed with respect to the right axis.

Figure 10.3 shows the fractional change of the integrated PL, $\Delta PL/PL$, at the direct gap measured at different delay times Δt between the optical pulse and the peak of the THz pulse. Even with a small fractional change of only a maximum of -0.27 %, an obvious quenching of the PL is observed. In the same manner, a THz-induced PL quenching at the indirect gap PL (see Figure F.2) was observed, with an optimum $\Delta PL/PL$ of -0.14%, and no other modulations were detected at longer times. The fact that PL quenching is observed, we rule out other known extreme nonlinear effects of intense THz in photogeneration, such as Zener tunneling and impact ionization [171, 345]. The results are similar with the reported PL quenching in GaAs and CdTe [16, 35, 346], however the $\Delta PL/PL$ in Ge is much less than the maximum -4% change achieved in GaAs [35, 346] and -17% obtained in CdTe [346] at less intense E_{THz} of $\leq$ 200 kV/cm.

It seems that more state filling reduces the effect of the THz field considering that the excitation energy of 1.55 eV is way above the band edges of Ge ($E_{g-dir} = 0.805$ eV and $E_{g-ind} = 0.664$ eV at T = 300 K [273]), having an excess energy of ~ 0.745 as compared to < 0.13 eV in

GaAs and CdTe (E_g = 1.42 eV for GaAs, E_g = 1.49 eV for CdTe [96]). Additionally, at an optical fluence of F = 1.27 mJ/cm^2, an estimated 134×10^{18} cm^{-3} carriers are injected into the bands. At this excitation level, scattering events becomes more dominant (see Section 8.3.1) and possibly an onset of Auger processes, as was presented in Section 8.2.2 in Chapter 8. In order to avoid Auger, ideally, the carrier density should be $< 4 \times 10^{19}$ cm^{-3}, however reasonable PL signals were difficult to achieve at very low excitation levels. Furthermore, the injection of large carrier density makes the sample highly conductive, which could probably reduce the effect of the intense THz electric field [15]. Thus, all of these factors, may all compete to the effects of intense THz at similar picosecond timescale.

It can be noticed that the time-domain $\Delta PL/PL$ have fluctuations at -0.5<Δt<0.5 ps that almost follows the modulations in the $|E_{THz}|$ waveform, and therefore directly correlates the effect of the intense THz electric field. This behaviour was not observed in the previous report in GaAs, whereby the $\Delta PL/PL$ only follows the THz waveform envelope (Hilbert transform of the E_{THz}) [35]. At $\Delta t > 1$ ps, the -$\Delta PL/PL$ recovers to 0% when E_{THz} reaches 0 kV/cm, similar to reported 'recovery time' in GaAs [35, 346]. Note that we define the recovery time here as the Δt that any THz-induced changes in the PL becomes no longer effective. It was explained that GaAs has faster recovery time compared to the THz-induced quenched PL of CdTe beacuse of its lighter electron effective mass of $0.067m_0$ ($0.11m_0$ in CdTe) and shorter Γ - L separation of 0.29 eV (1.4 eV in CdTe), which increases its scattering time in the event of THz-induced intervalley scattering [347]. Ge has a smaller effective mass of m_e^*=$0.041m_0$ at the Γ point of k-space (direct) and has only Γ - L separation of 0.14 eV at room temperature (see Figure 8.1 for the Ge band structure) [273]. However, at the L valley (indirect), the effective mass of $0.22m_0$ is even double than that of CdTe. Thus, the fast recovery times in both $\Delta PL/PL$ in the direct and indirect gap do not agree with the proposed mechanism that the recovery time is related to the intervalley scattering time that is influenced by the effective masses.

The fact that both indirect and direct $\Delta PL/PL$ show quenching does not fully support the proposed mechanism of THz-induced intervalley scattering from the Γ to L valley (or vice versa) because if carriers are to be added arising from intervalley scattering, a PL enhancement should be expected in either the indirect or direct PL. Otherwise, if the intense THz is able to drive intervalley scattering, carriers in both indirect and direct band could have scattered in other side bands upon

the THz excitation. However, this is unlikely to happen into the other neareast satellite valley $X_{[100]}$ that has a higher energy (E_{g-X}=0.85 eV) and larger effective mass ($0.32m_0$). On the other hand, the observed overall small fraction of PL quenching could support the idea of THz-induced heating of the lattice [346] which further fascilitates non-radiative recombination *via* electron-electron or electron-phonon scattering. Similarly, the PL quenching could also agree with the THz-induced hot-carrier diffusion model [35], where intense THz allows carriers to penetrate deeper into the bulk thereby allowing them more time to recombine through nonradiative channels and decrease the rate of *e-h* recombination. To elaborate on the effect of intense THz with carrier density, a fluence dependence was carried out as displayed in Figure 10.4 for both direct and indirect PL. Overall, reduced $\Delta PL/PL$ is observed at carrier densities ranging from ~30 to 240 $\times 10^{18}$ cm^{-3} for our range of optical fluences.

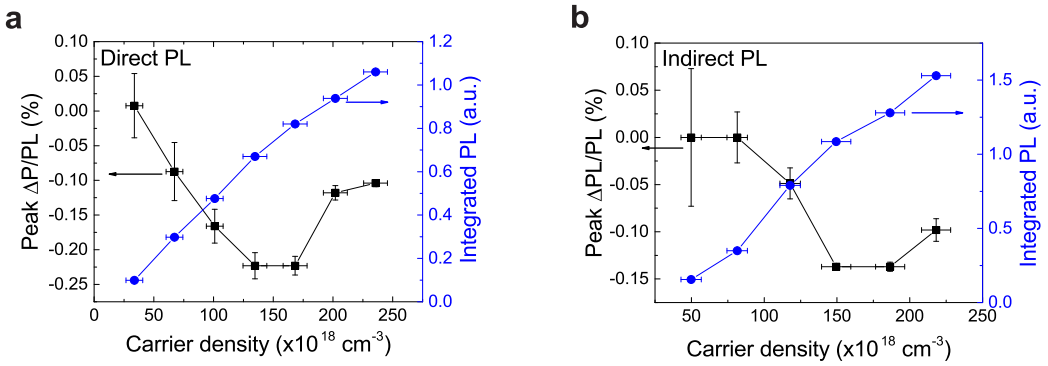

*Figure 10.4: Fluence dependence of the integrated PL (blue circles) and the peak amplitudes of the $\Delta PL/PL$ (black squares) at the **a)** direct transition and at the **b)** indirect transition of Ge, at an applied E_{THz} = 230 ± 10 kV/cm.*

To understand the behavior of the $\Delta PL/PL$, we investigate first the integrated PL with respect to the right axes of Figure 10.4. The integrated PL enhances with the increasing carrier density but at $n > 134 \times 10^{18}$ cm^{-3} (F > 1.27 mJ/cm^2), the integrated PL deviates from the linear increase (more noticeable in the direc PL), which corresponds to reduced efficiency of recombination. This large carrier concentration could contribute to higher order of nonradiative recombination. Note that in Section 8.2.2 of Chapter 8, we have estimated that Auger processes may occur at carrier densities above ~4×10^{19} cm^{-3}. Thus, the increase of the PL is rather linear at weak excitation and

then starts to depart from this linear trend at much higher n values. Besides Auger, other processes may also play a role here at higher excitation level; *e-h* and lattice scattering that dominates at higher carrier densities and temperature (as was also discussed in Section 8.3.1). Consequently, as the recombination becomes less efficient, at $n > 150 \times 10^{18}$ cm^{-3} the fractional PL quenching in the integrated PL ($\Delta PL/PL$) starts to decrease. Thus, an optimum THz-induced PL quenching $\Delta PL/PL$ can only be obtained at certain range of carrier density where the *e-h* recombination is more efficient (or at the highest bimolecular recombination rate). Note that in GaAs [35], no optimum $\Delta PL/PL$ was observed as the optical fluence is continually increased (although at lower excitation levels, an optimum ΔPL was observed.)

10.5 THz-modulated PL at low temperature

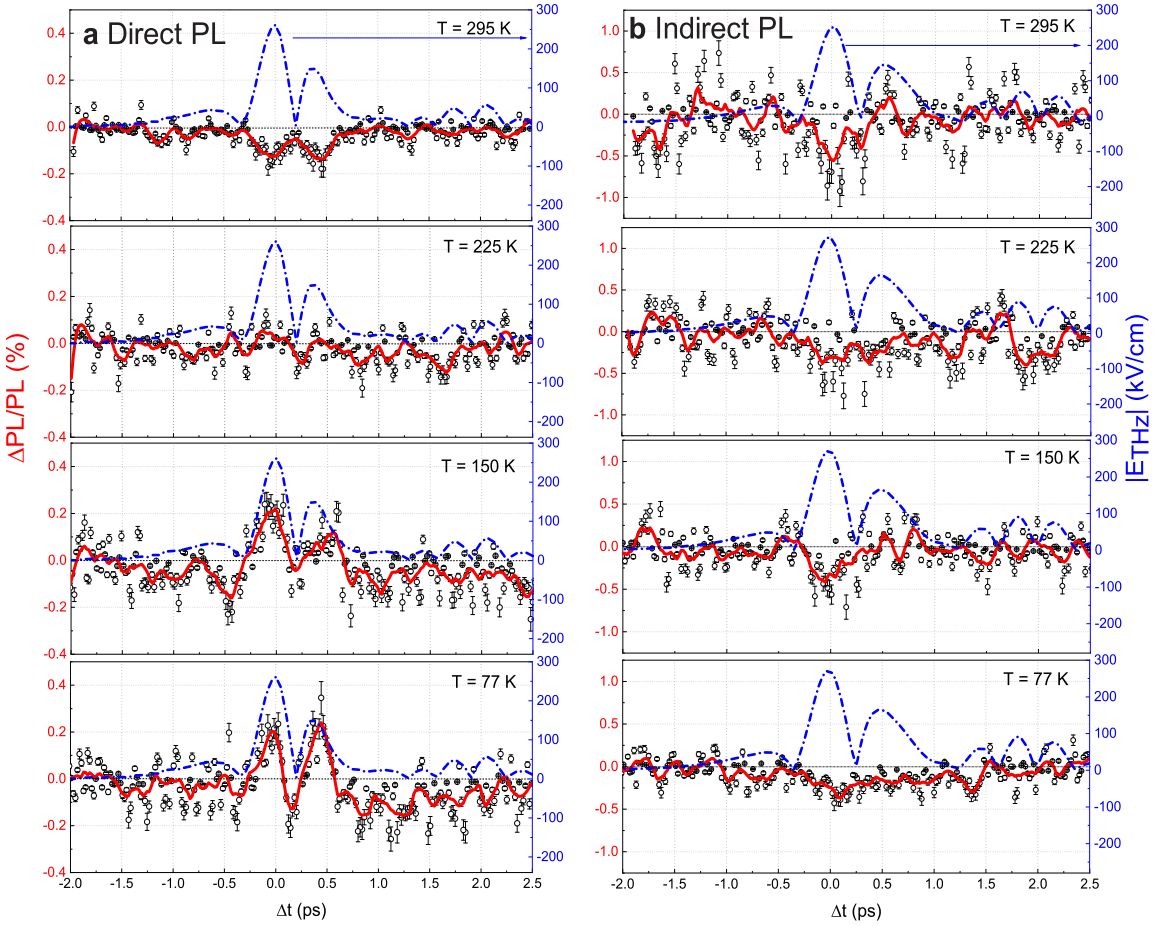

Figure 10.5: Plots of $\Delta PL/PL$ (left axis) and $|E_{THz}|$ (right axis) at various temperatures measured at the ***a)*** *direct gap and* ***b)*** *indirect gap at a fluence of $F = 1.27$ mJ/cm^2, and $E_{THz} = 260 \pm 10$ kV/cm. Due to the very small S/N ratio, the data points of the $\Delta PL/PL$ were smoothed to the red curves to serve as guides to the eye.*

The THz-induced modulated PL is further investigated by lowering the temperature to reduce heating effects. An excitation fluence of F = 1.27 mJ/cm^2 were maintained, as this is where the optimum THz-induced PL quenching occurs. Figure 10.5 shows the time domain $\Delta PL/PL$ at various temperatures. Whereas Figure 10.6 shows the plots of the temperature dependence of the integrated PL (blue circles) and the highest fractional PL change (black squares, peak of $\Delta PL/PL$ taken from

the time domain in Figure 10.5 within the vicinity of $\Delta t = 0$ ps), for both direct and indirect PL measurements.

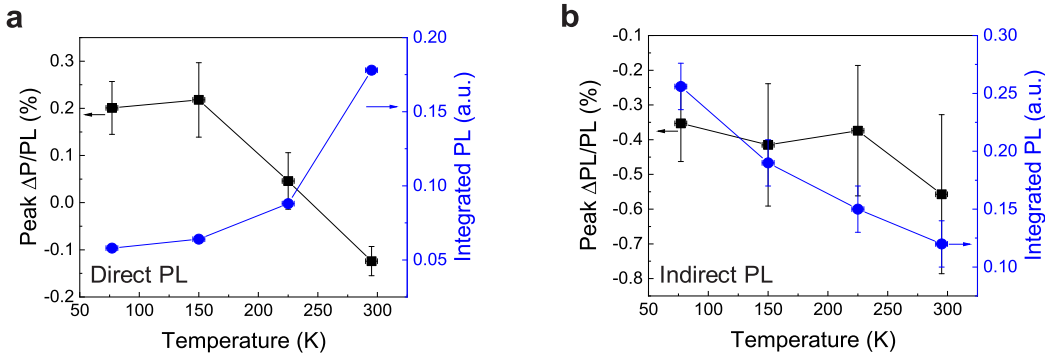

*Figure 10.6: Temperature dependence of the integrated PL (blue circles) and the peak amplitudes of the $\Delta PL/PL$ (black squares) at the **a)** direct and at the **b)** indirect transitions at a maximum electric field of $E_{THz} = 230$ kV/cm. The peak amplitudes of the $\Delta PL/PL$ were taken from the time-domain waveforms and the error bars were determined from the baseline at $E_{THz} = 0$ kV/cm.*

Firstly, we look at the temperature dependence of the integrated PL (blue circles with respect to the right axes in Figure 10.6). The integrated direct PL is shown to decrease at low temperature while it is opposite in the indirect PL. The decreasing PL has been observed in steady-state PL measurements of Ge from the direct transition especially at extremely low temperatures (T < 10 K) [282, 299]. One explanation is due to the reduced thermal excitation of electrons from the L valley to the Γ valley [282]. This could be a reasonable point with the decreased integrated PL from the indirect transition at elevated temperatures, however in our case, the integrated direct PL do not follow an Arrhenius plot (see Figure F.3), which is commonly used for extracting the thermal activation energy [23]. Thus, the decrease in direct PL cannot be only attributed to less thermal activation of carriers. One possible reason is the temperature dependence of the Fermi level, which reduced the amount of the direct gap PL, in agreement to reported direct PL of Ge [299]. In the case of the increasing indirect PL at low temperature, the reason is still unclear. In a previous report [280], it was demonstrated that although the indirect PL peak intensity increased at low temperature, the integrated PL over the energy range of the spectrum is still lower at 100 K compared to room temperature. The report [280] explains that the decrease of integrated PL at low

temperature is due to the reduced radiative recombination efficiency arising from higher transverse acoustic phonon absorption. The reported behaviour of the integrated indirect PL is inconsistent with our observation. Unfortunately, this could not be explained fully due to the lack of experimental reports in low temperature PL of undoped bulk single-crystalline Ge and complimentary theoretical studies.

Despite the fact that the integrated PL intensity in the direct gap decreases at low temperature, the THz-induced $\Delta PL/PL$ display a dynamic case. PL quenching was observed first at room temperature, which slowly transitioned to enhancement with upto 0.22 ± 0.8 % at T = 150 K. While in the indirect $\Delta PL/PL$, quenching was only observed throughout the whole temperature regime. It is interesting to note that the time-domain $\Delta PL/PL$ also follow the modulations in the $|E_{THz}|$ waveform (see Figure 10.5), which again clearly demonstrates the immediate effect of $|E_{THz}|$. At latter times, $\Delta t \gg 0$ ps, no further modulations were observed. It is also noteworthy to mention that no $\Delta PL/PL$ was observed when we gated the transient PL at 1.33, 2.87, and 5.83 ns after the arrival of the E_{THz} peak to check any late effects.

With the enhanced $\Delta PL/PL$ observed at the direct gap and quenched $\Delta PL/PL$ at the indirect gap at low temperature, one may reason out that this could possibly be due to intervalley scattering of carriers from the L valley to the Γ valley. If this is the case, the modulation of the $\Delta PL/PL$, that closely follows the $|E_{THz}|$ in the time domain, implies that the THz-induced ballistic transport of carriers is much faster than a phonon-assisted scattering, which happens at $\sim 230 \pm 25$ fs [5] (reported for Γ to L transfer time at high carrier densities of 10^{18}-10^{19} cm^{-3} using ultrafast time-resolved luminescence and transmission techniques). Note that in GaAs, with an application of E_{THz}=130 kV/cm, it only takes at least 40 fs for carriers to gain necessary energy for intervalley scattering (Γ - L) and the effective transfer time has an extremely short value of 20 fs [349]. Also, unlike the presumed scattering to the less mobile L valley in bulk GaAs and InAs [177, 178, 180, 347], the enhancement of the direct PL observed here implies that the carriers in Ge are scattered to the more mobile Γ valley as illustrated in Figure 10.7a. In this case, our result of THz-induced PL enhancement agrees with the reported increase of free-carrier absorption in Ge at intermediate THz energies [296]. In this report [296], the increased absorption, with an application of certain range of THz energies, strongly indicates increased carrier population in Γ valley compared to how much is expected from its density of states. This observation, once again, is unique compared to GaAs and

InAs [177, 178, 180], as well as Si [296], because electrons may have scattered or accelerated to the Γ valley that has much higher mobility (compared to its satellite valleys). The absorption investigations [296] was done at room temperature however in our case, the THz-induced PL enhancement (or the THz-induced absorption counterpart) at the direct valley was only observed at T < 225 K.

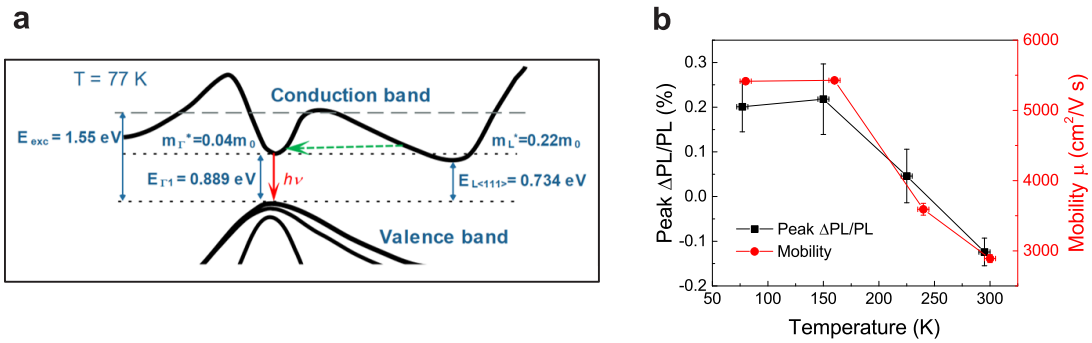

Figure 10.7: ***a)*** *A schematic diagram of the band structure of Ge at T = 77 K adapted from [273]. A possible intervalley scattering is depicted from the L valley to the Γ valley that is more mobile,* ***b)*** *Temperature dependence of the peak amplitudes of the $\Delta PL/PL$ (black squares) from the direct transition, plotted together with the electron mobility taken from the TRTS measurements (see Figure 8.10 in Chapter 8).*

Thus, we compare the temperature-dependent direct $\Delta PL/PL$ to the overall electron mobility μ of Ge, which was measured using TRTS (refer to Figure 8.10 in Chapter 8). Remarkably, the temperature dependence of the direct gap $\Delta PL/PL$ coincide with behaviour of μ at low temperatures, as shown in Figure 10.7b. The increasing μ at lower temperature is due to reduced lattice scattering, while the ionized impurity scattering competes at T < 150 K, resulting in a sudden reduction of μ value at T = 80 K. Hence, we can infer from this observation that the quenching of $\Delta PL/PL$ at high temperatures could be associated with THz-induced heating, whereby carrier-phonon scattering reduces the photogeneration and recombination (similar to the GaAs reports [16, 35, 346]), or even possibly due to THz-induced hot phonon effects. However, at low temperatures where the effects of phonons are reduced, the PL enhancement of the direct $\Delta PL/PL$ could have been made possible by a more dominant THz-induced intervalley scattering.

If THz-induced intervalley scattering is not the case and if the mechanism is purely THz-induced heating throughout the temperature regime, a consistent PL quenching should be observed.

At low temperatures, the increasing optical penetration depth [350] will fascilitate more carrier diffusion into the bulk and THz-induced hot-carrier diffusion [35] could mediate further non-radiative processes resulting in reduced PL efficiency, which is not the case especially in the direct $\Delta PL/PL$. In another perspective, the enhancement of the $\Delta PL/PL$ could also be due to impact ionization. THz-induced impact ionization was explained to be responsible in the quadratic increased absorption in InSb [172] at $E_{THz} > 75$ kV/cm, and decreased conductivity in n-doped InAs at E_{THz}=110 kV/cm [180]. Also, the authors [172] report that the ionization in InSb is from shallow impurities, thus this may support the effect of ionization scattering in the reduced $\Delta PL/PL$ at T $<$ 150 K. However, generation of carriers from impact ionization should be observed at longer times (even after $>$ 1 ps) [172, 180, 296], which is not apparent in our results. Moreover, impact ionization does not agree with the THz-induced quenching observed in the indirect PL. Therefore, these mechanisms (THz-induced heating and impact ionization) alone, are insufficient to explain the temperature dependent interplay of the direct and indirect $\Delta PL/PL$ at low temperature.

10.6 Summary

Modulations of the direct and indirect PL of photoexcited Ge were investigated *via* the application of intense THz electric field pulses. The changes in the integrated PL intensity at the time-domain closely follows the modulation of the THz pulses in the picosecond scale, thus an immediate effect of intense THz electric fields is observed in the acceleration of carriers. THz-induced PL quenching was observed at room temperature and enhancement at lower temperatures for the direct PL only. It is proposed that the quenching could be due to dominant THz-induced heating. At lower temperatures, a dominant THz-induced intervalley scattering from the indirect to the direct valley takes place.

To further understand the nonlinear effect of the intense THz electric fields in the modulation of the PL of Ge, deeper analysis could be performed by incorporating quantitative interpretation that would account for diffusion [351], hot phonons [352] and hot electrons [353], recombination and scattering rates [354], in the presence of intense THz electric field pulses. The 'dynamic Drude model' described in Section 4.4.4 [15, 177], as well as simulations including temperature dependent many-body effects and phonon modes, are also recommended. In terms of the experiment, it is recommended to investigate with tunable excitation energies ranging from the indirect band gap

energy to higher energies than the direct band gap for the observation of the onset of THz-induced intervalley scattering. As such, NIR ultrafast sources would be needed or the use of operational parametric amplifiers with a powerful laser source (to compensate the loss of efficiency in the conversion). Unfortunately, due to the weak PL of Ge, spectral measurements were not carried out at the excitation levels of our experiment, which could reveal more information on the intense THz effects in the temperature dependence of the band structure of Ge [355]. Doped Ge samples could be investigated, where intense PL could be achieved, however ionization to impurities would be more pronounced. THz near field enhancement could also be employed at the surface of Ge on device structures. This could lead to potential technological applications especially that the direct PL peak of Ge is at 1550 nm, which is the standard telecommunication wavelength.

CHAPTER 11

Conclusions and Future Directions

In conclusion, we have investigated the photoluminescence and photoconductivity dynamics of different types of semiconductors, from bulk to low dimensional materials, using photoluminescence (PL) and terahertz (THz) spectroscopy. This collective work provides a comprehensive picture of the light emission and carrier transport from a molecular to band structure, long-range to short-range transport in a pristine and disordered materials, and nonlinear transport at high electric fields.

Due to the unique band structure of Ge, the PL spectra of a photoexcited bulk Ge followed a combined lineshape of both direct and indirect band gap semiconductors. An interplay of the direct and indirect PL was observed as a function of excitation carrier density, possibly due to the competing effect of Auger recombination. At relatively low excitation density, an interplay was also demonstrated by an application of intense THz electric field pulses. PL quenching was observed at room temperature for both direct and indirect PL, which could be a result of THz-induced heating effects. When other scattering events became less dominant at low temperature, enhancement and quenching were observed in the small modulations of the integrated direct and indirect PL, respectively. It is proposed that the enhancement at the direct band gap is due to additional population of carriers by means of THz-induced intervalley scattering. These findings have not been reported so far in terms of THz-induced modulations of PL from direct and indirect transitions in a semiconductor. Thus, the information could be relevant in the use of intense THz electric fields in high-field transport and manipulation of light emission in bulk semiconductors. To carry out an in-depth study, it is recommended to measure the temperature-dependent PL spectra, which would reveal more information on the effect of intense THz electric field into the density of states and band structure of Ge. Incorporating quantitative analysis that would account for carrier

diffusion, hot phonons, hot electrons, recombination and scattering rates, could also provide better insight into the underlying physics of the THz-induced heating and intervalley scattering in Ge.

Photoconductivity measurements for a bulk Ge were also carried out using TRTS. The ac complex conductivity that follows the Drude model of free carriers demonstrates a proof-of-principle on the capability of TRTS in probing ultrafast carrier dynamics in materials. Additionally, the effect of scattering was observed in the fluence and temperature dependent mobilities. In the case of a disordered semiconductor, such as the Ge films with inverse opals, the frequency-resolved complex conductivities follow the Drude-Smith model of carrier localization. Also, the transient photoconductivities only last at less than a hundred picosecond and the photoconductivity dynamics imply a dispersive transport of carriers, whereby carriers experience multiple trapping in the localized states that extends below the mobility edge of the band (Urbach tail). Despite of this, a relatively high mobility was obtained, which is remarkable for drop-casted Ge inverse opal films synthesized from a wet-chemical process. The mobility values were comparable to reported polycrystalline Ge films that were fabricated by more elaborate methods. Thus, in addition to the rather straightforward approach in the synthesis, the excellent electrical properties of the Ge inverse opal films make them a good candidate as battery anodes. Future directions of this study include investigation of Ge and Si hybrid inverse opal films with different percentage of Si content and a detailed temperature dependence measurement to further elucidate the mechanism of the carrier mobility.

The disordered nature of semiconductor was also observed in the PL of freestanding two-dimensional functionalized silicon nanosheets (SiNSs). Due to the structural disorder, the Urbach tail was observed in the broad PL spectra, which indicates the amorphous character of the SiNS. The PL is shown to originate from the hydrogenation of the SiNSs and various functionalizations did not affect the PL spectra. But the effects of the functionalizations were noticeable in the PL dynamics that follow an inverse power law decay, indicative of diffusion-limited bimolecular recombination. The transport is more dispersive depending on the functionalization and the surrounding environment of the SiNSs. Low temperature measurements were also carried out, which shows improved carrier transport despite the static structural disorder. At lower thermal energy, carriers can escape from non-radiative channels, thereby improving the PL efficiency. Investigations of the carrier dynamics in various functionalized SiNSs is demonstrated here for the first time, which is essential in understanding the optical properties of two-dimensional silicon-based nanostructures.

In the future, TRTS will be carried out in order to probe the carrier transport at earlier timescale before the recombination takes place, which will provide more details in the role of carrier traps in the SiNSs.

In a series of Bismuth-based molecular compounds, the emergence of two PL spectra were observed at different energies, which correspond to fluorescence and phosphorescence. Due to the 'heavy element effect' of bismuth, enhanced spin-orbit coupling could be achieved which facilitated the efficient intersystem crossing from singlet to triplet states, resulting in dual emission. Such effect became more pronounced at low temperature with the suppression of metastable vibrational states. The study provided relevant information on the ongoing research on the synthesis of phosphorescent bismoles for organic light-emitting diode and bioimaging applications. It would also be interesting to look at how external field can affect the dual emission. Because of the non-perturbative advantage of THz wave, a study can be performed with an application of intense THz electric fields on the photoexcitation of bismole compounds.

References

[1] Rullière, C. (Ed.) **2005**. Femtosecond Laser Pulses Principles and Experiments. USA: Springer Science+Business Media, Inc.

[2] Diels, J.-C. & Rudolph, W. **1996**. Ultrashort Laser Phenomena Fundamentals, Techniques, and Applications on a Femtosecond Time Scale. USA: Academic Press, Inc.

[3] Prasankumar, R. P. & Taylor, A. J (Eds). **2012**. Optical Techniques for Solid-State Materials Characterization. USA: CRC Press, pp. 443-447.

[4] Ulbricht, R.; Hendry, E.; Shan, J.; Heinz, T. F.; Bonn, M. Carrier Dynamics in Semiconductors Studied with Time-Resolved Terahertz Spectroscopy. *Rev. Mod. Phys.* **2011**, 83(2), 543-586.

[5] Zhou, X. Q.; van Oriel; H. M.; Mak, G. Femtosecond kinetics of photoexcited carriers in germanium. *Physical Review B* **1994**, 50, 8, 5226-5229.

[6] Vardeny, Z. V. (Ed.) **2009**. Ultrafast Dynamics and Laser Action of Organic Semiconductors. USA: CRC Press.

[7] Svelto, O.; Silvestri, S.; Denardo, G. (Eds.) **1996**. Ultrafast Processes in Spectroscopy. New York: Plenum Press.

[8] Lloyd-Hughes, J.; Jeon, T. I. A Review of the Terahertz Conductivity of Bulk and Nano-Materials. *J. Infrared, Millimeter, Terahertz Waves* **2012**, 33(9), 871-925.

[9] De los Reyes, G. B. **2015**. Ultrafast Photoluminescence Spectroscopy of Silicon Nanocrystals (Doctoral dissertation). University of Alberta.

[10] Hegmann, F. A.; Ostroverkhova, O.; Cooke, D. G. **2006**. Probing Organic Semiconductors with Terahertz Pulses In Lanzani, G. (Ed.), Photophysics of Molecular Materials From Single Molecules to Single Crystals. Weinhem: Wiley-VCH Verlag GmbH & Co. KGaA, pp. 367-419.

[11] Cooke, D. G. **2007**. Time-resolved terahertz spectroscopy of bulk and nanoscale semiconductors (Doctoral dissertation). University of Alberta.

[12] Cocker, T. L. **2012**. Exploring Conductivity in Nanomaterials with Terahertz Pulses (Doctoral dissertation). University of Alberta.

[13] Hirori, H.; Blanchard, F.; Tanaka, K. Single-cycle terahertz pulses with amplitudes exceeding 1 MV/cm generated by optical rectification in $LiNbO_3$. *Appl. Phys. Lett.* **2011**, 98, 091106.

[14] Fülöp, J. A. & Hebling, J. **2012**. Applications of Tilted-Pulse-Front Excitation In K. Y. Kim (Ed.), Recent Optical and Photonic Technologies. Croatia: InTech, pp. 207-230.

[15] Ayesheshim, A. K. **2015**. High-power Terahertz Pulse Generation and Nonlinear Terahertz Carrier Dynamics in Semiconductors (Doctoral dissertation). University of Alberta.

[16] Purschke, D. N. **2016**. Modulation of Semiconductor Photoluminescence with Intense Terahertz Pulses (Masters dissertation). University of Alberta.

[17] Tanaka, K.; Hirori, H.; Nagai, M. THz Nonlinear Spectroscopy of Solids. *IEEE Trans. Terahertz Sci. Technol.* **2011**, 1(1), 301-312.

[18] Kampfrath, T.; Tanaka, K.; Nelson, K. A. Resonant and Nonresonant Control over Matter and Light by Intense Terahertz Transients. *Nat. Photonics* **2013**, 7(9), 680-690.

[19] Hirori, H.; Tanaka, K. Dynamical Nonlinear Interactions of Solids with Strong Terahertz Pulses. *J. Phys. Soc. Japan* **2016**, 85(8), 26-29.

[20] Peyghambarian, N.; Koch, S. W.; Mysyrowicz, A. **1993**. Introduction to Semiconductor Optics. USA: Prentice-Hall, Inc.

[21] Lakowicz, J. R. (Ed.). **2002**. Topics in Fluorescence Spectroscopy, Nonlinear and Two-Photon-Induced Fluorescence, Vol. 5. USA: Kluwer Academic Publishers.

[22] Landsberg, P. T. **1991**. Recombination in semiconductors. Cambridge: Cambridge University Press.

[23] Pelant, I. & Valenta, J. **2012**. Luminescence Spectroscopy of Semiconductors. New York: Oxford University Press.

[24] Abakumov, V. N.; Perel, V. I.; Yassievich, I. N. **1991**. Nonradiative recombination in semiconductors. Netherlands: Elsevier Science Publishers B.V.

[25] Herz, L. M. & Johnston, M. B. Hybrid Perovskites for Photovoltaics: Charge-Carrier Recombination, Diffusion, and Radiative Efficiencies. *Acc. Chem. Res.* **2016**, 49, 146-154.

[26] Pankove, J. I. **1971**. Optical Processes in Semiconductors. USA: Prentice-Hall, Inc., pp. 28-29.

[27] Ronda, C. (Ed.) **2008**. Luminescence From Theory to Applications. Germany: Wiley-VCH.

[28] Fox, M. **2012**. Optical Properties of Solids. 2nd ed. New York: Oxford University Press.

[29] Fang, Y.; Wang, L.; Sun, Q.; Lu, T.; Deng, Z.; Ma, Z.; Jiang, Y.; Jia, H.; Wang, W.; Zhou, J.; Chen, H. Investigation of temperature dependent photoluminescence in multi-quantum wells. *Scientific Reports* **2015**, 5, 12718.

[30] Valeur, B. & Berberan-Santos, M. N. A Brief History of Fluorescence and Phosphorescence before the Emergence of Quantum Theory. *J. Chem. Educ.* **2011**, 88, 731-738.

[31] Nilsson, N. G. Band-to-band Auger Recombination in Silicon and Germanium. *Physica Scripta.* **1973**, 8, 165-176.

[32] Galeckas, A.; Linnros, J.; Grivickas, V.; Lindefelt, U.; Hallin, C. Auger recombination in 4H-SiC: Unusual temperature behavior. *Appl. Phys. Lett.* **1997**, 71, 3269.

[33] Strauss, U. & Rühle, W. W. Auger recombination in intrinsic GaAs. *Appl. Phys. Lett.* **1993**, 62, 55.

[34] Beard, M. C.; Turner, G. M.; Schmuttenmaer, C. A. Transient photoconductivity in GaAs measured by time-resolved spectroscopy. *Physical Review B* **2000**, 62, 15764.

[35] Purschke, D. N.; Na, M.; Longman, A.; Titova, L. V.; F. A. Hegmann. Enhancement of hot-carrier photoluminescence with intense terahertz pulses. *Appl. Phys. Lett.* **2018**, 112, 072105.

[36] Robel, I.; Gresback, R.; Kortshagen, U.; Schaller, R. D.; Klimov, V. I. Universal Size-Dependent Trend in Auger Recombination in Direct-Gap and Indirect-Gap Semiconductor Nanocrystals. *Phys. Rev. Lett.* **2009**, 102(17), 1-4.

[37] Grove, A. S. **1967**. Physics and Technology of Semiconductor Devices. USA: John Wiley & Sons.

[38] Ischenko, A. A., Fetisov, G. V. and Ashanov, L. A. **2015**. Nanosilicon Properties, Synthesis, Applications, Methods of Analysis and Control. Boca Raton: CRC Press.

[39] Pavesi, L. Luminescence of Porous and Amorphous Hydrogenated Silicon: Analogies and Differences. *Solid State Phenom.* **1995**, 44-46, 261-274.

[40] Joshi, N. V. **1990**. Photoconductivity: Art, Science, and Technology. New York: Marcel Dekker, Inc.

[41] Böttcher, E. H.; Ketterer, K.; Bimberg, D.; Weimann, G.; Schlapp, W. Excitonic and electron-hole contributions to the spontaneous recombination rate of injected charge carriers in GaAs-GaAlAs multiple quantum well lasers at room temperature. *Appl. Phys. Lett.* **1987**, 50, 1074.

[42] McLean, D. G.; Roe, M. G.; D'Souza, A. I.; Wigen, P. E. Picosecond recombination of charged carriers in GaAs. *Appl. Phys. Lett.* **1986**, 48, 992.

[43] Kittel, C. **2005**. Introduction to Solid State Physics (8th Ed.) USA: John-Wiley & Sons, Inc. p. 208.

[44] Kusová, K.; Hapala, P.; Valenta, J.; Jelínek, P.; Cibulka, O.; Ondič, L.; Pelant, I. Direct Bandgap Silicon: Tensile-Strained Silicon Nanocrystals. *Adv. Mater. Interfaces* **2014**, 1, 1300042.

[45] Morigaki, K.; Kugler, S.; Shimakawa, K. **2017**. Amorphous Semiconductors Structural, Optical, and Electronic Properties. UK: John Wiley & Sons Ltd.

[46] Anderson, P. M. Absence of Diffusion in Certain Random Lattices. *Physical Review* **1958**, 109(1), 1492.

[47] Marshall, J. M. Carrier diffusion in amorphous semiconductor. *Rep. Prog. Phys.* **1986**, 46, 1235-1282.

[48] Mott, N. F.; Davis, E. A.; Street, R. A. States in the gap and recombination in amorphous semiconductors. *Philosophical Magazine* **1975**, 32(5), 961-996.

[49] Urbach, F. The Long-Wavelength Edge of Photographic Sensitivity and of the Electronic Absorption of Solids. *Physical Review* **1953**, 92, 1324.

[50] Tauc, J. Absorption Edge and Internal Electric Fields in Amorphous Semiconductors. *Mat. Res. Bull.* **1970**, 5, 721-730.

[51] Skumanich, A.; Frova, A.; Amer, N. M. Urbach Tail and Gap States in Hydrogenated a-SiC and a-SiGe Alloys. *Solid State Communications* **1985**, 54(7), 597-601.

[52] Drabold, D. A.; Li, Y.; Cai, B.; Zhang, M. Urbach tails of amorphous silicon. *Physical Review B* **2011**, 83, 045201.

[53] Tanaka, K. & Shimakawa, K. **2011**. Amorphous Chalcogenide Semiconductors and Related Materials. New York: Springer Science+Business Media, LLC.

[54] Grundmann, M. **2006**. The Physics of Semiconductors: An Introduction Including Devices and Nanophysics. Germany: Springer-Verlag Berlin Heidelberg.

[55] Pan, Y.; Inam, F.; Zhang, M.; Drabold, D. A. Atomistic Origin of Urbach Tails in Amorphous Silicon. *Physical Review Letters* **2008**, 100, 206403.

[56] Statz, H.; DeMars, G. A.; Davis, Jr., L.; Adams, Jr., A. Surface states on Silicon and Germanium Surfaces. *Physical Review* **1956**, 101(4), 1272.

[57] Kasap, S. & Capper, P. (Eds.) **2006**. Springer Handbook of Electronic and Photonic Materials. USA: Springer Science+Business Media.

[58] Stutzmann, M. The defect density in amorphous silicon. *Philosophical Magazine* **1989**, 60(4), 531-546.

[59] Ikhmayies. S. J.; Ahmad-Bitar, R. N. A study of the optical bandgap energy and Urbach tail of spray-deposited CdS:In thin films. *J. Mater Res Technol.* **2013**, 2(3), 221-227.

[60] Gogineni, C.; Riordan, N. A.; Johnson, S. R.; Lu, X. & Tiedje, T. Disorder and the Urbach edge in dilute bismide GaAsBi. *Appl. Phys. Lett.* **2013**, 103, 041110.

[61] Street, R. A. Luminescence and recombination in hydrogenated amorphous silicon. *Advances in Physics* **1981**, 30(5), 593-676.

[62] Collins, R. W., Paesler, M. A. & Paul, W. The Temperature Dependence of Photoluminescence in a-Si:H alloys. *Solid State Communications* **1980**, 34, 883-836.

[63] Davis, E. A. Optical Absorption, Transport, and Photoconductivity in Amorphous Selenium. *Journal of Non-Crystalline Solids* **1970**, 4, 107-116.

[64] Onsager, L. Initial Recombination of Ions. *Physical Review* **1938**, 54, 554-557.

[65] Luterová, K.; Pelant, I.; Fojtík, P.; Nikl, M.; Gregora, I.; Kočka, J.; Dian, J.; Valenta, J.; Malý, P.; Kudrna, J.; Štěpánek, J.; Poruba, A.; Horváth, P. Visible photoluminescence and electroluminescence in wide-bandgap hydrogenated amorphous silicon. *Philosophical Magazine Part B* **2000**, 80(10), 1811-1832.

[66] Tiedje, T. & Rose, A. A Physical Interpretation of Dispersive Transport in Disordered Semiconductors. *Solid State Communications* **1980**, 37, 49-52.

[67] Seki, K;. Murayama, K.; Tachiya, M. Dispersive photoluminescence decay by geminate recombination in amorphous semiconductors. *Physical Review B* **2005**, 71, 235212.

[68] Ohkita, H. & Ito, S. **2013**. Chapter 5 Exciton and Charge Dynamics in Polymer Solar Cells Studied by Transient Absorption Spectroscopy In Choy, W.C.H. (Ed.), Organic Solar Cells, Green Energy and Technology. London: Springer-Verlag, pp. 128-129.

[69] Leonelli, R. & Brebner, J. L. Evidence for Bimolecular Recombination in the Luminescence Spectra of SrTiO3. *Solid State Communications* **1985**, 54(6), 505-507.

[70] Leonelli, R. & Brebner, J. L. Time-resolved spectroscopy of the visible emission band in strontium titanate. *Physical Review B* **1986**, 33(12) 8649-8656.

[71] Poolton, N. R. J.; Kars, R. H.; Wallinga, J.; Bos, A. J. J. Direct evidence for the participation of band-tails and excited-state tunnelling in the luminescence of irradiated feldspars. *J. Phys.: Condens. Matter* **2009**, 21, 485505.

[72] Seki, K.; Wojcik, M.; Tachiya, M. Dispersive-diffusion-controlled distance-dependent recombination in amorphous semiconductors. *J. Chem. Phys.* **2006**, 124, 044702.

[73] Huntley, D. J. An explanation of the power-law decay of luminescence. *J. Phys. Condens. Matter* **2006**, 18(4), 1359-1365.

[74] Jonscher, A. K. & de Polignac, A. The time dependence of luminescence in solids. *J. Phys. C: Solid State Phys.* **1984**, 17, 6493-6519.

[75] Nelson, J. Diffusion-limited recombination in polymer-fullerene blends and its influence on photocurrent collection. *Physical Review B* **2003**, 67, 155209.

[76] Scher, H. & Montroll, E. W. Anomalous transit-time dispersion in amorphous solids. *Physical Review B* **1975**, 12(6), 2455.

[77] Scher, H.; Shlesinger, M. F.; Bendler, J. T. Time-Scale Invariance in Transport and Relaxation. *Physics Today* **1991**, 44, 1, 26.

[78] Orlowski, T. E. & Scher, H. Picosecond Photoluminescence: A Probe of Band-Tail Thermalization in Amorphous Semiconductors. *Physical Review Letters* **1985**, 54(3), 220-223.

[79] Thejokalyani, N. & Dhoble, S. J. **2014**. Importance of Eco-Friendly OLED Lighting In Virk, H. S. (Ed.), Luminescence Basic Concepts, Applications and Instrumentation. Switzerland: Trans Tech Publications Ltd., pp. 11-14.

[80] Omary, M. A. & Patterson, H. H. **1999**. Luminescence, Theory. USA: Elsevier, pp. 1186-1207.

[81] Kasap, S. O. **2006**. Principles of Electronic Materials and Devices (3rd Ed.). Boston: McGraw-Hill.

[82] Moses, D.; Sinclair, M.; Heeger, A. J. Carrier Photogeneration and Mobility in Polydiacetylene: Fast Transient Photoconductivity. *Physical Review Letters* **1987**, 58(25), 2710.

[83] Ostroverkhova, O. *et. al.* Optical and transient photoconductive properties of pentacene and functionalized pentacene thin films: Dependence on film morphology. *Journal of Applied Physics* **2005**, 98, 033701.

[84] Ostroverkhova, O.; Cooke, D. G.; Shcherbyna, S.; Egerton, R. F.; Hegmann, F. A. Bandlike transport in pentacene and functionalized pentacene thin films revealed by subpicosecond transient photoconductivity measurements. *Physical Review B* **2005**, 71, 035204.

[85] Soci, C.; D. Moses; Xu, Q. - H.; Heeger, A. J. Charge-carrier relaxation dynamics in highly ordered poly(p-phenylene vinylene): Effects of carrier bimolecular recombination and trapping. *Physical Review B* **2005**, 72, 245204.

[86] Morigaki, K. **1999**. Physics of Amorphous Semiconductors. London: World Scientific.

[87] Rudenko, A. I. & Arkhipov, V. I. Drift and diffusion in materials with traps III. Analysis of transient current and transit time characteristics. *Philosophical Magazine B* **1982**, 45(2), 209-226.

[88] Orenstein, J.; Kastner, M. A.; Vaninov, V. Transient photoconductivity and photo-induced optical absorption in amorphous semiconductors. *Philosophical Magazine Part B* **1982**, 46(1), 23-62.

[89] Tiedje, T.; Cebulka, J. M.; Morel, D. L.; Abeles, B. Evidence for Exponential Band Tails in Amorphous Silicon Hydride. *Physical Review Letters* **1981**, 46(21), 1425.

[90] Monroe, D. Hopping in Exponential Band Tails. *Physical Review Letters* **1985**, 54, 146-149.

[91] Jakobs, A. & Kehr, K. W. Theory and simulation of multiple-trapping transport through a finite slab. *Physical Review B* **1993**, 48(12), 8780-8789.

[92] Stoddart, H. A.; Vardeny, Z.; Tauc, J. Transient-photomodulation-spectroscoy studies of carrier thermalization and recombination in a-Si:H. *Physical Review B* **1988**, 38(2), 1362-1377.

[93] Gao, J. **2009**. Charge Carrier Photogeneration and Transport in Pentacene Thin Films (Doctoral dissertation). Retrieved from University of Alberta library.

[94] Dressel, M. & Scheffer, M. Verifying the Drude response. *Ann. Phys. (Leipzig)* **2006**, 15, No. 7-8, 535-544.

[95] Hummel, R. E. **2012**. Electronic Properties of Materials (4th Ed.). USA: Springer, p. 84.

[96] Madelung, O. (Ed.). **1996**. Semiconductors - Basic Data (2nd Rev. Ed.). New York: Springer, p. 29.

[97] Smith, N. V. Classical generalization of the Drude formula for the optical conductivity. *Physical Review B* **2001**, 64, 155106.

[98] Smith, N. V. Memory effects in the magnetotransport properties of the classical Drude metal. *Physical Review B* **2003**, 68, 132406.

[99] Lovrinčić R. & Pucci, A. Infrared optical properties of chromium nanoscale films with a phase transition. *Physical Review B* **2009**, 80, 205404.

[100] Cocker, T. L.; Baillie, D.; Buruma, M.; Titova, L. V.; Sydora, R. D.; Marsiglio, F.; Hegmann, F. A. Microscopic origin of the Drude-Smith model. *Physical Review B* **2017**, 96, 205439.

[101] Cooke, D. G.; MacDonald, A. N.; Hryciw, A.; Wang, J.; Li, Q.; Meldrum, A.; Hegmann, F. A. Transient terahertz conductivity in photoexcited silicon nanocrystal films. *Physical Review B* **2006**, 73, 193311.

[102] Cooke, D. G.; MacDonald, A. N.; Hryciw, A.; Meldrum, A.; Wang, J.; Li, Q.; Hegmann, F. A. Ultrafast terahertz conductivity of photoexcited nanocrystalline silicon. *J Mater Sci: Mater Electron* **2007**, 18, S447-S452.

[103] Titova, L. V.; Cocker, T. L.; Xu, S.; Baribeau, J.-M.; Wu, X.; Lockwood, D. J.; Hegmann, F. A. Ultrafast carrier dynamics and the role of grain boundaries in polycrystalline silicon thin films grown by molecular beam epitaxy. *Semicond. Sci. Technol.* **2016**, 31, 105017.

[104] Cocker, T. L.; Titova, L. V.; Fourmaux, S.; Bandulet, H.-C.; Brassard, D.; Kieffer, J.-C.; El Khakani, M. A.; Hegmann, F. A. Terahertz conductivity of the metal-insulator transition in a nanogranular VO_2 film. *Appl. Phys. Lett.* **2010**, 97, 221905.

[105] Cocker, T. L.; Titova, L. V.; Fourmaux, S.; Holloway, G.; Bandulet, H.-C.; Brassard, D.; Kieffer, J.-C.; El Khakani, M. A.; Hegmann, F. A. Phase diagram of the ultrafast photoinduced insulator-metal transition in vanadium dioxide. *Physical Review B* **2012**, 85, 155120.

[106] Cooke, D. G.; Krebs, F. C.; Jepsen, P. U. Direct Observation of Sub-100 fs Mobile Charge Generation in a Polymer-Fullerene Film. *Physical Review Letters* **2012**, 108, 056603.

[107] Jensen, S. A.; Ulbricht, R.; Narita, A.; Feng, X.; Mullen, K.; Hertel, T.; Turchinovich, D.; Bonn, M. Ultrafast Photoconductivity of Graphene Nanoribbons and Carbon Nanotubes. *Nano. Lett.* **2013**, 13, 5925-5930.

[108] Chattopadhyay, D. & Queisser, H. J. Electron scattering by ionized impurity in semiconductors. *Reviews of Modern Physics* **1981**, 53(4), Part l.

[109] Debye, P. P. & Cornwell, E. M. Electrical Properties of N-type Germanium. *Physical Review* **1954**, 93(4), 693.

[110] Zylbersztein, A. Theory of Low-Temperature Impact Ionization in High-Purity Germanium. *Physical Review* **1962**, 127(3), 744.

[111] Long, D. & Myers, J. Ionized-Impurity Scattering Mobility of Electrons in Silicon. *Physical Review* **1959**, 115(5), 1107.

[112] Nomura, K.; Ohta, H.; Tagaki, A.; Kamiya, T.; Hirano, M.; Hosono, H. Room-temperature fabrication of transparent flexible thin-film transistors using amorphous oxide semiconductors. *Nature* **2004**, 432, 488-492.

[113] Ansari, M. Z. & Khare, N. Thermally activated band conduction and variable range hopping conduction in Cu_2ZnSnS_4 thin films. *Journal of Applied Physics* **2015**, 117, 025706.

[114] Mott, N. F. Conduction in non-crystalline materials. *Philosophical Magazine* **1969**, 19(160), 835-852.

[115] Jonscher, A. K. The 'universal' dielectric response. *Nature* **1977**, 267, 673-679.

[116] Harimochi, H.; Kitagawa, J.; Ishizaka, M.; Kadoya, Y.; Yamanishi, M.; Matsuishi, S.; Hosono, H. Observation of Jonscher law in ac hopping conduction of the electron-doped nanoporous crystal $12CaO{\cdot}7Al_2O_3$ in THz frequency range. *Physical Review B* **2004**, 70, 193104.

[117] Chopra, K. L.; Bahl, S. K. Structural, Electrical, and Optical Properties of Amorphous Germanium Films. *Physical Review B* **1970**, 1, 2545-2556.

[118] Long, A.R. Frequency-dependent loss in amorphous semiconductors. *Advances in Physics* **1982**, 31, 553-637.

[119] Richter, C. & Schmuttenmaer, C.A. Exciton-like trap states limit electron mobility in TiO_2 nanotubes. *Nature Nanotechnology* **2010**, 5, 769-772.

[120] Lunkenheimer, P. & Loidl, A. Response of Disordered Matter to Electromagnetic Fields. *Physical Review Letters* **2003**, 91(20), 207601.

[121] Siegel, P. H. Terahertz Technology. *IEEE Transactions on Microwave Theory and Techniques* **2002**, 50(3), 910-928.

[122] Tonouchi, M. Cutting-Edge Terahertz Technology. *Nat. Photonics* **2007**, 1(2), 97-105.

[123] Mittleman, D. (Ed.). **2003**. Sensing with Terahertz Radiation. Germany: Springer-Verlag Berlin Heidelberg.

[124] Miles, R. E.; Zhang, X. C.; Eisele, H.; Krotkus, A. (Eds.). **2007**. Terahertz Frequency Detection and Identification of Materials and Objects. Netherlands: Springer.

[125] Dhillon, S. S.; Vitiello, M. S.; Linfield, E. H.; Davies, A. G.; Hoffmann, M.; Booske, J.;...Johnston, M. B. The 2017 terahertz science and technology roadmap. *J. Phys. D: Appl. Phys.* **2017**, 50, 043001.

[126] Smye, S. W.; Chamberlain, J. M.; Fitzgerald, A. J.; Berry, E. The Interaction between Terahertz Radiation and Biological Tissue. *Phys. Med. Biol.* **2001**, 46, 101-111.

[127] Grootendorst, M. R.; Fitzgerald, A. J.; De Koning, B.; Santaolalla, A.; Portieri, A.; Van Hemelrijck, M.; Young, M. R.; Owen, J.; Cariati, M.; Pepper, M.; Wallace, V. P.; Pinder, S. E.; Purushotham, A. Use of a Handheld Terahertz Pulsed Imaging Device to Differentiate Benign and Malignant Breast Tissue. *Biomed. Opt. Express* **2017**, 8(6), 2932.

[128] Abraham, E.; Younus, A.; Delagnes, J. C.; Mounaix, P. Non-Invasive Investigation of Art Paintings by Terahertz Imaging. *Appl. Phys. A Mater. Sci. Process.* **2010**, 100(3), 585-590.

[129] Klarskov, P.; Kim, H.; Colvin, V. L.; Mittleman, D. M. Nanoscale Laser Terahertz Emission Microscopy. *ACS Photonics* **2017**, 4 (11), 2676-2680.

[130] Mittleman, D. M. Perspective: Terahertz Science and Technology. *Journal of Applied Physics* **2017**, 122, 230901.

[131] Cocker, T. L.; Jelic, V.; Gupta, M.; Molesky, S. J.; Burgess, J. A. J.; Reyes, G. D. L.; Titova, L. V.; Tsui, Y. Y.; Freeman, M. R.; Hegmann, F. A. An Ultrafast Terahertz Scanning Tunnelling Microscope. *Nat. Photonics* **2013**, 7(8), 620-625.

[132] Lee, Y.-S. **2009**. Principles of Terahertz Science and Technology. New York: Springer Science+Business Media, LLC.

[133] Dexheimer, S. R. (Ed.). **2008**. Terahertz Spectroscopy Principles and Applications. USA: CRC Press.

[134] Schmuttenmaer, C. A. Exploring Dynamics in the Far-Infrared with Terahertz Spectroscopy. *Chem. Rev.* **2004**, 104(4), 1759-1779.

[135] Hwang, H. Y.; Fleischer, S.; Brandt, N. C.; Perkins, B. G.; Liu, M.; Fan, K.; Sternbach, A.; Zhang, X.; Averitt, R. D.; Nelson, K. A. A Review of Non-Linear Terahertz Spectroscopy with Ultrashort Tabletop-Laser Pulses. *J. Mod. Opt.* **2015**, 62(18), 1447-1479.

[136] Lewis, R. A. **2012**. Terahertz Physics. UK: Cambridge University Press.

[137] Hafez, H. A.; Chai, X.; Ibrahim, A.; Mondal, S.; Férachou, D.; Ropagnol, X.; Ozaki, T. Intense Terahertz Radiation and Their Applications. *J. Opt.* **2016**, 18, 093004.

[138] Zelmon, D. E.; Small, D. L.; Jundt, D. Infrared corrected Sellmeier coefficients for congruently grown lithium niobate and 5 mol.% magnesium oxide-doped lithium niobate. *J. Opt. Soc. Am. B* **1997**, 14, 3319-3322.

[139] Marple, D. T. F. Refractive index of ZnSe, ZnTe, and CdTe. *J. Appl. Phys.* **1964**, 35, 539-542.

[140] Ferguson, B. & Zhang, X. C. Materials for terahertz science and technology. *Nature Materials* **2002**, 1, 26-33.

[141] Tamasino, A.; Parisi, A.; Stivala, S.; Livreri, P.; Cino, A. C.; Busacca, A. C.; Peccianti, M.; Morandotti, R. Wideband THz Time Domain Spectroscopy based on Optical Rectification and Electro-Optic Sampling. *Scientific Reports* **2013**, 3, 3116.

[142] Boyd, R. W. **2008**. Nonlinear Optics (3rd Ed.). New York: Elsevier.

[143] Peiponen, K. A.; Zeitler, J. A.; Kuwata-Gonokami, M. (Eds.) Terahertz Spectroscopy and Imaging. USA: Springer.

[144] Gallot, G.; Zhang, J.; McGowan, R. W.; Jeon, T.-I.; Grischkowsky, D. Measurements of the THz absorption and dispersion of ZnTe and their relevance to the electro-optic detection of THz radiation. *Appl. Phys. Lett.* **1999**, 74, 3450.

[145] Hebling, J.; Almási, G.; Kozma, I. Z.; Kuhl, J. Velocity matching by pulse front tilting for large-area THz-pulse generation. *Opt. Express* **2002**, 10, 1161-1166.

[146] Auston, D. H.; Cheung, K. P.; Valdmanis, J. A.; Kleinman, D. A. Cherenkov Radiation from Femtosecond Optical Pulses in Electro-Optic Media. *Physical Review Letters* **1984**, 53(16), 1555-1558.

[147] Wang, Z.; Su, F. H.; Hegmann, F. A. Ultrafast imaging of terahertz Cherenkov waves and transition-like radiation in LiNbO3. *Opt. Express* **2015**, 23(6), 008073.

[148] Wu, Q. & Zhang, X.-C. Free-space electro-optics sampling of mid-infrared pulses. *Appl. Phys. Lett.* **1997**, 71, 1285.

[149] Novikov, M. A.; Stepanov, A. A.; Khyshov, A. A. Electro-Optical Effects in Anisotropic Crystals: I. The Pockels Effect. *Crystallography Reports* **2016**, 61(5), 849-856.

[150] Leitenstorfer, A.; Hunsche, S.; Shah, J.; Nuss, M. C. Detectors and sources for ultrabroadband electro-optic sampling: Experiment and theory. *Appl. Phys. Lett.* **1999**, 74(11), 1516.

[151] Tinkham, M. Energy Gap Interpretation of Experiments on Infrared Transmission through Superconducting Films. *Physical Review* **1956**, 104, 845.

[152] Hoffmann, M. C. & Fülöp, J. A. Intense ultrashort terahertz pulses: generation and applications. *J. Phys. D: Appl. Phys.* **2011**, 44, 083001.

[153] Leitenstorfer, A.; Nelson, K. A.; Reimann, K.; Tanaka, K. Focus on nonlinear terahertz studies. *New J. Phys.* **2014**, 16, 045016.

[154] Ganichev, S. D. & Prettl, W. **2006**. Intense Terahertz Excitation of Semiconductors. New York: Oxford University Press.

[155] Ferry, D. K.; Barker, J. R.; Jacoboni, C. (Eds.). **1980**. Physics of Nonlinear Transport in Semiconductors. New York: Springer.

[156] Makram-Ebeid, S. & Lannoo, M. Electric-Field-Induced Phonon-Assisted Tunnel Ionization from Deep Levels in Semiconductors. *Physical Review Letters* **1982**, 48(18), 1281-1284.

[157] Ganichev, S. D.; Yassievich, I. N.; Perel, V. I.; Ketterl, H.; Prettl, W. Tunneling ionization of deep centers in high-frequency electric fields. *Physical Review B* **2002**, 65, 085203.

[158] Ganichev, S. D. Tunnel ionization of deep impurities in semiconductors induced by terahertz electric fields. *Physica B* **1999**, 273-274, 737-742.

[159] Ganichev, S. D.; Yassievich, I. N.; Prettl, W. Tunnel ionization of deep impurities by far-infrared radiation. *Semicond. Sci. Technol.* **1996**, 11, 679-691.

[160] Nagai, M.; Kamon, Y.; Monowa, Y.; Matsubara, E.; Ashida, M. Coherent transitions between the shallow acceptor levels in germanium using intense THz pulses. *New J. Phys.* **2013**, 15 065012.

[161] Ziemann, E.; Ganichev, S. D.; Prettl, W.; Yassievich, I. N.; Perel, V. I. Characterization of deep impurities in semiconductors by terahertz tunneling ionization. *Journal of Applied Physics* **2000**, 87(8), 3843.

[162] Keldysh, L. V. Ionization in the field of a strong electromagnetic wave. *Soviet Physics JETP* **1965**, 20(5), 1307-1314.

[163] Grojo, D.; Leyder, S.; Delaporte, P.; Marine, W.; Sentis, M.; Utéza, O. Long-wavelength multiphoton ionization inside band-gap solids. *Physical Review B* **2013**, 88, 195135.

[164] Zhao, S.-F.; Liu, L.; Zhou, Z.-X. Multiphoton and tunneling ionization probability of atoms and molecules in an intense laser field. *Optics Communications* **2014**, 313, 74-79.

[165] Long, Z.-J. & Liu, W.-K. Keldysh theory of strong-field ionization. *Can. J. Phys.* **2010**, 88, 227-245.

[166] Watanabe, S.; Minami, N.; Shimano, R. Intense terahertz pulse induced exciton generation in carbon nanotubes. *Opt. Express* **2011**, 19(2), 1528-1538.

[167] Ridley, B. K. **1999**. Quantum Processes in Semiconductors (4th Ed.). Oxford: Clarendon Press.

[168] Kuehn, W.; Gaal, P.; Reimann, K.; Woerner, M.; Elsaesser, T.; Hey, R. Terahertz-induced interband tunneling of electrons in GaAs. *Physical Review B* **2010**, 82, 075204.

[169] Lange, C.; Maag, T.; Hohenleutner, M.; Baier, S.; Schubert, O.; Edwards, E. R. J.; Bougeard, D; Woltersdorf, G; Huber, R. Extremely Nonperturbative Nonlinearities in GaAs Driven by Atomically Strong Terahertz Fields in Gold Metamaterials. *Physical Review Letters* **2014**, 113, 227401.

[170] Landsberg, P. T. Impact ionization and Auger Recombination in Bands. *Solid State Communications* **1972**, 10, 479-482.

[171] Hirori, H.; Shinokita, K.; Shirai, M.; Tani, S.; Kadoya, Y.; Tanaka, K. Extraordinary carrier multiplication gated by a picosecond electric field pulse. *Nature Communications* **2011**, 2(594).

[172] Hoffmann, M. C.; Hebling, J.; Hwang, H. Y.; Yeh, K.-L.; Nelson, K. Impact ionization in InSb probed by terahertz pump-terahertz probe spectroscopy. *Physical Review B* **2009**, 79, 161201(R).

[173] Hoffmann, M. C.; Hebling, J.; Hwang, H. Y.; Yeh, K.-L.; Nelson, K. THz-pump/THz-probe spectroscopy of semiconductors at high field strengths. *J. Opt. Soc. Am. B* **2009**, 26(9), A29-A34.

[174] Razzari, L.; Su, F. H.; Sharma, G.; Blanchard, F.; Ayesheshim, A.; Bandulet, H.-C.; Morandotti, R.; Kieffer, J.-C.; Ozaki, T.; Reid, M.; Hegmann, F. A. Nonlinear ultrafast modulation of the optical absorption of intense few-cycle terahertz pulses in n-doped semiconductors. *Physical Review B* **2009**, 79, 193204.

[175] Jensen, C. E. **2017**. Ultrafast imaging of nonlinear terahertz dynamics in semiconductors (Masters dissertation). University of Alberta.

[176] Al-Naib, I.; Sharma, G.; Dignam, M. M.; Hafez, H.; Ibrahim, A.; Cooke, D. G.; Ozaki, T.; Morandotti, R. Effect of local field enhancement on the nonlinear terahertz response of a silicon-based metamaterial. *Physical Review B* **2013**, 88, 195203.

[177] Su, F. H.; Blanchard, F.; Sharma, G.; Razzari, L.; Ayesheshim, A.; Cocker, T. L.; Titova, L. V.; Ozaki, T.; Kieffer, J.-C.; Morandotti, R.; Reid, M.; Hegmann, F. A. Terahertz pulse induced intervalley scattering in photoexcited GaAs. *Opt. Express* **2009**, 17(12), 9620.

[178] Sharma, G.; Al-Naib, I.; Hafez, H.; Morandotti, R.; Cooke, D.G.; Ozaki, T. Carrier density dependence of the nonlinear absorption of intense THz radiation in GaAs. *Opt. Express* **2012**, 20(16), 18016.

[179] Ho, I.-C.; Guo, X.; Zhang, X.-C. Design and performance of reflective terahertz air-biased-coherent-detection for time-domain spectroscopy. *Opt. Express* **2010**, 18, 2872.

[180] Ho, I.-C. & Zhang, X.-C. Driving intervalley scattering and impact ionization in InAs with intense terahertz pulses. *Appl. Phys. Lett.* **2011**, 98, 241908.

[181] Becker, W. **2005**. Advanced Time-Correlated Single Photon Counting Techniques. Germany: Springer.

[182] Iwaszczuk, K.; Cooke, D. G.; Fujiwara, M.; Hashimoto, H.; Jepsen, P. U. Simultaneous reference and differential waveform acquisition in time-resolved terahertz spectroscopy. *Opt. Express* **2009**, 17(24), 21969-21976.

[183] Bond, C. & Pipan, C. How To Align An Off-Axis Parabolic Mirror. *Proc. SPIE 1113, Reflective Optics II* **1989**, October 11.

[184] Liu, Y.; Jiang, S.; Glusac, K.; Powell, D.; Anderson, D.; Schanze, K. Photophysics of Monodisperse Platinum-Acetylide Oligomers: Delocalization in the Singlet and Triplet Excited States. *J. Am. Chem. Soc.* **2002**, 124, 12412-12413.

[185] Ohshita, J.; Matsui, S.; Yamamoto, R.; Mizumo, T.; Ooyama, Y.; Harima, Y.; Murafuji, T.; Tao, K.; Kuramochi, Y.; Kaikoh, T.; Higashimura, H. *Organometallics* **2010**, 29, 3239-3241.

[186] Ly, K. T.; Chen-Cheng, R.-W.; Lin, H.-W.; Shiau, Y.-J.; Liu, S.-H.; Chou, P.-T.; Tsao, C.-S.; Huang, Y.-C.; Chi, Y. Near infrared organic light-emitting diodes with very high external quantum efficiency and radiance. *Nat. Photonics* **2017**, 11, 63-68.

[187] Zhao, Q.; Huang, C.; Li, F. Phosphorescent heavy metal complexes for bioimaging. *Chem. Soc. Rev.* **2011**, 40, 2508-2524.

[188] McClure, D. Triplet-Singlet Transitions in Organic Molecules. Lifetime Measurements of the Triplet State. *The Journal of Chemical Physics* **1949**, 17, 905.

[189] Parke, S. M.; Boone, M. P. and Rivard, E. Marriage of heavy main group elements with π-conjugated materials for optoelectronic applications. *Chem. Commun.* **2016**, 52, 9485-9505.

[190] Morisaki, Y.; Ohashi, K.; Na, H.-S. and Chujo, Y. First Synthesis of the Bismole-Containing Conjugated Polymer. *J. Polym. Sci., Part A: Polym. Chem.* **2006**, 44, 4857-4863.

[191] Miyaura, N. & Suzuki, A. Stereoselective synthesis of arylated (E)-alkenes by the reaction of alk-1-enylboranes with aryl halides in the presence of palladium catalyst. *J. Chem. Soc., Chem. Commun.* **1979**, 0, 866-867.

[192] Uoyama, H.; Goushi, K.; Shizu, K.; Nomura, H.; Adachi, C. Highly efficient organic light-emitting diodes from delayed fluorescence. *Nature* **2012**, 492, 234-238.

[193] Delgado, W. T.; Braun, C. A.; Boone, M. P.; Shynkaruk, O.; Qi, Y.; McDonald, R.;...Rivard, E. Moving Beyond Boron-Based Substituents to Achieve Phosphorescence in Tellurophenes. *ACS Appl. Mater. Interfaces* **2018**, 10(15), 12124-12134.

[194] Matsumoto, T.; Tanaka, K.; Tanaka, K.; Chujo, Y. Synthesis and characterization of heterofluorenes containing four-coordinated group 13 elements: theoretical and experimental analyses and comparison of structures, optical properties and electronic states. *Dalton Trans.* **2015**, 44, 8697-8707.

[195] Castellanos-Gomez, A. Why all the fuss about 2D semiconductors? *Nat. Photonics* **2016**, 10, 202-204.

[196] Franklin, A. D. Nanomaterials in transistors: From high-performance to thin-film applications. *Science* **2015**, 349, aab2750.

[197] Osada, M. & Sasaki, T. Two-dimensional Dielectric Nanosheets: Novel Nanoelectronics From Nanocrystal Building Blocks. *Adv. Mater.* **2012**, 24, 210-228.

[198] Nakano, H.; Tetsuka, H.; Spencer, M. J. S.; Morishita, T. Chemical modification of group IV graphene analogs. Sci. Technol. *Adv. Mater.* **2018**, 19, 78.

[199] Oughaddou, H.; Enriquez, H.; Tchalala, M. R.; Yildirim, H.; Mayne, A. J.; Bendounan, A.; Dujardin, G.; Ali, M. A.; Kara, A. Silicene, a promising new 2D material. *Progress in Surface Science* **2015**, 90, 46-83.

[200] Dávila, M. E.; Xian, L.; Cahangirov, S.; Rubio, A.; Le Lay, G. Germanene: a novel two-dimensional germanium allotrope akin to graphene and silicene. *New Journal of Physics* **2014**, 16, 095002.

[201] Eda, G.; Yamagushi, H.; Voiry, D.; Fujita, T.; Chen, M.; Chhowalla, M. Photoluminescence from Chemically Exfoliated MoS_2. *Nano Lett.* **2011**, 11, 5111-5116.

[202] Kushnir, K.; Wang, M.; Fitzgerald, P. D.; Koski, K. J.; Titova, L.V. Ultrafast Zero-Bias Photocurrent in GeS Nanosheets: Promise for Photovoltaics. *ACS Energy Lett.* **2017**, 2, 1429-1434.

[203] Yu, H.; Helbich, T.; Scherf, L. M.; Chen, J.; Cui, K.; Fässler, T. F.; Rieger, B.; Veinot, J. G. C. Radical-Initiated and Thermally Induced Hydrogermylation of Alkenes on the Surfaces of Germanium Nanosheets. *Chem. Mater.* **2018**, 30, 2274-2280.

[204] Jiang, S.; Butler, S.; Bianco, E.; Restrepo, O. D.; Windl, W.; Goldberger, J. E. Improving the stability and optical properties of germanane *via* one-step covalent methyl-termination. *Nat. Comm.* **2014**, 5, 3389.

[205] Wei, W.; Jacob, T. Strong many-body effects in silicene-based structures. *Physical Review B* **2013**, 88, 045203.

[206] Helbich, T.; Lyuleeva, A.; Höhlein, I. M. D.; Marx, P.; Scherf, L. M.; Kehrle, J.; Fässler, T. F.; Lugli, P.; Rieger, B. Radical-Induced Hydrosilylation Reactions for the Functionalization of Two-Dimensional Hydride Terminated Silicon Nanosheets. *Chem. - A Eur. J.* **2016**, 22(18), 6194-6198.

[207] Okamoto, H.; Sugiyama, Y.; Nakano, H. Synthesis and Modification of Silicon Nanosheets and Other Silicon Nanomaterials. *Chem. Eur. J.* **2011**,17, 9864-9887.

[208] Helbich, T.; Lyuleeva, A.; Ludwig, T.; Scherf, L. M.; Fässler, T. F.; Lugli, P.; Rieger, B. One-Step Synthesis of Photoluminescent Covalent Polymeric Nanocomposites from 2D Silicon Nanosheets. *Adv. Funct. Mater.* **2016**, 26(37), 6711-6718.

[209] Osborn, T. H.; Farajian, A. A.; Pupysheva, O. V.; Aga, R. S.; Lew Yan Voon, L. C. Ab initio simulations of silicene hydrogenation. *Chemical Physics Letters* **2011**, 511, 101-105.

[210] Nakano, H.; Nakano, M.; Nakanishi, K.; Tanaka, D.; Sugiyama, Y.; Ikuno, T.; Okamoto, H.; Ohta, T. Preparation of alkyl-modified silicon nanosheets by hydrosilylation of layered polysilane (Si6H6). *J. Am. Chem. Soc.* **2012**, 134(12), 5452-5455.

[211] Li, F.; Lu, R.; Yao, Q.; Kan, E.; Liu, Y.; Wu, H. Yuan, Y.; Xiao, C.; Deng, K. Geometric and Electronic Structures as well as Thermodynamic Stability of Hexyl-Modified Silicon Nanosheet. *J. Phys. Chem. C* **2013**, 117, 13283-13288.

[212] Wang, R.; Pi, X.; Ni, Z.; Liu, Y.; Yang, D. Density functional theory study on organically surface-modified silicene. *RSC Adv.* **2015**, 5(43), 33831-33837.

[213] Quhe, R.; Fei, R.; Liu, Q.; Zheng, J.; Li, H.; Xu, C.; Ni, Z.; Wang, Y.; Yu, D.; Gao, Z.; Lu, J. Tunable and sizable band gap in silicene by surface adsorption. *Scientific Reports* **2012**, 2, 853.

[214] Voon, L.C.L.Y.; Zhu, J.; Schwingenschlögl, U. Silicene: Recent theoretical advances. *Appl. Phys. Rev.* **2016**, 8, 040802.

[215] Liu, Y.; Shu, H.; Liang, P.; Cao, D.; Chen, X.; Lu, W. Structural, Electronic, and Optical Properties of Hydrogenated Few-Layer Silicene: Size and Stacking Effects. *Journal of Applied Physics* **2013**, 114(9), 094308.

[216] Zhang, P.; Li, X. D.; Hu, C. H.; Wu, S. Q.; Zhu, Z. Z. First-principles studies of the hydrogenation effects in silicene sheets. *Phys. Lett. Sect. A Gen. At. Solid State Phys.* **2012**, 376(14), 1230-1233.

[217] Lebègue, S.; Klintenberg, M.; Eriksson, O.; Katsnelson, M. I. Accurate electronic band gap of pure and functionalized graphane from GW calculations. *Physical Review B* **2009**, 79, 245117.

[218] Haberer D.; Vyalikh, D. V.; Taioli, S.; Dora, B.; Farjam, M.; Fink, J.; Marchenko, D.; Pichler, T.; Ziegler, K. Simonucci, S.; Dresselhaus, M. S.; Knupfer, M.; Büchner, B.; Grüneis, A. Tunable Band Gap in Hydrogenated Quasi-Free-Standing Graphene. *Nano Lett.* **2010**, 10, 3360-3366.

[219] Kolobov, A. V. & Tominaga, J. **2016**. Two-Dimensional Tranistion-Metal Dichalcogenides. Switzerland: Springer International Publishing, p. 14.

[220] Nakano, H.; Mitsuoka, T.; Harada, M.; Horibuchi, K.; Nozaki, H.; Takahashi, N.; Nonaka, T.; Seno, Y.; Nakamura, H. Soft synthesis of single-crystal silicon monolayer sheets. *Angew. Chemie - Int. Ed.* **2006**, 45(38), 6303-6306.

[221] Okamoto, H.; Kumai, Y.; Sugiyama, Y.; Mitsuoka, T.; Nakanishi, K.; Ohta, T.; Nozaki, H.; Yamaguchi, S.; Shirai, S.; Nakano, H. Silicon nanosheets and their self-assembled regular stacking structure. *J. Am. Chem. Soc.* **2010**, 132(8), 2710-8.

[222] Okamoto, H.; Sugiyama, Y.; Nakanishi, K.; Ohta, T.; Mitsuoka, T.; Nakano, H. Surface Modification of Layered Polysilane with n-Alkylamines, α, ω-Diaminoalkanes, and ω-Aminocarboxylic Acids. *Chem. Mater.* **2015**, 27(4), 1292-1298.

[223] Ohshita, J.; Yamamoto, K.; Tanaka, D.; Nakashima, M.; Kunugi, Y.; Ohashi, M.; Nakano, H. Preparation and Photocurrent Generation of Silicon Nanosheets with Aromatic Substituents on the Surface. *J. Phys. Chem. C* **2016**, 120, 10991-10996.

[224] Helbich, T.; Lyuleeva, A.; Marx, P.; Scherf, L. V.; Purkait, T. K.; Fässler, T. F.; Lugli, P.; Veinot, J. G. C.; Rieger, B. Lewis Acid Induced Functionalization of Photoluminescent 2D Silicon Nanosheets for the Fabrication of Functional Hybrid Films. *Adv. Funct. Mater.* **2017**, 27(21), 1606764.

[225] Lyuleeva, A.; Helbich, T.; Rieger, B.; Lugli, P. Polymer-silicon nanosheet composites: bridging the way to optoelectronic applications. *J. Phys. D. Appl. Phys.* **2017**, 50(13), 135106.

[226] Tongay S.; Suh, J.; Ataca, C.; Fan, W.; Luce, A.; Kang, J. S.; Liu. J.; Ko, C.; Raghunathanan, R.; Zhou, J.; Ogletree, F.; Li, J.; Grossman, J. C.; Wu, J. Defects activated photoluminescence in two-dimensional semiconductors: interplay between bound, charged, and free excitons. *Scientific Reports* **2013**, 3, 2657.

[227] Scheuschner, N.; Ochedowski, O.; Kaulitz, A.-M.; Gillen, R.; Schleberger M.; Maultzsch, J. Photoluminescence of freestanding single- and few-layer MoS_2. *Physical Review B* **2014**, 89, 125406.

[228] Furukawa, K.; Fujino, M.; Matsumoto, N. Optical properties of Silicon Network Polymers. *Macromolecules* **1990**, 23(14), 3423-3426.

[229] Abdulraheem, Y.; Gordon, I.; Bearda, T.; Meddeb, H.; Poortmans, J. Optical bandgap of ultra-thin amorphous silicon films deposited on crystalline silicon by PECVD. *AIP Advances* **2014**, 4, 057122.

[230] Kim, S. W.; Lee, J.; Sung, J. H.; Seo, D.; Kim, I.; Jo, M.-H.; Kwon, B. W.; Choi, W. K.; Choi, H.-J. Two-Dimensionally Grown Single- Crystal Silicon Nanosheets with Tunable Visible-Light Emissions. *ACS Nano* **2014**, 8(7), 6556-6562.

[231] Nakano, H.; Ohtani, O.; Mitsuoka, T.; Akimoto, Y.; Nakamura, H. Synthesis of Amorphous Silica Nanosheets and Their Photoluminescence. *J. Am. Ceram. Soc.* **2005**, 88(12), 3522-3524.

[232] Tsybeskov, L.; Vandyshev, Ju. V.; Fauchet, P. M. Blue emission in porous silicon: Oxigen-related photoluminescence. *Physical Review B* **1994**, 49(11), 7821-7824.

[233] Dasog, M.; Yang, Z.; Regli, S.; Atkins, T. M.; Faramus, A.; Singh, M. P.; Muthuswamy, E.; Kauzlarich, S. M.; Tilley, R. D.; Veinot, J. G. C. Chemical Insight into the Origin of Red and Blue Photoluminescence Arising from Freestanding Silicon Nanocrystals. *ACS Nano* **2013**, 7(3), 2676-2685.

[234] Tessler, L. R. & Solomon, I. Photoluminescence of tetrahedrally coordinated a-$Si_{1-x}C_x$:H. *Physical Review B* **1995**, 52, 10962-10971.

[235] Amato, G., Delerue, C. & von Bardeleben, H.-J. (Ed.) **1997**. Structural and Optical Properties of Porous Silicon Nanostructures. Vol. 5, USA: Gordon and Breach Science Publishers, pp. 18-20.

[236] Nunomura, S.; Sakata, I.; Matsubara, K. Electronic properties of ultrathin hydrogenated amorphous silicon. *Appl. Phys. Express* **2017**, 10, 081401.

[237] Venkateshvaran, D.; Nikolka, M.; Sadhanala, A.; Lemaur, V.; Zelazny, M.; Kepa, M.; Hurhangee, M.; Kronemeijer, A. J.; Pecunia, V.; Nasrallah, I.; Romanov, I.; Broch, K.; McCulloch, I.; Emin, D.; Olivier, Y.; Cornil, J.; Beljonne, D.; Sirringhaus, H. Approaching disorder-free transport in high mobility conjugated polymers. *Nature* **2014**, 515, 384-388.

[238] Cody, G. D.; Tiedje, T.; Abeles, B.; Brooks, B.; Goldstein, Y. Disorder and the optical-absorption edge of hydrogenated amorphous silicon. *Physical Review Letters* **1981**, 47(20), 1480-1483.

[239] Street, R. A. **1991**. Hydrogenated Amorphous Silcon. USA: Cambridge University Press, p. 91.

[240] Li, S.; Wu, Y.; Tu, Y.; Wang, Y.; Jiang, T.; Liu, W.; Zhao, Y. Defects in Silicene: Vacancy Clusters, Extended Line Defects, and Di-adatoms. *Scientific Reports* **2015**, 5, 7881.

[241] Yan, J. A.; Stein, R.; Schaefer, D. M. Electron-phonon coupling in two-dimensional silicene and germanene. *Physical Review B* **2013**, 88, 121403(R).

[242] Kim, U.; Kim, I.; Park, Y.; Lee, K.-Y.; Yim, S.-Y.; Park, J.-G.; Ahn, H.-J.; Park, S.-H.; Choi, H.-J. Synthesis of Si nanosheets by a chemical vapor deposition process and their blue emissions. *ACS Nano* **2011**, 5(3), 2176-2181.

[243] De los Reyes, G. B.; Dasog, M.; Na, M.; Titova, L. V.; Veinot, J. G. C.; Hegmann, F. Charge transfer state emission dynamics in blue-emitting functionalized silicon nanocrystals. *Phys. Chem. Chem. Phys.* **2015**, 17, 30125.

[244] Zatryb, G.; Podhorodecki, A.; Misiewicz, J.; Cardin, J.; Gourbilleau, F. On the nature of the stretched exponential photoluminescence decay for silicon nanocrystals. *Nanoscale Res. Lett.* **2011**, 6(1), 106.

[245] Lockwood, R.; Hryciw, A.; Meldrum, A. Nonresonant carrier tunneling in arrays of silicon nanocrystals. *Appl. Phys. Lett.* **2006**, 89, 263112.

[246] Kanemitsu, Y. Photoluminescence spectrum and dynamics in oxidized silicon nanocrystals: A nanoscopic disorder system. *Physical Revew B* **1996**, 53(20), 13525.

[247] Rabouw, F. T.; van der Bok, J. C.; Spinicelli, P.; Mahler, B.; Nasilowski, M.; Pedetti, S.; Dubertret, B.; Vanmaekelbergh, D. Temporary Charge Carrier Separation Dominates the Photoluminescence Decay Dynamics of Colloidal CdSe Nanoplatelets. *Nano Lett.* **2016**, 16(3), 2047-2053.

[248] Wang, X.; Feng, Z.; Shi, J.; Jia, G.; Shen, S.; Zhouab, J.; Li, C. Trap states and carrier dynamics of TiO2 studied by photoluminescence spectroscopy under weak excitation condition. *Phys. Chem. Chem. Phys.* **2010**, 12(26), 7083.

[249] Labastide, J. A.; Baghgar, M.; McKenna, A.; Barnes, M. D. Time- and polarization-resolved photoluminescence decay from isolated polythiophene (P3HT) nanofibers. *J. Phys. Chem. C* **2012**, 116(44), 23803-23811.

[250] Kim, Y.; Cook, S.; Tuladhar, S. M.; Choulis, S. A.; Nelson, J.; Durrant, J. R.; Bradley, D. D. C.; Giles, M.; McCulloch, I.; Ha, C.-S.; Ree, M. A strong regioregularity effect in self-organizing conjugated polymer films and high-efficiency polythiophene: fullerene solar cells. *Nature Materials* **2006**, 5, 197-203.

[251] Leonelli, R. & Brebner, J. L. Time-resolved spectroscopy of the visible emission band in strontium titanate. *Physical Review B* **1986**. 33(12), 8649-8656.

[252] Poolton, N. R. J.; Kars, R. H.; Wallinga, J.; Bos, A. J. J. Direct evidence for the participation of band-tails and excited-state tunnelling in the luminescence of irradiated feldspars. *J. Phys.: Condens. Matter* **2009**, 21, 485505.

[253] Spencer, M. J. S.; Morishita, T.; Snook, I. K. Reconstruction and electronic properties of silicon nanosheets as a function of thickness. *Nanoscale* **2012**, 4(9), 2906-13.

[254] Hegmann, F. A.; Tykwinski, R. R.; Lui, K. P. H.; Bullock, J. E.; Anthony, J. E. Picosecond Transient Photoconductivity in Functionalized Pentacene Molecular Crystals Probed by Terahertz Pulse Spectroscopy. *Physical Review Letters* **2002**, 89(22), 227403.

[255] Street, R. A. (Ed.) **2000**. Technology and Applications of Amorphous Si. New York: Springer-Verlag Berlin Heidelberg.

[256] Cinquanta, E. Getting through the Nature of Silicene: An sp^2-sp^3 Two-Dimensional Silicon Nanosheet. J. Phys. Chem. C 2013, 117, 16719-16724.

[257] Guha, S.; Yang, J.; Williamson, D. L.; Lubianiker, Y.; Cohen, J. D.; Mahan, A. H. Structural, defect, and device behavior of hydrogenated amorphous Si near and above the onset of microcrystallinity. *Appl. Phys. Lett.* **1999**, 74, 1860.

[258] Thiessen, A. N., Ha, M., Hooper, R. W., Yu, H., Oliynyk, A. O., Veinot, J. G. C. and Michaelis, V. K., Silicon Nanoparticles: Are They Crystalline from the Core to the Surface? *Chem. Mater.* **2019**, 31(3), 678-688.

[259] Yesinowski, J. P. Solid-State NMR of Inorganic Semiconductors. In Solid State NMR, Chan, J. C. C. (Ed.) **2012**. Springer Berlin Heidelberg: Berlin, Heidelberg, pp. 229-312.

[260] Bercier, J. J.; Jirousek, M.; Graetzel, M.; Klink, J. J. v. d. Evidence from NMR for Temperature-Dependent Bardeen-Friedel Oscillations in Nanometre-Sized Silver Particles. *J. Phys.: Conden. Matter* **1993**, 5, L571-L576.

[261] Charles, R. J.; Harrison, W. A. Size Effect in Nuclear Magnetic Resonance. *Phys. Rev. Lett.* **1963**, 11, 75-77.

[262] Javadi, M.; Michaelis, V. K.; Veinot, J. G. C. Thermally-Induced Evolution of 'Ge(OH)2': Controlling the Formation of Oxide-Embedded Ge Nanocrystals. *J. Phys. Chem. C* **2018**, 122(30), 17518-17525.

[263] Cadars, S.; Smith, B. J.; Epping, J. D.; Acharya, S.; Belman, N.; Golan, Y.; Chmelka, B. F. Atomic Positional Versus Electronic Order in Semiconducting ZnSe Nanoparticles. *Phys. Rev. Lett.* **2009**, 103, 136802.

[264] Mobarok, M. H.; Luber, E. J.; Bernard, G. M.; Peng, L.; Wasylishen, R. E.; Buriak, J. M. Phase-Pure Crystalline Zinc Phosphide Nanoparticles: Synthetic Approaches and Characterization. *Chem. Mater.* **2014**, 26, 1925-1935.

[265] Ratcliffe, C. I.; Yu, K.; Ripmeester, J. A.; Badruz Zaman, M.; Badarau, C.; Singh, S. Solid State NMR Studies of Photoluminescent Cadmium Chalcogenide Nanoparticles. *Phys. Chem. Chem. Phys.* 2006, 8, 3510-3519.

[266] Tomaselli, M.; Yarger, J. L.; Bruchez, M.; Havlin, R. H.; deGraw, D.; Pines, A.; Alivisatos, A. P. NMR Study of InP Quantum Dots: Surface Structure and Size Effects. *J. Chem. Phys.* **1990**, 110, 8861-8864.

[267] Marbella, L. E. & Millstone, J. E. NMR Techniques for Noble Metal Nanoparticles. *Chem. Mater.* **2015**, 27, 2721-2739.

[268] MacKenzie, K. J. D. & Smith, M. E. Multinuclear Solid-State NMR of Inorganic Materials. **2002**. Oxford: Elsevier Science, pp. 201-268.

[269] Smith, J. V. & Blackwell, C. S. Nuclear Magnetic Resonance of Silica Polymorphs. *Nature* **1983**, 303, 223.

[270] Pines, A.; Gibby, M. G.; Waugh, J. S. Proton-Enhanced Nuclear Induction Spectroscopy. A Method for High Resolution NMR of Dilute Spins in Solids. *J. Chem. Phys.* **1972**, 56, 1776-1777.

[271] Bennet, A. E.; Rienstra, C. M.; Auger, M.; Lakshmi, K. V.; Griffin, R. G. Heteronuclear Decoupling in Rotating Solids. *J. Chem. Phys.* **1995**, 103, 6951-6958.

[272] Hayashi, S. & Hayamizu, K. Chemical Shift Standards in High-Resolution Solid-State NMR ^{1}3C, ^{29}Si, and ^{1}H Nuclei. *Bull. Chem. Soc. Jpn.* **1991**, 64, 685-687.

[273] Othonos, A. Probing Ultrafast Carrier and Phonon Dynamics in Semiconductors. *Journal of Applied Physics* **1998**, 83(4), 1789-1830.

[274] Ferry, D. K. First-order optical and intervalley scattering in semiconductors. *Physical Review B* **1976**, 14(4), 1605.

[275] Khan, F. S. & Allen, P. B. Deformation potentials and electron-phonon scattering: Two new theorems. *Physical Review B* **1984**, 29(6), 3341.

[276] Guillaume, C. B. & Voos, M. Electron-Hole Drops in Pure Ge. *Physical Review B* **1973**, 7(4), 4, 1724-1727.

[277] Klingenstein, W.; Schweizer, H. Direct Gap Recombination in Germanium at High Excitation Level and Low Temperature. *Solid State Electron.* **1978**, 21(11-12), 1371-1374.

[278] Martin, R. W.; Stormer, H. L.; Ruhle, W.; Bimberg, D. Photoluminescence of Electron-Hole Drops in Germanium at High Magnetic Fields. *Journal of Luminescence* **1976**, 12(13), 645 649.

[279] Wagner, J.; Vina, L. Radiative recombination in heavily doped p-type germanium. *Physical Review B* **1984**, 30(12), 7030-7036.

[280] Lieten, R. R.; Bustillo, K.; Smets, T.; Simoen, E.; Ager III, J. W.; Haller, E. E.; Locquet, J.-P. Photoluminescence of bulk germanium. *Physical Review B* **2012**, 86, 035204.

[281] El Kurdi, M.; Kociniewski, T.; Ngo, T.-P.; Boulmer, J.; Débarre, D.; Boucaud, P.; Damlencourt, J. F.; Kermarrec, O.; Bensahel, D. Enhanced Photoluminescence of Heavily *n*-Doped Germanium. *Appl. Phys. Lett.* **2009**, 94, 191107.

[282] Sun, X.; Liu, J.; Kimerling, L. C.; Michel, J. Direct Gap Photoluminescence of n-Type Tensile-Strained Ge-on-Si. *Appl. Phys. Lett.* **2009**, 95, 011911.

[283] El Kurdi, M.; Bertin, H.; Martincic, E.; de Kersauson, M.; Fishman, G.; Sauvage, S.; Bosseboeuf, A.; Boucaud, P. Control of Direct Band Gap Emission of Bulk Germanium by Mechanical Tensile Strain. *Appl. Phys. Lett.* **2010**, 96, 041909.

[284] Cheng, T.-H.; Ko, C.-Y.; Chen, C.-Y.; Peng, K.-L.; Luo, G.-L.; Liu, C. W.; Tseng, H.-H. Competitiveness between Direct and Indirect Radiative Transitions of Ge. *Appl. Phys. Lett.* **2010**, 96, 091105.

[285] Kawamura, Y.; Huang, K. C. Y.; Thombare, S. V.; Hu, S.; Gunji, M.; Ishikawa, T.; Brongersma, M. L.; Itoh, K. H.; McIntyre, P. C. Direct-Gap Photoluminescence from Germanium Nanowires. *Phys. Rev. B - Condens. Matter Mater. Phys.* **2012**, 86, 035306.

[286] Hashemi, F. S. M.; Thombare, S.; Morral, A. F. I.; Brongersma, M. L.; McIntyre, P. C. Effects of Surface Oxide Formation on Germanium Nanowire Band-Edge Photoluminescence. *Appl. Phys. Lett.* **2013**, 102, 251122.

[287] Boztug, C.; Sánchez-Pérez, J. R.; Sudradjat, F. F.; Jacobson, R. B.; Paskiewicz, D. M.; Lagally, M. G.; Paiella, R. Tensilely Strained Germanium Nanomembranes as Infrared Optical Gain Media. *Small* **2013**, 9(4), 622-630.

[288] Süess, M. J.; Geiger, R.; Minamisawa, R. A.; Schiefler, G.; Frigerio, J.; Chrastina, D.; Isella, G.; Spolenak, R.; Faist, J.; Sigg, H. Analysis of Enhanced Light Emission from Highly Strained Germanium Microbridges. *Nat. Photonics* **2013**, 7(6), 466-472.

[289] Shimura, T.; Matsue, M.; Tominaga, K,; Kajimura, K.; Amamoto, T.; Hosoi, T.; Watanabe, H. Enhancement of photoluminescence from n-type tensile-strained GeSn wires on an insulator fabricated by lateral liquid-phase epitaxy. *Appl. Phys. Lett.* **2015**, 107, 221109.

[290] Kondo, K.; Makihara, K.; Ikeda, M.; Miyazaki, S. Photoluminescence Study of High Density Si Quantum Dots with Ge Core. *Journal of Applied Physics* **2016**, 119, 033103.

[291] Lee, L. Y. T.; Watanabe, Y.; Nishi, Y. Increased photoluminescence from single-mode microwave annealing of N-type Ge-on-Si. *Appl. Phys. Lett.* **2016**, 108, 112105.

[292] Xu, C.; Gallagher, J. D.; Senaratne, C. L.; Menéndez, J.; Kouvetakis, J. Optical properties of Ge-rich $Ge_{1-x}Si_x$ alloys: Compositional dependence of the lowest direct and indirect gaps. *Physical Review B* **2016**, 93(12), 125206.

[293] Bollani, M.; Giliberti, V.; Sakat, E.; Baldassarre, I.; Celebranoc, M.; Frigerio, J.; Isella, G.; Finazzi, M.; Melli, M.; Weber-Bargioni, A.; Cabrini, S.; Biagioni, P.; Ortolani, M. Photoluminescence Emission from a Nanofabricated Scanning Probe Tip Made of Epitaxial Germanium. *Microelectron. Eng.* **2016**, 159, 164-168.

[294] Joyce, W. B. & Dixon, R. W. Analytic approximations for the Fermi energy of an ideal Fermi gas. *Appl. Phys. Lett.* **1977**, 31, 354.

[295] Urbanociwz, A.; Adomavičius, R.; Krotkus, A. Terahertz emission from photoexcited surfaces of Ge crystals. *Physica B* **2005**, 367, 152-157.

[296] Hebling, J.; Hoffman, M. C.; Hwang, H. Y.; Yeh, K.-L.; Nelson, K. A. Observation of nonequilibrium carrier distribution in Ge, Si, and GaAs by terahertz pump-terahertz probe measurements. *Physical Review B* **2010**, 81, 035201.

[297] Tanaka, K.; Ohtake, H.; Suemoto, T. Determination of Intervalley Scattering Time in Germanium by Subpicosecond Time-Resolved Raman Spectroscopy. *Physical Review Letters* **1993**, 71, 1935-1938.

[298] Arguirov, E.; Kittler, M.; Abrosimov, N. V. Room temperature luminescence from Germanium. *Journal of Physics: Conference Series* **2011**, 281, 012021.

[299] van Driel, H. M.; Elci, A.; Bessey, J. S.; Scully, M. O. Photoluminescence Spectra of Germanium at High Excitation Intensities. *Solid State Communications* **1976**, 20, 837-840.

[300] Katahara, J. K.; Hillhouse, H. W. Quasi-Fermi level splitting and sub-bandgap absorptivity from semiconductor Photoluminescence. *Journal of Applied Physics* **2014**, 116, 173504.

[301] Burnstein, E. Anomalous Optical Absorption Limit in InSb. *Physical Review* **1954**, 93, 632.

[302] Jain, S. C. & Roulstonm D. J. A Simple Expression for Band Gap Narrowing (BGN) in heavily doped Si, Ge, GaAs and Ge_xSi_{1-x} Strained Layers. *Solid State Electronics* **1991**, 34(5), 453-465.

[303] Lindle, J. R.; Moss, S. C.; Smirl, A. L. Effects of parametric scattering, energy-gap narrowing, and state filling on the picosecond optical response of germanium. *Physical Review B* **1979**, 20(6), 2401.

[304] Saw, K. G.; Aznan, N. M.; Yam, F. K,; Ng, S. S.; Pung, S. Y. New Insights on the Burstein-Moss Shift and Band Gap Narrowing in Indium-Doped Zinc Oxide Thin Films. *PLoS One* **2018**, 10(10), e0141180.

[305] Jain, A.; Sagar, P.; Mehra, R. M. Band gap widening and narrowing in moderately and heavily doped n-ZnO films. *Solid-State Electronics* **2006**, 50, 1420-1424.

[306] Brill, P. & Schwarz, R. Radiative Recombination in Germanium. *Physical Review* **1958**, 112, 2, 330-333.

[307] Conradt, R. & Aengenheister, J. Minority Carrier Lifetime In Highly Doped Ge. *Solid State Communications* **1972**, 10, 321-323.

[308] Huldt, L. Phonon-Assisted Auger Recombination in Germanium. *Phys. Stat. Sol. (a)* **1976**, 33, 607.

[309] Gaubas, E. & Vanhellemont, J. Dependence of carrier lifetime in germanium on resisitivity and carrier injection level. *Appl. Phys. Lett.* **2006**, 89, 142106.

[310] Moss, T. S. & Hawkins, T. D. H. Interband Photoconductivity in Germanium. *Proc. Phys. Soc.* **1960**, 76, 565.

[311] Alberding, B. G.; Thurber, W. R.; Heilweil, E. J. Direct comparison of time-resolved terahertz spectroscopy and Hall Van der Pauw methods for measurement of carrier conductivity and mobility in bulk semiconductors. *Journal of the Optical Society of America B* **2017**, 34(7), 1392.

[312] McLean, T. P. & Paige, S. A Theory of the Effects of Carrier-Carrier Scattering on Mobility of Semiconductors. *J. Phys. Chem. Solids.* **16**, 220-263.

[313] Feng, T. & Ruan, X. Quantum mechanical prediction of four-phonon scattering rates and reduced thermal conductivity of solids. *Physical Review B* **2016**, 93, 045202.

[314] Cuttriss, D. B. Relation Between Surface Concentration and Average Conductivity in Diffused Layers in Germanium. *Bell System Technical Journal* **1961**, 40(2), 509 - 521.

[315] Prince, M. B. Drift Mobilities in Semiconductors. I. Germanium. *Physical Review* **1953**, 92(3), 681.

[316] Morin, F. J. Lattice-Scattering Mobility in Germanium. *Physical Review* **1954** 93(1), 62-63.

[317] McLean, T. P. & Paige, S. Electron-Hole Scattering and Minority Carrier Mobility in Germanium. *J. Phys. Chem. Solids.* **1961**, 18(2/3), 139-149.

[318] Jordan, C.; Donegan, J. F.; Hegarty, J.; Roycroft, B. J.; Taniguchi, S.; Hino, T.; Kato, E.; Noguchi, N.; Ishibashi, A. Carrier-density dependence of the photoluminescence lifetimes in ZnCdSe/ZnSSe quantum wells at room temperature. *Appl. Phys. Lett.* **1999**, 74(22), 3359.

[319] Kumar, N.; He, D.; Wang, Y.; Zhao, H. Charge carrier dynamics in bulk MoS2 crystal studied by transient absorption microscopy. *Journal of Applied Physics* **2013**, 113, 133702.

[320] Schäffer, F. High-mobility Si and Ge structures. *Semicond. Sci. Technol.* **1997**, 12, 1515-1549.

[321] Soref, R. Mid-infrared photonics in silicon and germanium. *Nature Photonics* **2010**, 4, 495-497.

[322] Prasankumar, R.P.; Choi, S.; Trugman, S.A.; Picraux, S.T., and A.J. Taylor. Ultrafast Electron and Hole Dynamics in Germanium Nanowires. *Nano Lett.* **2008**, 8, 1619-1624.

[323] Strait, J.H.; George, P.A.; Levendorf, M.; Blood-Forsythe, M.; Rana, F.; Park, J. Measurements of the Carrier Dynamics and Terahertz Response of Oriented Germanium Nanowires using Optical-Pump Terahertz-Probe Spectroscopy. *Nano Lett.* **2009**, 9, 2967-2972.

[324] Li, Y.; Clady, R.; Marshall, A. N.; Park, J.; Thombare, S. V.; Chan, G.; Schmidt, T. W.; Brongersma, M. L.; McIntyre, P. C. Ultrafast Carrier Dyamics of a Photo-Excited Germanium Nanowire-Air Metamaterial. *ACS Photonics* **2015**, 2, 1091-1098.

[325] Purkait, T. K.; Swarnakar, A. K., De Los Reyes, G. B.; Hegmann, F. A.; Rivard, E.; Veinot, J. G. C. One-pot synthesis of functionalized germanium nanocrystals from a single source precursor. *Nanoscale* **2015**, 7, 2241.

[326] Sun, D.; Riley, A. E.; Cadby, A. J.; Richman, E. K., Korlann, S. D.; Tolbert, S. H. Hexagonal nanoporous germanium through surfactant-driven self-assembly of Zintl clusters. *Nature* **2006**, 441, 1126-1130.

[327] Bentlohner, M. M.; Waibel, M.; Zeller, P.; Sarkar, K.; Müller-Buschbaum, P.; Fattakhova-Rohlfing, D.; Fässler, T.F. Zintl Clusters as Wet-Chemical Precursors for Germanium Nanomorphologies with Tunable Composition. *Angewandte Chemie* **2016**, 128, 2487-2491.

[328] Armatas, G.S. and Kanatzidis, G. Hexagonal Mesoporous Germanium. *Science* **2006**, 313, 5788, 817-820.

[329] Zao, X.; Conradsson, T.; Klingstedt, M.; Dadachov, M. S.; OâĂŹKeeffe, M. A mesoporous germanium oxide with crystalline pore walls and its chiral derivative. *Nature* **2005**, 437, 716-719.

[330] Ngo, D. T.; Le, H. T. T.; Kim, C.; Lee, J.-Y.; Fisher, J. G.; Kim, I.-L.; Park, C.-J. Mass-scalable synthesis of 3D porous germanium-carbon composite particles as an ultra-high rate anode for lithium ion batteries. *Energy Environ. Sci.* **2015**, 8, 3577-3588.

[331] Park, M.-H.; Kim, K.; Kim, J.; Cho, J. Flexible Dimensional Control of High-Capacity Li-Ion-Battery Anodes: From 0D Hollow to 3D Porous Germanium Nanoparticle Assembles. *Adv. Mater.* **2010**, 22, 415-418.

[332] Geier, S.; Jung, R.; Peters, K.; Gasteiger, H. A.; Fattackhova-Rohlfing, D.; Fässler, T. F. A wet-chemical route for macroporous inverse opal Ge anodes for lithium ion batteries with high capacity retention. *Sustainable Energy Fuels* **2018**, 2, 85-90.

[333] Zhou, L.; Zhao, C.; Giri, B.; Allen, P.; Xu, X.; Joshi, H.; Fan, Y.; Titova, L. V.; Rao, P. High Light Absorption and Charge Sepraration Efficiency at Low Applied Voltage from Sb-doped SnO_2/$BiVO_4$ Core/Shell Nanorod-Array Photoanodes. *Nano Lett.* **2016**, 16, 3463-3474.

[334] LaForge, M.; Cocker, T. L.; Beaudry, A. L.; Cui, K.; Tucker, R. T.; Taschuk, M. T.; Hegmann, F. A.; Brett, M. J. Conductivity control of as-grown branched indium tin oxide nanowire networks. *Nanotechnology* **2014**, 25, 035701.

[335] Lloyd-Hughes, J.; Merchant, S. K. E.; Sirbu, L.; Tiginyanu, I. M.; Johnston, M. B. Terahertz photoconductivity of mobile electrons in nanoporous InP honeycombs. *Physical Review B* **2008**, 78, 085320.

[336] Míguez, H.; Chomski, E.; García-Santamaría, F.; Ibisate, M.; John, S.; López, C.; Meseguer, F.; Mondia, J. P.; Ozin, G. A.; Toader, O.; van Driel, H. M. Photonic Bandgap Engineering in Germanium Inverse Opals by Chemical Vapor Deposition. *Adv. Mater.* **2001**, 13(21), 1634-1637.

[337] Fang, C.; Föll, H.; Cartensen, J. Electrochemical pore etching in germanium. *Journal of Electroanalytical Chemistry* **2006**, 589, 259-288.

[338] Tauc, J.; Grigorovici, R.; Vancu, A. Optical Properties and Electronic Structure of Amorphous Germanium. *Phys. Stat. Sol.* **1966**, 15, 627.

[339] Liu, P.; Longo, P.; Zaslavsky, A.; Pacifici, D. Optical bandgap of single- and multi-layered amorphous germanium ultra-thin films. *Journal of Applied Physics* **2016**, 119, 014304.

[340] Titova, L. V.; Cocker, T. L.; Cooke, D. G.; Wang, X.; Meldrum, A.; Hegmann, F. A. Ultrafast percolative transport dynamics in silicon nanocrystal films. *Physical Review B* **2011**, 83. 085403.

[341] Marshall, J. M.; LeComber, P. G.; Spear, W. E. Comments on the Calculation of the Extended State Electron Mobility in Amorphous Silicon. *Solid State Communications* **1985**, 54(1), 11-14.

[342] Clark, A. H. Electrical and Optical Properties of Amorphous Germanium. *Physical Review* **1967**, 164(3), 750-757.

[343] Watakabe, H.; Sameshima, T.; Kanno, H.; Miyao, M. Electrical properties for poly-Ge films fabricated by pulsed laser annealing. *Thin Solid Films* **2006**, 508, 315-317.

[344] Toko, K.; Yoshimine, R,; Moto, K.; Suemasu, T. High-hole mobility polycrystalline Ge on an insulator formed by controlling precursor atomic density for solid-phase crystallization. *Scientific Reports* **2017**, 7, 16981.

[345] Shinokita, K.; Hirori, H.; Tanaka, K.; Mochizuki, T.; Kim, C.; Akiyama, H.; Pfeiffer, L. N.; West. K. W. Terahertz-Induced Optical Emission of Photoexcited Undoped GaAs Quantum Wells. *Physical Review Letters* **2013**, 111, 067401.

[346] Liu, J.; Kaur, G.; Zhang, X.-C. Photoluminescence quenching dynamics in cadmium telluride and gallium arsenide induced by ultrashort terahertz pulse. *Appl. Phys. Lett.* **2010**, 97, 111103.

[347] Chu, Z.; Liu, J.; Liu, J. Study of THz-wave-induced photoluminescence quenching in GaAs and CdTe. *Appl. Phys. B* **2012**, 109, 113-119.

[348] Clady, R.; Tayebjee, M. J. Y.; Aliberti, P.; König, D.; Ekins-Daukes, N. J.; Conibeer, G. V.; Schmidt, T. W.; Green, M. A. Interplay between the hot phonon effect and intervalley scattering on the cooling rate of hot carriers in GaAs and InP. *Prog. Photovolt: Res. Appl.* **2012**, 20, 82-92.

[349] Leitenstorfer, A.; Hunsche, S.; Shah, J.; Nuss, M. C.; Knox, W. H. Femtosecond Charge Transport in Polar Semiconductors. *Physical Review Letters* **1999**, 82(25), 5140.

[350] Dash, W. C. & Newman, R. Intrinsic Optical Absorption in Single-Crystal Germanium and Silicon at 77 K and 300 K. *Physical Review* **1955**, 99(4).

[351] Jacoboni; C.; Nava, F.; Canali, C.; Ottaviani, G. Electron drift velocity and diffusivity in germanium. *Physical Review B* **1981**, 24(2), 1014-1026.

[352] van Driel, H. M. Influence of hot phonons on energy relaxation of high-density carriers in germanium. *Physical Review B* **1979**, 19(11), 5928-5932.

[353] Kennedy, C. J.; Matter, J. C.; Smirl, A. L.; Weiche, H.; Hopf, F. A.; Pappu, S. V. Nonlinear Absorption and Ultrashort Carrier Relaxation Times in Germanium under Irradiation by Picosecond Pulses. *Physical Review Letters* **1974**, 32(8), 419-421.

[354] Arabshahi, H.; Golafrooz, S. Monte Carlo Based Calculation of Electron Transport Properties in Bulk InAs, AlAs and InAlAs. *Bulg. J. Phys.* **2010**, 37, 215-222.

[355] Allen, P. B. & Cordona, M. Theory of the temperature dependence of the direct gap of germanium. *Physical Review B* **1981**, 23(4), 1495.

APPENDIX A

Supporting information to Chapter 5

A.1 TRPL of GaAs

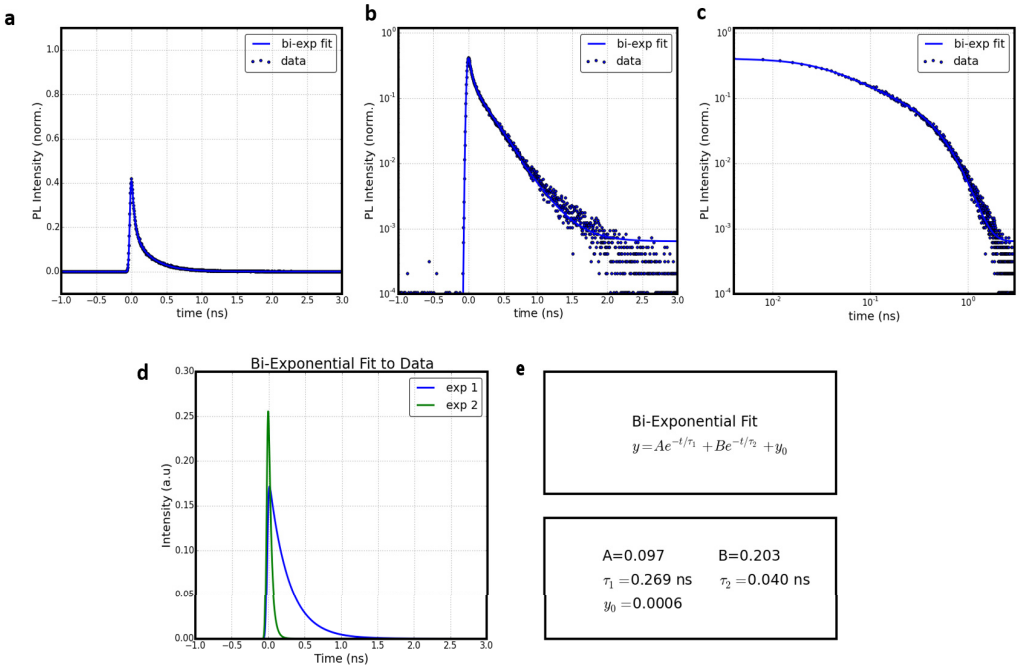

Figure A.1: a) Linear, b) Semi-log, c) Log-log plots of the TRPL of GaAs measured at 885 nm using an optical excitation of 400 nm (blue dots). The solid blue lines corresponds to the convolution fit to a Gaussian function and bi-exponential decay. The Gaussian function provided a time width of 37 ps while the d) bi-exponential decay fit shows d) the lifetime measurements in the nanosecond scale.[1]

[1]TRPL data were measured by M.A.B. Narreto and C. Mannes, and the fits were performed by D. N. Purschke.

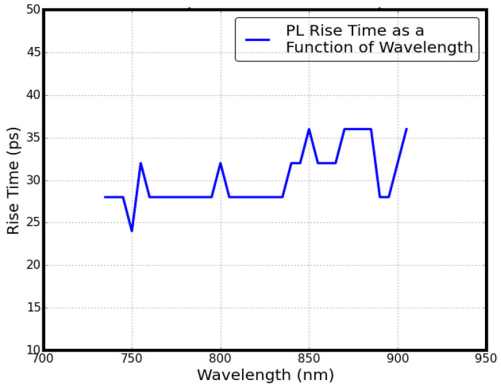

Figure A.2: Wavelength dependence of the instrument response of the TRPL setup using Grating 3 at 200 μm entrance slit taken from the TRPL data of GaAs excited at 400 nm.

A.2 NIR PL Setup

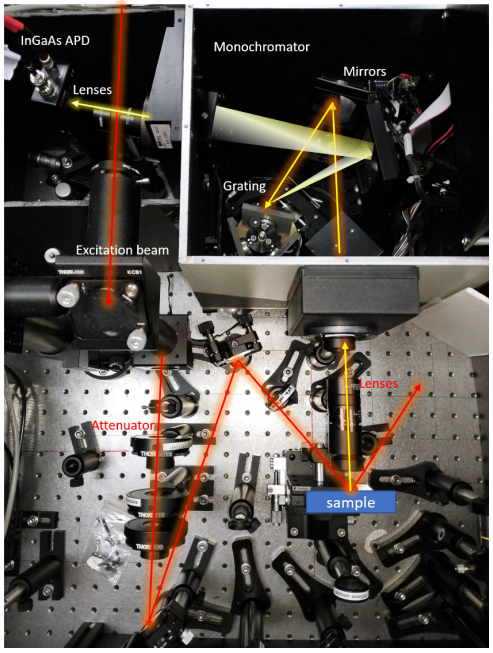

Figure A.3: Image of the NIR PL experimental setup.

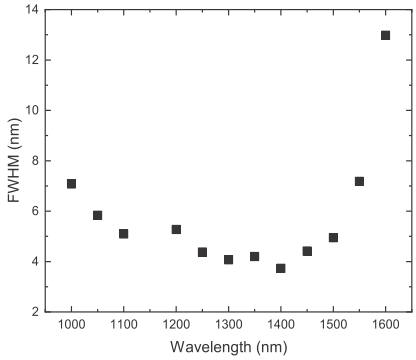

Figure A.4: FWHM of each spectrum measured by an NIR spectrometer (Ocean Optics) as a function of wavelength (that is set using a Labview program that controls the monochromator (Triax 180, Horiba)). The monochromator is set at 2 mm entrance and exit slits. The light source is a tungsten filament at T = 3100 K (Ocean Optics).

A.3 Details of the experimental setup for the intense THz generation and detection

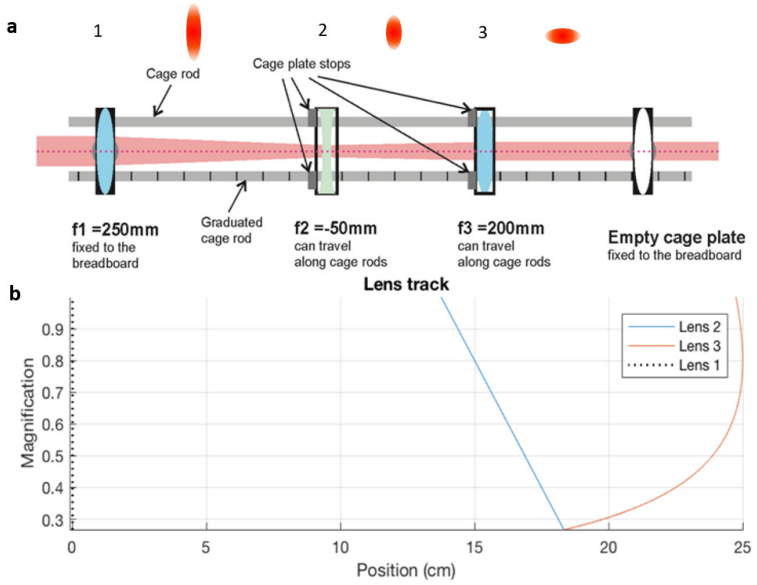

Figure A.5: ***a)*** *Telescope design for the pump beam, which is composed of three cylindrical lenses. The first lens focuses the spherical pump beam into a vertical line. Then the combination of the second and third lenses collimates and reshapes it into a cylindrical horizontal beam.* ***b)*** *At specific distances for the second and third lenses, while maintaining the collimation, a demagnification of the pump beam is obtained in the horizontal dimension.*[2]

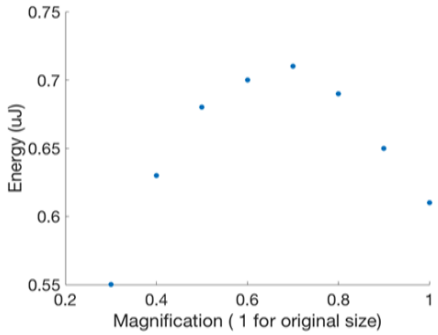

Figure A.6: THz energy as a function of demagnification based on the adjustment of the telescope lenses.[3]

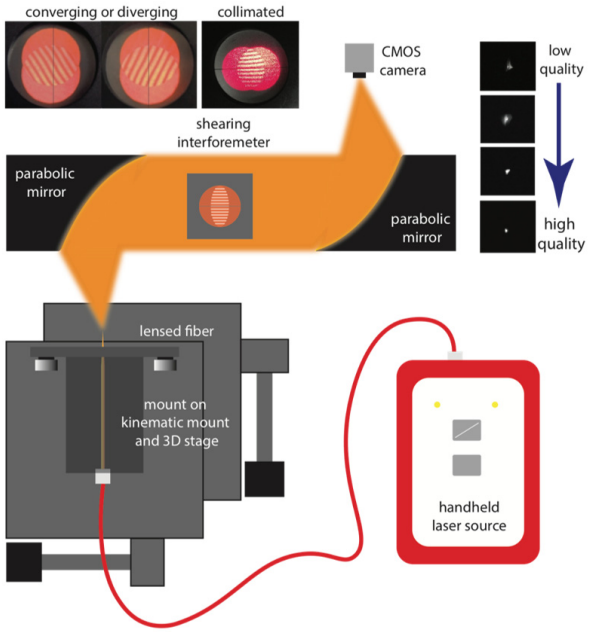

Figure A.8: Alignment procedure for the parabolic mirrors. A handheld laser source at 635 nm (HLS635, Thorlabs) coupled to a single mode optical fiber with a variable attenuator (VOA50-APC, Thorlabs) was used to aid a uniform propagation of coherent light through the parabolic mirrors. The output of the optical fiber was coupled to a bare silica fiber with a core size of 0.5 mm. The end of the silica fiber acts as a point source at the focus of the parabolic mirror for the EO detection (PM5). To ensure that the coherent beam is collimated as it propagates after the parabolic mirror PM5, the beam diameter size was maintained by markers. In addition, a shearing interferometer (SI254, Thorlabs) was used to aid the minute adjustments of the parabolic mirrors by providing a qualitative measure of the light collimation. For the adjustment of the focusing parabolic mirrors, the focused beam was imaged using a CMOS camera (DCC3240M, Thorlabs).

[2]a) Designed by C. Huang and D. N. Purschke and b) Measured by C. Huang
[3]Measured by C. Huang

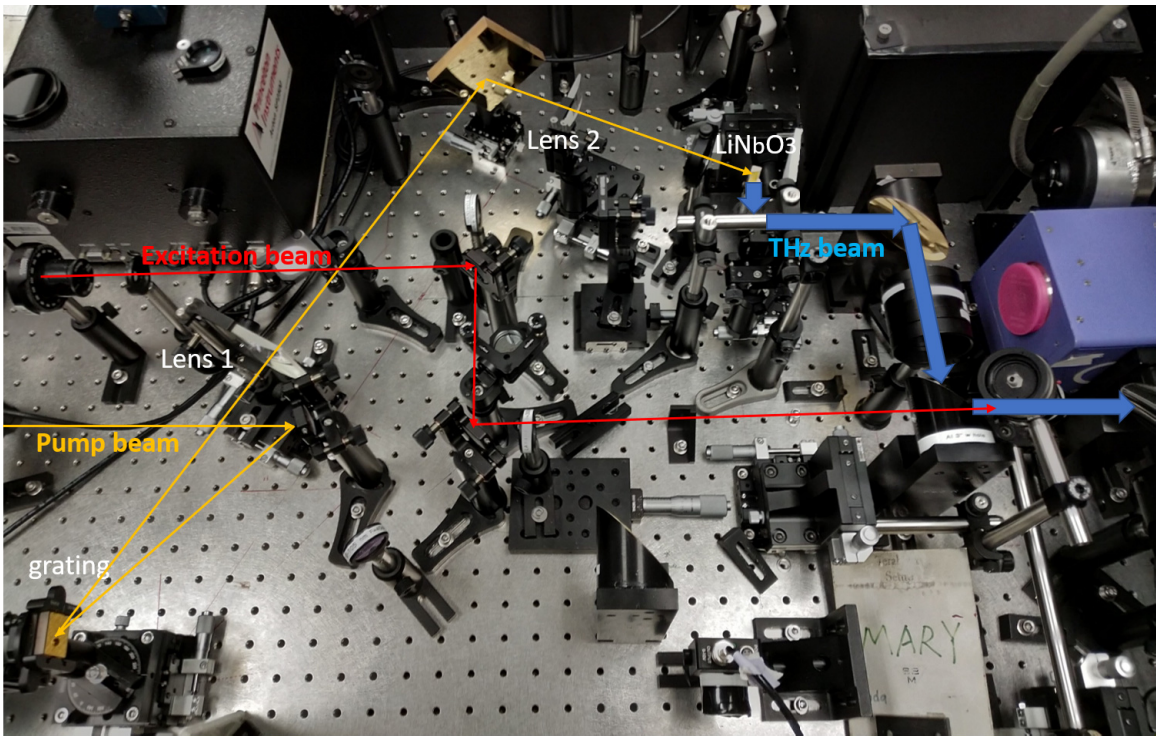

Figure A.9: Picture of the THz source setup.

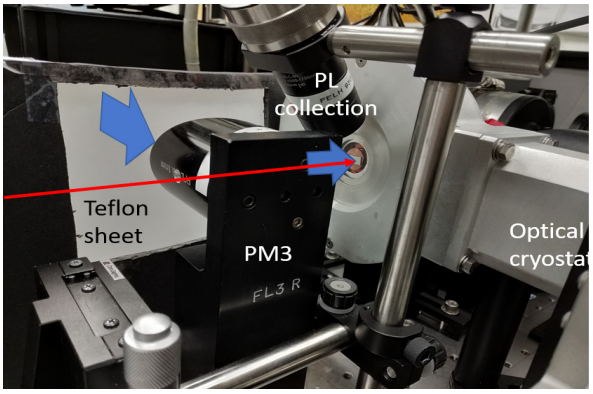

Figure A.10: Picture of the optical cryostat placed after PM3. The red line illustrates the excitation beam path, while the blue arrow represents the THz beam.

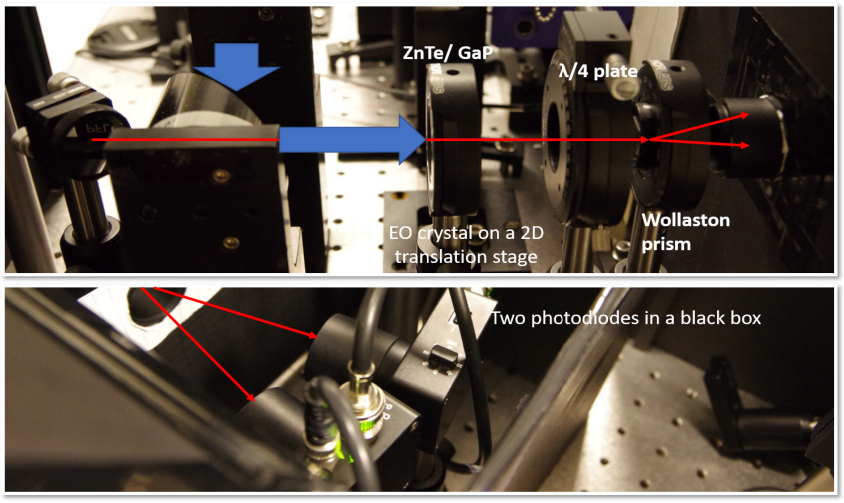

Figure A.11: Picture of the EO setup. The red line illustrates the sampling beam path, while the blue arrow represents the THz beam.

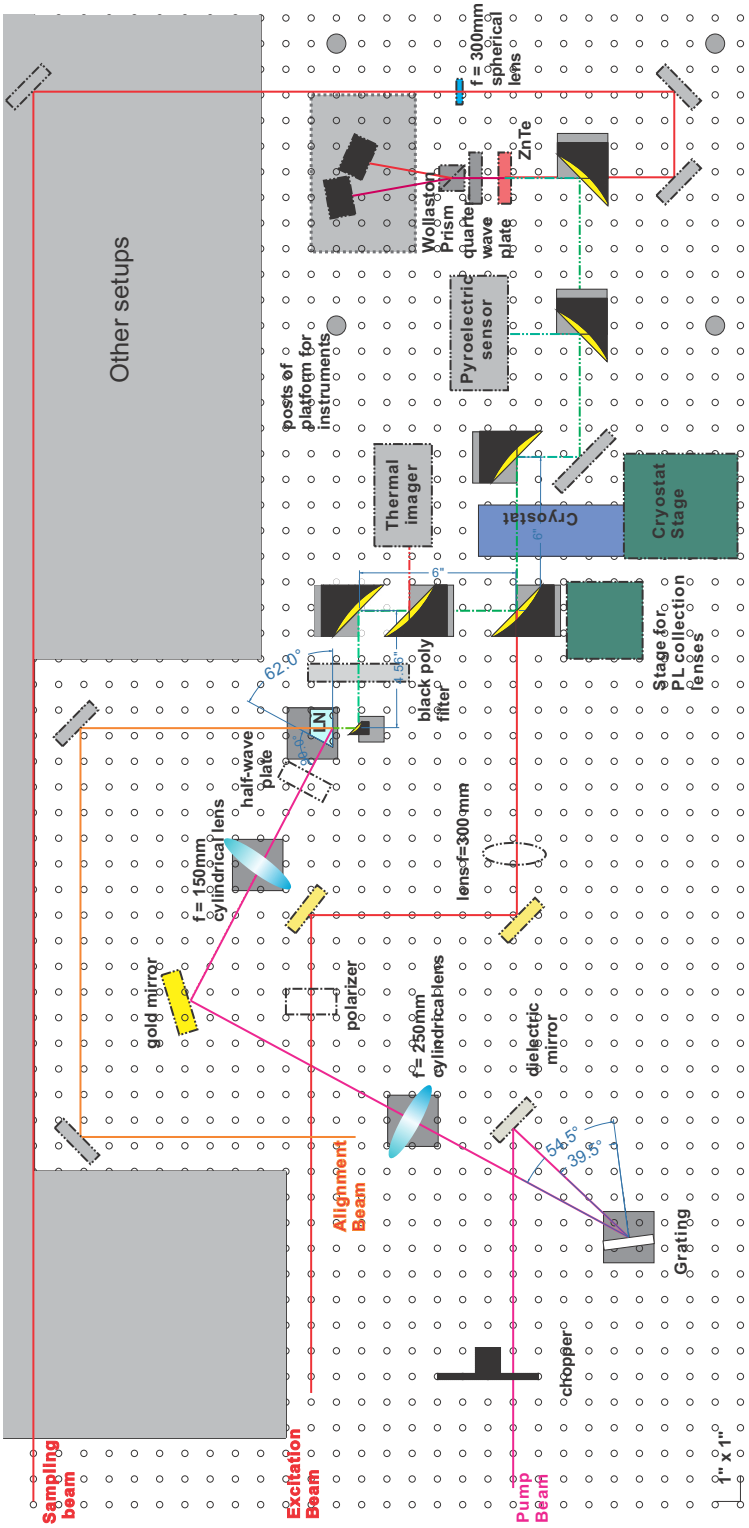

Figure A.7: Schematic diagram of the setup on the optical table. Distances between optical elements are scaled to the 1 inch distances between the screw holes (circles) on the table.

APPENDIX B

Supporting information to Chapter 6

B.1 TIPL and TRPL measurements

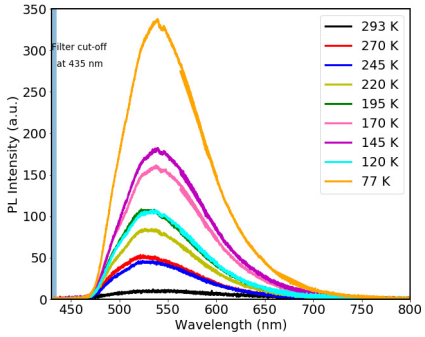

Figure B.1: Low temperature TIPL spectra of Bismole 1.

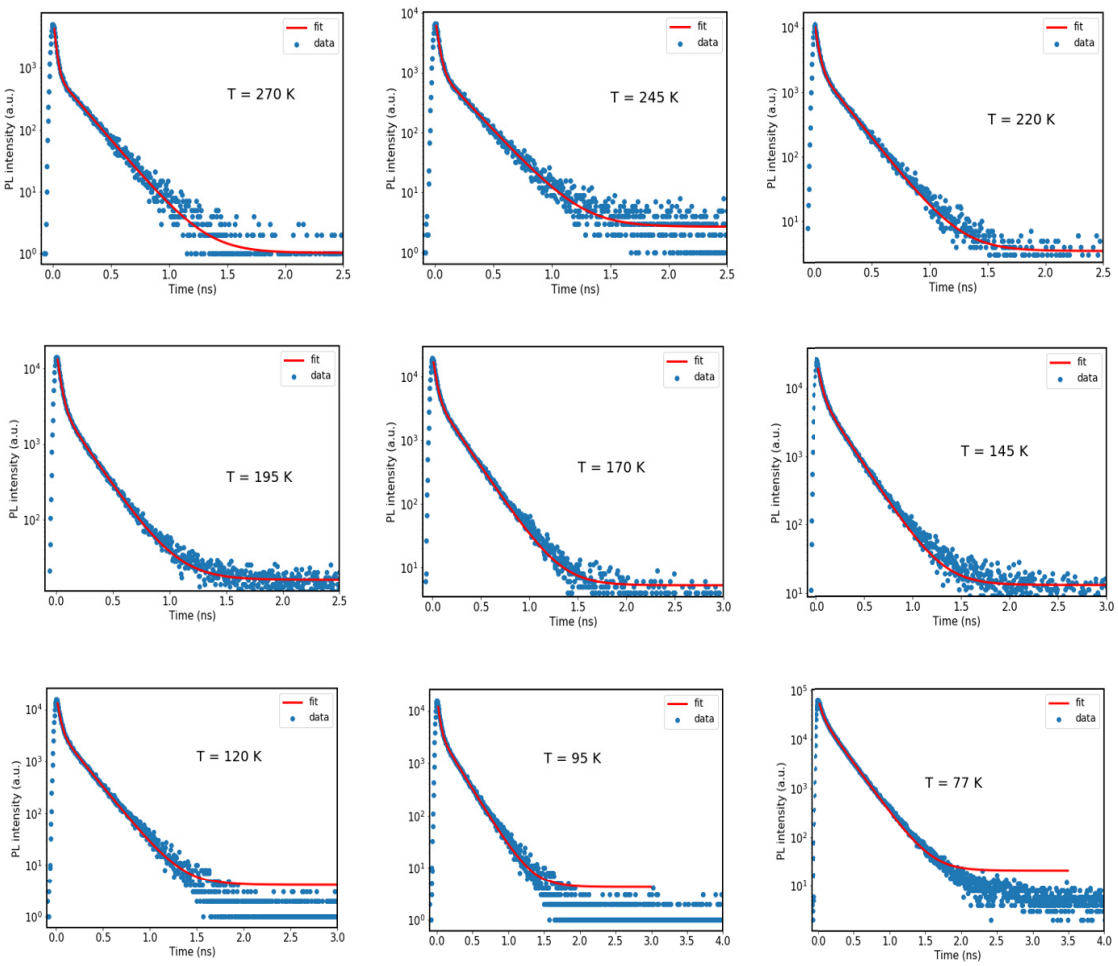

Figure B.2: Low temperature TRPL measurements of Bismole 1 with their correspoding fits to a bi-exponential decay.

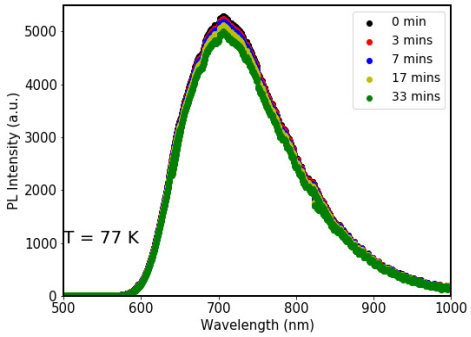

Figure B.3: TIPL spectra of Bismole 3 at T = 77 K measured over time.

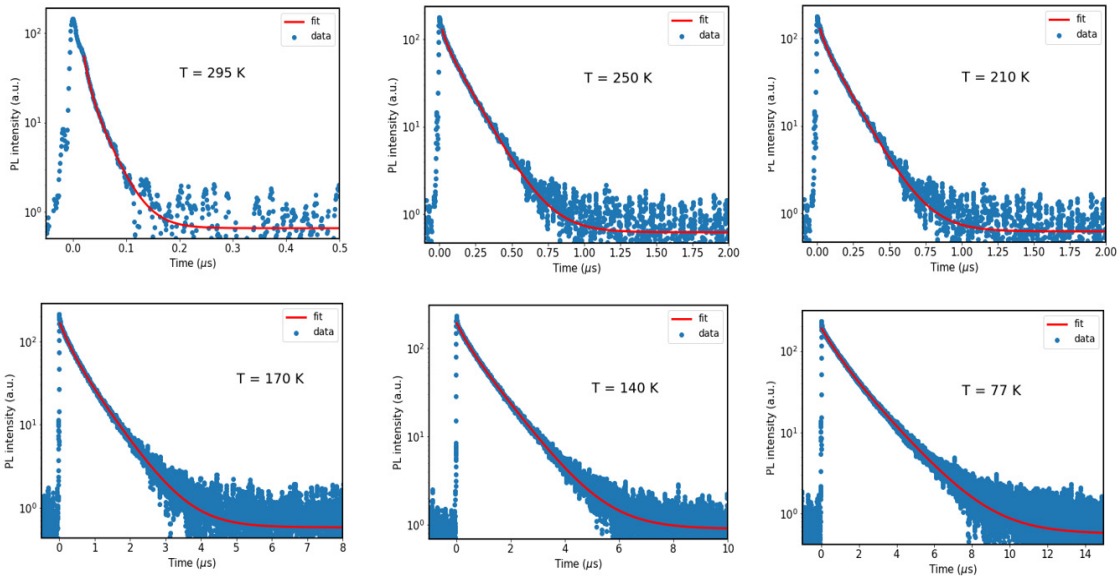

Figure B.4: Low temperature TRPL-μs measurements of Bismole 3 with their correspoding fits to a bi-exponential decay.

B.2 TD-DFT calculations[1]

[1]TD-DFT calculations were performed by E. Hupf

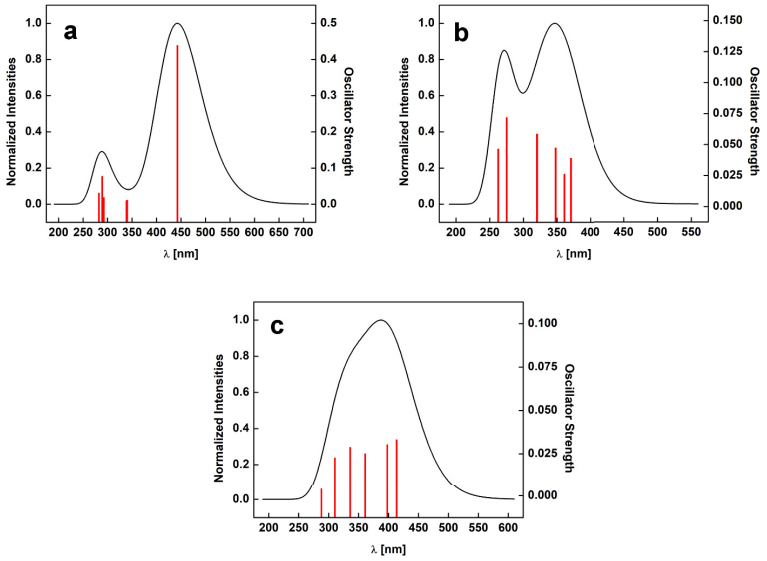

Figure B.5: Calculated UV-vis spectra of a) Bismole 1, b) Bismole 2, and c) Bismole 3 including the six singlet excitation states with the highest oscillator strength (red bars).

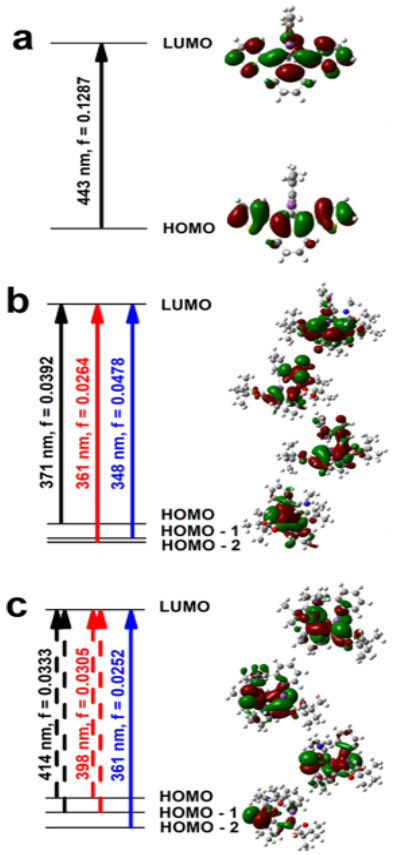

Figure B.6: TD-DFT computed main transitions for a) Bismole 1, b) Bismole 2, and c) Bismole 3 to low-lying singlet states and the associated molecular orbitals.

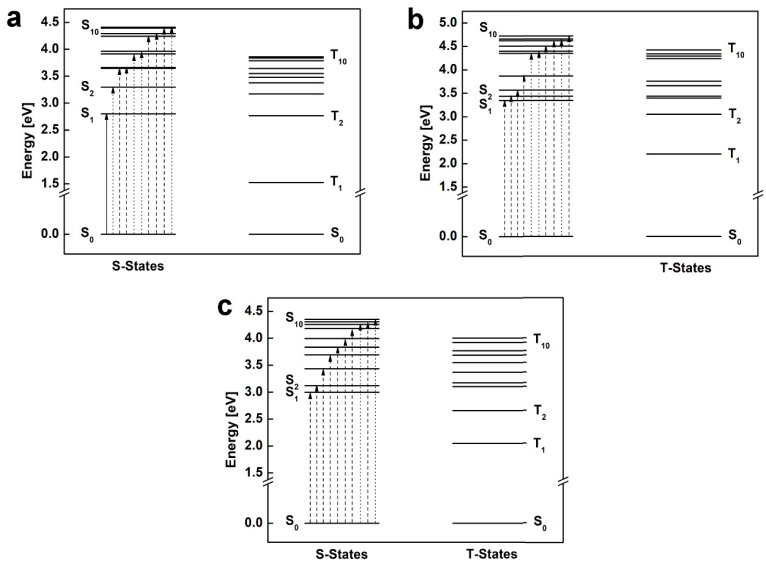

Figure B.7: Calculated singlet and triplet states of a) Bismole 1, b) Bismole 2, and c) Bismole 3.

APPENDIX C

Supporting information to Chapter 7

C.1 Preparation and characterization of the samples[1]

General Information on sample preparation: The reagents were purchased from Sigma-Aldrich, Wacker and Alfa Aesar and were, if not stated otherwise, used without further purification. Styrene and acrylic acid (AA) were distilled under reduced pressure and stored under argon at 7 °C. Azobisisobutyronitrile (AIBN) was recrystallized from methanol. Prior to its usage, toluene was dried with a MBraun solvent purification system MB SPS-800 whereby argon 5.0 (99.9990 %, Westfalen AG) was used as inert gas. Acetone was distilled, dried over molecular sieve, degassed and stored under argon. The exfoliated SiNSs were stored in a LABmaster 130 (MBraun) glove box with argon 4.8 (99.998 %, Westfalen AG). Air or water sensitive reactions were executed under standard Schlenk techniques.

Synthesis and etching of SiNS-H: These steps were performed following the established procedure as described previously [206, 208].

4-DDB induced functionalization with 1-dodecene: The dispersed SiNS-H in dry, degassed toluene (2 mL) is transferred into a Schlenk-tube and 1-dodecene (3 mmol, 0.66 mL) is added. The reaction mixture is degassed via three freeze-thaw-pump cycles, filled with argon and 4-DDB (5 mg) is added. After stirring overnight, the mixture is transferred into a centrifuge tube, mixed with methanol (3 mL) and centrifuged (9000 rpm, 5 min). The residue is twice re-dispersed in toluene and centrifuged with the corresponding anti-solvent (2 mL). The SiNS-$C_{12}H_{25}$ were re-dispersed in toluene (SiNS-$C_{12}H_{25}$(toluene)) for further use. In the solid form, the SiNS-$C_{12}H_{25}$ were drop casted onto a 1 mm thick optical grade fused quartz, referred as SiNS-$C_{12}H_{25}$(solid).

AIBN based radical induced functionalization and polymerization: In a Schlenk-tube a dispersion (12 mL) of SiNS-H (corresponds to 0.088 g exfoliated $(Si_6H_6)n$) in water-free degassed toluene (or ethanol for acrylic acid) is mixed with the substrate (3.30 g, 3 wt%, with regard to compound before etching). After degassing via three freeze-thaw-pump cycles, AIBN (0.020 g) is added and the reaction mixture is stirred at 70 °C for 16 h. After stirring, the mixture is transferred into a centrifuge tube, mixed with methanol (3 mL) and centrifuged (9000 rpm, 5 min). The residue is twice re-dispersed in toluene and centrifuged with the corresponding anti-solvent (2 mL).

Isolation of SiNS-substrate@polymer: The reaction mixture is precipitated in methanol (or toluene for poly(acrylic acid) (PAA)) and centrifuged (9000 rpm/2 min). The hybrid material is re-dispersed (2 times), precipitated and isolated by freeze drying from benzene (or water for SiNS-PAA@PAA).

Material preparation for the PL measurements in solution: The SiNSs are dispersed in water-free toluene and transferred in a sealed quartz cuvette, referred to as SiNS substrate(toluene).

[1] Synthesis of the samples were performed by A. Lyuleeva and T. Helbich, NMR spectroscopy was performed by M. Ha.

Material preparation for the PL measurements in solid state: The material ($\sim$ 500 μm thickness) is drop-casted from toluene dispersion on a non-fluorescent glass plate ($\sim$ 1 mm thickness), referred as SiNS-substrate(solid). The measurements of the composites are done after melting ($\sim$ 150 °C) the SiNSs-polymer@polymer on a non fluorescent glass substrate.

AFM: SiNS-$C_{12}H_{25}$ is spin-coated from a dispersion in toluene (9000 rpm, 150 sec) and dried at 120 °C. Tapping mode AFM image is taken using contact mode (Asylum Research MFP-3D AFM with an ARC Controller).

Transmittance: Measurements were conducted using a xenon arc lamp (300 W, 77 Hz) chopped at 77 Hz through an Oriel Cornerstone 260 $\frac{1}{4}$ m monochromator (Newport) and an Oriel Merlin digital lock-in amplifier (Newport).

Absolute Quantum Yields (AQY): AQY were measured on a Hamamatsu Absolute PL Quantum Yield C11347 spectrometer.

^{29}*Si Solid-State Nuclear Magnetic Resonance Spectroscopy*: Silicon-29 NMR spectra were acquired on a Bruker Avance II HD 400 NMR spectrometer at 9.39 T ($\nu_0(^{29}\text{Si}) = 79.46$ MHz) using a 4 mm double-resonance (H-X) MAS Bruker probe. All samples were prepared under inert atmosphere and packed in air-tight 4 mm zirconia rotors. Magic-angle spinning conditions with a spinning frequency of 10.0 kHz were used to acquire all NMR data using a cross-polarization [270] pulse sequence (4.0 μ $\pi/2$ pulse, ramped Hartman-Hahn match condition on ^{29}Si, 5.0 ms contact time, recycle delay of 8.0 s and 10.0 s for SiNS-$C_1 2H_2 5$ and SiNS-H respectively, and TPPM [271] high-power ($\gamma B_1/2\pi =$ 62.5 kHz) ^{1}H decoupling). All ^{29}Si NMR spectra were referenced to TMS ($\delta = 0$ ppm) using the secondary reference, tetrakis(trimethylsilyl)silane, and setting the high frequency peak to -9.8 ppm [272].

C.2 Supporting Figures

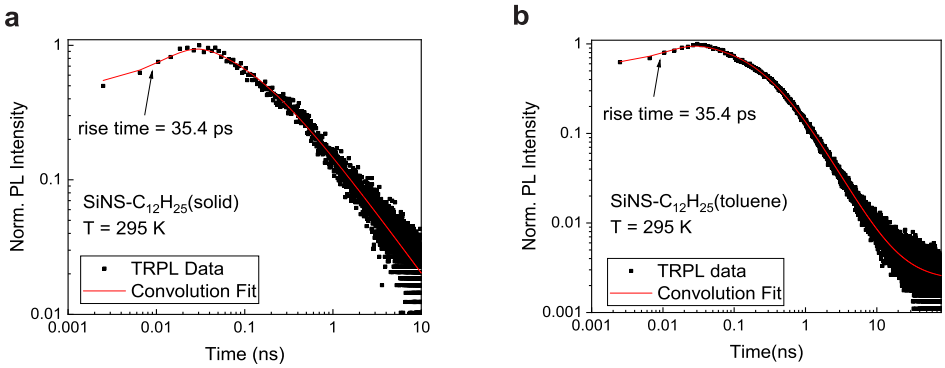

Figure C.1: Examples of convolution fits to the TRPL data of ***a)*** *SiNS-$C_{12}H_{25}$(solid) and* ***b)*** *SiNS-$C_{12}H_{25}$(solid) at $T = 295$ K. The fits were also applied to SiNS-H, SiNS-PS@PS and SiNS-PAA@PAA at $T = 295$ K. All of the convolution fits (Equation 5.1) of Gaussian function $g(t)$ (Equation 5.2) and inverse power law function (Equation 7.2) provided a rise time of 35 $\pm$ 1 ps.*

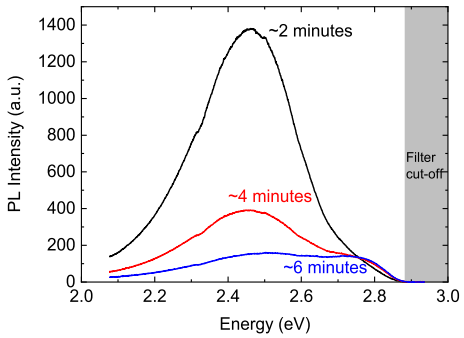

Figure C.2: PL intensity vs. wavelength of SiNS-PS@PS measured in air. Quenched and blue-shifted PL are observed through time. In addition, another peak arises at ∼ 2.78 eV due to oxidized surface states.

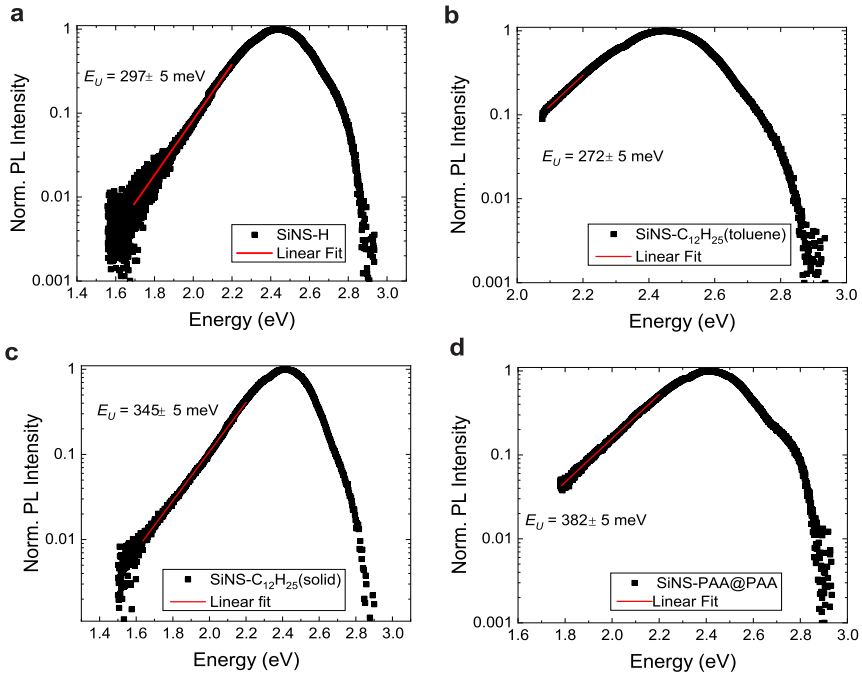

Figure C.3: Log plots of the normalized PL intensity of ***a)*** *SiNS-H,* ***b)-c)*** *SiNS-$C_{12}H_{25}$(substrate) and* ***d)*** *SiNS PAA@PAA. The intensity of the PL is ∼ $exp(h\nu/E_U)$ at photon energies below the band edge where the characteristic energy of the Urbach tail, E_U, can be estimated. Linear fits were taken at $E < 2.2$ eV.*

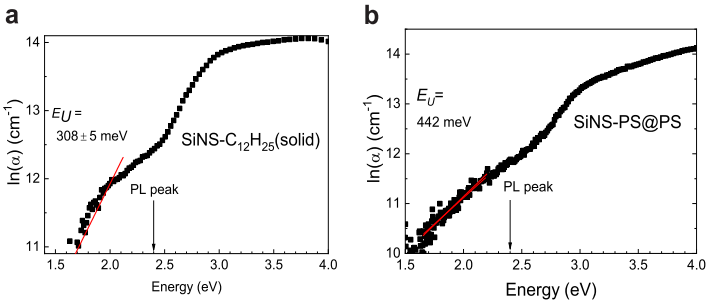

Figure C.4: Plots of the natural log of the absorption coefficient, $ln(\alpha)$, against energy $h\nu$ of ***a)*** *SiNS-$C_{12}H_{25}$(solid) and* ***b)*** *SiNS-PS@PS. The absorption coefficient follows an Urbach rule given as $\alpha = \alpha_0 exp(h\nu/E_U)$ where E_U is the characteristic energy of the Urbach tail. Rewriting the equation gives $ln(\alpha) = ln(\alpha_0) + (h\nu/E_U)$ thus E_U can be taken from the inverse of the slope at photon energies below the PL peak. However, multiple slopes can be observed due to the scattering effects from both SiNSs and polymer substrate. No absorbance measurements were done on the solution samples due to the limitation of the instrument and the SiNS-PAA@PAA due to large noise from the scattering in PAA substrate.*[2]

[2]Absorbance was conducted by A. Lyuleeva and M.A.B. Narreto. Analysis was performed by M.A.B. Narreto.

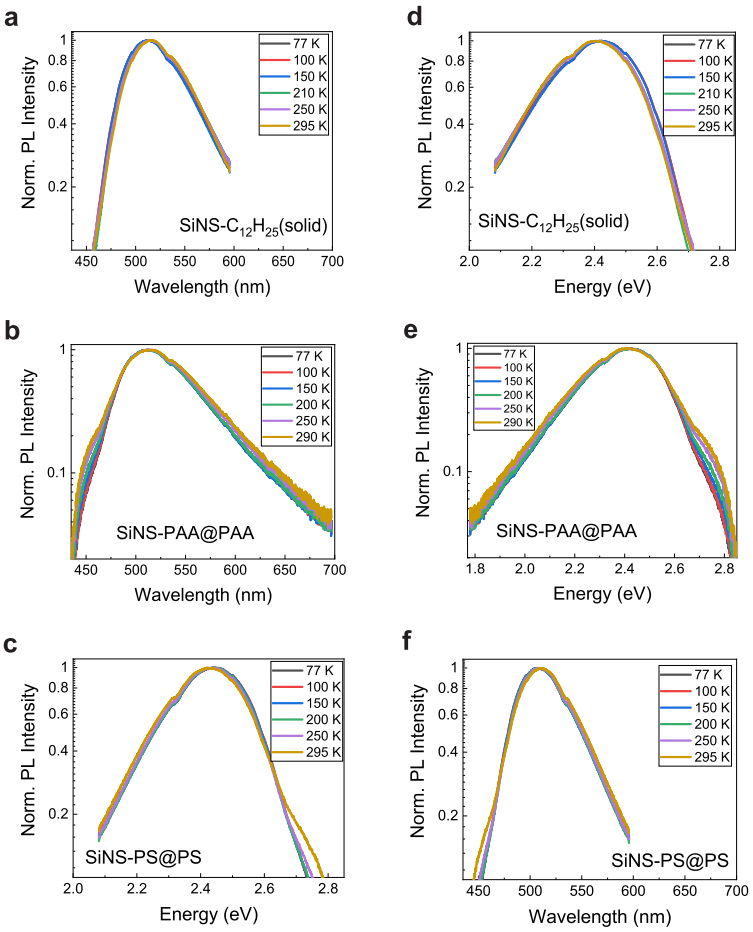

Figure C.5: Normalized PL Spectra of the SiNS-$C_{12}H_{25}$(solid), SiNS-PS@PS, and SiNS-PAA@PAA plotted against ***a-c)*** *wavelength (nm) and* ***d-f)*** *energy (eV), respectively, at various temperatures. No significant change in the spectral bandwidths is observed at low temperature.*

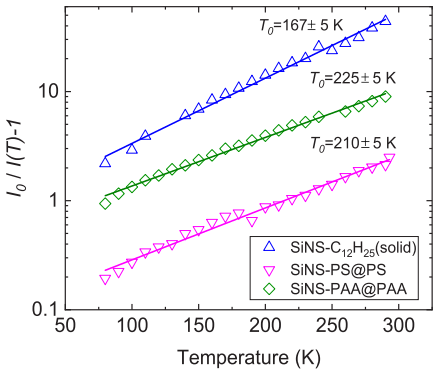

Figure C.6: Plot of the $(I_0/I(T)-1)$ in log scale as a function of the temperature. In this case, the I_0 values are arbitrarily assigned, which yielded to a linear dependence of the plot over all the temperature range of measurement. The corresponding T_0 values were extracted from the slopes (solid lines). The I_0 and T_0 values are listed in Table C.2.

Using the T_0 values from Figure C.6, the estimated carrier lifetime τ is within the range of 10^{-8} to 10^{-5} s, which is higher than the estimated τ using values in Figure 7.2d (Chapter 7). These are still over-estimated values because the QY is only $< 2\%$.

Table C.1: I_0 values used in plotting Equation 7.1 for Figure 7.2d (Chapter 7) and Figure C.6, and the corresponding T_0 values extracted from the slopes.

Sample	Figure7.2d		Figure C.6	
	I_0 (a.u.)	$T_0(K)$	I_0 (a.u.)	$T_0(K)$
SiNS-$C_{12}H_{25}$(solid)	$I(80K)$	152 ± 5	3.19$[I(80K)]$	167 ± 5
SiNS-PS@PS	$I(80K)$	192 ± 5	1.19$[I(80K)]$	210 ± 5
SiNS-PAA@PAA	$I(80K)$	187 ± 5	1.94$[I(80K)]$	225 ± 5

Table C.2: Absolute Average Quantum Yield (%) of solution and solid samples.[3]

SiNS-H(toluene)	SiNS-$C_{12}H_{25}$(toluene)	SiNS-$C_{12}H_{25}$(solid)	SiNS-PS@PS
0.98	2.10	0.91	2.33

[3]AQY measurements were conducted by P. Altman (TUM).

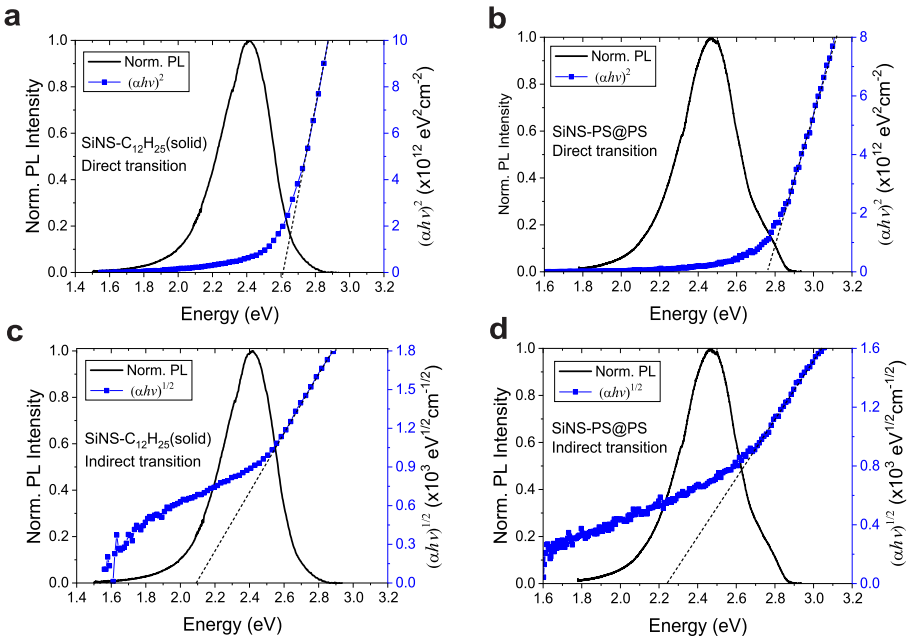

Figure C.7: Plots of the normalized PL intensity of SiNS-$C_{12}H_{25}$(solid) and SiNS-PS@PS overlaid with the ***a-b)*** *square and* ***c-d)*** *square roots of the absorbance plots, respectively. For direct transition, the absorbance is expressed as* $(\alpha h\nu) \propto (h\nu - E_g)^{1/2}$ *and for indirect transition,* $(\alpha h\nu) \propto (h\nu - E_g)^2$*. Thus, the extrapolated linear dashed lines show the y-offset of the absorption coefficients* $(\alpha h\upsilon)^2$ *and* $(\alpha h\upsilon)^{1/2}$*, which are the estimated direct and indirect optical band gap energies* E_g*, respectively. Here, the absorption coefficient is* $\alpha = ln(10) \times A/d$*. The Absorbance A is calculated from the Transmittance (%T) using Beer's law* $A = 2 - log_{10}(\%T)$ *and d is the sample thickness. No absorbance measurements were done on the solution samples due to the limitation of the instrument and the SiNS-PAA@PAA due to large noise from the scattering in PAA substrate.*[4]

[4]Absorbance was conducted by A. Lyuleeva and M.A.B. Narreto. Analysis were performed by M.A.B. Narreto.

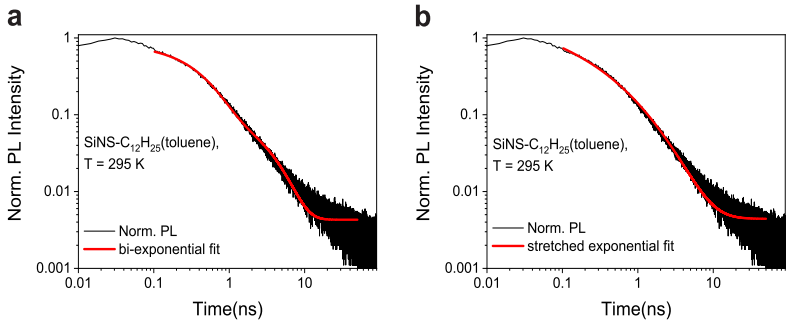

Figure C.8: Examples of **a)** *bi-exponential decay and* **b)** *stretched exponential decay fits to the TRPL of SiNS-$C_{12}H_{25}$(toluene) at $T = 295$ K.*

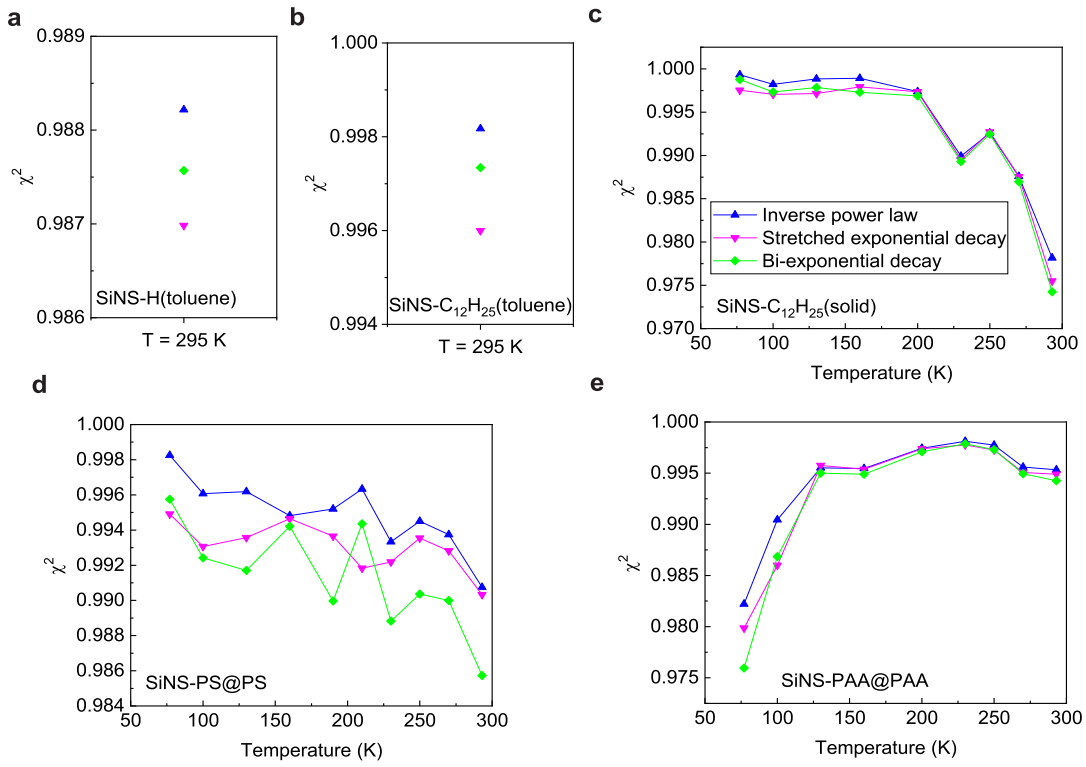

Figure C.9: χ^2 values extracted from the non-linear least square fits of the TRPL at various temperatures for **a)** *SiNS-H,* **b)** *SiNS-$C_{12}H_{25}$(toluene),* **c)** *SiNS-$C_{12}H_{25}$(solid),* **d)** *SiNS-PS@PS, and* **e)** *SiNS-PAA@PAA. Fits to the inverse power law decay (blue up triangle symbols) have the best χ^2 compared to fits to stretched exponential decay (down magenta triangle symbols) and bi-exponential decay (green diamond symbols).*

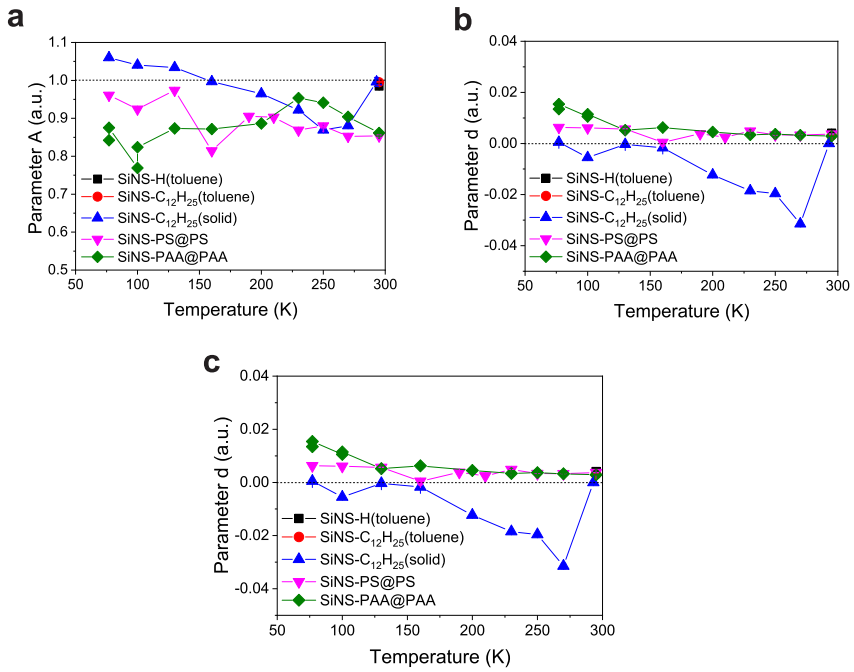

Figure C.10: The parameters **a)** *A,* **b)** *b and* **c)** *d (y-offset) taken from the normalized TRPL fits to inverse power law decay shown in Equation 6.2. Dashed lines are guide to eye for ideal values. Errors are within the data points.*

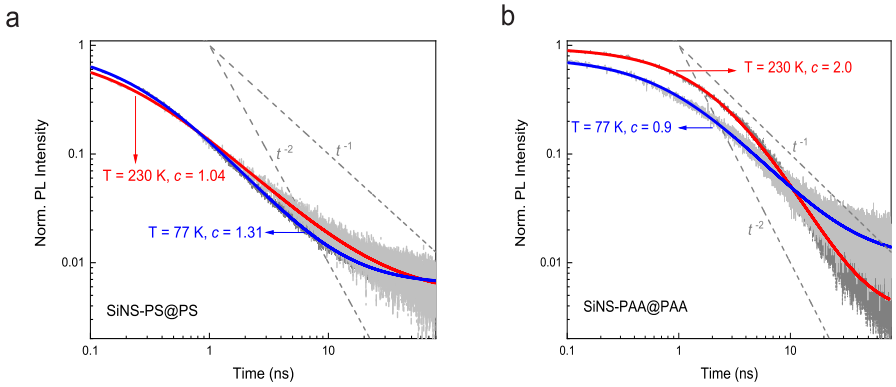

Figure C.11: Inverse power law fits (blue and red solid lines) of Equation 6.2 to the TRPL measurements (gray shades) at 230 K and 77 K for **a)** *SiNS-PS@PS and* **b)** *SiNS-PAA@PAA displaying different c values. The dashed lines are quide to the eye for t^{-2} and t^{-1} dependence.*

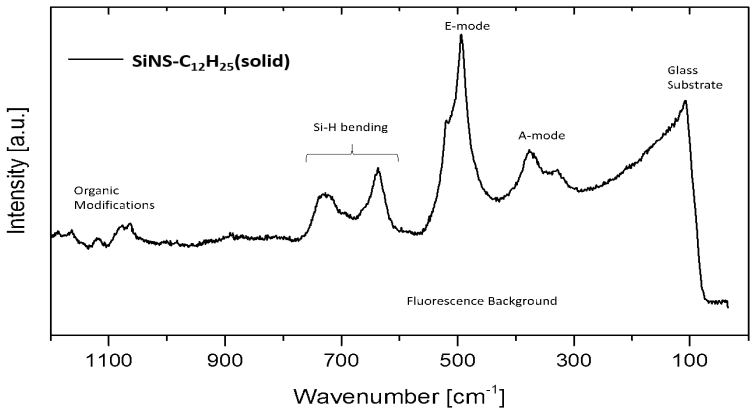

Figure C.12: Raman spectrum of SiNS-$C_{12}H_{25}$(solid)[5]*. The bands at 494 cm^{-1} (E-mode) and 376 cm^{-1} (A-mode) are Si-Si modes at the lateral and vertical directions, respectively. In previous report [256], the local vertical distortions in the SiNSs 2D structure is associated to the activation of A-mode (A_{1g}) peaks, whose intensity is a function of the amount and distribution of buckled Si atoms. However, comparison of the Raman spectra should be treated with caution. The authors [256] report an expitaxially grown SiNSs on a substrate which was hypothesized to be initially planar with sp^2 arrangements and that the distorted buckling was induced by the substrate, which resulted in mixed $sp^2 - sp^3$ structure. In our work, the freestanding hydrogenated and functionalized SiNSs are ideally sp^3-hybridized. Thus, the Raman spectrum is inconclusive.*

[5]Raman spectroscopy was performed by M. J. Kloberg (TUM).

APPENDIX D

Supporting information to Chapter 8

D.1 Absorption within the material

In this section, we shall briefly discuss the absorption in semiconductors, which would help us calculate the actual carrier density from an optical excitation. The number of photoexcited carrier density n, by means of absorption, is proportional to the intensity of the illumination source, which can be estimated if the fundamental optical properties of the material are known, such that

$$n = \frac{(1-R)F_0}{(h\nu)\delta}. \tag{D.1}$$

R is the reflection coefficient and δ is the penetration depth, where both values depends on the excitation energy $h\nu$. F_0 is the average fluence given as $F_0 = P/[f(\pi r^2)]$, where P is the time average power, f is the repetition rate of the laser, and r is the radius of the photoexcited surface [318, 319]. The penetration depth, which is the distance at which the light wave travels through the material, is inverse of the absorption coefficient α. It is wavelength (λ) dependent, given as

$$\delta = \frac{1}{\alpha} = \frac{c}{2\omega k} = \frac{\lambda}{4\pi k}, \tag{D.2}$$

where $\omega = 2\pi f$ is the angular frequency, c is the speed of light, and k is the extinction coefficient. One can also describe the penetration depth as the decay of the light wave inside the material. According to the Beer-Lambert law $I = I_0 exp(-\frac{L}{\delta})$, the intensity of the incident light on the material, with thickness L, decays exponentially in which the light wave has decreased by $1/e$ or 37% of the original intensity I_0.

For Ge, at $\lambda = 400$ nm ($E = 3.1$ eV), $\delta = 15$ nm, R= 0.47. At $\lambda = 800$ nm ($E = 1.55$ eV), δ = 220 nm, R= 0.42 [96].

Referring to Figure 10.3 of Chapter 10, the 1.55 eV optical pump pulses at $f = 1$ kHz has an average measured power of $P = 6.4 \pm 0.2$ mW and a beam spot with a radius of $r = 0.4 \pm 0.01$ mm, providing a fluence of $F = 1.27 \pm 0.05$ mJ/cm^2. Thus, the estimated carrier density is $n = 134 \pm 10 \times 10^{18}$ cm^{-3}. At this carrier density, an optimum direct $\Delta PL/PL$ is obtained, as shown in Figure 10.4.

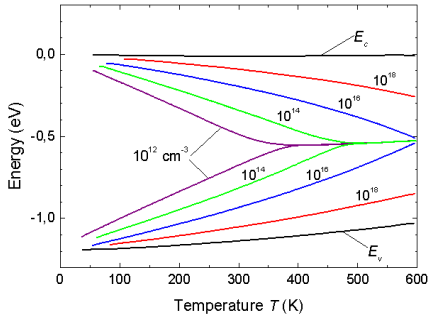

Figure D.1: Fermi level at $T = 0$ K for different carrier doping concentrations in Ge, taken from Ref. [37].

D.2 TRTS of Ge

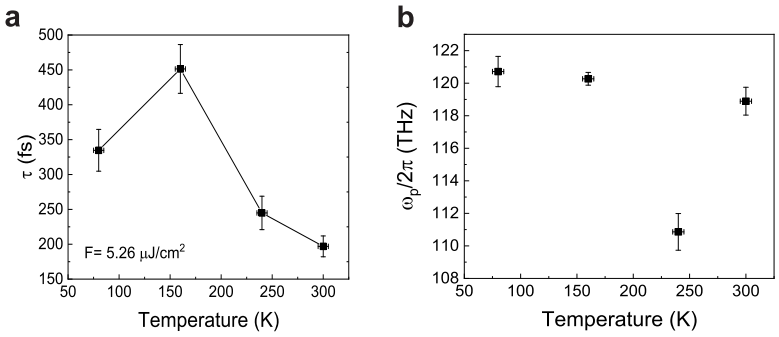

*Figure D.2: Parameters taken from the Drude model fits to the measured complex conductivity of Ge: **a)** scattering time τ, and **b)** plasma frequency ω_p. The measurements were carried out at constant $F = 5.6\ \mu J/cm^2$. These provided almost constant values of ω_p except at 240 K where ω_p is less than 10 THz compared to other data. This could be more likely an inconsistency in the optical fluence.*

APPENDIX E

Supporting information to Chapter 9

E.1 Sample preparation[1]

Ge unstructured: Quartz substrate was cleaned in a solution of Extran (alkaline solution), water and then acetone in an ultrasonic bath (15 min each). For better adhesion, the substrate was put into an O_2-Plasma (50% power) for 10 min. Subsequentely, a solution of K_4Ge_9 in Ethylenediamine (en) was dropcasted onto the substrate. After the solution was dried, the substrate was placed in a Schlenk next to a vial containing $GeCl_4$ so that a linking reaction could occur (K_4Ge_9 + $GeCl_4$ → 4 KCl + 10 Ge^0). Remaining solvent was removed by drying the sample in vacuo at 100 °C for 1 h. Subsequently, the sample was annealed at 500 °C for 5 min. Finally, the sample was washed with dmso then thf (30 min each) to remove any residual KCl and dried in vacuo.

Ge INOP-1: Quartz substrate was cleaned in a solution of Extran (alkaline solution), water and then acetone in an ultrasonic bath (15 min each). For better adhesion, the substrate was put into an O_2-Plasma (50% power) for 10 min. A solution of PMMA (150 nm spheres, 15%wt in water) was dipcoated onto the subtrate and any residual solvent was removed in vacuo at 100 °C for 4 h. Subsequentely, a solution of K_4Ge_9 in Ethylenediamine (en) was dropcasted onto the substrate. After the solution was dried, the substrate was placed in a Schlenk next to a vial containing $GeCl_4$ so that a linking reaction could occur (K_4Ge_9 + $GeCl_4$ → 4 KCl + 10 Ge^0). Remaining solvent was removed drying the sample in vacuo at 100 °C for 1 h. PMMA was destroyed by annealing the sample at 500 °C for 5 min. Residual KCl as well as PMMA degradation products were removed by washing with dmso then thf (30 min each). Finally, the sample was dried in vacuo.

Ge INOP-2: Quartz substrate was cleaned in a solution of Extran (alkaline solution), water and then acetone in an ultrasonic bath (15 min each). For better adhesion, the substrate was put into an O_2-Plasma (50% power) for 10 min. A solution of PMMA (340 nm spheres, 15%wt in water) was dipcoated onto the subtrate and any residual solvent was removed in vacuo at 100 °C for 4 h. Subsequentely, a solution of K_4Ge_9 in Ethylenediamine (en) was dropcasted onto the substrate. After the solution was dried, the substrate was placed in a Schlenk next to a vial containing $GeCl_4$ so that a linking reaction could occur (K_4Ge_9 + $GeCl_4$ → 4 KCl + 10 Ge^0). Remaining solvent was removed drying the sample in vacuo at 100 °C for 1 h. PMMA was destroyed by annealing the sample at 500 °C for 5 min. Residual KCl as well as PMMA degradation products were removed by washing with dmso then thf (30 min each). Finally, the sample was dried in vacuo.

[1]Synthesis of the samples were performed by M. A. Giebel. This section was written by M. A. Giebel (TUM).

E.2 SEM images[2]

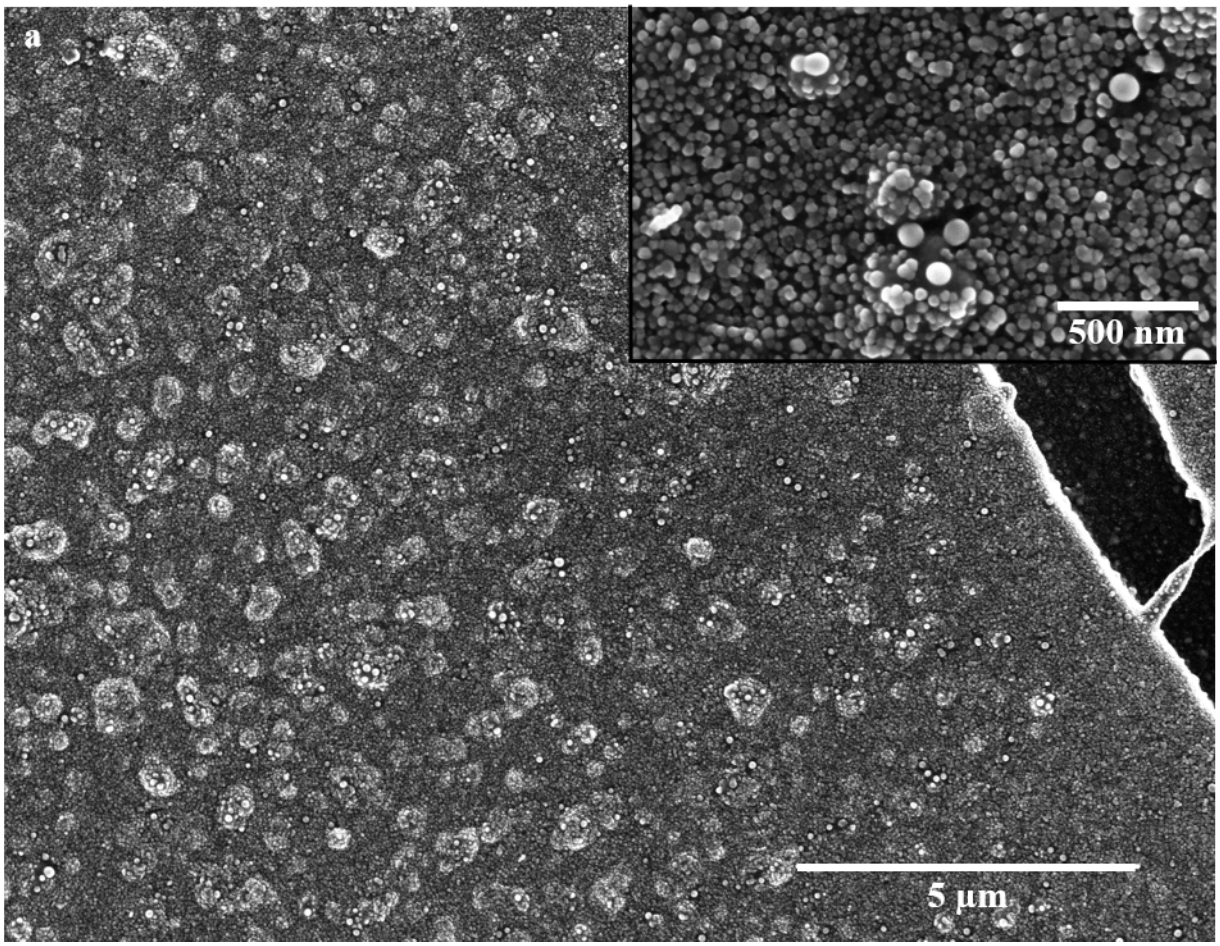

Figure E.1: SEM images of the Ge unstructured film showing a loose granular structure.

[2]Images taken by M. A. Giebel (TUM).

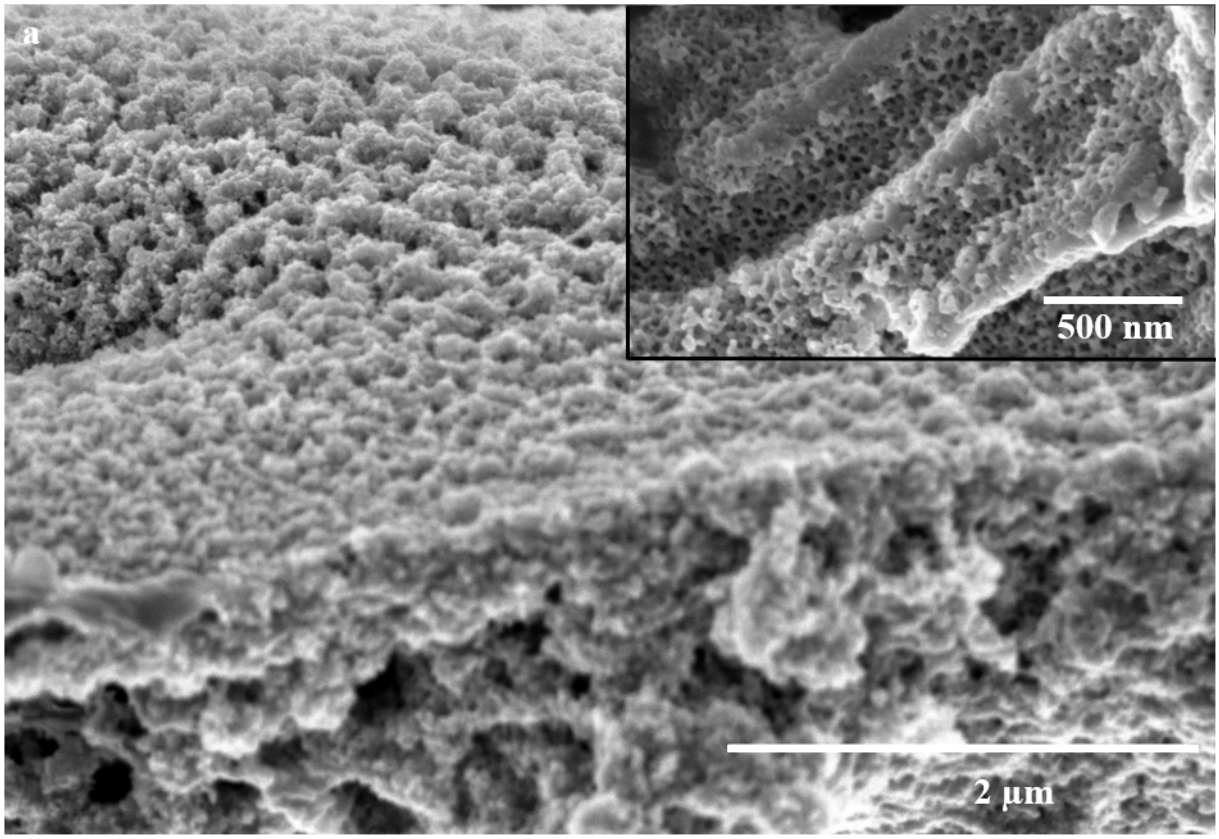

Figure E.2: SEM images of the Ge film with 150 nm PMMA removed (Ge INOP-1) showing structured material with a rough surface. The thin film thickness is 2.1 - 3.0 µm determined using a profilometer.

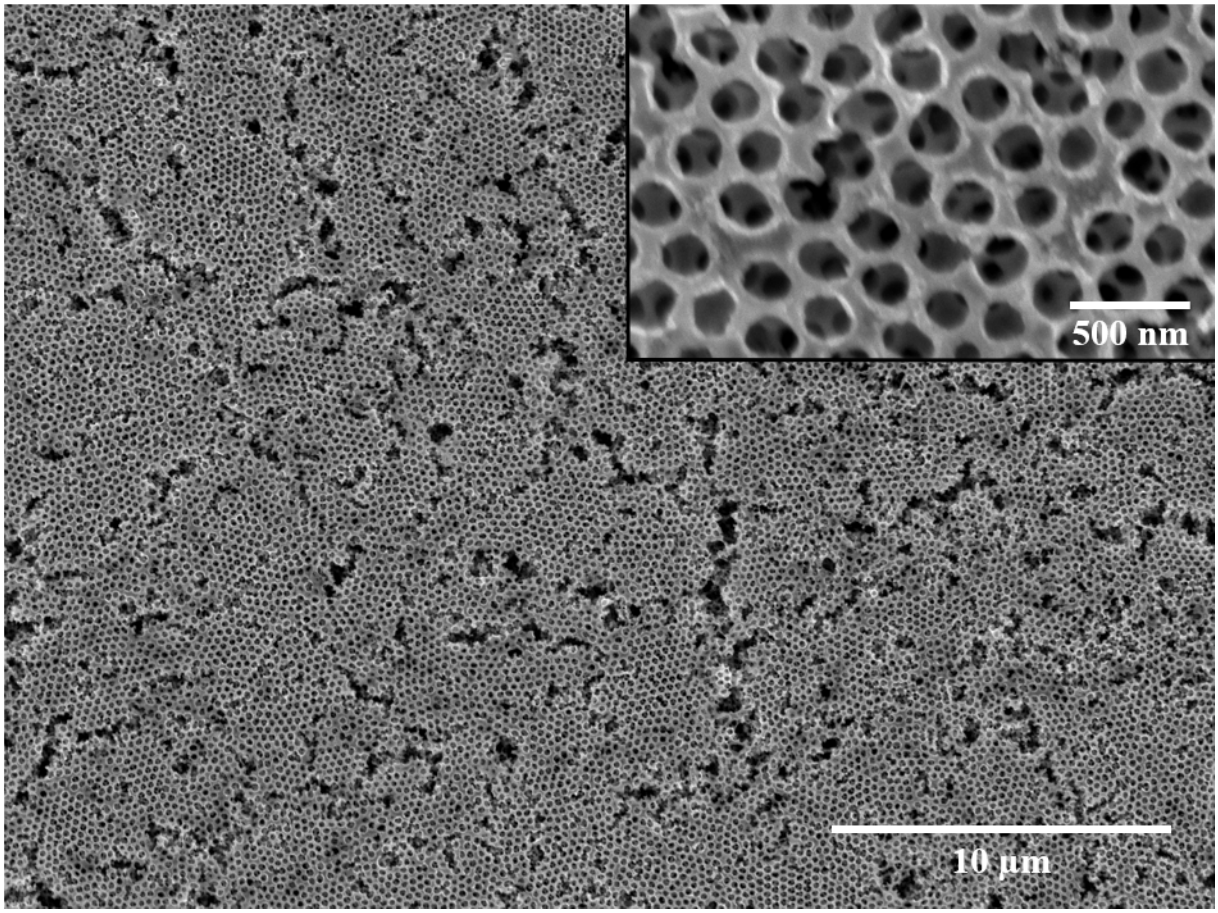

Figure E.3: SEM images of the Ge film with with 340 nm PMMA removed (Ge INOP-2) showing inverse opal structured material throughout large area. The thin film thickness is 2.4 - 2.8 µm determined using a profilometer.

E.3 Photothermal Deflection Spectroscopy

The Ge film on a substrate is placed in a cuvette filled with perfluorohexane. A continuous wave laser is directed across the top of the surface of the sample. Perpendicular to the laser, a pumping beam of monochromatic light with adjustable wavelength is directed onto the sample. The laser beam passing through is therefore slightly deflected during the measurement. This deflection (which is proportional to the absorption of the film) is measured by an optical detector. The detected PDS signal were normalized onto the highest signal detected in each sample and the following empiric formula was used to determine the absorption coefficient α,

$$\alpha \approx -\frac{1}{d} \cdot ln(1 - 0.96 \cdot PDS_{signal}) \tag{E.1}$$

Here, d stands for thickness of the sample.

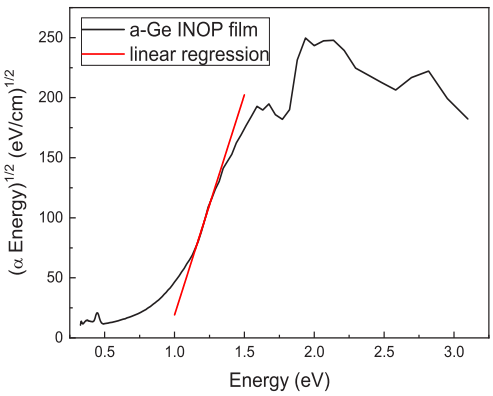

Figure E.4: Determination of a band gap from the absorbance of the Ge film that was annealed for 5 min at 500 °C. The band gap of 0.95(3) eV is determined from the the x-intercept (x_0) of the linear fit (red line).[3]

The absorption coefficient α of an indirect semiconductor is given as:

$$\alpha(E) \sim \frac{(E - E_{g-ind})^2}{E} \tag{E.2}$$

Therefore, $\sqrt{\alpha \cdot E}$ plotted against E in Figure E.4 provided a band gap of 0.95(3) eV. A transition from linear to logarithmic dependence is shown at lower photon energies. This behaviour is known as Urbach tail and covers a broad energy range.

For a 1.53 eV (810 nm) of optical excitation, the absorption coefficient is found to be $\alpha = 0.212{\times}10^9$ cm^{-1} or a penetration depth of $\delta = \frac{1}{\alpha} = 455$ nm. Further annealing of the Ge film upto 8 hours resulted to $E_{g-ind} = 0.662$ eV, in agreement with the indirect band gap of crystalline Ge.

[3]PDS measurement was performed by M. A. Giebel and futher analyzed by M.A.B. Narreto.

E.4 Supporting figures

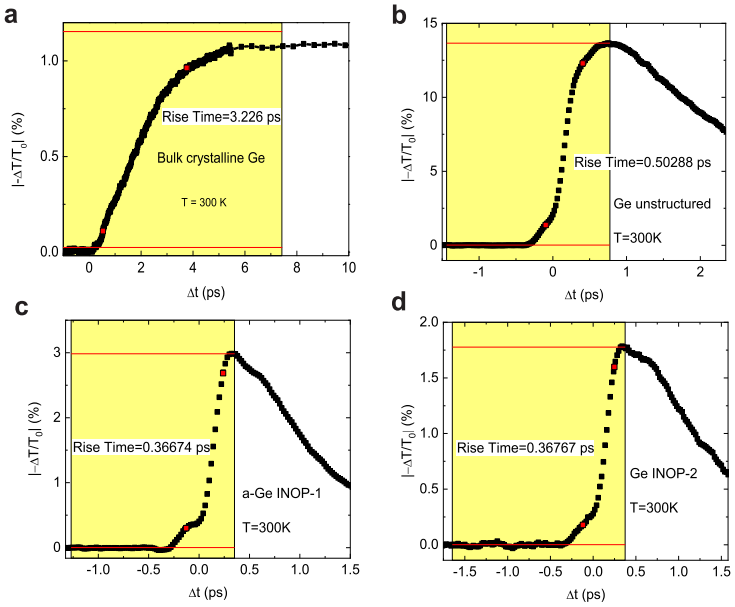

Figure E.5: Plots of the transient photoconductivities, with 10 - 90% rise times, of ***a)*** *bulk crystalline Ge at $F = 0.67\ \mu J/cm^2$, and the samples* ***b)*** *Ge unstructured,* ***c)*** *Ge INOP-1, and* ***d)*** *Ge INOP-2 measured at a fluence of $F = 760 \pm 10\ \mu J/cm^2$.*

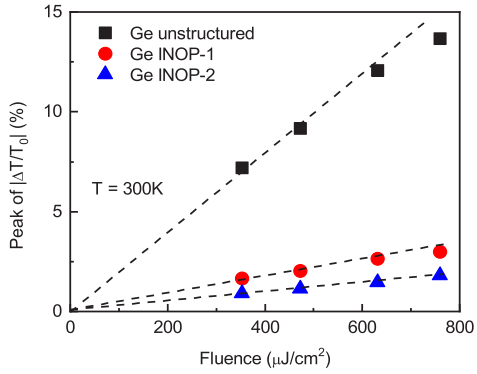

Figure E.6: Fluence dependence of the peak of $|-\Delta T/T_0|$. Broken lines are guide to the eye for the linear trend.

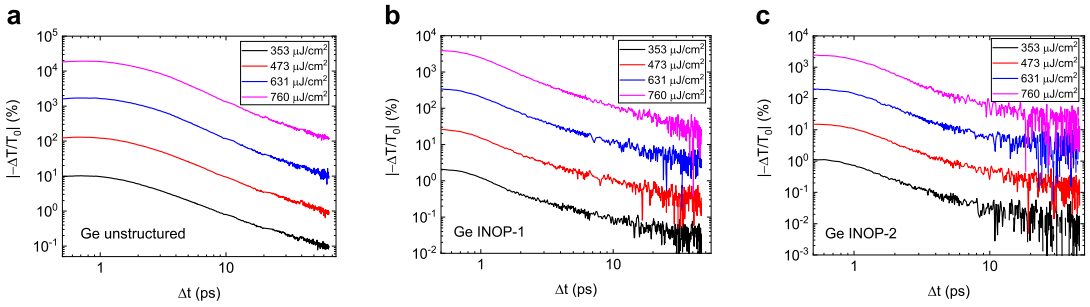

Figure E.7: Fluence dependence of the $|-\Delta T/T_0|$ of ***a)*** *Ge unstructured,* ***b)*** *Ge INOP-1, and* ***c)*** *Ge INOP-2. The amplitudes were offset by a factor of 10.*

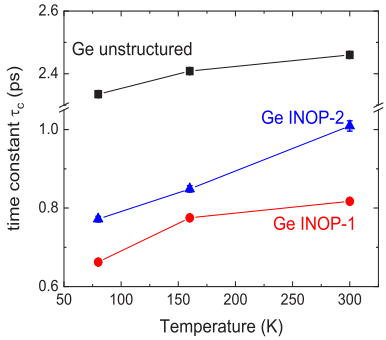

Figure E.8: Time constant parameter τ_c taken from the single exponential fit at the earlier timescale of the $|-\Delta T/T_0|$ plotted against various temperatures for the Ge unstructured (black square), Ge INOP-1 (red circles), and Ge INOP-2 (blue triangles).

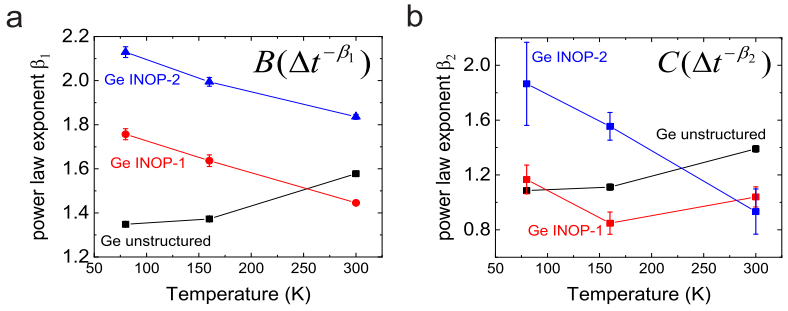

Figure E.9: Exponents ***a)*** *β_1 and b) β_2 extracted from the two power law decay fits to the slower timescale of the $|-\Delta T/T_0|$. The dependence of β_1 and β_2 against temperature is inconsistent and thus the mechanism of multiple trapping charge transport, represented by these power law decay exponents, is unclear.*

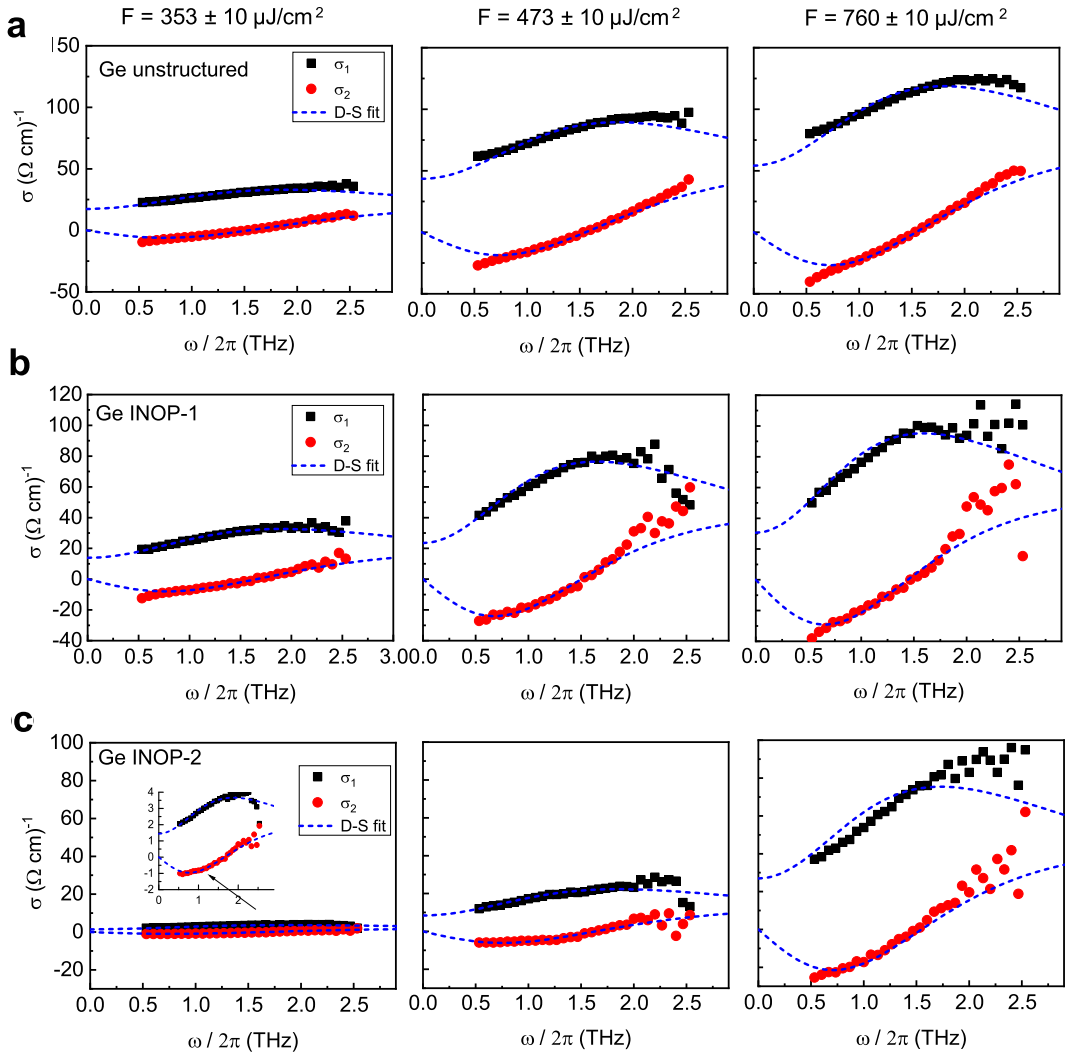

Figure E.10: Sample figures of the complex conductivity $\tilde{\sigma}(\omega)$ of ***a)*** *Ge unstructured at Δt = 1.25 ps,* ***b)*** *Ge INOP - 1, and* ***c)*** *Ge INOP - 2 at Δt = 0.85 ps measured at room temperature and at different pump fluences. Blue dashed lines are the Drude-Smith (D-S) fits to the real part (σ_1) and imaginary part (σ_2) of the $\tilde{\sigma}(\omega)$.*

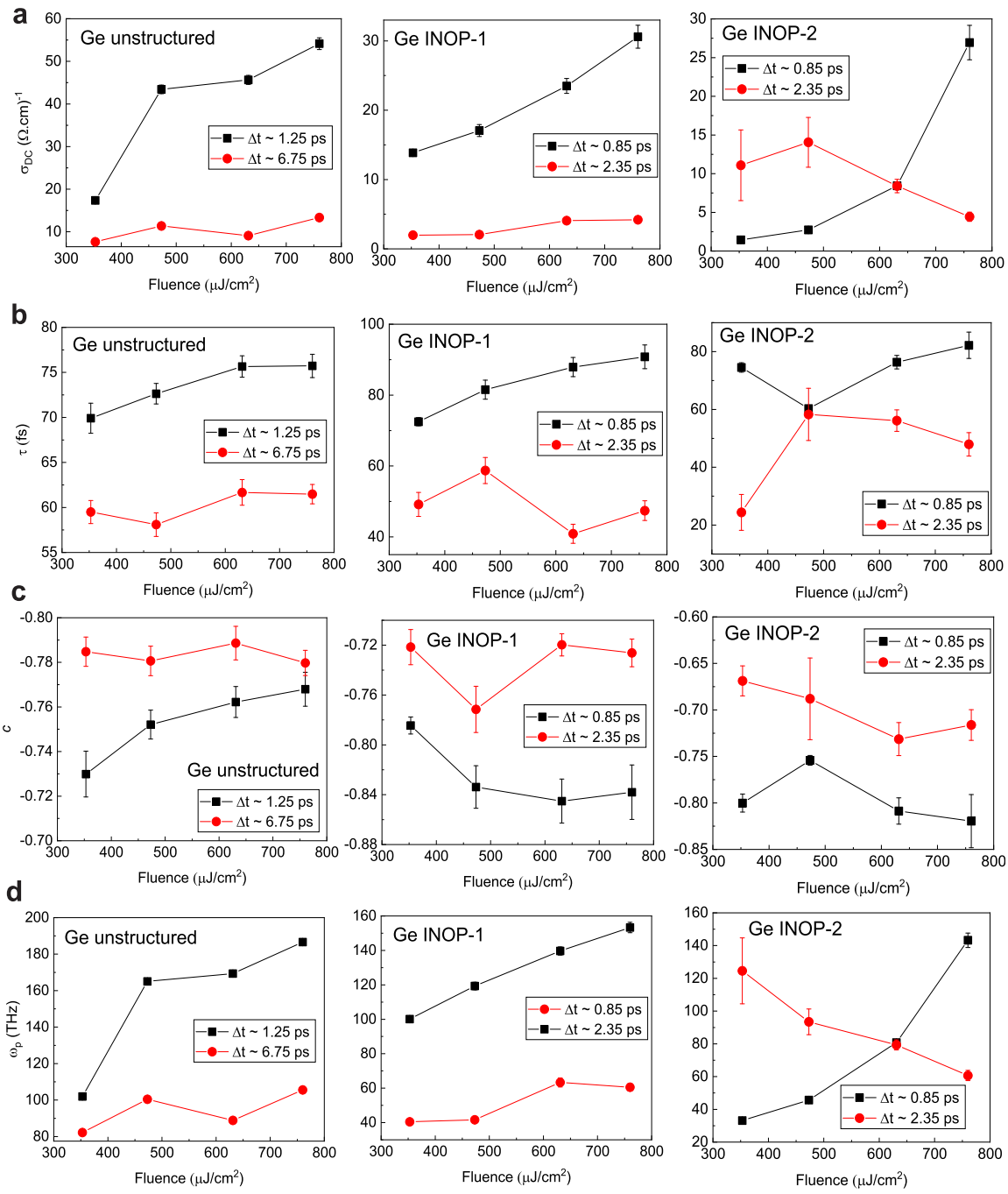

*Figure E.11: Parameters extracted from the Drude-Smith fits to the $\tilde{\sigma}(\omega)$ of the Ge films at various fluences and Δt at $T = 300$ K; **a)** dc conductivity σ_{dc}, **b)** scattering time τ, **c)** persistence of velocity c, and **d)** plasma frequency ω_p. Notice that the σ_{dc} is more constant at latter Δt in the regime of dispersive transport.*

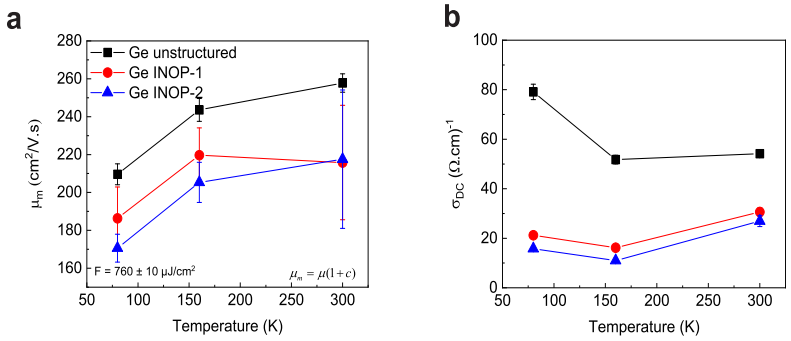

Figure E.12: ***a)*** *Macroscopic carrier mobility μ_m and* ***b)*** *dc conductivity σ_{dc} extracted from the Drude-Smith fits to the complex conductivity of Ge films at various temperatures, at a fluence of $F = 760 \pm 10\ \mu J/cm^2$ and at $\Delta t = 1.25$ ps (for Ge unstructured) and 0.85 ps (for the Ge INOPs). The μ_m decreases with temperature, which could be due to impurity scattering.*

APPENDIX F

Supporting information to Chapter 10

F.1 Supporting figures

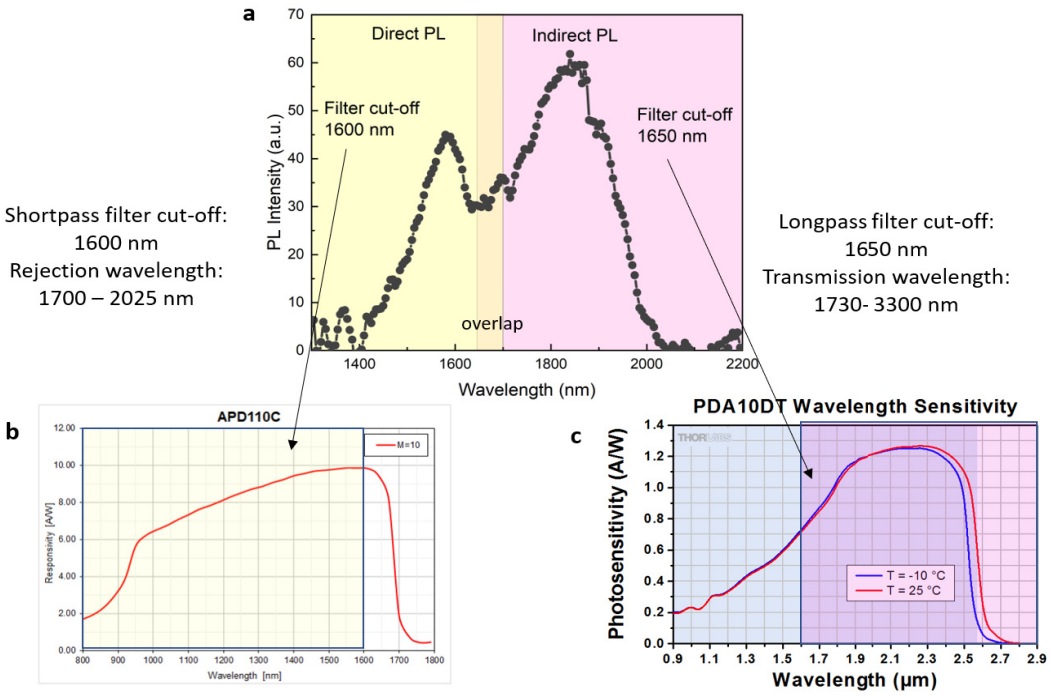

Figure F.1: ***a)*** *An example of the PL spectrum of undoped Ge showing the direct and indirect PL peaks. The shaded portions are the filter cut-offs for the measurement of the integrated direct PL (yellow) and integrated indirect PL (pink). The 1600 nm (#84-656) shortpass and 1650 nm (#68-652) longpass are manufactured by Edmund Optics. Unfortunately, the wavelength transmission/rejection plots are not provided. Based on the specifications, the transmission and rejection wavelength ranges are indicated in the plot. Because the filter response is not sharp, an overlap is indicated in the middle of the shaded portions of the filter cut-off.* ***b)*** *Responsivity of the InGaAs avalanche photodetector (Thorlabs APD110C) for the measurement of integrated direct PL.* ***c)*** *Responsivity of the InGaAs amplified photodetector (Thorlabs PDA10D) for the measurement of the integrated indirect PL. Shaded portions indicate the filter cut-off.*

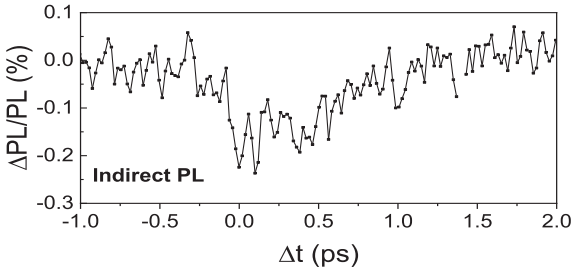

Figure F.2: Differential change in the indirect PL ($\Delta PL/PL$) plotted against the optical pump - THz pulse delay time (Δt) measured at an optical pump fluence of 1.41 ± 0.08 mJ/cm^2 with an applied peak THz electric field of E_{THz} = 210 ± 10 kV/cm.

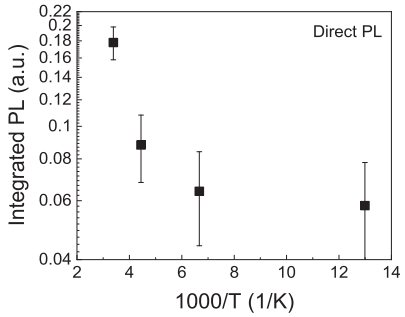

Figure F.3: The integrated PL from the direct gap plotted against the inverse of temperature. The nonlinear trend shows that the dependence do not follow an Arrhenius plot, $k = Aexp(-E_a/(k_BT))$, where k is the rate constant, which could be correlated to the quantum yield, $\eta = 1/\tau$, and is directly proportional to the integrated PL. E_a is the activation energy and A is a pre-exponential factor. The concept is similar to Equation 3.25.

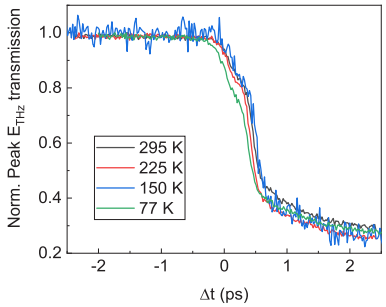

Figure F.4: Normalized peak amplitude of the E_{THz}, detected by the EO sampling, as it transmits through the photoexcited Ge surface at a time delay of Δt.

APPENDIX G

Presentations

The following are list of conference and symposium presentations based on the content of this dissertation.

G.1 Conferences

- M. A. B. Narreto; C. Huang; D. N. Purschke; F. A. Hegmann. Frontiers in Optics and Laser Science, Talk and Poster: Modulated Photoluminescence of Germanium *via* Intense Terahertz Pulse Electric Fields, Washington DC, USA, September 14-21, 2018
- M. A. B. Narreto; A. Lyuleeva; T. Helbich; J. C. Veinot; B. Reiger; P. Lugli; F. A. Hegmann. Photonics North, Talk: Photoluminescence dynamics of functionalized two-dimensional silicon nanosheets, Montreal, Quebec, Canada, June 5-7, 2018.
- M. A. B. Narreto; M. Giebel; N. Amer; T. F. Fässler; F. A. Hegmann. Photonics North, Talk: Terahertz photoconductivity of germanium inverse opal structures, Montreal, Quebec, Canada, June 5-7, 2018.
- M. A. B. Narreto; M. Giebel; N. Amer; T. F. Fässler; F. A. Hegmann. International Workshop on "Novel Concepts and Electronic Phenomena in Heterosystems", Invited Talk: Time-resolved Terahertz Spectroscopy of Inverse Opal Ge Films, Tutzing, Germany, May 28-30, 2018.
- M. A. B. Narreto; M. Giebel; N. Amer; T. F. Fässler; F. A. Hegmann. Optical Terahertz Science and Technology 2017, Poster: Time-resolved Terahertz Spectroscopy of Inverse Opal Ge Films, London, U.K., April 2-7, 2017
- M. A. B. Narreto & F. A. Hegmann. Women in Physics Canada Conference, Talk: Interplay between the Direct and Indirect Transient Photoluminescence of Bulk Ge, Saskatoon, Saskatchewan, Canada, July 27-29, 2016
- M. A. B. Narreto & F. A. Hegmann. 7th International Conference on Optical, Optoelectronic and Photonic Materials and Applications (ICOOPMA), Poster: Interplay between the Direct and Indirect Transient Photoluminescence of Bulk Ge, Montreal, Quebec, Canada, June 13-17, 2016

G.2 Symposia

- M. A. B. Narreto; C. Huang; D. N. Purschke; F. A. Hegmann. Graduate Physics Student Association Summer Series Talks, Talk: Modulated Photoluminescence of Germanium *via* Intense Terahertz Pulse Electric Fields, Department of Physics, University of Alberta, September 23, 2016

- M. A. B. Narreto; M. Giebel; N. Amer; T. F. Fässler; F. A. Hegmann. 3rd Annual ATUMS Meeting, Talk: Time-resolved Terahertz Spectroscopy of Inverse Opal Ge Films, Jasper, AB, Canada, November 13-15, 2017
- M. A. B. Narreto; M. Giebel; N. Amer; T. F. Fässler; F. A. Hegmann. 8th Graduate Physics Student Association Symposium, Poster: Time-resolved Terahertz Spectroscopy of Inverse Opal Ge Films, Department of Physics, University of Alberta, September 29, 2017
- M. A. B. Narreto; M. Giebel; N. Amer; T. F. Fässler; F. A. Hegmann. Alberta Nanosymposium, Talk: Time-resolved Terahertz Spectroscopy of Inverse Opal Ge Films, Calgary, Alberta, Canada, May 4-5, 2017
- M. A. B. Narreto; A. Lyuleeva; A. Angi; T. Helbich; B. Reiger; P. Lugli; F. A. Hegmann. ATUMS research presentation, Talk: Photoluminescence of CNTs and P3HTs functionalized with SiNSs and SiNCs, University of Alberta, May 16, 2017
- M. A. B. Narreto; A. Lyuleeva; S. Parke; T. Helbich; J. C. Veinot; B. Reiger; E. Rivard; P. Lugli; F. A. Hegmann. Prof. Martin Stutzmann Experimental Semiconductor Physics Group Seminar, Walter Schotkky Institute, Technical University of Munich), Salzburg, Austria, February 9-11, 2017
- M. A. B. Narreto; A. Lyuleeva; S. Parke; T. Helbich; J. C. Veinot; B. Reiger; E. Rivard; P. Lugli; F. A. Hegmann. 2nd Annual ATUMS Meeting. Talk and Poster: Ultrafast Photoluminescence Spectroscopy of Semiconductor and Molecular Materials, Raitenhaslach, Germany, November 6-11, 2016
- M. A. B. Narreto; A. Lyuleeva; S. Parke; T. Helbich; J. C. Veinot; B. Reiger; E. Rivard; P. Lugli; F. A. Hegmann. 7th Graduate Physics Student Association Symposium, Talk: Photoluminescence Spectroscopy of Semiconductor and Molecular Materials, Prize: Runner-Up, Department of Physics, University of Alberta, September 23, 2016
- M. A. B. Narreto; A. Lyuleeva; T. Helbich; J. C. Veinot; B. Reiger; P. Lugli; F. A. Hegmann. Alberta Nanosymposium, Talk: Time-resolved Photoluminescence of Hydrogenated and Dodecyl-functionalized Silicon Nanosheets, Edmonton, Alberta, Canada, May 26-27, 2016